

Ministry of Education and Science of the Russian Federation  
Saint Petersburg National Research University of Information  
Technologies, Mechanics, and Optics

***NANOSYSTEMS:***  
***PHYSICS, CHEMISTRY, MATHEMATICS***

**2020, volume 11(6)**

**Наносистемы: физика, химия, математика**

**2020, том 11, № 6**



# NANOSYSTEMS:

## PHYSICS, CHEMISTRY, MATHEMATICS

### ADVISORY BOARD MEMBERS

**Chairman:** V.N. Vasiliev (*St. Petersburg, Russia*),  
V.M. Buznik (*Moscow, Russia*); V.M. Ievlev (*Voronezh, Russia*), P.S. Kop'ev (*St. Petersburg, Russia*), N.F. Morozov (*St. Petersburg, Russia*), V.N. Parmon (*Novosibirsk, Russia*),  
A.I. Rusanov (*St. Petersburg, Russia*),

### EDITORIAL BOARD

**Editor-in-Chief:** I.Yu. Popov (*St. Petersburg, Russia*)

#### Section Co-Editors:

Physics – V.M. Uzdin (*St. Petersburg, Russia*),  
Chemistry, material science – V.V. Gusarov (*St. Petersburg, Russia*),  
Mathematics – I.Yu. Popov (*St. Petersburg, Russia*).

#### Editorial Board Members:

V.M. Adamyan (*Odessa, Ukraine*); O.V. Al'myasheva (*St. Petersburg, Russia*);  
A.P. Alodjants (*Vladimir, Russia*); S. Bechta (*Stockholm, Sweden*); J. Behrndt (*Graz, Austria*);  
M.B. Belonenko (*Volgograd, Russia*); A. Chatterjee (*Hyderabad, India*); A.V. Chizhov  
(*Dubna, Russia*); A.N. Enyashin (*Ekaterinburg, Russia*), P.P. Fedorov (*Moscow, Russia*);  
E.A. Gudilin (*Moscow, Russia*); V.K. Ivanov (*Moscow, Russia*), H. Jónsson (*Reykjavik, Iceland*);  
A.A. Kiselev (*Durham, USA*); Yu.S. Kivshar (*Canberra, Australia*); S.A. Kozlov  
(*St. Petersburg, Russia*); P.A. Kurasov (*Stockholm, Sweden*); A.V. Lukashin (*Moscow, Russia*);  
I.V. Melikhov (*Moscow, Russia*); G.P. Miroshnichenko (*St. Petersburg, Russia*);  
I.Ya. Mittova (*Voronezh, Russia*); Nguyen Anh Tien (*Ho Chi Minh, Vietnam*); V.V. Pankov  
(*Minsk, Belarus*); K. Pankrashkin (*Orsay, France*); A.V. Ragulya (*Kiev, Ukraine*);  
V. Rajendran (*Tamil Nadu, India*); A.A. Rempel (*Ekaterinburg, Russia*); V.Ya. Rudyak  
(*Novosibirsk, Russia*); D Shoikhet (*Karmiel, Israel*); P Stovicek (*Prague, Czech Republic*);  
V.M. Talanov (*Novocherkassk, Russia*); A.Ya. Vul' (*St. Petersburg, Russia*);  
A.V. Yakimansky (*St. Petersburg, Russia*), V.A. Zagrebnov (*Marseille, France*).

#### Editors:

I.V. Blinova; A.I. Popov; A.I. Trifanov; E.S. Trifanova (*St. Petersburg, Russia*),  
R. Simoneaux (*Philadelphia, Pennsylvania, USA*).

**Address:** University ITMO, Kronverkskiy pr., 49, St. Petersburg 197101, Russia.

**Phone:** +7(812)607-02-54, **Journal site:** <http://nanojournal.ifmo.ru/>,

**E-mail:** [popov1955@gmail.com](mailto:popov1955@gmail.com)

### AIM AND SCOPE

The scope of the journal includes all areas of nano-sciences. Papers devoted to basic problems of physics, chemistry, material science and mathematics inspired by nanosystems investigations are welcomed. Both theoretical and experimental works concerning the properties and behavior of nanosystems, problems of its creation and application, mathematical methods of nanosystem studies are considered.

The journal publishes scientific reviews (up to 30 journal pages), research papers (up to 15 pages) and letters (up to 5 pages). All manuscripts are peer-reviewed. Authors are informed about the referee opinion and the Editorial decision.

# CONTENT

## MATHEMATICS

- A.M. Vorobiev, E.S. Trifanova, I.Y. Popov  
**Resonance asymptotics for a pair quantum waveguides  
with common semitransparent perforated wall** 619

## PHYSICS

- M.N. Potkina, I.S. Lobanov V.M. Uzdin  
**Nonmagnetic impurities in skyrmion racetrack memory** 628

- A.S. Bagmutov, I.Y. Popov  
**Window-coupled nanolayers: window shape influence  
on one-particle and two-particle eigenstates** 636

- K.R. Bushuev, I.S. Lobanov  
**Machine learning method for computation of optimal  
transitions in magnetic nanosystems** 642

- M.P. Faleeva, I.Y. Popov  
**On quantum bit coding by Gaussian beam modes for the quantum  
key distribution** 651

- M.S. Shustin, M.N. Potkina  
**Effective easy-axis anisotropy of the two-sublattice single-chain  
magnet with twisted easy planes** 659

## CHEMISTRY AND MATERIAL SCIENCE

- Dedhila Devadathan, Baiju V., Deepa J.P., Raveendran R.  
**The Novel polyindole based ZnO / MgO nanocomposite adsorbent  
for the removal of heavy metal ions from industrial effluents** 666

- S. Sathya, J. Vijayapriya, K. Parasuraman,  
D. Benny Anburaj, S. Joshua Gnanamuthu  
**ZnO nanoparticles as solar photocatalysts: synthesis,  
effect of annealing temperature and applications** 672

- M.V. Dorokhin, P.B. Demina, Yu.M. Kuznetsov, I.V. Erofeeva,  
A.V. Zdoroveyshchev, M.S. Boldin, E.A. Lantsev, A.A. Popov,  
E.A. Uskova, V.N. Trushin  
**Nanostructured SiGe:Sb solid solutions with improved  
thermoelectric figure of merit** 680

M.E. Belenkov, V.M. Chernov <b>Dependence of the electronic and crystal structure of a functionalized graphene on the concentration of chemically adsorbed fluorine</b>	<b>685</b>
A.A. Naberezhnov, S.A. Borisov, A.V. Fokin, A.Kh. Islamov, A.I. Kuklin, Yu.A. Kumzerov <b>SANS studies of nanostructured low-melting metals at room temperature</b>	<b>690</b>
A.T. Nguyen, H.L.T. Tran, Ph.U.T. Nguyen, I.Ya. Mittova, V.O. Mittova, E.L. Viryutina, V.H. Nguyen, X.V. Bui, T.L. Nguyen <b>Sol-gel synthesis and the investigation of the properties of nanocrystalline holmium orthoferrite</b>	<b>698</b>
M.O. Enikeeva, O.V. Proskurina, D.P. Danilovich, V.V. Gusarov <b>Formation of nanocrystals based on equimolar mixture of lanthanum and yttrium orthophosphates under microwave-assisted hydrothermal synthesis</b>	<b>705</b>
O.I. Shevaleevskiy <b>Perovskite solar cells: recent progress and future prospects</b>	<b>716</b>
A.I. Shuklina, A.V. Smirnov, B.A. Fedorov, S.A. Kirillova, O.V. Almjasheva <b>Structure of nanoparticles in the <math>ZrO_2 - Y_2O_3</math> system, as obtained under hydrothermal conditions</b>	<b>729</b>
<b>Information for authors</b>	<b>739</b>

## Resonance asymptotics for a pair quantum waveguides with common semitransparent perforated wall

A. M. Vorobiev, E. S. Trifanova, I. Y. Popov

ITMO University, Kronverkskiy, 49, St. Petersburg, 197101, Russia  
lenden31@yandex.ru, etrifanova@gmail.com, popov1955@gmail.com

DOI 10.17586/2220-8054-2020-11-6-619-627

A nanostructure model, which is represented as a pair of coupled two-dimensional quantum waveguides with common semitransparent wall, is considered. That wall has small window which induces a resonance state localized near the window. Semitransparency is the reason for the asymptotics difference in comparison with the non-transparent case. Using the matching of asymptotic expansions method, we obtain formulas for resonances and resonance states.

**Keywords:** resonance, resonance state, waveguide, asymptotics.

*Received: 29 November 2020*

### 1. Introduction

There is a large class of mathematical and physical problems concerning “systems with small coupling windows”, actually this means systems of connected quantum waveguides, Helmholtz resonators, and other structures with perturbation caused by small coupling windows. Such systems have long been of interest to physicists and mathematicians. The transport properties of waveguides and other additional phenomena caused by resonators are widely used in electrodynamics, radiophysics and theories of acoustic and electromagnetic waves.

The development of nanoelectronics led to the creation of a new class of objects used inside devices – quantum threads (nanowhiskers), quantum dots, antidots and so on. Of course, “quantum” is the keyword here because studying mesoscopic systems (systems where the coherence of the phases of the electrons is preserved on a scale much larger than atomic) is absolutely impossible if we don't respect quantum properties of electron. Obviously, taking into account the quantum behavior of an electron requires the development of fundamentally new physical, and, most importantly, also mathematical approaches.

When we consider mesoscopic systems, we actually mean studying wave propagation in waveguides and other structures. Properties of this propagation are related to spectral properties of the corresponding mathematical operator. This is usually the Schrödinger operator which coincides with the Laplace operator for the ballistic regime. Resonance phenomena are widely used for development of new nanoelectronic devices. Knowledge about the quasi-eigenvalue asymptotics allows one to ensure a proper control of the electron transmission through the device.

Such problems have a long history. They became interesting for mathematicians and theoretical physics after Rayleigh's work in 1916 [1]. Probably he was the first who successfully considered the Helmholtz resonator from a mathematical point of view. He calculated the real part of the smallest quasi-eigenvalue. Although it was not very significant physical result, that work used a real mathematical approach so it was the beginning of the story. Rayleigh's result was not significant, because the imaginary part of quasi-eigenvalue is much more important – it actually represents time of resonance states existing and it is really important physical metric. Half a century later imaginary part was calculated by Morse and Feshbach [2] using the Rayleigh's method.

Such problems are popular today as well, as they became after first mathematical approaches. Currently, we use term “asymptotic analysis” for big class of problem including resonance phenomena. Great variety of electronic device caused great variety of systems in resonance problems. Firstly, a system can contain different units like quantum waveguides, Helmholtz resonators, angles and so on. Also it can contain combination of such units. There are several examples, such as two connected resonators [3], a single resonator opened to space [4], a pair of waveguides with a common boundary [5] or even a system of waveguides with resonators [6]. System geometry is also changeable factor, so we can vary shape of resonator (like square, circle, arbitrary domain) [7], number of dimensions (plane is not less actual than three-dimensional case) [8], window position and numbers (both are explicit physical factors, but they can lead us to quite different results) [9, 10]. Changing of the boundary conditions in the problem was studied by Gadyshin and Borisov [11].

The core of mathematical approach in this work is “Matching asymptotic expansions of solutions of boundary problems”. This method was described in prior literature [12]. Let's consider a global problem, the solution of which necessitates a similar tool. This method is intended for boundary problems of equations containing naturally occurring

small parameter. This is very typical for mathematical physics problems, in particular for problems with Helmholtz resonator and quantum waveguides where the small parameter characterizes the window size. The most interesting problem is that solution in such problems almost always can't be decomposed into some simple functions. For example, in the Helmholtz resonator with the small perturbation we can't express the above exact decision so we only can use asymptotic expansions.

We will consider a couple of waveguides in which the common wall is semitransparent. Such a system was studied by Exner and Kreicirik in [13, 14] but in terms of spectral and scattering properties. Resonance asymptotics for a single waveguide with semitransparent barrier were considered in [15]. Semitransparency is also related to previous paragraph because, in our case, specific boundary conditions on the common wall are required.

## 2. Preliminaries

Let us describe the system and prepare common formulas, which are required to construct our case-specific asymptotics.

There is a pair of quantum waveguides in two-dimensional Cartesian coordinates with widths  $d_-$  and  $d_+$ . We will consider  $d_- < d_+ < 2d_-$ , which is a very important assumption, as we will see later.

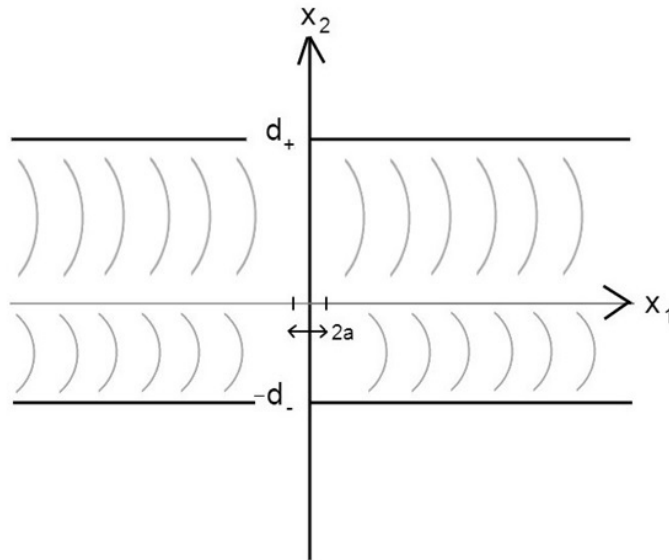


FIG. 1. waveguides with common semitransparent wall

Wall semitransparency is described by the parameter  $\alpha$ . Generally  $\alpha \in (0; +\infty)$ , where zero value means no barrier and infinity means absolutely nontransparent barrier. Zero value is not included because actually it is not a case of considered problem.

As mentioned previously, boundary conditions on the walls are very important. On non-common walls, we choose the Dirichlet conditions, but common wall conditions are more complicated. When a wave passes through the barrier, a jump occurs in the derivative of the considered function  $u(x_1, x_2)$ , so we will set specific boundary conditions:

$$\begin{cases} u_+ = u_-, \\ u'_+ - u'_- = \alpha u, \end{cases} \quad (1)$$

where  $u'_{\pm}$  are vertical derivatives at the top and bottom of the wall. The conditions of such type appear if one considers singular potential supported on hypersurface. These potentials are intensively investigated during last two decades (see, e.g., [16–22]).

We construct asymptotics in window size, so one of the most important parameters is  $a$  – we will consider it as half of the window size.

As mentioned previously, the most important point is selected threshold. In similar problems, resonances are considered near “threshold” values. Threshold is such value of  $\lambda_n$ , that there are no summands with imaginary part exponent in Green's function series which are lower than  $\lambda_n$ . Imaginary exponent corresponds to periodic summands

which mean propagating waves. We will seek terms of asymptotic expansions close to the first threshold  $\lambda_1^- = \left(\frac{\pi}{d_-}\right)^2$ . Choice of  $\left(\frac{\pi}{d_-}\right)^2$  but not  $\left(\frac{\pi}{d_+}\right)^2$  is also key point as we will see later.

“Perturbed” eigenvalue  $k_a^2$ , also known as quasi-eigenfrequency will be denoted as  $k_a$ . The difference between  $k_a^2$  and  $\lambda_1^-$  is actually small value. We will use convenient expansion for its asymptotics:

$$\sqrt{\left(\frac{\pi}{d_-}\right)^2 - k_a^2} = \sum_{j=2}^{\infty} \sum_{i=0}^{[j/2]-1} k_{ji} a^j \ln^i \frac{a}{a_0}. \quad (2)$$

Finally, we can write down system of equations for eigenfunctions in perturbed case:

$$\begin{cases} \psi_a(x) = -\sqrt{\left(\frac{\pi}{d_-}\right)^2 - k_a^2} \cdot \sum_{j=0}^{\infty} a^j P_{j+1} \left( D_y, \ln \frac{a}{a_0} \right) G^+(x, y, k) \Big|_{y=0}, & x \in \Omega^+ \setminus S_{a_0(a/a_0)^{1/2}}, \\ \psi_a(x) = \sum_{j=1}^{\infty} \sum_{i=0}^{[(j-1)/2]} v_{ji} \left(\frac{x}{a}\right) a^j \ln^i \frac{a}{a_0}, & x \in S_{2a_0(a/a_0)^{1/2}}, \\ \psi_a(x) = \sqrt{\left(\frac{\pi}{d_-}\right)^2 - k_a^2} \cdot \sum_{j=0}^{\infty} a^j P_{j+1} \left( D_y, \ln \frac{a}{a_0} \right) G^-(x, y, k) \Big|_{y=0}, & x \in \Omega^- \setminus S_{a_0(a/a_0)^{1/2}}. \end{cases} \quad (3)$$

### 3. Asymptotics construction

#### 3.1. Eigenfunctions for semitransparent wall

Eigenfunctions and corresponding eigenvalues for case without semitransparency and perturbing are well-known:

$$\begin{cases} \psi_n^{\pm}(x) = \sqrt{\frac{2}{d_{\pm}}} \sin \frac{\pi n x_2}{d_{\pm}}, \\ \lambda_n^{\pm} = \left(\frac{\pi n}{d_{\pm}}\right)^2. \end{cases}$$

But we should match conditions (1), so let's consider eigenfunction in such form:

$$\chi_n(x) = \begin{cases} A_n \sin((x_2 - d_+)\nu), & x_2 > 0, \\ B_n \sin((x_2 + d_-)\nu), & x_2 < 0. \end{cases} \quad (4)$$

So we obtain then following equations:

$$\begin{cases} -A_n \sin(d_+\nu) = B_n \sin(d_-\nu), \\ A_n \nu \cos(d_+\nu) - B_n \nu \cos(d_-\nu) = \alpha B_n \sin(d_-\nu). \end{cases} \Leftrightarrow$$

$$\begin{cases} \frac{A_n}{B_n} = -\frac{\sin(d_-\nu)}{\sin(d_+\nu)}, \\ -B_n \frac{\sin(d_-\nu)}{\sin(d_+\nu)} \nu \cos(d_+\nu) - B_n \nu \cos(d_-\nu) = \alpha B_n \sin(d_-\nu). \end{cases} \Leftrightarrow$$

$$\begin{cases} \frac{A_n}{B_n} = -\frac{\sin(d_-\nu)}{\sin(d_+\nu)}, \\ -\nu \operatorname{ctg}(d_+\nu) - \nu \operatorname{ctg}(d_-\nu) = \alpha. \end{cases}$$

$$\chi_n(x) = \begin{cases} -C_n \sin(d_-\nu) \sin((x_2 - d_+)\nu), & x_2 > 0, \\ C_n \sin(d_+\nu) \sin((x_2 + d_-)\nu), & x_2 < 0. \end{cases}$$

$C_n$  is normalizing coefficient. Actually it means that  $\nu$  can be found as solution of equation

$$-\nu \cot(d_+\nu) - \nu \cot(d_-\nu) = \alpha$$

but we won't consider corresponding formulas in details.

**3.2. Green’s function**

Matching of asymptotic expansions corresponding to (3) requires Green’s function calculating. Its common formula for a waveguide is well known [23]:

$$G^\pm(x, y, k) = \sum_{n=1}^\infty \frac{\chi_n(x_2) \cdot \chi_n(y_2)}{2p_n^\pm} \cdot e^{-p_n^\pm(x_1-y_1)},$$

where  $p_n^\pm = \sqrt{\left(\frac{\pi n}{d_\pm}\right)^2 - k_a^2}$ .

For our expressions, it takes the form:

$$\begin{cases} G^+(x, y, k) = \sum_{n=1}^\infty \frac{C_n^2 \sin^2(d_-\nu) \sin((x_2 - d_+)\nu) \sin((y_2 - d_+)\nu)}{2p_n^+} \cdot e^{-p_n^+(x_1-y_1)}, \\ G^-(x, y, k) = \sum_{n=1}^\infty \frac{C_n^2 \sin^2(d_+\nu) \sin((x_2 + d_-\nu) \sin((y_2 + d_-\nu)\nu)}{2p_n^-} \cdot e^{-p_n^-(x_1-y_1)}. \end{cases}$$

The differential operator  $P_n$  from formula (3) can be described as follows:

$$P_0 \left( D_y, \ln \frac{\varepsilon}{\varepsilon_0} \right) = a_{10}^{(0)} I, \quad P_1 \left( D_y, \ln \frac{\varepsilon}{\varepsilon_0} \right) = a_{10}^{(1)} D_y^1, \quad D_y^n = \frac{\partial^n}{\partial n_y^n},$$

$$P_m \left( D_y, \ln \frac{\varepsilon}{\varepsilon_0} \right) = \sum_{q=1}^{m-1} \sum_{i=0}^{[(q-1)/2]} a_{qi}^{(m)} \left( \ln \frac{\varepsilon}{\varepsilon_0} \right)^i D_y^{m-q+1}, \quad m \geq 2.$$

Actually, operator  $D_y$  should be just a combination of n tangent or normal derivatives in dot y. Here, we choose always normal derivatives. Finally, we obtain the following representation for  $D_y^n G$ :

$$D_y^j G^\pm(x, 0, k) = \frac{C_1^2 \sin^2(d_\mp \nu) (\sin(x_2 \nu) \cos(d_\pm \nu) \mp \cos(x_2 \nu) \sin(d_\pm \nu)) D_y^j \sin((y_2 \mp d_\pm) \nu)}{2p_1^\pm} \Big|_{y=0} \cdot e^{-x_1 p_1^\pm} + \Phi_j(x, k) \ln \frac{r}{a_0} + g_j^\pm(x, k) + \sum_{i=0}^{[j/2]} \sum_{t=0}^{j-2i-1} b_{it}^{(j)} r^{-j+2(i+t)} \left( \cos(j-2i)\theta \pm \frac{\alpha}{2(j-2i)} \sin(j-2i)\theta \right). \tag{5}$$

where  $(r, \theta)$  are polar coordinates. Terms  $b_{it}^{(j)}$ ,  $\Phi_j(x, k)$ ,  $g_j^\pm(x, k)$  are analytic in respect to  $\tau$  some vicinity of the point  $\lambda_1$ :

$$b_{00}^j = (-1)^{[(j+1)/2]} (j-1)!/\pi, \quad b_{10}^3 = \frac{k^2}{2\pi} = \frac{\pi}{2d_-^2}, \quad \Phi_{1n}(0, k) = -\frac{\tau^2}{2\pi} = -\frac{\pi}{2d_-^2}.$$

Sines and cosines in last summand are selected in such way because  $D_y^n G$  should satisfy conditions (1).

Let’s notice that the first summand has imaginary part and no k-singularity for  $G^+$  and has no imaginary part but k-singularity for  $G^-$ .

**3.3. Calculating**

Boundary problems for  $v_{ji} \left( \frac{x}{a} \right)$  from (3) can be obtained by the following manner. We substitute the series (3) and (2) into the Helmholtz equation (for  $k = k_a$ ) and then change variables  $\xi = \frac{x}{a}$ . The coefficients in the terms with the same powers of  $a$  and  $\ln \frac{a}{a_0}$  should be equal. Hence, we obtain the following problems:

$$\begin{aligned} \Delta_\xi v_{ji} &= - \sum_{p=0}^{j-3} \sum_{q=0}^{[p/2]} \Lambda_{pq} v_{j-p-2, i-q}, \quad \xi \in R^2 \setminus \gamma, \\ v_{ji} &= 0, \quad \xi \in \gamma, \end{aligned} \tag{6}$$

where  $\gamma = \{\xi | \xi_2 = 0 \wedge \xi_1 \in (-\infty; -1] \cup [1; +\infty)\}$  and  $\Lambda_{pq}$  are the coefficients of the series:

$$k_a^2 = \sum_p \sum_q \Lambda_{pq} a^p \ln^q \frac{a}{a_0}.$$

We can notice for future that (6) gives us the homogeneous Laplace equation for  $v_{10}$  and  $v_{20}$  but for  $v_{30}$  we get the inhomogeneous Laplace equation (Poisson equation) and it looks like  $\Delta_\xi v_{30} = -k_0^2 v_{10}$  because of corresponding  $\Lambda_{00}$  value.

As a next step, we need to introduce operator  $M_{pq}(U)$  – it changes variables in expressions  $U$  ( $\xi = \frac{x}{\varepsilon}$ ,  $\ln r = \ln \rho + \ln \varepsilon$ ) and filters summand with  $\varepsilon^p \ln^q \frac{\varepsilon}{\varepsilon_0} \varphi(\xi)$ . Also  $M_p = \sum_q M_{pq}$ , it is used to get all summand with  $\varepsilon^p$ .

#### 4. Calculating of $k_{20}$

Let's find summand of order  $a^1$  from (3) using this operator.

$$a^{-1}M_1 \left( -\sqrt{\frac{\pi^2}{d_-^2} - k_a^2} \cdot P_1 G^+(x, 0, k_a) \right) = \frac{1}{\pi} k_{20} a_{10}^{(1)} \rho^{-1} \left( \cos \theta + \frac{\alpha}{2} \sin \theta \right), \quad (7)$$

$$a^{-1}M_1 \left( \sqrt{\frac{\pi^2}{d_-^2} - k_a^2} \cdot P_1 G^-(x, 0, k_a) \right) = -\frac{1}{\pi} k_{20} a_{10}^{(1)} \rho^{-1} \left( \cos \theta - \frac{\alpha}{2} \sin \theta \right) + \rho \sin \theta \cdot \frac{a_{10}^{(1)} C_1^2 \sin^2(d_+ \nu) \nu^2 \cos^2(d_- \nu)}{2}. \quad (8)$$

To find  $v_{10}$ , we use the following lemma:

There exist harmonic functions  $Y_{q1}(\xi)$ ,  $Y_{q2}(\xi)$  in  $\mathbb{R}^2 \setminus (\mathbb{R} \setminus (-1; 1))$ ,  $Y_{qs}|_{\mathbb{R} \setminus (-1; 1)} = 0$ ,  $Y_{qs} \in W_{2,loc}^1(\mathbb{R}^2)$ , which have the following differentiable asymptotics by  $\rho$ ,  $\rho \rightarrow \infty$ :

$$Y_{q1} = \begin{cases} -\sum_{j=1}^{\infty} \rho^{-j} a_{qj}^+ \cos j\theta, & \xi_2 > 0, \\ \rho^q a_q^0 \cos q\theta + \sum_{j=1}^{\infty} \rho^{-j} a_{qj}^- \cos j\theta, & \xi_2 < 0, \end{cases}$$

$$Y_{q2} = \begin{cases} -\sum_{j=1}^{\infty} \rho^{-j} b_{qj}^+ \sin j\theta, & \xi_2 > 0, \\ \rho^q b_q^0 \sin q\theta + \sum_{j=1}^{\infty} \rho^{-j} b_{qj}^- \sin j\theta, & \xi_2 < 0. \end{cases}$$

Each harmonic in  $\mathbb{R}^2 \setminus (\mathbb{R} \setminus (-1; 1))$  function  $V$  that is 0 on  $\mathbb{R} \setminus (-1; 1)$  and has the order  $O(\rho^q)$  is a linear combination of  $Y_{j1}(\xi)$ ,  $Y_{j2}(\xi)$ ,  $Y_{j1}(\xi^*)$ ,  $Y_{j2}(\xi^*)$  for  $j \leq q$ , where  $\xi^* = (\xi_1, -\xi_2)$ .

To match terms increasing on  $\rho \rightarrow \infty$  in according to (8) we shall select  $v_{10}(\xi)$  in such way:

$$v_{10}(\xi) = \frac{a_{10}^{(1)} C_1^2 \sin^2(d_+ \nu) \nu^2 \cos^2(d_- \nu)}{2b_1^0} Y_{12}(\xi).$$

Hence, matching terms of order  $\rho^{-1} \sin \theta$  in (7), (8) with  $Y$  can be used as follows:

$$\begin{cases} \frac{a_{10}^{(1)} C_1^2 \sin^2(d_+ \nu) \nu^2 \cos^2(d_- \nu) b_{11}^-}{2b_1^0} = \frac{\alpha}{2\pi} k_{20} a_{10}^{(1)}, \\ b_{11}^- = -b_{11}^+. \end{cases}$$

And finally:

$$k_{20} = \frac{\pi C_1^2 \sin^2(d_+ \nu) \nu^2 \cos^2(d_- \nu) b_{11}^-}{b_1^0 \alpha}.$$

#### 5. Calculating of $k_{30}$

Process of calculating for next coefficient is not much different.

Positive powers of  $\rho$  appear from summands of order  $a^2$  in  $P_1$ ,  $P_2$ , so:

$$a^{-2}M_2 \left( -\sqrt{\frac{\pi^2}{d_-^2} - k_a^2} \cdot P_1 G^+(x, 0, k_a) \right) = \frac{1}{\pi} k_{30} a_{10}^{(1)} \rho^{-1} \left( \cos \theta + \frac{\alpha}{2} \sin \theta \right), \quad (9)$$

$$a^{-2}M_2 \left( \sqrt{\frac{\pi^2}{d_-^2} - k_a^2} \cdot P_1 G^-(x, 0, k_a) \right) = -\frac{1}{\pi} k_{30} a_{10}^{(1)} \rho^{-1} \left( \cos \theta - \frac{\alpha}{2} \sin \theta \right) + \rho^2 \cos 2\theta \cdot \frac{a_{10}^{(1)} C_1^2 \sin^2(d_+ \nu) \nu^3 \cos(d_- \nu) \sin(d_- \nu)}{8}, \quad (10)$$

$$a^{-2}M_2 \left( -\sqrt{\frac{\pi^2}{d_-^2} - k_a^2} \cdot a \cdot P_2 G^+(x, 0, k_a) \right) = \frac{1}{\pi} k_{30} a_{10}^{(2)} \rho^{-2} \left( \cos 2\theta + \frac{\alpha}{4} \sin 2\theta \right), \quad (11)$$

$$\begin{aligned}
 a^{-2}M_2 \left( \sqrt{\frac{\pi^2}{d_-^2} - k_a^2} \cdot a \cdot P_2 G^-(x, 0, k_a) \right) &= -\frac{1}{\pi} k_{30} a_{10}^{(2)} \rho^{-2} \left( \cos 2\theta - \frac{\alpha}{4} \sin 2\theta \right) + \\
 + \rho \sin \theta \cdot \frac{-a_{10}^{(2)} C_1^2 \sin^2(d_+\nu) \nu^3 \cos(d_-\nu) \sin(d_-\nu)}{2}.
 \end{aligned} \tag{12}$$

In (9)–(12) we consider only summands with  $\deg \rho \in \{-1\} \cup N$ , actually right side in (11) is not 0 of course.

Because of given positive degrees of  $\rho$  we shall select  $v_{20}(\xi)$  in such way:

$$v_{20}(\xi) = -\frac{a_{10}^{(2)} C_1^2 \sin^2(d_+\nu) \nu^3 \cos(d_-\nu) \sin(d_-\nu)}{2b_1^0} Y_{12}(\xi) + \frac{a_{10}^{(1)} C_1^2 \sin^2(d_+\nu) \nu^3 \cos(d_-\nu) \sin(d_-\nu)}{8a_2^0} Y_{21}(\xi).$$

Hence matching terms of order  $\rho^{-1} \sin \theta$  and  $\rho^{-1} \cos \theta$  in (7), (8) with  $Y$  can be used as follows:

$$\left\{ \begin{aligned}
 \frac{-a_{10}^{(2)} C_1^2 \sin^2(d_+\nu) \nu^3 \cos(d_-\nu) \sin(d_-\nu)}{2b_1^0} (-a_{21}^+) &= \frac{1}{\pi} k_{30} a_{10}^{(1)}, \\
 \frac{-a_{10}^{(2)} C_1^2 \sin^2(d_+\nu) \nu^3 \cos(d_-\nu) \sin(d_-\nu)}{2b_1^0} (-a_{22}^+) &= \frac{1}{\pi} k_{30} a_{10}^{(2)}, \\
 \frac{a_{10}^{(1)} C_1^2 \sin^2(d_+\nu) \nu^3 \cos(d_-\nu) \sin(d_-\nu)}{8a_2^0} (-b_{11}^+) &= -\frac{\alpha}{2\pi} k_{30} a_{10}^{(1)}, \\
 \frac{a_{10}^{(1)} C_1^2 \sin^2(d_+\nu) \nu^3 \cos(d_-\nu) \sin(d_-\nu)}{8a_2^0} (-b_{12}^+) &= -\frac{\alpha}{4\pi} k_{30} a_{10}^{(2)}, \\
 a_{21}^+ &= a_{21}^-, \\
 a_{22}^+ &= a_{22}^-, \\
 b_{12}^+ &= -b_{12}^-.
 \end{aligned} \right.$$

Finally:

$$k_{30} = \frac{\pi a_{22}^+ C_1^2 \sin^2(d_+\nu) \nu^3 \cos(d_-\nu) \sin(d_-\nu)}{2b_1^0}.$$

Using other equations we can obtain relations for coefficients.

### 6. Calculating of $k_{40}, k_{41}$

As we noticed previously, equation (6) is homogeneous for  $v_{10}(\xi), v_{20}(\xi)$  but becomes more complicated for next step. So we need to solve Poisson equation:  $\Delta_\xi v_{30} = -\frac{\pi^2}{d_-^2} v_{10}, v_{30}(\xi) = 0, \xi \in \gamma, \gamma = \{\xi | \xi_2 = 0 \wedge \xi_1 \in (-\infty; -1] \cup [1; +\infty)\}$ .

Solution of this boundary problem can be presented as:

$$v_{30}(\xi) = \widehat{v}_{30}(\xi) + \widetilde{v}_{30}(\xi),$$

where  $\widehat{v}_{30}(\xi)$  is solution of homogeneous Laplace equation satisfying the boundary conditions (as we seek for previous steps) and  $\widetilde{v}_{30}(\xi)$  is particular solution of inhomogeneous Laplace equation satisfying the boundary conditions.

Let's separate summands of order  $a^3$ . To get all positive degrees of  $\rho$  it's enough to consider  $P_1, P_2, P_3$ . Analogously to (9)–(12), we won't get profit (except coefficients relations) considering any negative degrees except  $-1$ , so we will consider only  $-1$  from negative  $\rho$  degrees:

$$\begin{aligned}
 a^{-3}M_{30} \left( -\sqrt{\frac{\pi^2}{d_-^2} - k_a^2} \cdot P_1 G^+(x, 0, k_a) \right) &= \rho^{-1} \frac{1}{\pi} \left( \cos \theta + \frac{\alpha}{2} \sin \theta \right) \cdot a_{10}^{(1)} k_{40} + \\
 + \rho \sin \theta \cdot \left[ -a_{10}^{(1)} k_{20} g_x^+ + i \frac{C_1^2 \sin^2(d_-\nu) a_{10}^{(1)} k_{20} \nu^2 d_+ \cos^2(d_+\nu)}{2\pi \sqrt{d_+^2 - d_-^2}} \right] - \\
 - \rho \cos \theta \frac{C_1^2 \sin^2(d_-\nu) a_{10}^{(1)} k_{20} \nu \cos(d_+\nu) \sin(d_+\nu)}{2},
 \end{aligned} \tag{13}$$

$$\begin{aligned}
 a^{-3}M_{30} \left( \sqrt{\frac{\pi^2}{d_-^2} - k_a^2} \cdot P_1 G^-(x, 0, k_a) \right) &= -\rho^{-1} \frac{1}{\pi} \left( \cos \theta - \frac{\alpha}{2} \sin \theta \right) a_{10}^{(1)} k_{40} + \\
 + \rho \sin \theta \cdot a_{10}^{(1)} k_{20} g_-^+ - \rho \cos \theta \frac{C_1^2 \sin^2(d_+ \nu) a_{10}^{(1)} k_{20} \nu \cos(d_- \nu) \sin(d_- \nu)}{2} + \\
 + \rho^3 \sin 3\theta \frac{C_1^2 \sin^2(d_+ \nu) a_{10}^{(1)} \nu^4 \cos^2(d_- \nu)}{48},
 \end{aligned} \tag{14}$$

$$a^{-3}M_{30} \left( -\sqrt{\frac{\pi^2}{d_-^2} - k_a^2} \cdot a \cdot P_2 G^+(x, 0, k_a) \right) = 0, \tag{15}$$

$$a^{-3}M_{30} \left( \sqrt{\frac{\pi^2}{d_-^2} - k_a^2} \cdot a \cdot P_2 G^-(x, 0, k_a) \right) = -\rho^2 \cos 2\theta \frac{C_1^2 \sin^2(d_+ \nu) a_{10}^{(2)} \nu^4 \sin^2(d_- \nu)}{8}, \tag{16}$$

$$a^{-3}M_{30} \left( -\sqrt{\frac{\pi^2}{d_-^2} - k_a^2} \cdot a^2 \cdot P_3 G^+(x, 0, k_a) \right) = -\rho^{-1} \left( \cos \theta + \frac{\alpha}{2} \sin \theta \right) \cdot \left[ a_{10}^{(3)} b_{10}^{(3)} k_{20} + 3a_{10}^{(3)} b_{01}^{(3)} k_{20} \right], \tag{17}$$

$$\begin{aligned}
 a^{-3}M_{30} \left( \sqrt{\frac{\pi^2}{d_-^2} - k_a^2} \cdot a^2 \cdot P_3 G^-(x, 0, k_a) \right) &= \\
 \rho \sin \theta \cdot \left[ -\frac{C_1^2 \sin^2(d_+ \nu) a_{10}^{(3)} k_{20} \nu^4 \cos^2(d_- \nu)}{2} - \frac{C_1^2 \sin^2(d_+ \nu) a_{20}^{(3)} k_{20} \nu^3 \cos(d_- \nu) \sin(d_- \nu)}{2} \right] + \\
 + \rho^{-1} \left( \cos \theta + \frac{\alpha}{2} \sin \theta \right) \cdot \left[ a_{10}^{(3)} b_{10}^{(3)} k_{20} + 3a_{10}^{(3)} b_{01}^{(3)} k_{20} \right].
 \end{aligned} \tag{18}$$

Separating summands with positive  $\rho$  degrees we can obtain the following representation for  $\widehat{v}_{30}(\xi)$ :

$$\widehat{v}_{30}(\xi) = \beta_{11} Y_{11}(\xi) + \beta_{12} Y_{12}(\xi) + \beta_{21} Y_{21}(\xi) + \beta_{32} Y_{32}(\xi) + \widetilde{\beta}_{11} Y_{11}(\xi^*) + \widetilde{\beta}_{12} Y_{12}(\xi^*),$$

where:

$$\begin{aligned}
 \beta_{11} &= -\frac{C_1^2 \sin^2(d_+ \nu) a_{10}^{(1)} k_{20} \nu \sin(d_- \nu) \cos(d_- \nu)}{2a_1^0}, \\
 \beta_{12} &= \frac{a_{10}^{(1)} k_{20} g_-^+}{b_1^0} - \frac{C_1^2 \sin^2(d_+ \nu) a_{10}^{(3)} \nu^4 \cos^2(d_- \nu)}{2b_1^0} - \frac{C_1^2 \sin^2(d_+ \nu) a_{20}^{(3)} \nu^3 \sin(d_- \nu) \cos(d_- \nu)}{2b_1^0}, \\
 \beta_{21} &= -\frac{C_1^2 \sin^2(d_+ \nu) a_{10}^{(2)} \nu^4 \sin^2(d_- \nu)}{8a_2^0}, \\
 \beta_{32} &= \frac{C_1^2 \sin^2(d_+ \nu) a_{10}^{(1)} \nu^4 \cos^2(d_- \nu)}{48b_3^0}, \\
 \widetilde{\beta}_{11} &= -\frac{C_1^2 \sin^2(d_- \nu) a_{10}^{(1)} k_{20} \nu \sin(d_+ \nu) \cos(d_+ \nu)}{2a_1^0}, \\
 \widetilde{\beta}_{12} &= \frac{a_{10}^{(1)} k_{20} g_x^+}{b_1^0} - i \frac{C_1^2 \sin^2(d_- \nu) a_{10}^{(1)} k_{20} \nu^2 \cos^2(d_+ \nu) d_- d_+}{2b_1^0 \sqrt{d_+^2 - d_-^2} \pi}.
 \end{aligned}$$

Particular solution of inhomogeneous equation can be obtained using integrating:

$$\begin{aligned}
 \widetilde{v}_{30}(\xi) &= -\frac{\pi^2 a_{10}^{(1)} C_1^2 \sin^2(d_+ \nu) \nu^2 \cos^2(d_- \nu)}{2b_1^0 d_-^2} \times \\
 &\begin{cases} -\frac{1}{2} b_{11}^\pm \rho \ln \rho \sin \theta + \frac{1}{4} b_{12}^+ \sin 2\theta + \sum_{j=3}^{\infty} \frac{b_{1j}^+}{4(j-1)} \rho^{2-j} \sin j\theta, & \xi_2 > 0, \\ \frac{1}{8} b_1^0 \rho^3 \sin \theta + \frac{1}{2} b_{11}^\pm \rho \ln \rho \sin \theta - \frac{1}{4} b_{12}^- \sin 2\theta - \sum_{j=3}^{\infty} \frac{b_{1j}^-}{4(j-1)} \rho^{2-j} \sin j\theta, & \xi_2 < 0. \end{cases}
 \end{aligned}$$

Finally, we obtain the full solution:

$$\begin{aligned}
 v_{30}(\xi) &= \widetilde{\beta}_{11} a_1^0 \rho \cos \theta - \widetilde{\beta}_{12} b_1^0 \rho \sin \theta + \\
 + \frac{\pi^2 a_{10}^{(1)} C_1^2 \sin^2(d_+ \nu) \nu^2 \cos^2(d_- \nu)}{2b_1^0 d_-^2} \cdot &\left[ \frac{1}{2} b_{11}^\pm \rho \ln \rho \sin \theta - \frac{1}{4} b_{12}^+ \sin 2\theta - \sum_{j=3}^{\infty} \frac{b_{1j}^+}{4(j-1)} \rho^{2-j} \sin j\theta \right] - \\
 - \sum_{j=1}^{\infty} (\beta_{11} a_{1j}^+ - \widetilde{\beta}_{11} a_{1j}^- + \beta_{21} a_{2j}^+) \rho^{-j} \cos j\theta &- \sum_{j=1}^{\infty} (\beta_{12} b_{1j}^+ + \widetilde{\beta}_{12} b_{1j}^- + \beta_{32} b_{3j}^+) \rho^{-j} \sin j\theta
 \end{aligned}$$

for  $\xi_2 > 0$  and

$$v_{30}(\xi) = \beta_{11}a_1^0\rho \cos \theta + \beta_{12}b_1^0\rho \sin \theta + \beta_{21}a_2^0\rho^2 \cos 2\theta + \beta_{32}b_3^0\rho^3 \sin 3\theta - \\ - \frac{\pi^2 a_{10}^{(1)} C_1^2 \sin^2(d_+\nu) \nu^2 \cos^2(d_-\nu)}{2b_1^0 d_-^2} \cdot \left[ \begin{array}{l} \frac{1}{8} b_1^0 \rho^3 \sin \theta + \frac{1}{2} b_{11}^\pm \rho \ln \rho \sin \theta - \\ - \frac{1}{4} b_{12}^- \sin 2\theta - \sum_{j=3}^{\infty} \frac{b_{1j}^-}{4(j-1)} \rho^{2-j} \sin j\theta \end{array} \right] + \\ + \sum_{j=1}^{\infty} (\beta_{11}a_{1j}^- - \tilde{\beta}_{11}a_{1j}^+ + \beta_{21}a_{2j}^-) \rho^{-j} \cos j\theta + \sum_{j=1}^{\infty} (\beta_{12}b_{1j}^- + \tilde{\beta}_{12}b_{1j}^+ + \beta_{32}b_{3j}^-) \rho^{-j} \sin j\theta$$

for  $\xi_2 < 0$ .

Matching terms of order  $\rho^{-1} \sin \theta$  gives us:

$$\frac{\alpha}{2} \left( \frac{1}{\pi} a_{10}^{(1)} k_{40} - a_{10}^{(3)} b_{10}^{(3)} k_{20} - 3a_{10}^{(3)} b_{01}^{(3)} k_{20} \right) = -\beta_{12}b_{11}^+ - \tilde{\beta}_{12}b_{11}^- - \beta_{32}b_{31}^+ - \frac{\pi^2 a_{10}^{(1)} C_1^2 \sin^2(d_+\nu) \nu^2 \cos^2(d_-\nu)}{2b_1^0 d_-^2} \cdot \frac{3b_{13}^-}{8} \Leftrightarrow$$

$$\frac{\alpha}{2} \cdot \frac{1}{\pi} a_{10}^{(1)} k_{40} = -\beta_{12}b_{11}^+ - \tilde{\beta}_{12}b_{11}^- - \beta_{32}b_{31}^+ - \frac{3b_{13}^- \pi^2 a_{10}^{(1)} C_1^2 \sin^2(d_+\nu) \nu^2 \cos^2(d_-\nu)}{16b_1^0 d_-^2} + \frac{\alpha}{2} (a_{10}^{(3)} b_{10}^{(3)} + 3a_{10}^{(3)} b_{01}^{(3)}) k_{20} \Leftrightarrow$$

$$k_{40} = \frac{2\pi}{a_{10}^{(1)} \alpha} \left[ -\beta_{12}b_{11}^+ - \tilde{\beta}_{12}b_{11}^- - \beta_{32}b_{31}^+ - \frac{3b_{13}^- \pi^2 a_{10}^{(1)} C_1^2 \sin^2(d_+\nu) \nu^2 \cos^2(d_-\nu)}{16b_1^0 d_-^2} + \frac{\alpha}{2} (a_{10}^{(3)} b_{10}^{(3)} + 3a_{10}^{(3)} b_{01}^{(3)}) k_{20} \right].$$

Imaginary part can be obtained from summand with  $\tilde{\beta}_{12}$ :

$$\text{Im } k_{40} = \frac{-2\pi C_1^4 \sin^2(d_+\nu) \sin^2(d_-\nu) \nu^4 \cos^2(d_+\nu) \cos^2(d_-\nu) d_- d_+ (b_{11}^-)^2}{\alpha \cdot 4(b_1^0)^2 \sqrt{d_+^2 - d_-^2}}.$$

## 7. Conclusion

The suggested procedure can be continued to obtain terms of the asymptotic expansion of any order. The results pertaining to the real part of the resonance, gives one an estimation of the shift of resonance with respect to the threshold. These results can be useful for the description of “quantum waveguide – quantum dot – quantum waveguide” systems. One can find such systems in different nanotechnological applications.

## Acknowledgments

The work was partially financially supported by Russian Science Foundation grant 16-11-10330.

## References

- [1] Lord Rayleigh O.M. The theory of Helmholtz Resonator. *Proceeding of Royal Society*, 1916, **638**, P. 265–275.
- [2] Morse F.M., Feshbach G. Methods of theoretical physics, V. 2. Foreign Literature Publishing House, 1960, 986 p.
- [3] Kiselev A.A., Pavlov B.S. The eigenfrequencies and eigenfunctions of the Laplace operator of the Neumann problem in a system of two coupled resonators. *Theor. Math. Phys.*, 1994, **100**(3), P. 354–366.
- [4] Gadyl'shin R.R. The existence and asymptotics of poles with a small imaginary part for the Helmholtz resonator. *Uspekhi of Mathematical Sciences*, 1997, **52**(313), P. 71–72.
- [5] Borisov D.I. Discrete spectrum of an asymmetric pair of waveguides coupled through a window. *Sb. Math.*, 2006, **197**(4), P. 475–504.
- [6] Achilleos V., Richoux O., et.al. Acoustic solitons in waveguides with Helmholtz resonators: Transmission line approach. *Phys.Rev. E.*, 2015, **91**, P. 023204.
- [7] Martinez A., Ned' elec L. Optimal lower bound of the resonance widths for a Helmholtz tube-shaped resonator. *J. Spectral Th.*, 2012, **2**, P. 203–223.
- [8] Gadyl'shin R.R. A two-dimensional analogue of the Helmholtz resonator with ideally rigid walls. *Translation in Diff. Eq.*, 1994, **30**(2), P. 201–209.
- [9] Gadyl'shin R.R. Influence of the position of the opening and its shape on the properties of a Helmholtz resonator. *Theor. Math. Phys.*, 1992, **93**, P. 1151–1159.
- [10] Borisov D., Exner P. Distant perturbation asymptotics in window-coupled waveguides. I. The non-threshold case. *J. Math. Phys.*, 2006, **47**(10), P. 113502(1–24).
- [11] Borisov D.I., Gadyl'shin R.R. On the spectrum of the Laplacian with frequently alternating boundary conditions. *Theor. Math. Phys.*, 1999, **118**(3), P. 272–277.
- [12] Ilyin A.M. Matching of the asymptotic expansions of solutions. *Science*, 1989, 336 p.
- [13] Exner P., Kreicirik D. Waveguides coupled through a semitransparent barrier: a Birman-Schwinger analysis. *Rev. Math. Phys.*, 2001, **13**, P. 307–334.
- [14] Exner P., Kreicirik D. Quantum waveguides with a lateral semitransparent barrier: spectral and scattering properties. *J. Phys. A*, 1999, **32**, P. 4475.

- [15] Vorobiev A.M., Bagmutov A.S., Popov A.I. On formal asymptotic expansion of resonance for quantum waveguide with perforated semitransparent barrier. *Nanosystems: Physics, Chemistry, Mathematics*, 2019, **10**(4), P. 415–419.
- [16] Behrndt J., Langer M., Lotoreichik V. Boundary triples for Schrodinger operators with singular interactions on hypersurfaces. *Nanosystems: Phys. Chem. Math.*, 2016, **7**(2), P. 290–302.
- [17] Mantile A., Posilicano A. Laplacians with singular perturbations supported on hypersurfaces. *Nanosystems: Phys. Chem. Math.*, 2016, **7**(2), P. 315–323.
- [18] Exner P., Kondej S., Lotoreichik V. Asymptotics of the bound state induced by delta-interaction supported on a weakly deformed plane. *J. Math. Phys.*, 2018, **59**, P. 013051.
- [19] Behrndt J., Exner P., et.al. Approximation of Schroedinger operators with delta-interactions supported on hypersurfaces. *Math. Nachr.*, 2017, **290**, P. 12151248.
- [20] Popov I.Yu. The operator extension theory, semitransparent surface and short range potential. *Math. Proc. Cambridge Phil. Soc.*, 1995, **118**, P. 555–563.
- [21] Popov I.Yu. The extension theory, domains with semitransparent surface and the model of quantum dot. *Proc. Royal Soc. London A*, 1996, **452**(1950), P. 1505–1515.
- [22] Popov I.Yu. The extension theory and the opening in semitransparent surface. *J. Math. Phys.*, 1992, **33**(4), P. 1685–1689.
- [23] Tikhonov A.N., Samarskii A.A. *Equations of Mathematical Physics.*, M.:Science, 1972, 531 p.

**Nonmagnetic impurities in skyrmion racetrack memory**M. N. Potkina<sup>1,2,3</sup>, I. S. Lobanov<sup>1,2</sup>, V. M. Uzdin<sup>1,2</sup><sup>1</sup>ITMO University, Kronverkskiy, 49, St. Petersburg, 197101, Russia<sup>2</sup>St. Petersburg State University, St. Petersburg, 198504, Russia<sup>3</sup>Science Institute and Faculty of Physical Sciences, Univ. of Iceland, 107 Reykjavík, Iceland

potkina.maria@yandex.ru, lobanov.igor@gmail.com, v\_uzdin@mail.ru

**PACS 75.10.Hk, 75.75.-c, 82.20.Pm****DOI 10.17586/2220-8054-2020-11-6-628-635**

The influence of non-magnetic defects of different sizes on the stability and anchoring of skyrmions in race track memory devices has been investigated. The energy surface of the system was built on the basis of the generalized Heisenberg model, which includes exchange, Dzyaloshinskii-Moriya interaction, anisotropy, and an external magnetic field. Minima and saddle points on the energy surface are used to estimate quantitatively the stability and pinning effects for skyrmions. The activation energies for attachment and detachment of skyrmions from defects, collapse and nucleation of skyrmions on a nonmagnetic impurity on a track of finite width are calculated. The joint effect of defects and the proximity of sample boundaries on the stability and localization of skyrmions has been studied. It is shown that skyrmion race track memory can only work if the track width is much greater than four times the skyrmion radius, and the spatial size of defects that can pin a skyrmion is small compared to its own size. Otherwise, the skyrmion will annihilate instead of moving under the action of the spin-polarized current.

**Keywords:** skyrmion, racetrack memory, impurity, pinning, transition state, stability.

*Received: 1 October 2020*

*Revised: 27 October 2020*

**1. Introduction**

Domain wall racetrack memory (DW-RM) was proposed in 2008 [1] as an alternative to hard disk drive (HDD) storage devices to prevent the use of slow mechanical parts and replace them with the movement of domain walls in ferromagnetic nanowires. Since then, hard drives are being supplanted by solid state drives (SSDs) which store data in semiconductor cells, that contain no moving parts and have a read/write speed much faster than HDD. DW-RM is still under development. Many new designs have been proposed [2], which in particular promises higher storage densities than SSDs, due to the three-dimensional organization of magnetic shift registers. After experimental observations of magnetic skyrmions (Sks), they were proposed as a better alternative to domain walls (DWs) as a storage unit for the magnetic racetrack memory [3]. Sks are chiral excitation-like particles ranging in size from a few nanometers to micrometers [4] and are stable up to room temperature [5]. Sk's small size makes them promising for data storage applications [6, 7]. The first studies showed that the pinning by impurities for Sk is very low in contrast to the case of DW [8]. Therefore, critical current density in Sk based racetrack memory (Sk-RM) for performing the shift in the register can be much smaller than that of the DW-RM, and overall power consumption can be reduced. However, theoretical calculations have shown that Sk can be captured by a non-magnetic impurity if the current density is sufficiently small [9]. At present, the problem of the interaction of Sk with impurities is considered very important in the context of the Sk-RM construction [10, 11].

Sk-RM memory control consists of several steps [12]. Each of them was implemented using at least one scheme: writing [13], shift operation [14], and reading [15]. In order to design a reliable device, constrained geometry and spatial defects should be taken into account from the very beginning. Thermal instability and Sk escape through the boundary were considered in [16], demonstrating that for certain parameters Sk in the track lives hours and more. Another important issue is the presence of impurities and point defects, which is usually considered an inevitable disadvantage. A controllable pinning however can be a functional part of the Sk-RM design [17, 18].

Spin transfer torque (STT) is commonly used to move skyrmions in the Sk-RT memory. Although there is usually a certain angle between the direction of the current flow and the velocity of the Sk, called the Hall angle, for certain parameters, when the Hilbert damping is equal to the non-adiabatic STT parameter, the Sk velocity can be parallel to the current [7]. For larger current density and multi-Sk states, more complex behavior such as the rotation of the Sk lattices [19] may appear. Zero Hall angle can be achieved with antiferromagnetic Sk [11, 20] or antiskyrmions for a specific direction of current flow [21, 22].

It is shown that various types of point defects have a different effect on Sk under the current flow. Local disturbance of the anisotropy has little effect on the motion of Sk, since Sk moves around the impurities, avoiding their

capture [8]. However, in disordered magnets with grain defects, new phases, such as Sk multiplication/annihilation and Sk segregation, appear together with the localized and depinned Sk [23] phases. Nonmagnetic impurities can capture Sk at low currents, but the pinning effect strongly depends on the parameters of the system. With certain parameters, even infinitesimal currents can separate the skyrmion from the non-magnetic impurity [9].

Wide range of point impurities demonstrating anti- and ferromagnetic coupling with the host material was analyzed in [24] on the basis of *ab initio* calculations. Different local magnetization and other magnetic characteristic make the impurity repulsive or attractive with respect to Sk, can give different stable positions within Sk, result in different dynamics [25]. Several ways to use impurities in Sk-RM have been proposed. The Sk velocity can unexpectedly be increased in the presence of non-magnetic impurity [9] or a linear defect [26]. The impurities can be used to make repelling and attractive rails for Sk guides [24, 27]. Simultaneous interaction of Sk with several impurities not only change its velocity, but also may lead to new qualitative behaviour [23]. That means that the effect of the restrains should be taken into account especially in restricted geometries such as Sk tracks. Recent modifications of the Sk-RM with enhanced capabilities have more complex geometry than the original design, hence, the effect of geometric frustration can be strongly pronounced in the devices, such as two-lane Sk-RM [28], or random access Sk-RM [29].

In this work, we study the interaction of Sk with an impurity inside a track of different widths. We show that the track width significantly affects the Sk stability and the activation energies of pinning and depinning. The pinned Sk in narrow tracks are not only less stable, but also have a greater barrier for dissociation. Since the critical current required to overcome the activation barrier should have the same qualitative behavior [9], we have concluded that most energy efficient Sk-RM devices should have a track width significantly greater than two Sk diameters. We also study the effect of the size of an atomic-resolved non-magnetic impurity on the activation energies of annihilation/nucleation, pinning/depinning processes. Sk remains stable even for impurities with a size of half the Sk radius. Both nucleation and annihilation barriers decrease with an increase in the impurity size, which makes the formation of Sk on impurities more probable, but the Sk decay rate also increases. The Sk attachment and detachment barrier increases with the impurity size, making the pinning more strong. Since anchoring Sk in the read and write phase may be desirable, this can be achieved by placing a sufficiently large non-magnetic defect at the appropriate location in the track. Both increase of the impurity size and miniaturization of the track (for constant Sk size) lead to rapid growth of depinning barrier and energy consumption by Sk-RM devices.

## 2. Method and simulated system

A thin magnetic film is modelled within the generalized Heisenberg model, which is a standard tool for Sk simulation with atomistic resolution. Exchange interaction, Dzyaloshinskii-Moriya interaction, anisotropy energy and Zeeman energy of interaction with an external field  $\mathbf{B}$  are included in the total energy  $E$ :

$$E = -J \sum_{\langle i,j \rangle} \mathbf{S}_i \cdot \mathbf{S}_j - \sum_{\langle i,j \rangle} \mathbf{D}_{ij} \cdot (\mathbf{S}_i \times \mathbf{S}_j) - \mu \sum_i \mathbf{B} \cdot \mathbf{S}_i - K \sum_i S_{i,z}^2, \quad (1)$$

where summation is taken over all pairs  $\langle i, j \rangle$  of nearest neighbours atoms, and over all atoms  $i$  of the triangular lattice except for impurities. Here,  $J$  is the exchange parameter,  $\mathbf{D}_{ij}$  is the Dzyaloshinskii-Moriya vector lying in the film plane perpendicular to the vector connecting atomic sites  $i$  and  $j$ ,  $K > 0$  is the anisotropy constant for easy axis  $z$  perpendicular to the film,  $\mathbf{B}$  is the external magnetic field parallel to the  $z$ -axis and  $\mathbf{S}_i$  is a three-dimensional vector of unit length in the direction of the magnetic moment at the site  $i$ . The magnitude of the moment,  $\mu$ , is assumed to be the same for all sites; impurities are considered as holes without magnetic moments in the lattice. The numerical values of the parameters correspond to experimentally observed skyrmions in the Pd/Fe/Ir(111) system:  $\mu B = 0.093J$ ,  $K = 0.07J$ ,  $D = |\mathbf{D}_{ij}| = 0.32J$ ,  $J = 7\text{meV}$  [30]. The parameters correspond to isolated free Sk of radius  $4a = 1.08\text{nm}$ , where  $a = 0.27\text{nm}$  is the lattice constant. To simulate a track of finite width we apply periodic boundary conditions along the  $x$ -axis and assume free boundaries along the  $y$ -axis. Track length  $l_x = 60a$  is the same for all simulations and is large enough to avoid Sk self interaction through the boundary. Track width  $l_y = Wa \sin \frac{\pi}{3}$  is a system parameter and varies from  $W = 19$  to  $W = 61$ , where the smallest width corresponds to the smallest stable Sk in the track, and for the largest  $W$  free boundary effect on the Sk energy is less than 0.007%. Nonmagnetic impurities are simulated by removing some of the spins forming a single cluster.

(Meta)stable states correspond to local minima on the multidimensional energy surface defined by the equation (1) for  $E$  as a function of the quantities determining the direction of all magnetic moments  $\mathbf{S}$ . For the given set of parameters the ground state corresponds to the ferromagnetic (FM) state with a perturbation near the impurity and rotating moments on the free boundary. Sk on an impurity and free Sk form two metastable states, where the preferred position of the impurity inside Sk is where the magnetic moments lie in the plane of the film. Sk shape is affected by the impurity. Metastable states were computed using conjugated gradient method in Cartesian coordinates [31]. Activation barriers for transition between pinned, depinned Sk and FM phase were computed using minimum energy

path (MEP), which gives the most probable transition scenario [32]. The maximum along the MEP determines the first-order saddle point on the energy surface and the activation barriers between states. A variant of geodesic nudged elastic band method [33] in Cartesian coordinates was applied to compute MEP with gradient at stationary points smaller than  $10^{-6} J/\text{rad}$ .

### 3. Effects of impurity size and track width

We consider a non-magnetic impurity consisting of 1, 3, 4, 7 and 8 non-magnetic atoms or vacancies that form a compact group on a two-dimensional triangular lattice. According to the previous studies [9], stable positions of the impurity on the pinned Sk are given by the minima of the pinning potential, which roughly corresponds to the local maxima of energy density of the free Sk, neglecting change of the Sk shape under pinning. The Sk on the cluster of impurities tends to rotate and shift to maximize the sum of energy contributions of all spins in Sk replaced by the vacancies. Fig. 1 shows the relative position of the Sk and the impurity corresponding to the minimum of energy. For all considered sizes and shapes of the defect, the impurity cluster is located near the region, where the magnetization vector lies in the film plane. For the elongated clusters the long axis tends to be along curve of constant energy density. Such arrangement was observed experimentally by scanning tunneling microscopy for skyrmions in a PdFe bilayer on the Ir (111) surface [34]. The energy of a Sk at an impurity, as our calculation shows, is lower than that far from the defect, which may be the possible explanation, why Skys are often created on the impurities.

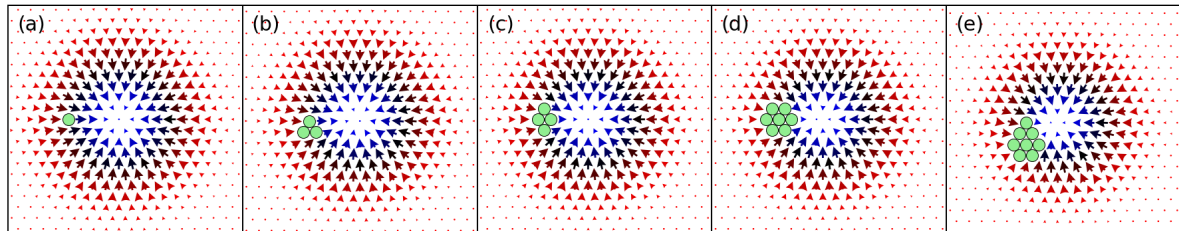


FIG. 1. Location of a skyrmion at non-magnetic defects consisting of (a) 1, (b) 3, (c) 4, (d) 7, (e) 8 atoms, corresponding to the minimum energy. Arrows show in-plane direction of magnetic moments, color denotes their out of plane component (red is for moment oriented along the external field, and blue for the opposite orientation). Impurities are marked by green dots.

Previous research has shown that repulsion from the free boundary significantly affects the shape of Sk and its stability up to disappearance of Sk metastable state for very narrow tracks [35, 36]. Despite the fact that Sk on the impurity has lower energy than the free Sk, the activation barrier for collapse of the pinned Sk is also lower than for the free one, making the pinned Sk less stable. In the proposed circuits [24], where Sk motion is directed by an impurities chain, as well as in Sk-RM [3], both interaction with impurities and effect of the boundary simultaneously affect Sk stability. The question arises how impurities in combination with track boundaries will influence the skyrmion localization and collapse. To answer this question, we calculated the MEP and energy barriers for pinning/depinning and for annihilation/nucleation processes for each impurity size shown in Fig. 1. The MEPs for attachment of skyrmion to seven-atomic impurity (1-2-3) and subsequent collapse (3-4-5) are shown in Fig. 2. Magnetic configurations along the MEPs are shown in insets. The pinned Sk state (3) has lower energy than the free Sk (1) in all considered cases, which in turn is significantly larger than the energy of the FM state meaning that the Sk phase corresponds to isolated Skys. Energy of the transition state (TS) (2) for the pinning process depends on the defect size and is higher for larger defects and narrower tracks. The energy of TS (4) for the annihilation process increases with the size of the impurity as well as with the compression of the track. Relative energies of TS (2) and TS (4) depend on the system parameters as will be shown below. Sk escape through the boundary is also possible, however the process typically proceeds in two steps: the depinning and after that the escape, except of very narrow tracks. Escape of the free Sk through the boundary was studied in [36], where crossover between collapse and escape is found depending on the external field.

The barriers for localization of a skyrmion on a defect (a) and for detachment from it (b) are shown in Fig. 3 for various impurity sizes as a function of track width  $W$ . For any particular size of the impurity the pinning barrier is less than barrier for the detachment, which is in agreement with the previous results [20, 36]. The difference in the activation energies means that Sk will occupy nonmagnetic impurities if thermal energy will be enough to overcome the barrier for attachment but not so large to dissociate from defect immediately.

Both barriers for the pinning of Sk to the defect and for the reverse process increase with the defect size. Therefore, pinning and depinning are less likely for larger defects. The barrier for the pinning is practically independent of the

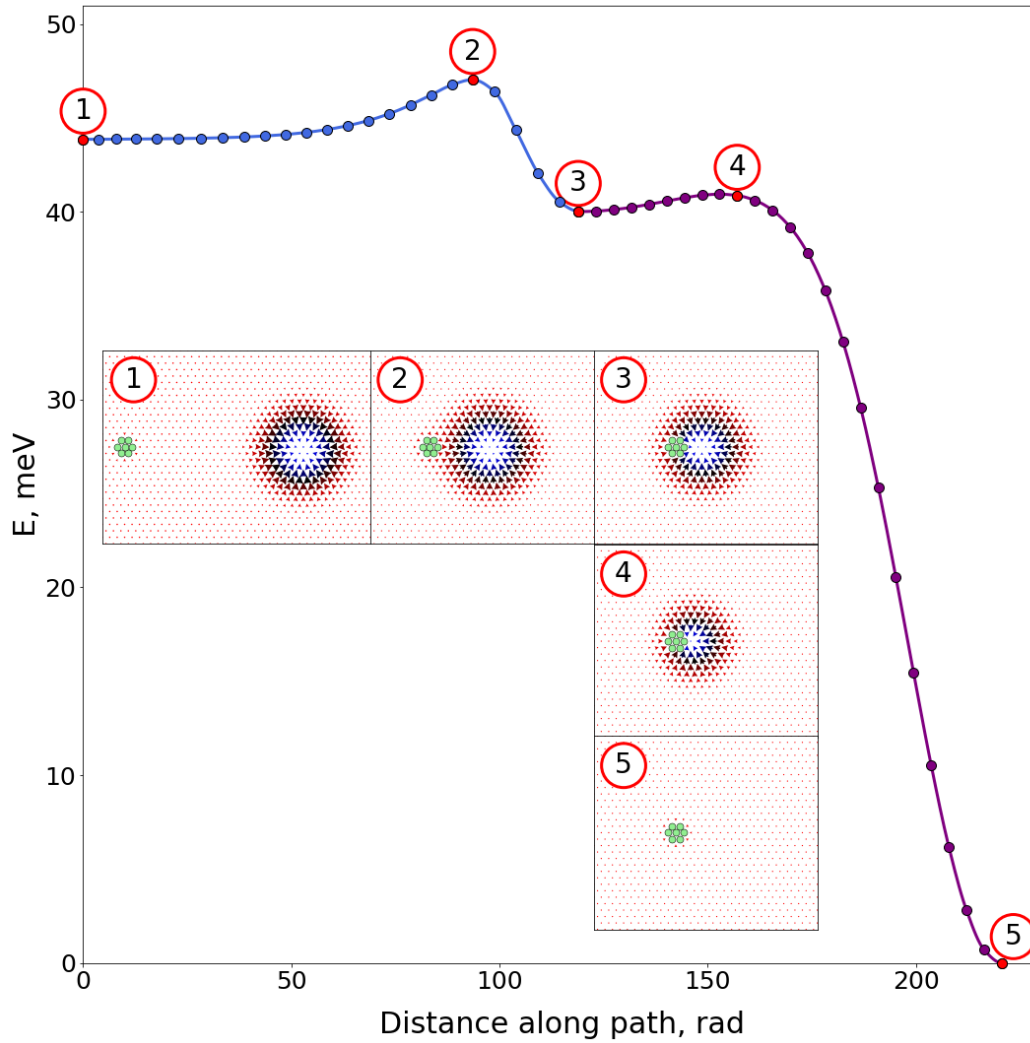


FIG. 2. Curve 1-2-3 represents the MEP between a skyrmion far from the defect and a skyrmion localized at a 7-atom nonmagnetic defect. Curve 3-4-5 represents the MEP between the skyrmion localized at the defect and the FM state with impurity. The insets show magnetic configurations along the MEPs. States 2 and 4 correspond to saddle points. Skyrmion is localized inside a track with a width of 61 atoms.

width of the track, being slightly smaller for narrow tracks. On the other hand, the activation energy for detachment rapidly increases when the track width becomes less than five Sk diameters, sharply enlarging the strength of fixation of the defect in the narrow track. The effect manifests itself for nonmagnetic defects of all sizes, although it is less pronounced for large defects. Since the critical current for the Sk motion over the nonmagnetic impurities can be estimated by the depinning barrier, the overall energy consumption by Sk-RM will be significantly higher in narrow tracks than for free Sk.

As track width is decreased, Sk decay rate became larger. When both the proximity of the sample boundary and non-magnetic defects act on Sk, its stability is expected to decrease even more. The smallest track width at which a Sk may exist increases with increase of the defect size, e.g. Sk localized at eight-atomic defect is not stable for  $W < 50$ , but Sk on the single site defect is stable up to  $W = 20$ . The non-magnetic defect significantly reduces the activation barrier for the collapse of a skyrmion in comparison with annihilation in a homogeneous medium. For example, the barrier for the decay of a skyrmion on a defect of seven atoms is less than 1 meV; without such a defect on a track of the same width, the barrier is 42 meV [35,36]. The energy barrier for the collapse decreases with track width for each impurity size, as shown in Fig. 4a. The decrease is faster for smaller defects and becomes fast when the track diameter

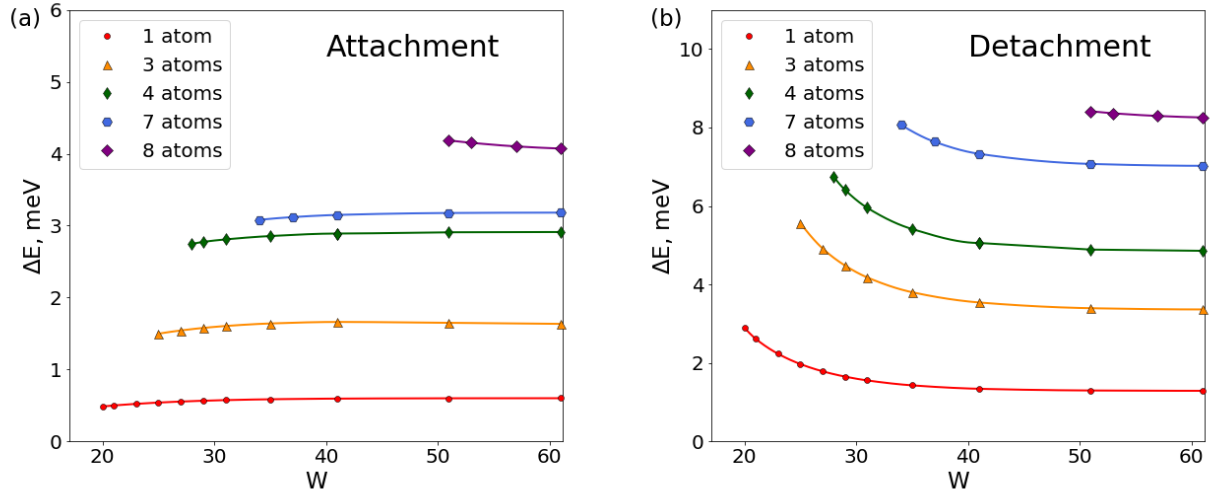


FIG. 3. Energy barrier for attachment (a) and detachment (b) of skyrmion from a defect of different sizes, depending on the width of the track  $W$ .

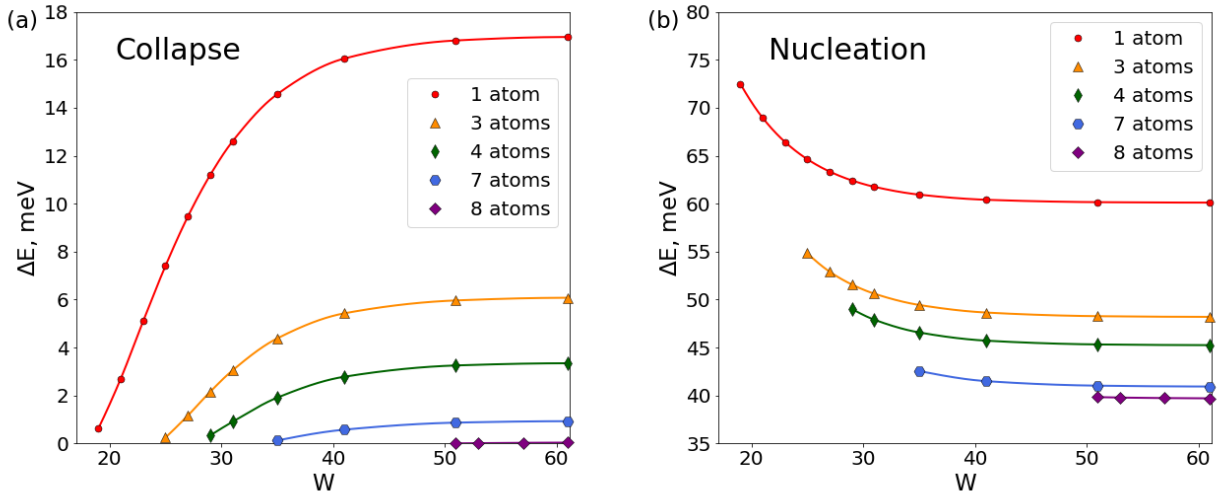


FIG. 4. Energy barrier for annihilation (a) and nucleation (b) of a skyrmion on impurities of different sizes depending on the track width  $W$ .

is less than five Sk for all defect sizes. This means that in narrow lanes, Sk is not only difficult to separate from the defect, but Sk is likely to be destroyed during separation.

The nucleation barrier decreases with the size of the defect in the same way as the annihilation barrier. Therefore, the state near the large defect is regularly perturbed creating new Sk's and annihilating them. In the presence of a depinning current, such impurity can be used as Sk generators. In contrast to the behavior of the activation energy for the collapse, the nucleation barrier increases with decreasing track width (Fig. 4b); therefore, the Sk concentration in narrow tracks will be extremely low. The influence of boundaries is less for localization-delocalization processes than for collapse-nucleation ones, because the configuration of the lateral part of a skyrmion interacting with an impurity changes weakly when a skyrmion is compressed by boundaries, while the entire skyrmion becomes elliptical and has a smaller radius.

A pinned Sk can be removed from the impurity by current flow or it can come off due to thermal vibrations, but it can also collapse during the process. In Sk-RM devices Sk collapse is undesirable, except of the read/write stages,

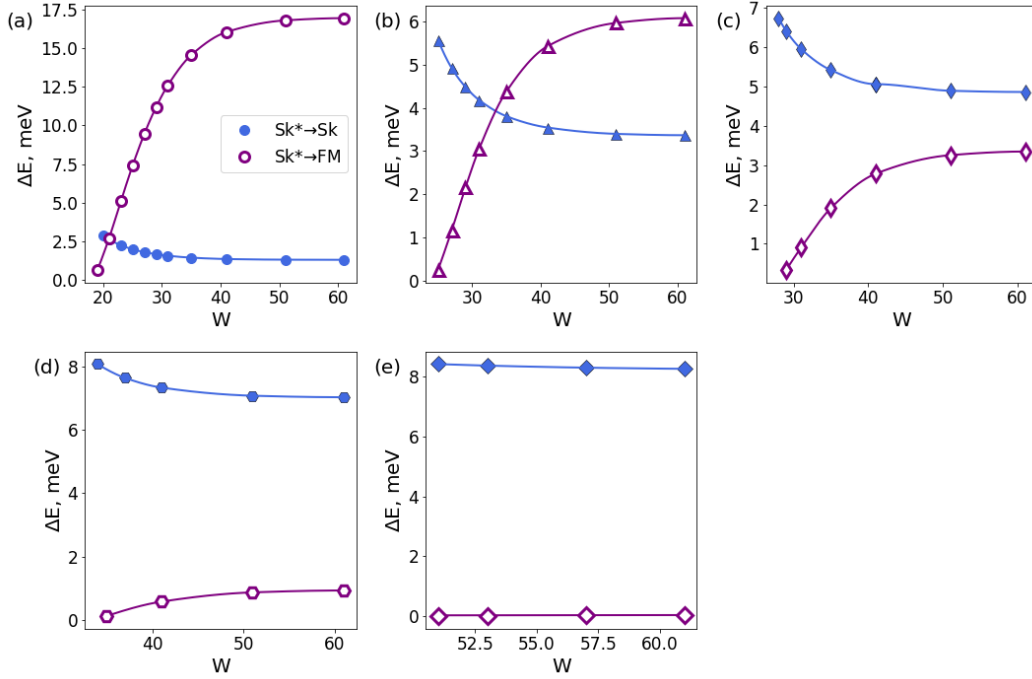


FIG. 5. Dependence of energy barriers for the detachment of a skyrmion from a defect and for annihilation of a skyrmion for various impurity sizes: (a) 1 atom, (b) 3 atoms, (c) 4 atoms, (d) 7 atoms, (e) 8 atoms on the width of the track.

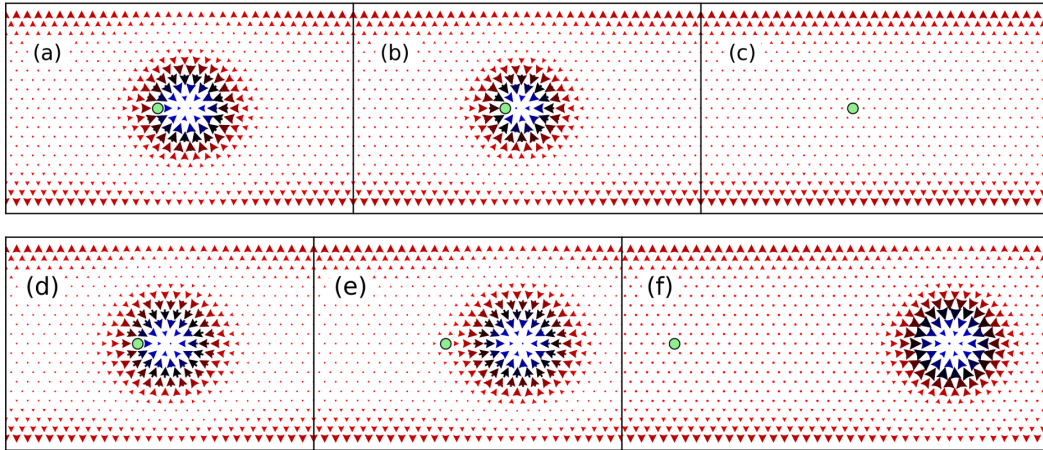


FIG. 6. Upper row: Configurations along MEP for skyrmion annihilation at one-atomic impurity: (a) initial minimum corresponding to skyrmion localized at impurity (b) saddle point (c) final minimum corresponding to FM state with impurity. Lower row: Configurations along MEP for skyrmion detachment from one-atomic impurity: (d) initial minimum corresponding to skyrmion localized at impurity (e) saddle point (f) final minimum corresponding to skyrmion far from impurity.

hence the depinning barrier is expected to be lower than the collapse activation energy. The actual barriers relation is however parameters dependent. The barriers for the Sk detachment and for the collapse at the impurity are compared in Fig. 5 as a function of the track width. For small defects (consisting of one and three atoms), the track width determines which process will be more probable: with a large width, the skyrmion is more likely to detach from impurity, and with a small one, it more likely collapses. There is crossover between these processes, the corresponding track width is the smallest one applicable in Sk-RM devices. For example, for one-atomic impurity the crossover occurs at the track width corresponding to  $W = 21$ . For this situation Fig. 6 shows the magnetic configurations along the MEPs for

collapse and for detachment from a defect: the initial state, the saddle point, and the final state. But, as shown in Fig. 5 c,d,e, if the defect is large, the barrier for collapse is always smaller than for detachment, and under random influences, for example, due to thermal fluctuations, skyrmions will likely collapse without dissociation from the defect. Using the activation barrier as a loose estimate for the critical current, we conjecture that Sk-RM is not functioning in the presence of defects larger than width of Sk domain wall, approximately.

#### 4. Acknowledgements

This work was funded by Russian Science Foundation (Grant 19-42-06302). MNP acknowledges the Icelandic Research Fund for financial support.

#### References

- [1] Parkin S.S.P., Hayashi M., Thomas L. Magnetic domain-wall racetrack memory. *Science*, 2008, **320**(5873), P. 190–194.
- [2] Mittal S. A survey of techniques for architecting processor components using domain-wall memory. *ACM Journal on Emerging Technologies in Computing Systems (JETC)*, 2016, **13**(2), P. 1–25.
- [3] Fert A., Cros V., Sampaio J. Skyrmions on the track. *Nature Nanotechnology*, 2013, **8**, P. 152–156.
- [4] Wiesendanger R. Nanoscale magnetic skyrmions in metallic films and multilayers: a new twist for spintronics. *Nature Reviews Materials*, 2016, **1**(7), P. 16044.
- [5] Soumyanarayanan A., Raju M., Oyarce A.L.G., Tan A.K.C., Im M.Y., Petrović A.P., Ho P., Khoo K.H., Tran M., Gan C.K., Ernult F., Panagopoulos C. Tunable room-temperature magnetic skyrmions in Ir/Fe/Co/Pt multilayers. *Nature Materials*, 2017, **16**(9) P. 898–904.
- [6] Fert A., Reyren N., Cros V. Magnetic skyrmions: advances in physics and potential applications. *Nature Reviews Materials*, 2017, **2**, P. 17031.
- [7] Finocchio G., Büttner F., Tomasello R., Carpentieri M., Kläui M. Magnetic skyrmions: from fundamental to applications. *Journal of Physics D: Applied Physics*, 2016, **49**(42), P. 423001.
- [8] Iwasaki J., Mochizuki M., Nagaosa N. Universal current-velocity relation of skyrmion motion in chiral magnets. *Nature Communications*, 2013, **4**(1), P. 1463.
- [9] Müller J., Rosch A. Capturing of a magnetic skyrmion with a hole. *Physical Review B*, 2015, **91**(5), P. 054410.
- [10] Back C.H., Cros V., Ebert H., Everschor-Sitte K., Fert A., Garst M., Ma T., Mankovsky S., Monchessy T., Mostovoy M.V., Nagaosa N. The 2020 skyrmionics roadmap. *Journal of Physics D: Applied Physics*, 2020, **53**(36), P. 363001.
- [11] Everschor-Sitte K., Masell J., Reeve R.M., Kläui M. Perspective: Magnetic skyrmions - Overview of recent progress in an active research field. *Journal of Applied Physics*, 2018, **124**(24), P. 240901.
- [12] Sampaio J., Cros V., Rohart S., Thiaville A., Fert A. Nucleation, stability and current-induced motion of isolated magnetic skyrmions in nanostructures. *Nature Nanotechnology*, 2013, **8**(11), P. 839.
- [13] Romming N., Hanneken C., Menzel M., Bickel J.E., Wolter B., von Bergmann K., Kubetzka A., Wiesendanger R. Writing and Deleting Single Magnetic Skyrmions. *Science*, 2013, **341**(6146), P. 636–639.
- [14] Hayashi M., Thomas L., Moriya R., Rettner Ch., Parkin S.S.P. Current-Controlled Magnetic Domain-Wall Nanowire Shift Register. *Science*, 2008, **320**(5873), P. 209–211.
- [15] Crum D.M., Bouhassoune M., Bouaziz J., Schweflinghaus B., Blügel S., Lounis S. Perpendicular reading of single confined magnetic skyrmions. *Nature Communications*, 2015, **6**(1), P. 8541.
- [16] Bessarab P.F., Müller G.P., Lobanov I.S., Rybakov F.N., Kiselev N.S., Jónsson H., Uzdin V.M., Blügel S., Bergqvist L., Delin A. Lifetime of racetrack skyrmions. *Scientific Reports*, 2018, **8**(1), P. 3433.
- [17] Yan Z.R., Liu Y.Z., Guang Y., Feng J.F., Lake R.K., Yu G.Q., Han X.F. Robust Skyrmion Shift Device Through Engineering the Local Exchange-Bias Field. *Physical Review Applied*, 2020, **14**(4), P. 044008.
- [18] Suess D., Vogler C., Bruckner F., Heistracher P., Slanove F., Abert C. Spin Torque Efficiency and Analytic Error Rate Estimates of Skyrmion Racetrack Memory. *Scientific Reports*, 2019, **9**(1), P. 4827.
- [19] Everschor K., Garst M., Binz B., Jonietz F., Mühlbauer S., Pfeleiderer C., Rosch A. Rotating skyrmion lattices by spin torques and field or temperature gradients. *Physical Review B*, 2012, **86**(5), P. 054432.
- [20] Potkina M.N., Lobanov I.S., Jnsson H., Uzdin V.M. Skyrmions in antiferromagnets: Thermal stability and the effect of external field and impurities. *Journal of Applied Physics*, 2020, **127**(21), P. 213906.
- [21] Potkina M.N., Lobanov I.S., Tretiakov O.A., Jónsson H., Uzdin V.M. Antiskyrmions in Ferromagnets and Antiferromagnets: Stability and Dynamics, 2019. arXiv preprint, arXiv:1906.06383v2.
- [22] Potkina M.N., Lobanov I.S., Tretiakov O.A., Jnsson H., Uzdin V.M. Stability of Long-lived Antiskyrmions in Mn-Pt-Sn Material. *Physical Review B*, 2020, **102**(13), P. 134430.
- [23] Koshibae W., Nagaosa N. Theory of current-driven skyrmions in disordered magnets. *Scientific Reports*, 2018, **8**(1), P. 6328.
- [24] Fernandes I.L., Bouaziz J., Blügel S., Lounis S. Universality of defect-skyrmion interaction profiles. *Nature Communications*, 2018, **9**(1), P. 4395.
- [25] Fernandes I.L., Chico J., Lounis S. Impurity-dependent gyrotropic motion, deflection and pinning of current-driven ultrasmall skyrmions in PdFe/Ir(111) surface. *Journal of Physics: Condensed Matter*, 2020, **32**(42), P. 425802.
- [26] Castell-Queralt J., González-Gómez L., Del-Valle N., Sanchez A., Navau C. Accelerating, guiding, and compressing skyrmions by defect rails. *Nanoscale*, 2019, **11**(26), P. 12589–12594.
- [27] Stosic D., Luderimir B.T., Miloevi V.M. Pinning of magnetic skyrmions in a monolayer Co film on Pt(111): Theoretical characterization and exemplified utilization. *Physical Review B*, 2017, **96**(21), P. 214403.
- [28] Müller J. Magnetic skyrmions on a two-lane racetrack. *New Journal of Physics*, 2017, **19**, P. 1740006.
- [29] Zhu D., Kang W., Li S., Huang Y., Zhang X., Zhou Y., Zhao W. Skyrmion Racetrack Memory With Random Information Update/Deletion/Insertion. *IEEE Transactions on Electron Devices*, 2018, **65**(1), P. 87–95.

- [30] Hagemester J., Romming N., von Bergmann K., Vedmedenko E.Y., Wiesendanger R. Stability of single skyrmionic bits. *Nature Communications*, 2015, **6**(1), P. 8455.
- [31] Lobanov I.S., Uzdin V.M. The lifetime of big size topological chiral magnetic states. Estimation of the pre-exponential factor in the Arrhenius law, 2020. arXiv preprint, arXiv:2008.06754 [cond-mat.mtrl-sci]
- [32] Bessarab P.F., Uzdin V.M., Jónsson H. Harmonic transition-state theory of thermal spin transitions. *Physical Review B*, 2012, **85**(18), P. 184409.
- [33] Bessarab P.F., Uzdin V.M., Jónsson H. Method for finding mechanism and activation energy of magnetic transitions, applied to skyrmion and antivortex annihilation. *Computer Physics Communications*, 2015, **196**, P. 335–347.
- [34] Hanneken C., Kubetzka A., von Bergmann K., Wiesendanger R. Pinning and movement of individual nanoscale magnetic skyrmions via defects. *New Journal of Physics*, 2016, **18**(5), P. 055009.
- [35] Uzdin V.M., Potkina M.N., Lobanov I.S., Bessarab P.F., Jónsson H. The effect of confinement and defects on the thermal stability of skyrmions. *Physica B: Condensed Matter*, 2018, **549**, P. 6–9.
- [36] Uzdin V.M., Potkina M.N., Lobanov I.S., Bessarab P.F., Jónsson H. Energy surface and lifetime of magnetic skyrmions. *Journal of Magnetism and Magnetic Materials*, 2018, **459**, P. 236–240.

## Window-coupled nanolayers: window shape influence on one-particle and two-particle eigenstates

A. S. Bagmutov, I. Y. Popov

ITMO University, Kronverkskiy, 49, Saint Petersburg, 197101, Russia

bagmutov94@mail.ru, popov1955@gmail.com

DOI 10.17586/2220-8054-2020-11-6-636-641

In this work, we present a number of numerical results for the bound state energies of one and two-particle systems in two adjacent 3D layers, connected through a window. We investigate the relation between the shape of a window and energy levels, as well as number of eigenfunction's nodal domains.

**Keywords:** nanolayer, eigenfunction, Hartree–Fock model.

*Received:* 13 September 2020

*Revised:* 1 November 2020

### 1. Introduction

In general, the waveguides can be modelled by the Dirichlet Laplacians in infinite planar strips and multidimensional layers, the spectra of which is a focus of many works in past decades. The problem is trivial as long as the strip or layer is straight, because one can then employ separation of variables. However, already a local perturbation such as bending, deformation, or a change of boundary conditions can produce a non-empty discrete spectrum. As examples of possible perturbations, we indicate local deformation of the boundary condition [1, 2], bending [3–6] or twisting [7, 8] the waveguide. Perturbation by adding a potential is considered in [9], and by a magnetic field in [10, 11], or by a second order differential operator as in [12]. The type of systems we are interested in is two adjacent parallel waveguides, coupled by the windows cut out in a common boundary. The two-dimensional case was studied quite intensively, we refer here to [13–20] (see also references therein). It was shown that the perturbation by the window(s) is a negative one, i.e., it leads to the presence of the isolated bound states below the essential spectrum; the latter is invariant w.r.t. to the window(s). In the case of one window, it was shown in [13, 15, 17] that widening the window one produces more and more isolated eigenvalues. They appear when the windows length passes through certain critical values; this phenomenon was studied in detail and the asymptotics expansions for the emerging eigenvalues were obtained, see [13, 15, 19]. In the three-dimensional case of window-coupled layers, it was shown that a small window generates one simple isolated eigenvalue emerging from the threshold of the essential spectrum [18]. This work also contains two-sided asymptotic estimates for the eigenvalue. The asymptotic expansion for this eigenvalue has been constructed formally in [21]. In the present work, we present a number of numerical results for two adjacent layers in  $\mathbb{R}^3$ , coupled through holes in the common boundary. Such a system was studied in [22], where it was shown that the window produces eigenvalues emerging from the threshold of essential spectrum, as the window passes through certain critical shapes. We continuously change window shape and look at evolution of bound states with fixed number and position of nodal domains. The questions concerning to number and position of nodal domains for the Dirichlet Laplacians are a point of active research. The first step was Courant's nodal theorem, and since then, various different cases have been investigated, such as nodal domains for quantum graphs ([29, 30]) and in a sphere ([31]). Also, within this geometry, we consider a case of two particles, with different shapes of a window. We make numerical calculations, with the application of Hartree–Fock estimation method (for the Hartree approximation accuracy, see [28]). As for previous studies of the multi-particle problems in deformed waveguides, see, e.g., [23–27]. We are concerned with the following two questions: how the energies of bound states and number/position of nodal domains are dependent on shape of a window and what is the relation between one and two-particle cases.

### 2. Hartree–Fock approach

Let us describe the Hartree–Fock model and algorithm.

We start with the Hamiltonian

$$\hat{H} = \sum_k (-\Delta_k + U_k) + \frac{1}{2} \sum_{\substack{j,k \\ j \neq k}} V_{jk} = \sum_k \hat{H}_k + \frac{1}{2} \sum_{\substack{j,k \\ j \neq k}} V_{jk}, \quad (1)$$

where  $\Delta_k = \frac{\partial^2}{\partial x_k^2}$  is the Laplace operators, acting on coordinates  $x_k$  of the  $k$ -th particle,  $U_k$  is the potential of the external field,  $V_{j,k}$  is the potential of particles interaction,  $\hat{H}_k = (-\Delta_k + U_k)$ . Then, we should approximate many-particle wave function by the Slater determinant:

$$\Psi(x_1, x_2, \dots, x_n) = \frac{1}{\sqrt{n!}} \begin{vmatrix} \psi_1(x_1) & \dots & \psi_n(x_1) \\ \dots & \dots & \dots \\ \psi_1(x_n) & \dots & \psi_n(x_n) \end{vmatrix}, \quad (2)$$

where  $\psi_k$  are single-particle wave functions and  $x_k = (r_k, s_k)$ , where  $r_k$  and  $s_k$  are the spatial and spin coordinates of the  $k$ -th particle. Following the Hartree–Fock method, we insert (2) in (1) and use variation of energy functional  $\langle \Psi | \hat{H} \Psi \rangle$  to get the Hartree–Fock equations:

$$\left[ \hat{H}_k + \sum_{j, j \neq k} \int \psi_j^*(x_j) V_{jk} \psi_j(x_j) dx_j \right] \psi_k(x_k) - \sum_{j, j \neq k} \left( \int \psi_j^*(x_j) V_{jk} \psi_k(x_j) dx_j \right) \psi_j(x_k) = E_k \psi_k(x_k). \quad (3)$$

Then, we should consider the spin of the particles. We ignore the spin-orbit interaction. Let  $n^\uparrow$  be the number of particles with spin 0.5 and  $n^\downarrow$  particles with spin  $-0.5$ . The wave functions of these particles are  $\psi_k^\uparrow$  and  $\psi_k^\downarrow$ . Then, due to independence of  $V_{jk}$  from the spin variable, one has

$$\int \psi_j^*(x_j) V_{jk} \psi_k(x_j) dx_j = \delta_{s_j s_k} \int \psi_j^{*s_j}(r_j) V_{jk} \psi_k^{s_k}(r_j) dr_j, \quad (4)$$

where  $\delta_{s_j s_k}$  is the Kronecker symbol, indices  $s_j, s_k$  take values  $\uparrow, \downarrow$ .

As an interaction potential, we use the delta-potential:  $V_{jk} = U \delta(r_j - r_k)$ , where  $U$  is a constant. Using the delta-potential and (4), from (3) we get the following system:

$$\begin{aligned} H_k \psi_j^\uparrow(r_k) + U \sum_j^{n^\downarrow} \left( |\psi_j^\downarrow(r_k)|^2 \psi_k^\uparrow(r_k) \right) &= E_k^\uparrow \psi_k^\uparrow(r_k), \quad (k = 1, \dots, n^\uparrow), \\ H_k \psi_j^\downarrow(r_k) + U \sum_j^{n^\uparrow} \left( |\psi_j^\uparrow(r_k)|^2 \psi_k^\downarrow(r_k) \right) &= E_k^\downarrow \psi_k^\downarrow(r_k), \quad (k = 1, \dots, n^\downarrow). \end{aligned} \quad (5)$$

To solve the system, we used the following iterative algorithm:

- (1) Find one-particle stationary solutions for a case of potential  $U_k = F z_k$  and arbitrarily choose  $N$  solutions as initial approximations for  $\psi_i(x_i)$ .
- (2) For each particle, calculate a potential  $P_i = U \sum_j |\psi_j(x_j)|^2$ , where sum includes particles with the opposite spins, then, use it to calculate a set of solutions.
- (3) From each of  $N$  sets choose a bound solution. (Here we can use arbitrary additional criteria, to speed up the process.)
- (4) Check if new solutions are close enough to previous ones. If not, return to step 2.

### 3. Results

The system we are studying consists of two adjacent infinite 3D layers of constant width, with a common border. In the common border there is a window, connecting two layers. We consider bound states for systems of one and two particles with delta interaction. On the borders of layers, we assume the Dirichlet boundary condition. The main focus of the study is the relation between shape of a window and energies of bound states. We consider two types of windows: elliptic windows and windows shaped like Cassini ovals (peanut-shaped), which transform into two separate circular windows. We show the dependence of bound state energy  $E$  as a function of parameter  $d$ , which in the case

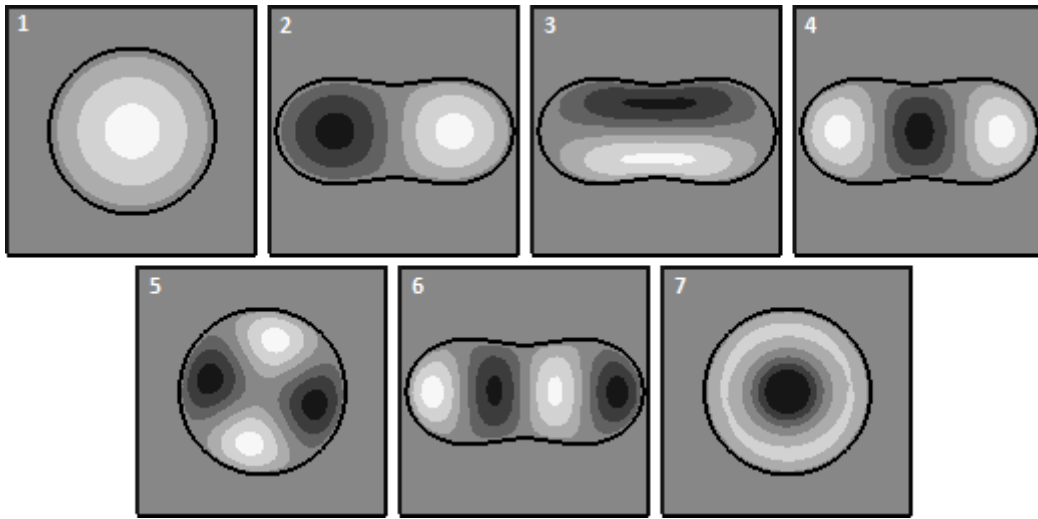


FIG. 1. Examples of bound state types, as a 2D slice along window's plane. Labels: 1 – one, 2 – two, 3 – transversal two, 4 – three, 5 – square four, 6 – row four, 7 – ring.

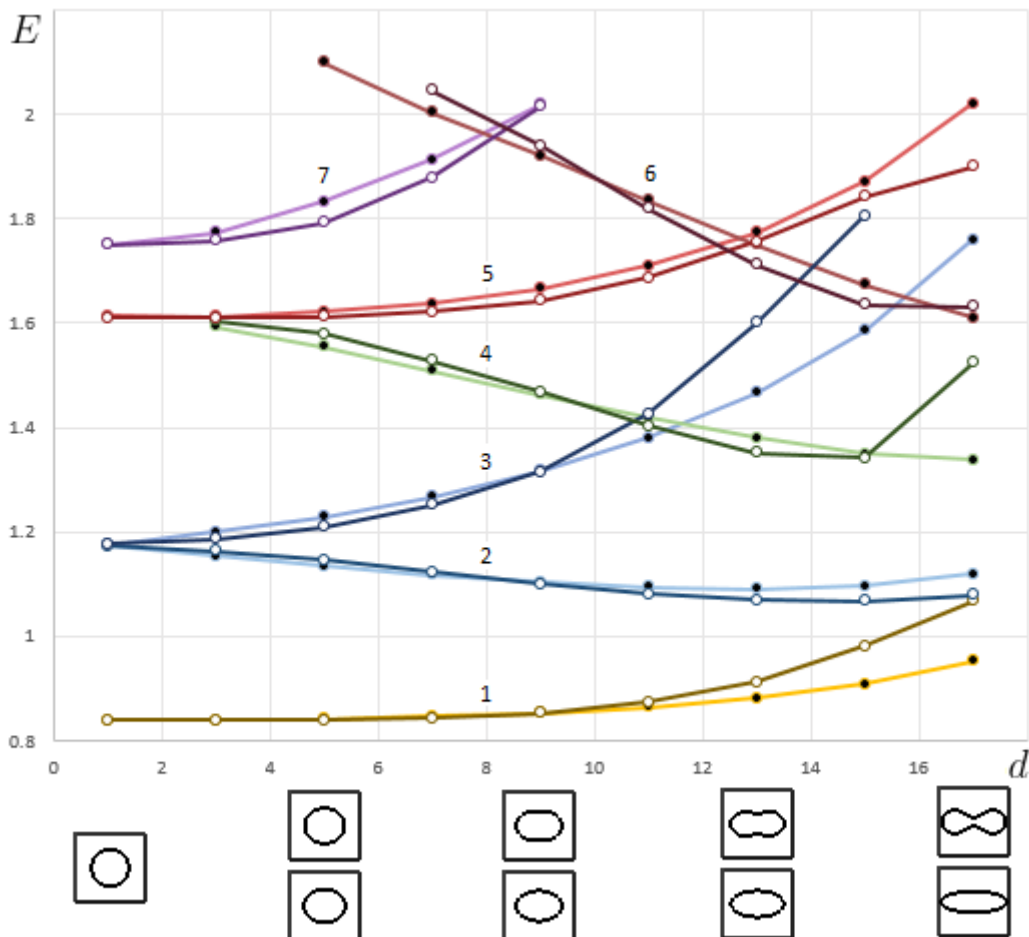


FIG. 2. Energies of different one-particle types of states as functions of distance between foci of Cassini ovals. The faint lines represent energies of the same type for the elliptic window of the same width. All windows have the same area. The types are labeled according to the enumeration in Fig. 1. Shapes of the windows are shown below the  $d$  axis.

of Cassini ovals, represents a distance between oval foci and for two apertures it is a distance between their centers. Ellipses are chosen to match Cassini ovals' width. All windows have the same area.

First, we consider the case of one particle. If we examine 2D slice of eigenfunctions through the plane of a window, we can distinguish a number of persistent types of solutions, categorized by the number and position of nodal domains. The Courant's nodal theorem states that for the Dirichlet Laplacian, the number of nodal domains can not exceed the index of a state in a list of all states, sorted by eigenvalues. In our case, we will first follow seven types, which are shown in Fig. 1. These types of bound states show consistent behavior with change of parameter  $d$  and their energies change in different ways, according to the geometry of the type. Results for the cases of an elliptic and Cassini oval shaped windows are shown on the Fig. 2.

As we can see, for the most types, bound levels tend in the positive direction with the increasing deformation of circular window, but for certain types, it is reversed. Let us note some features. The first two states for Cassini ovals converge to the same energy, because the first state evolve in a copy of the second, but with both peaks pointing in the same direction. The transversal two (3) and the three (4) types are affected by the final Cassini evolution most of all (the energy of the former for the last aperture is too high for the shown range), because their constant-sign zone is in the center and deformed by the closing gap. With the further closing of a bridge, type (4) will get closer to type (6), but in conformity with the Courant's theorem, will not exceed it.

For the two-particle system, we consider the Cassini oval window, and look at the lowest bound energy level for the different strengths of delta interaction (see Fig. 3), and compare it to the first two levels from the Fig. 2. We also extended the deformation of the window, adding three states with two circular windows at the end. For the case of two holes, all different strengths have indistinguishable on our scale levels. The plot shows that with the increase of interaction strength two particle states tend from first, toward second type of state. The energy for two holes is almost independent on the distance between the holes.

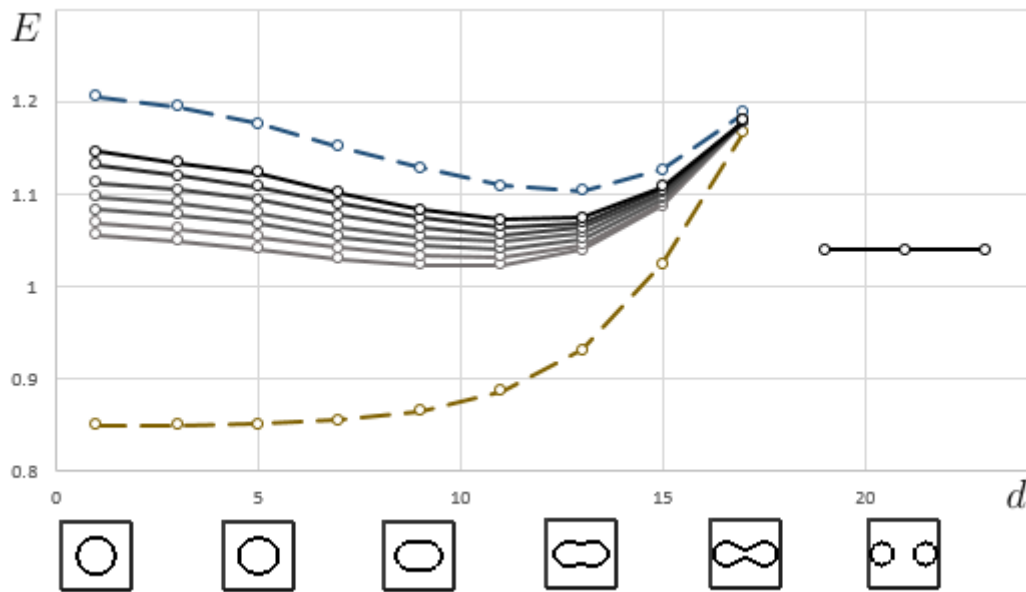


FIG. 3. Lowest bound energies for two particles. Dotted plots represent the first two one-particle types for Cassini Windows from Fig. 2 for comparison, which differ because of different precision for the case of more complex computation. Grey lines represent energies of each particle in lowest two-particle bound states, each line corresponds to different strength of delta-interaction. The strengths used: 30, 50, 85, 140, 250, 500, 1000 (arbitrary units) from the lowest to the highest line respectively. For the case of two separate circular openings all strengths have very similar energies, plotted in the right part.

On the Fig. 4 we compare the energies of elliptic bound state with the Cassini ones for the same interaction strength. The plots for different interaction strengths show the same relations.

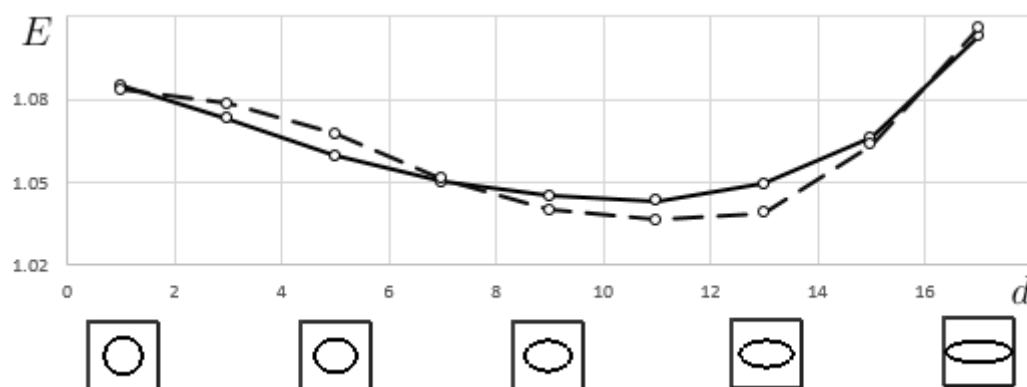


FIG. 4. Comparison of two particle bound state energies for elliptic window (solid line), with corresponding levels for Cassini oval window (dotted line).

### Acknowledgements

This work was partially financially supported by grant 20-31-90050 of Russian Foundation for Basic Research.

### References

- [1] Borisov D., Exner P., Gadylshin R., Krejcirik D. Bound states in weakly deformed strips and layers, *Annales Henri Poincare*, 2001, **2**(3), P. 553–572.
- [2] Bulla W. and Renger W. Existence of bound states in quantum waveguides under weak conditions. *Lett. Math. Phys.*, 1995, **35**(1), P. 1–12.
- [3] Duclos P. and Exner P. Curvature-induced bound state in quantum waveguides in two and three dimensions. *Rev. Math. Phys.*, 1995, **7**(1), P. 73–102.
- [4] Duclos P., Exner P., Stovicek P. Curvature-induced resonances in a two-dimensional Dirichlet tube. *Annales Henri Poincare*, 1995, **62**(1), P. 81–101.
- [5] Chenaud B., Duclos P., Freitas P. and Krejcirik D. Geometrically induced discrete spectrum in curved tubes. *Diff. Geom. Appl.*, 2005, **23**(2), P. 95–105.
- [6] Exner P. and Vugalter S.A. Bound States in a Locally Deformed Waveguide: The Critical Case. *Lett. Math. Phys.*, 1997, **39**(1), P. 59–68.
- [7] Briet Ph., Kovarik H., Raikov G. and Soccorsi E. Eigenvalue asymptotics in a twisted waveguide. *Comm. PDE*, 2009, **34**(8), P. 818–836.
- [8] Ekholm T., Kovarik H. and Krejcirik D. A Hardy inequality in twisted waveguides. *Arch. Rat. Mech. Anal.*, 2008, **188**(2), P. 245–264.
- [9] Duclos P. and Exner P. Curvature-induced bound state in quantum waveguides in two and three dimensions. *Rev. Math. Phys.*, 1995, **7**(1), P. 73–102.
- [10] Borisov D., Ekholm T. and Kovarik H. Spectrum of the magnetic Schrodinger operator in a waveguide with combined boundary conditions. *Annales Henri Poincare*, 2005, **6**(2), P. 327–342.
- [11] Ekholm T. and Kovarik H. Stability of the magnetic Schrodinger operator in a waveguide. *Comm. PDE*, 2005, **30**(4), P. 539–565.
- [12] Grushin V.V. On the eigenvalues of finitely perturbed laplace operators in infinite cylindrical domains. *Math. Notes*, 2004, **75**(3), P. 331–340.
- [13] Borisov D. Discrete spectrum of a pair of non-symmetric waveguides coupled by a window. *Sbornik Mathematics*, 2006, **197**(4), P. 475–504.
- [14] Borisov D. and Exner P. Distant perturbation asymptotics in window-coupled waveguides. I. The non-threshold case. *J. Math. Phys.*, 2006, **47**(11), P. 113502-(1–24).
- [15] Borisov D., Exner P. and Gadylshin R. Geometric coupling thresholds in a two-dimensional strip. *Journal of Mathematical Physics*, 2002, **43**(12), P. 6265–6278.
- [16] Bulla W., Gesztesy F., Renger W., Simon B. Weakly coupled bound states in quantum waveguides. *Proc. Amer. Math. Soc.*, 1997, **125**(5), P. 1487–1495.
- [17] Exner P., Seba P., Tater M., and Van?ek D. Bound states and scattering in quantum waveguides coupled laterally through a boundary window. *J. Math. Phys.*, 1996, **37**(10), P. 4867–4887.
- [18] Exner P. and Vugalter S. Bound-state asymptotic estimate for windowcoupled Dirichlet strips and layers. *J. Phys. A.*, 1997, **30**(22), P. 7863–7878.
- [19] Gadylshin R. On regular and singular perturbation of acoustic and quantum waveguides. *Comptes Rendus Mechanique*, 2004, **332**(8), P. 647–652.
- [20] Vorobiev A.M., Bagmutov A.S., Popov A.I. On formal asymptotic expansion of resonance for quantum waveguide with perforated semitransparent barrier. *Nanosystems: Physics, Chemistry, Mathematics*, 2019, **10**(4), P. 415–419.
- [21] Popov I.Yu. Asymptotics of bound states and bands for laterally coupled waveguides and layers. *J. Math. Phys.*, 2002, **43**(1), P. 215–234.
- [22] Borisov D. On the spectrum of two quantum layers coupled by a window. *J. Phys. A: Math. Theor.*, 2007, **40**(19), P. 5045–5066.
- [23] Linde H. Geometrically induced two-particle binding in a waveguide. *J. Phys. A: Math. Gen.*, 2006, **39**(18), P. 5105–5114.
- [24] Popov S.I., Gavrilov M.I. and Popov I.Yu., Two interacting particles in deformed nanolayer: discrete spectrum and particle storage. *Phys. Scripta*, 2012, **86**(3), P. 035003.
- [25] Melikhov I.F. and Popov I.Yu. Hartree–Fock approximation for the problem of particle storage in deformed nanolayer. *Nanosystems: Physics, Chemistry, Mathematics*, 2013, **4**(4), P. 559–563.

- [26] Popov I.Y., Bagmutov A.S., Melikhov I.F., Najjar H. Numerical analysis of multi-particle states in coupled nano-layers in electric field. *AIP Conference Proceedings*, 2020, **2293**, P. 360006.
- [27] Popov I.Y., Melikhov I.F. Multi-particle bound states in window-coupled 2D quantum waveguides. *Chinese J. of Physics – Taipei*, 2015, **53**(3), P. 0802/1–12.
- [28] Calogero F. and Degasperis A. Comparison between the exact and Hartree solutions of a one-dimensional many-body problem. *Phys. Rev. A*, 1975, **11**(1), P. 265–269.
- [29] Band R., Berkolaiko G., Raz H. et al. The Number of Nodal Domains on Quantum Graphs as a Stability Index of Graph Partitions. *Commun. Math. Phys.*, 2012, **311**, P. 815–838.
- [30] Band R., Oren I., Smilansky U. Nodal domains on graphs – how to count them and why? In: *Analysis on graphs and its applications. Proc. Sympos. Pure Math.*, 2008, **77**, P. 5–27.
- [31] Helffer B., Sundqvist M.P. On nodal domains in Euclidean balls. *Proc. Amer. Math. Soc.*, 2016, **144**(11), P. 4777–4791.

**Machine learning method for computation of optimal transitions in magnetic nanosystems**K. R. Bushuev<sup>1</sup>, I. S. Lobanov<sup>1,2</sup><sup>1</sup>ITMO University, Kronverkskiy, 49, Saint Petersburg, 197101, Russia<sup>2</sup>Saint Petersburg State University, Saint Petersburg, 198504, Russia

lobanov.igor@gmail.com

**PACS 75.10.Hk, 75.75.-c, 82.20.Pm, 07.05.Mh****DOI 10.17586/2220-8054-2020-11-6-642-650**

Minimum energy path (MEP) is an important tool for computation of activation barriers and transition rates for magnetic systems. Recently, new methods for numeric computation of MEP were proposed based on conjugate gradient and L-BFGS methods [1] significantly improved convergence rate compared to nudged elastic band (NEB) method. Due to lack of strict mathematical theory for MEP optimization other more effective methods are expected to exist. In this article, we propose a machine learning based approach to search for MEP computation methods. We reformulate the NEB method as a differentiable transformation in the space of all paths parametrized by a family of metaparameters. Using rate of convergence as the loss function, we train NEB optimizer to find optimal metaparameters. This meta learning technique can be the basis for deriving new optimization methods for computing MEP and other non-classical optimization problems.

**Keywords:** Transition state, minimum energy path, machine learning, meta learning.

*Received: 3 October 2020*

*Revised: 6 November 2020*

**1. Introduction**

Magnetic systems are prominent candidates for the implementation of high-density storage and computing devices [2, 3]. The manufacturing of reliable magnetic devices is possible only using materials such that lifetime of metastable states carrying the information is long, but the states can be created and annihilated cheaply due to an external control such as spin current [4,5]. Since the desirable lifetime is many orders of magnitude larger than the period of the Larmor precession, direct simulation of stochastic dynamics is not suitable for the decay rate estimation [6–11]. State of the art transition rate estimation is based on transition rate theory [12–15]. The two most challenging tasks of the lifetime estimation, both in harmonic transition state theory and in Langer’s theory, are computation of determinants of Hessian matrix of energy (an analog of the partition function) and computation of the transition state itself [12, 16]. The transition state can be computed by an undirected search as an arbitrary first order saddle point on the energy surface using dimer method and similar approach [17–19]. The methods unfortunately do not return transition states of minimal energy, therefore the methods are of limited use for the activation barrier calculation. The activation barriers between two known metastable states are commonly computed by minimum energy path (MEP) based methods, such as nudged elastic band (NEB) [20–27]. Despite the high popularity of these methods, the mathematical theory of optimization methods for MEP evaluation is not well established, which is partially related to the multi-objective nature of the optimization, where the energy of each image on the path should be optimized as well as distribution of images along the path. Although higher order methods for MEP computation exist, such as conjugate gradient or L-BFGS [1], the steepest descent based method is still widely used. Due to lack of the mathematical theory, the optimization methods suffer from instability and poor choice of optimization parameters.

In recent years optimization theory, especially gradient based methods, gained acceptance due to the wide spread of machine learning methods. The right choice of the training method and meta parameters reduce training time and sometimes make problems tractable, which are not solvable by other means. Methods for tuning of optimization parameters for a specific class of problems belong to a subfield of machine learning called meta learning or learning to learn. In this article, we propose to use a meta learning approach to improve parameters of NEB method for MEP computation of magnetic systems.

There are several approaches to meta learning or in other words to optimization of the training procedure by machine learning techniques. In [28], genetic algorithms were used to speeding up the learning rate by changes of the learners policy based on “success-story algorithm”. Meta-neural network approach in [29] demonstrated great potential to replace standard optimizer methods with neural network that was trained for solving optimization tasks. In [30], the automatic tuning of parametric learning rules is shown to lead to better generalization properties for the model. A new method for boosting up learner’s average reward based on the inductive bias is proposed in [31] thus reducing the average number of interactions during training. A new type of neural network layers, called long short

term memory (LSTM), was introduced in [32]; the layer has a memory of events and improves adoption using historical data. Meta learning techniques were used to perform better generalization for training not only for single task but for groups of tasks with similar structure [33]. The meta learning approach can boost the training of neural network on large scale datasets [34]. In [35], it was shown that neural networks can be substituted for classical training algorithm in a wide range of applications. The widely used Adam training method [36] can be considered as kind of the meta learning, since it tunes its parameters according to the training history. The Adam method outperforms non-adaptive methods such as stochastic gradient descent and more primitive adaptive methods such as AdaGrad. A general strategy for training optimizers for black-box systems based on reinforcement learning was stated in [37, 38], the approach demonstrated good generalization ability. Studies in optimization of hyper parameters for neural networks with LSTM layers allow us to conclude that such architecture can boost up convergence rate in lot of application [39–42].

In the section 2 we recall basics of harmonic transition state theory for magnetic systems and give review of methods for MEP calculation focusing on NEB with improved tangent (IT) estimate. Then in the section 3 we modify IT-NEB to be suitable for machine learning, introduce criteria of comparison of discretized MEP, and implement a meta learning method to improve rate of convergence of the modified IT-NEB method.

## 2. Magnetic system transition state theory

In the Heisenberg model, states of magnetic system are defined by vectors of magnetic moments  $\mathbf{M}_n$ , where  $n$  is an atom of the lattice. Length  $\mu_n$  of every vector is assumed to be fixed, since its relaxation time is much shorter than period of Larmor precession, therefore the state is convenient to express in terms of moments orientations  $\mathbf{S}_n$ ,  $\mathbf{M}_n = \mu_n \mathbf{S}_n$ . When doing analysis of chiral states in magnetic systems, it is common to consider energy of the system given by the following quadratic form [8, 9]:

$$E[\mathbf{S}] = - \sum_{\langle n,k \rangle} J_{n,k} \mathbf{S}_n \cdot \mathbf{S}_k - \sum_{\langle n,k \rangle} \mathbf{D}_{n,k} \cdot (\mathbf{S}_n \times \mathbf{S}_k) - \sum_{n,m} K_m (\mathbf{K}_m \cdot \mathbf{S}_n)^2 - \sum_n \mathbf{H}_n \cdot \mathbf{S}_n,$$

where the summation is taken over pairs of interacting atoms  $\langle n, k \rangle$ ,  $J_{n,k}$  are Heisenberg exchange constants,  $\mathbf{D}_{n,k}$  are Dzyaloshinskii-Moriya vectors,  $K_m$  and  $\mathbf{K}_m$  are easy axis or easy plane anisotropy constant and vector respectively,  $\mathbf{H}_n$  is the external magnetic field. Since the length of the direction vectors are restricted by constraints  $\mathbf{S}_n^2 = 1$ , special efforts should be undertaken to satisfy the constraints. The simplest way is to introduce spherical coordinates  $\phi_n, \theta_n$ :  $\mathbf{S}_n = (\cos \phi_n \cos \theta_n, \sin \phi_n \cos \theta_n, \sin \theta_n)$ . The spherical coordinates approach suffers from singularities near the poles  $\theta_n = \pm\pi/2$ , which leads to loss of precision in optimization and may ruin convergence; in this case, trigonometric functions are involved in the computation, thus reducing its speed. There are more advanced approaches that do not have these disadvantages, e.g. Cartesian coordinates based approach with Lagrange multipliers [16], an approach utilizing stereographic projection coordinates [43], rotation matrix based formulation [1]. In the article we will use spherical coordinates to facilitate idea of machine learning and avoid details of implementation of the advance methods.

In the thermal equilibrium with temperature  $T$ , the distribution of states is given by Boltzmann distribution with probability density:  $\rho(\mathbf{S}) = Z^{-1} \exp(-E[\mathbf{S}]/(k_B T))$ , where  $Z$  is the partition function. The magnetic system typically has many metastable states, such as ferromagnetic state, domain walls, skyrmions, skyrmionium, bag of skyrmions and other exotic particle-like states [43]. The states (especially domain wall and skyrmions) are proposed to be used as information carrier for magnetic data storage and processing devices [3–5]. To ensure operability of the devices, the metastable states should have long enough lifetimes, but they also should be easily annihilated and created in a controllable way to write the information. Stochastic dynamics of the magnetic systems can be simulated numerically integrating LandauLifshitzGilbert (LLG) equation [44]:

$$\frac{d\mathbf{S}_n}{dt} = -\gamma \mathbf{S}_n \times \mathcal{H}_n + \gamma \alpha \mathbf{S}_n \times \frac{d\mathbf{S}_n}{dt} + W(t), \quad \mathcal{H}_n = -\frac{\partial E[\mathbf{S}]}{\partial \mathbf{S}_n} + \tau_n,$$

where  $\gamma$  is the gyromagnetic ratio,  $\alpha$  is the damping constant,  $W(t)$  is the thermal noise, and  $\mathcal{H}$  is the effective magnetic field including torques  $\tau$  due to spin currents. The direct simulation of the dynamics is not suitable for transition rate computation, since typically, the transitions are very rare events [8, 9]. Although there are attempts to solve the problem by path sampling [45], the widespread approach is transition state theory (TST). In TST, the probability to leave the state within a given time is estimated as the product of probabilities to be in the vicinity of the transition state and the probability to cross the dividing surface. Commonly, the transition rate is derived in the harmonic approximation giving rise to harmonic transition state theory [13] and Langers theory [6, 14]. In harmonic

transition state theory the transition rate is expressed as:

$$\kappa = \frac{\kappa^{dyn} \kappa^{ent}}{2\pi} e^{-\frac{\Delta E}{k_B T}}, \quad \kappa^{ent} = \sqrt{\frac{\det H^{MS}}{|\det H^{TS}|}},$$

where  $\Delta E$  is the activation barrier, that is, the difference between the energy of the transition state (TS) and the metastable state (MS). The entropy prefactor is expressed in terms of determinants of the Hessian matrices  $H^{TS}$  and  $H^{MS}$  of energy at TS and MS, respectively. The dynamical prefactor is expressed in term of the eigenvector of Hessian corresponding to the negative eigenvalue (HTST, see details in [16]), or it equals to the positive eigenvalue of the matrix of the linearized LLG equation (Langer's theory). Computation of the determinant of the Hessians is the most challenging part in the formula, however recently a fast algorithm for computation of the determinants was proposed in [16] suitable for local interactions; long range dipole-dipole interaction probably can be taken into account by introducing a demagnetizing field [46]. Another important ingredient of the computation is search of TSs, which are first order saddle points on the energy surface. There are two main classes of methods for TS computation: undirected methods and minimum energy path (MEP) based methods. Undirected methods start from an initial state (commonly a metastable state) and follow minimum energy mode until the state is attracted to a TS, see e.g. dimer method [17] and review [18, 19]. Undirected methods are suitable, when resulting state of transition is not known.

For analysis of transitions between two given metastable states, MEP is the primary tool [20]. By definition MEP is a continuous path in the state space, connecting the metastable states, such that maximum of the energy on the path is the smallest among all possible paths. The maximum of the energy on the path is TS, clearly the TS is a first order saddle point of energy. According to the definition, the MEP is not unique, since essentially only the maximum is fixed. To restrict the set of MEP, it is common to assume that all point of the MEP obtain higher energy under variation of the path, hence all the points of the PATH have lowest possible energy. Since energy functional is generally quite complex, MEPs are computed by numerical methods. The path is discretized, introducing finite set of states (called images) along the path. The discretized path is called MEP, if for every image  $S^k = (S_n^k) = (\theta_n^k, \phi_n^k)$  on the path projection of the effective field onto the orthogonal plane to the path equals zero [47]:

$$\mathcal{H}_\perp^k = \frac{\partial E[S^k]}{\partial S_n} - \left( \frac{\partial E[S^k]}{\partial S_n} \cdot \tau_n \right) \tau_n = 0 \quad \forall n, \quad (1)$$

here  $\tau_n$  is the unit tangent vector to the path. The two main problems of the definition are readily seen in the definition of the discrete MEP: (1) the energy is not necessarily monotone between neighbor images, hence energy barrier can be missed; (2) the tangent  $\tau_n$  is not known explicitly and should be estimated numerically. To find the MEP numerically, an analog of the steepest descent method can be used, but special attention should be paid to avoid drift of images toward metastable states. The nudged elastic band method does iterations of the following form [47]:

$$S^k \mapsto S^k - \gamma \mathcal{H}_\perp^k + \mu e_k \tau_k, \quad e_k = \text{dist}(S^{k+1}, S^k) - \text{dist}(S^{k-1}, S^k), \quad (2)$$

where  $e_k$  are quasi-elastic forces,  $\mu$  is the elasticity constant and  $\gamma$  is optimization step size. To ensure that TS will be among images on the path, so called climbing image modification of NEB is used, where for the image with largest energy, the component of the energy gradient parallel to the path is not eliminated but inverted [21, 24]:

$$\mathcal{H}_{\perp, \text{CI}}^k = \frac{\partial E[S^k]}{\partial S_n} - 2 \left( \frac{\partial E[S^k]}{\partial S_n} \cdot \tau_n \right) \tau_n = 0 \quad \forall n,$$

forcing the image to move towards the TS. The optimization technique is successfully used for computation of activation barriers in the chemical reactions [22, 48, 49] as well as for magnetic systems [12, 50] and many others. A modification of the method for computation of only part of the MEP was proposed in [51], which is suitable for analysis MEP having TS much smaller than meta-stable states.

The naive tangent estimation  $\tau_n$  using the central difference, unfortunately, makes NEB unstable, especially for a large number of images. The stability of method can be improved using direction to the neighbor image of the higher energy as an approximation to the tangent [24]. The maximum of energy along the path should be treated separately to avoid jumps when another image becomes maximum. According to [24], the tangent estimate can be chosen as follows:

$$\tau_n = \begin{cases} \tau_n^+, & \text{if } E_{n+1} > E_n > E_{n-1}, \\ \tau_n^-, & \text{if } E_{n+1} < E_n < E_{n-1}, \\ \tau_n^+ \Delta E_n^{\max} + \tau_n^- \Delta E_n^{\min}, & \text{if } E_{n+1} > E_{n-1}, \\ \tau_n^+ \Delta E_n^{\min} + \tau_n^- \Delta E_n^{\max}, & \text{if } E_{n+1} < E_{n-1}, \end{cases} \quad (3)$$

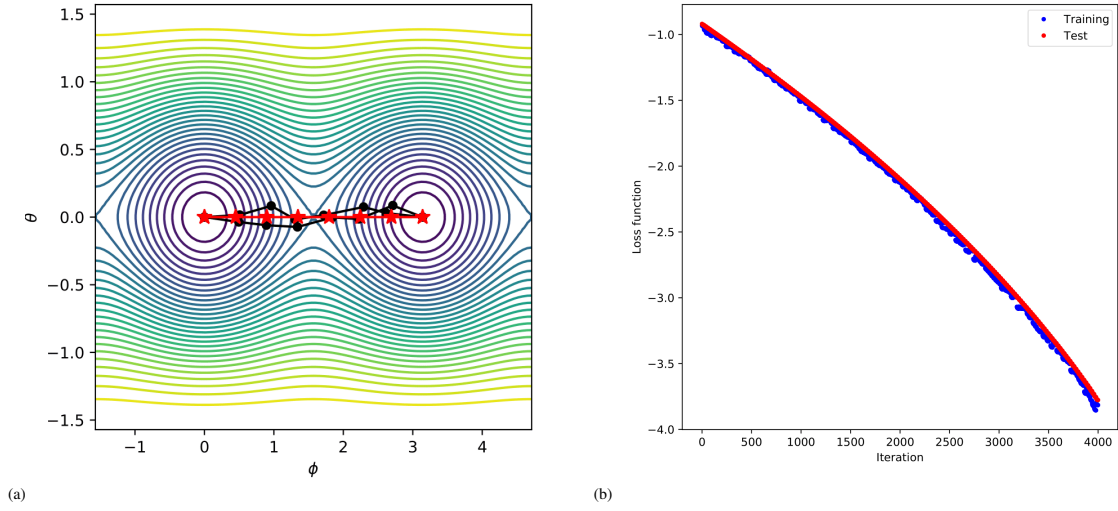


FIG. 1. (a) Energy surface for single spin system with easy axis  $x$  anisotropy  $K_1 = 1$  and easy plane anisotropy  $K_2 = -2$  with axis  $z$ . MEP is shown by star markers. Initial approximation of the path is marked by dots. (b) Decay of loss  $L$  during training. Lower blue dots are loss on the training set. Upper red dots are loss on the test set. Training set consists of 100 paths, and is regenerated every 20 steepest descent iterations. The convergence rate was improved 20 times over the 200 epoch.

where the last two cases are applied if  $n$  is either maximum of minimum of energy on the path,  $\tau_n^+ = S^{n+1} - S^n$ ,  $\tau_n^- = S^n - S^{n-1}$  are right and left tangents at the image  $n$ ,  $E_n = E[S^n]$  is energy of the image  $n$ ,

$$\Delta_n^{max} = \max(|E_{n+1} - E_n|, |E_{n-1} - E_n|), \quad \Delta_n^{min} = \min(|E_{n+1} - E_n|, |E_{n-1} - E_n|).$$

The choice of the elasticity parameter  $\mu$  is somewhat arbitrary, and is said to not affect results significantly. However, in practice, the right choice of the elasticity parameter is crucial, since too large or too small value of  $\mu$  ruins convergence, creating kinks on the path. Instead of elastic forces that push images toward their equidistant distribution, images can be redistributed every few optimization steps using linear interpolation of the path choosing uniform grid of local coordinates on the path, the method is known as the string method [25, 26]. The string method does not have arbitrary constants, but the redistribution step does not play well with higher order methods.

The NEB method can be used as a basis for gradient based method of second order. Interpreting equation (2) as steepest descend step  $S \mapsto S - \gamma g$ , where  $g$  is a quasi-gradient, one can apply conjugate gradient (CG) or L-BFGS method with  $g$  used instead of the gradient to obtain a higher order method. It seems that there is no potential function  $f$  such that  $g = \partial f / \partial S$ . Nevertheless both CG and L-BFGS methods demonstrate convergence, reducing optimization time in orders of magnitude [1].

Although methods for computation of the discrete MEP are widely used, their mathematical basis is far from being well established. While attempts are being made to apply variations of classical methods to MEP calculation, which is beyond the scope of the methods, the specialized methods for paths optimization are waiting to be discovered. The two features of the problem make discovery of the methods complicated: (1) the absence of a single functional for optimization (instead energy of each image is optimized separately) and (2) the need of simultaneous minimization of energy and equalization of images along the path. However, given a parametrized family of optimizers (implementing e.g. NEB method), the best optimizer can be found using machine learning techniques.

### 3. Training of optimization

To apply machine learning techniques for optimization of an algorithm, the algorithm must be expressed in terms of a parametrized family of transformations, which must be differentiable, as well as the loss function. The NEB method can be formulated as transformation  $M$  acting on paths, defined by the equation (2). We do not update the end points assuming that they are already relaxed to metastable states. Projected gradient defined by (1) and spring forces defined by (2) are differentiable function of its arguments, but improved tangent estimate given by (3) is not smooth. Here we introduce an analog of the improved tangent estimate from [24], but in a differentiable manner. We

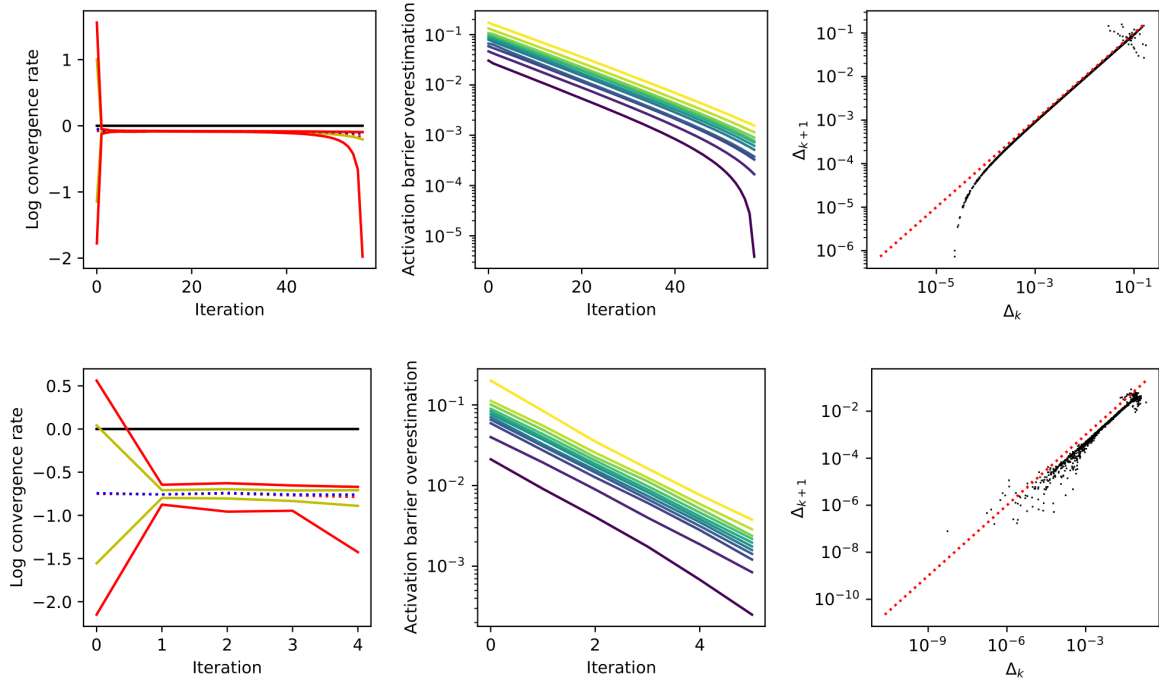


FIG. 2. Convergence of NEB for (upper row) initial set of parameters  $\gamma = 0.01$ ,  $\mu = 1$ ,  $\beta = 3$ ; (bottom row) for optimized parameters  $\gamma = 0.077$ ,  $\mu = 1$ ,  $\beta = 3$ , estimated for 100 random paths. Left column: rate of convergence as function of the iteration number. Red lines represent minimum and maximum values, dotted line is the mean value, yellow lines are 10 and 90 percentile. Optimized parameters result in 20 times faster convergence. Center column: error of the activation barrier estimation as function of iteration number. Lines show all percentiles from 0 to 100 with step 10. Right column: activation barrier estimation error  $\Delta_{k+1}$  on the next step as function of the error on the previous step  $\Delta_k$ . Red dotted lines show sublinear convergence region. Optimized parameters give better convergence for large errors, however the optimization invalidates superlinear convergence in the limit of small errors, due to the definition of the loss depending only on finite number of iteration steps.

redefine the tangent estimate  $\tau_n$  as a linear combination of left  $\tau^-$  and right  $\tau^+$  tangents  $\tau_n = a_n^+ \tau_n^+ + a_n^- \tau_n^-$ , where the coefficients  $a^+$  and  $a^-$  are functions of the energy grows rate on the adjacent segments:

$$a_n^+ = W \left( \frac{\partial E[S^n]}{\partial S} \cdot \tau_n^-; \frac{\partial E[S^n]}{\partial S} \cdot \tau_n^+ \right), \quad a_n^- = W \left( -\frac{\partial E[S^n]}{\partial S} \cdot \tau_n^+; -\frac{\partial E[S^n]}{\partial S} \cdot \tau_n^- \right).$$

We defined the weight  $W$  as a function of the gradient, which allows us to completely avoid energy computation during optimization, in contrast to the approach of [24]. The weight function  $W$  should select the right tangent if the energy increases at the image, be a smooth function and have symmetry with respect to path inversion; the assumptions are formalized as following natural conditions:

- (1) (smoothness)  $W(a; b)$  is an analytic function of  $a$  and  $b$ .
- (2) (being a weight)  $W(a; b) \geq 0$  and  $W(a; b) + W(-b; -a) = 1$  for all  $a$  and  $b$  ().
- (3) (stabilization of NEB) For positive  $a$  and  $b$  the right tangent is selected, that is  $W(a; b) \approx 1$ .

All the conditions are satisfied by the family of functions

$$W(a; b) = \frac{e^{\beta a} + e^{\beta b}}{e^{\beta a} + e^{-\beta a} + e^{\beta b} + e^{-\beta b}},$$

parametrized by  $\beta > 0$ . For  $a, b \rightarrow 0$ , the tangent estimate is close to the central finite difference, that is,  $W(a; b) \approx 1/2$  regardless of signs of the arguments, which is different from the approach of [24]. However, the estimate coincides with the right tangent,  $W \rightarrow 1$ , as  $a, b \rightarrow +\infty$ . The parameter  $\beta$  controls sensitivity of  $W$  to the value of its arguments.

The NEB transformation  $M$  defined above depends on three parameters: step size  $\gamma$ , elasticity  $\mu$  and smoothness of the tangent  $\beta$ . Whereas  $\gamma$  can be in theory estimated using e.g. Barzilai-Borwein method, the choice of  $\mu$  and  $\beta$

is unclear. We suggest to consider the mapping  $M$  as an artificial neural network with weights  $(\gamma, \mu, \beta)$  and train it using machine learning techniques to obtain the best convergence. According to definition of MEP as a continuous path, the maximum of energy along the path should be minimal among all the paths. Hence the optimality of the path is expressed by the value  $Q[S] = \max_t E[S(t)]$  (smaller is better), where  $t$  runs all over the path and  $S(t)$  is the continuous path obtain by linear interpolation of the discrete path  $S^k$ . We expect any optimization method for MEP computation to decrease  $Q$ -value doing its iterations. Suppose initial approximation to the MEP is given by path  $S^{(1)}$ , the path gradually optimized by the sequence of transformations  $S^{(k+1)} = MS^{(k)}$ . Denote by  $\Delta^{(k)}$  the value of overestimation of the energy barrier:  $\Delta^{(k)} = Q[S^{(k)}] - Q^0$ , where  $Q^0 = \min_S Q[S]$  is the true height of the activation barrier. The rate of convergence is given by the ratio  $\rho^{(k)} = \Delta^{(k+1)}/\Delta^{(k)}$ . It is desirable to have superlinearly convergent method, that is  $\lim_{k \rightarrow \infty} \rho^{(k)} = 0$ . In practice we do only finite number of optimization steps, therefore we want all  $\rho^{(k)}$  to be as close to zero as possible. We define the loss function as mean of logarithms of the rates:

$$L[S^{(0)}] = \frac{1}{K} \sum_{k=1}^K \ln \rho^{(k)},$$

where only first  $K$  iterations of the method are considered. We said the parameters  $(\gamma, \mu, \beta)$  are optimal, if they minimize loss function:

$$L = \operatorname{argmin}_{\gamma, \mu, \beta} \mathbb{E}(L[S^{(0)}]),$$

where the expectation value is taken for some distribution of paths near the MEP. The expectation value is estimated by arithmetic mean of  $L[S]$  values for a set of random paths  $^{(p)}S$ :

$$L \approx \frac{1}{P} \sum_p L[{}^{(p)}S].$$

For computation of the maximum  $Q$  along the piecewise linear path defined by images  $S^k$ , we apply a combination of golden section search and successive parabolic interpolation on each line segment  $S^k S^{k+1}$ . We perform optimization of the parameters by steepest descent:

$$\gamma \mapsto \gamma - \nu \frac{\partial L}{\partial \gamma}, \quad \mu \mapsto \mu - \nu \frac{\partial L}{\partial \mu}, \quad \beta \mapsto \beta - \nu \frac{\partial L}{\partial \beta},$$

with the step size  $\nu$  estimated by Barzilai-Borwein method.

The explicit form of derivative of  $L$  with respect to the parameters are quite complicated, therefore we use automatic differentiation to obtain the derivatives. The transform  $M$  was implemented in Python, and JAX library [52] was used to compute gradients and JIT compile functions. Due to extreme complexity of the gradient of the loss (we differentiate the algorithm for computation of maximum  $Q$  along the path and iterations of NEB method) and hardware limitations, we consider a simple case of single magnetic spin with easy axis anisotropy  $K_1 > 0$  having the axis  $\mathbf{K}_1 = \mathbf{x}$ , and easy plane anisotropy  $K_2 < 0$  having the axis  $\mathbf{K}_2 = \mathbf{z}$ . Since NEB does not take into account exact form of the energy and number of degrees of freedom, the result should be qualitatively the same for general magnetic systems. Energy of the considered system has the following forms in the Cartesian and in the spherical coordinates:

$$E[\mathbf{S}] = -K_1 S_x^2 - K_2 S_z^2 = -K_1 \cos^2 \theta \cos^2 \phi - K_2 \sin^2 \theta.$$

The system has two metastable states  $(S_x, S_y, S_z) = (\pm 1, 0, 0)$  (or in polar coordinates  $(\theta, \phi) = (0, 0)$  and  $(0, \pi)$ ) having energy  $-K^1$ . The transition states are at the points  $(S_x, S_y, S_z) = (0, \pm 1, 0)$ ; the energies of the both TS are the same and equal to  $-K^2$ . The MEP in the case lies in the  $Oxy$  plane avoiding problematic poles  $\theta = \pm\pi/2$ . Since we want NEB to reduce error in MEP estimation, and NEB has no proven convergence for arbitrary initial paths, we train and test our optimization method on the ideal MEP with position of points perturbed no more than 5% of the path length as shown in Fig. 1(a). Path consisting from 8 to 14 images were considered, demonstrating a qualitatively identical convergence pattern. We ran the optimization for the 200 epoch 20 iterations each in batches of 100 paths regenerated for each epoch. The loss function is computed using mean convergence rate estimation doing 5 iterations of the modified IT-NEB method. According to our tests, the initial NEB parameters can be chosen arbitrary, except for too large values of  $\gamma$ , where the NEB method diverges, and too small values of  $\mu$ , when NEB is unstable. The loss function decrease history is shown in Fig. 1(b) for the initial parameters  $\gamma = 0.01$ ,  $\mu = 1$ ,  $\beta = 3$ . In the 200, epoch the convergence rate was improved 20 fold. Inspection of the gradient of loss function shows that the value of  $\beta$  is least significant for convergence rate. The value of  $\mu$  affects the convergence only slightly, but it is important for stability of the method, which was not a subject of study of the current article.

Due to hardware restrictions, the considered loss function takes into account only rate of convergence of several first iterations of NEB method, therefore long time convergence of the method can be different. One of the reasons

to expect different behavior is change in the shape of the path, which is not covered by our ansatz on distribution of paths in the training set. Another possible issue in the real usage of NEB method is that initial approximation of the path can be very different from the actual MEP. We made benchmarks on the bended path doing 60 iteration of NEB with initial set of parameters and optimized parameters. The history of convergence of 100 random paths are shown in Fig. 2. The convergence of the NEB after training was also improved for bended paths. The optimized parameters give better mean convergence, at the same time, for some paths, the convergence has become worse, but is still better than worst case with the initial parameters. For large perturbations of path, the convergence of NEB is not monotonic, however for smaller error the convergence becomes linear. For moderate values of step size the convergence may become superlinear, unfortunately, the proposed training method does not improve  $Q$ -convergence.

#### 4. Conclusion

In this article we demonstrated that existing software technologies such as automatic differentiation of arbitrary code, e.g. using JAX [52], can be used to implement meta learning to improve convergence rate of existing optimization methods such as NEB method by tuning meta parameters. The approach is most useful for the problems, such as MEP evaluation, which do not have an elaborated mathematical theory. Previously, the effectiveness of meta learning was shown for tuning of parameters of simple methods, such as gradient descent. In this article, we reveal that meta learning can be used to train much more complex methods, such as NEB, however, the complexity of the gradients of the loss function in the case imposes restrictions on the complexity of the method, i.e. number of iterations made by parts of the algorithm can not be too high.

The real power of this method can be revealed by training of parameter free higher order methods, which do not need tuning for every energy functional. The conjugate gradient (CG) and L-BFGS methods are examples of the methods, but their convergence for MEP computation is not proven. Meta learning techniques with neural networks capable of simulation of CG and L-BFGS iterations and more general transforms probably can be trained to obtain a higher order method specialized for MEP calculations.

One important issue with meta learning for optimization methods is choice of loss function, which can estimate the limit of convergence rate, when only finite (and rather small) number of iteration steps can be made. The related question is estimation of the stability of the method. In our research, we encountered large variation of the convergence rate on random samples, which make the choice of the loss function even harder.

Although we mentioned computation of lifetime of the magnetic metastable states as our motivational example, computation of MEP is an important tool for other problems with large numbers of degrees of freedom. MEP was introduced as a method the activation barriers estimation in chemical reactions, and the NEB method is still a valuable approach in the field [47, 48, 53, 54]. MEP for an artificial potential fields can be considered as an optimal path in motion planning problem for a mobile robot [55]. In all the subject the same meta learning technique can be applied, if higher order derivatives for the potential is accessible.

#### Acknowledgements

The study of classical optimization methods for transition state computation in the sections 1 and 2 was funded by Government of the Russian Federation (Grant 08-08). The development of meta learning algorithm for nudged elastic band method in the section 3 was funded by Russian Science Foundation (Grant 19-42-06302).

#### References

- [1] Ivanov A.V., Dagbartsson D., Tranchida J., Uzdin V.M., Jansson H. Efficient optimization method for finding minimum energy paths of magnetic transitions. *Journal of Physics: Condensed Matter*, 2020, **32**(34).
- [2] Everschor-Sitte K., Masell J., Reeve R.M., Klaui M. Perspective: Magnetic skyrmions - Overview of recent progress in an active research field. *J. Appl. Phys.*, 2018, **124**, P. 240901.
- [3] Mittal S. A survey of techniques for architecting processor components using domain-wall memory. *ACM Journal on Emerging Technologies in Computing Systems (JETC)*, 2016, **13**(2), P. 1–25.
- [4] Parkin S.S.P., Hayashi M., Thomas L. Magnetic domain-wall racetrack memory. *Science*, 2008, **320**(5873), P. 190–194.
- [5] Fert A., Cros V., Sampaio J. Skyrmions on the track. *Nature Nanotech.*, 2013, **8**, P. 152–156.
- [6] Schratzberger J., Lee J., Fuger M., Fidler J., Fiedler G., Schref T., Suess D. *Validation of the transition state theory with Langevin-dynamics simulations. Journal of Applied Physics*, 2010, **108**, P. 033915.
- [7] Desplat L., Suess D., Kim J-V., Stamps R.L. Thermal stability of metastable magnetic skyrmions: Entropic narrowing and significance of internal eigenmodes. *Phys. Rev. B*, 2018, **98**, P. 134407.
- [8] Bessarab P.F., Miller G.P., Lobanov I.S. et. al. Lifetime of racetrack skyrmions. *Sci. Rep.*, 2018, **8**, P. 3433.
- [9] Potkina M.N., Lobanov I.S., Jansson H., Uzdin V.M. Skyrmions in antiferromagnets: Thermal stability and the effect of external field and impurities. *Journal of Applied Physics*, 2020, **127**, P. 213906.
- [10] Uzdin V.M., Potkina M.N., Lobanov I.S., Bessarab P.F., Jansson H. The effect of confinement and defects on the thermal stability of skyrmions. *Physica B: Condensed Matter*, 2018, **549**, P. 6–9.

- [11] Lobanov I.S., Jnsson H., Uzdin V.M. Mechanism and activation energy of magnetic skyrmion annihilation obtained from minimum energy path calculations. *Phys. Rev. B.*, 2016, **94**, P. 174418–2016.
- [12] Bessarab P.F., Uzdin V.M., Jnsson H. Method for finding mechanism and activation energy of magnetic transitions, applied to skyrmion and antivortex annihilation. *Comp. Phys. Commun.*, 2015, **196**, P. 335–347.
- [13] Bessarab P.F., Uzdin V.M., and Jnsson H. Harmonic transition-state theory of thermal spin transitions. *Phys. Rev. B*, 2012, **85**, P. 184409.
- [14] Langer J.S. Statistical theory of the decay of metastable states. *Annals of Physics*, 1969, **54**(2), P. 258–275.
- [15] Liashko S.Y., Lobanov I.S., Uzdin V.M., Jnsson H. Thermal stability of magnetic states in submicron magnetic islands. *Nanosystems: Physics, Chemistry, Mathematics*, 2017, **8**(5), P. 572–578.
- [16] Lobanov I.S., Uzdin V.M. *The lifetime of big size topological chiral magnetic states. Estimation of the pre-exponential factor in the Arrhenius law*. 2020. arXiv:2008.06754
- [17] Henkelman G., Jnsson H. A dimer method for finding saddle points on high dimensional potential surfaces using only first derivatives. *J. Chem. Phys.*, 1999, **111**(15), P. 7010–7022.
- [18] Olsen R.A., Kroes G.J., Henkelman G., Arnaldsson A., Jnsson H. Comparison of methods for finding saddle points without knowledge of the final states. *J. Chem. Phys.*, 2004, **121**(20), P. 9776–9792.
- [19] Gutierrez M.P., Argaez C., Jnsson H. Improved minimum mode following method for finding first order saddle points. *J. Chem. Theo. Comput.*, 2017, **13**(1), P. 125–134.
- [20] Henkelman G., Johannesson G., Jnsson H. Methods for finding saddle points and minimum energy paths. *Theoretical Methods in Condensed Phase Chemistry*, 2002, **5**, P. 269–302.
- [21] Henkelman G., Uberuaga B.P., Jnsson H. A climbing image nudged elastic band method for finding saddle points and minimum energy paths. *J. Chem. Phys.*, 2000, **113**(22), P. 9901–9904.
- [22] Maragakis P., Andreev S.A., Brumer Y., Reichman D.R., Kaxiras E. Adaptive nudged elastic band approach for transition state calculation. *J. Chem. Phys.*, 2002, **117**, P. 4651–4658.
- [23] Hoffmann M., Miller G.P., Blgel S. Atomistic Perspective of Long Lifetimes of Small Skyrmions at Room Temperature. *Phys. Rev. Lett.*, 2020, **124**, P. 247201.
- [24] Henkelman G., Jnsson H. Improved tangent estimate in the nudged elastic band method for finding minimum energy paths and saddle points. *J. Chem. Phys.*, 2000, **113**(22), P. 9978–9985.
- [25] Weinan E., Weiqing R., Vanden-Eijnden E. String method for the study of rare events. *Phys. Rev. B.*, 2002, **66**, P. 052301(4).
- [26] Sheppard D., Terrell R., Henkelman G. Optimization methods for finding minimum energy paths. *J. Chem. Phys.*, 2008, **128**, P. 134106(10).
- [27] Heistracher P., Abert C., Bruckner F., Vogler C., Suess D., GPU-Accelerated Atomistic Energy Barrier Calculations of Skyrmion Annihilations. *IEEE Transactions on Magnetics*, 2018, **54**(11), P. 1–5.
- [28] Schmidhuber J. *Evolutionary Principles in Self-Referential Learning*. On Learning how to Learn: The Meta-Meta-Meta...-Hook. PhD thesis, Institut f. Informatik, Tech. Univ. Munich, 1987.
- [29] Naik D.K., Mammone R.J. Meta-neural networks that learn by learning. In International Joint Conference on Neural Networks, *IEEE*, 1992, **1**, P. 437–442.
- [30] Bengio S., Bengio Y., Cloutier J. On the search for new learning rules for ANNs. *Neural Processing Letters*, 1995, **2**(4), P. 26–30.
- [31] Schmidhuber J., Zhao J., Wiering M. Shifting Inductive Bias with Success-Story Algorithm, Adaptive Levin Search, and Incremental Self-Improvement. *Machine Learning*, 1997, **28**, P. 105–130.
- [32] Hochreiter S., Schmidhuber J. Long Short-Term Memory. *Neural Computation*, 1997.
- [33] Thrun S., Pratt L. *Learning to learn*. Springer Science and Business Media, 1998.
- [34] Younger A.S., Conwell P.R., Cotter N.E. Fixed-weight on-line learning. *Transactions on Neural Networks*, 1999, **10**(2), P. 272–283.
- [35] Runarsson T.P., Jonsson M.T. Evolution and design of distributed learning rules. In IEEE Symposium on Combinations of Evolutionary Computation and Neural Networks, 2000, P. 59–63.
- [36] Diederik P. Kingma, Jimmy Ba. Adam: A Method for Stochastic Optimization. 3rd International Conference for Learning Representations, San Diego, 2015.
- [37] Andrychowicz M., Denil M., Gomez S., Hoffman M.W., Pfau D., Schaul T., Shillingford B., de Freitas N. *Learning to learn by gradient descent by gradient descent*. 2016, arXiv:1606.04474.
- [38] Chen Y., Hoffman M.W., Gomez S.C., Denil M., Lillicrap T.P., Botvinick M., de Freitas N. *Learning to Learn without Gradient Descent by Gradient Descent*. 2016, arXiv:1611.03824.
- [39] Wichrowska O., Maheswaranathan N., Hoffman M.W., Gomez S.C., Denil M., de Freitas N., Sohl-Dickstein J. *Learned Optimizers that Scale and Generalize*. 2017, arXiv:1703.04813.
- [40] Hospedales T., Antoniou A., Micaelli P., Storkey A. *Meta-Learning in Neural Networks: A Survey*. 2020, arXiv:2004.05439.
- [41] Carlon A., Espath L., Lopez R., Tempone R. *Multi-iteration stochastic optimizers*. 2020, arXiv:2011.01718
- [42] Khromova K. *Optimization of the neural network training method*. Master dissertation. ITMO University, 2020.
- [43] Rybakov F.N., Borisov A.B., Blgel S., Kiselev N.S. New Type of Stable Particlelike States in Chiral Magnets. *Phys. Rev. Lett.*, 2015, **115**, P. 117201.
- [44] Mentink J.H., Tretyakov M.V., Fasolino A., Katsnelson M.I., Rasing Th. Stable and fast semi-implicit integration of the stochastic Landau-Lifshitz equation. *Journal of Physics: Condensed Matter*, 2010, **22**(17), P. 176001.
- [45] Desplat L., Vogler C., Kim J.-V., Stamps R. L., Suess D. Path sampling for lifetimes of metastable magnetic skyrmions and direct comparison with Kramers' method. *Phys. Rev. B.*, 2020, **101**, P. 060403(R).
- [46] Moskalenko M.A., Lobanov I.S., Uzdin V.M. Demagnetizing fields in chiral magnetic structures. *Nanosystems: Physics, Chemistry, Mathematics*, 2020, **11**(4), P. 401–407.
- [47] Jonsson H., Mills G., Jacobsen K.W., Berne B.J., Ciccotti G., Coker D.F. *Nudged elastic band method for finding minimum energy paths of transitions, in Classical and Quantum Dynamics in Condensed Phase Simulations*. World Scientific, Singapore, 1998, P. 385–404.
- [48] Henkelman G., Arnaldsson A., Jonsson H. Theoretical calculations of  $CH_4$  and  $H_2$  associative desorption from Ni(111): Could subsurface hydrogen play an important role? *J. Chem. Phys.*, 2006, **124**, P. 044706(9).
- [49] Einarsdottir D.M., Arnaldsson A., Oskarsson F., Jonsson H. Path optimization with application to tunneling. *Lecture Notes in Computer Science*, 2012, **7134**, P. 45–55.

- [50] Malottki S.V., Dupe B., Bessarab P.F., Delin A., Heinze S. Enhanced skyrmion stability due to exchange frustration. *Sci. Rep.*, 2017, **7**(10), P. 12299.
- [51] Lobanov I.S., Potkina M.N., Jansson H., Uzdin V.M. Truncated minimum energy path method for finding first order saddle points. *Nanosystems: Physics, Chemistry, Mathematics*, 2017, **8**(5), P. 586–595
- [52] Bradbury J., Frostig R., Hawkins P., Johnson M.J., Leary C., Maclaurin D., Necula G., Paszke A., Vanderlas J., Wanderman-Milne S., Zhang Q. JAX: composable transformations of Python+NumPy programs. (<http://github.com/google/jax>), 2018.
- [53] Mills G., Jonsson H., Schenter G.K. Reversible work based transition state theory: Application to  $H_2$  dissociative adsorption. *Surf. Sci.*, 1995, **324**, P. 305–337.
- [54] Zhu T., Li J., Samanta A., Kim H.G., Suresh S. Interfacial plasticity governs strain rate sensitivity and ductility in nanostructured metals. *PNAS*, 2007, **104**(9), P. 3031–3036.
- [55] Fakoor M., Kosari A., Jafarzadeh M. Revision on fuzzy artificial potential field for humanoid robot path planning in unknown environment. *International Journal of Advanced Mechatronic Systems (IJAMECHS)*, 2015, **6**(4), P. 174–183

## On quantum bit coding by Gaussian beam modes for the quantum key distribution

M. P. Faleeva, I. Y. Popov

ITMO University, Kronverkskiy, 49, Saint Petersburg, 197101, Russia  
popov1955@gmail.com

DOI 10.17586/2220-8054-2020-11-6-651-658

This paper deals with possibility of implementation of quantum key distribution algorithm through turbulent atmosphere. Beam wandering is considered as the main perturbation. For description of the density matrix, the Glauber–Sudarshan P-function technique is used. The probabilities of detectors triggering are determined.

**Keywords:** quantum bit, gaussian beam, entanglement, quantum key distribution.

*Received: 30 November 2020*

### 1. Introduction

Nanoscience progress opens new opportunities in the development of quantum technologies, particularly, quantum computing and quantum communications. We are studying the quantum key distribution algorithm implementation in a turbulent atmosphere. There are a variety of optical techniques for implementing quantum key distribution [1]. The most common class of solutions encode each bit of private information onto discrete degrees of freedom of optical signals, and it is named as discrete-variable quantum key distribution. An alternative approach employs coherent communication techniques to encode the private information, and is known as continuous-variable quantum key distribution. Both approaches face a similar obstacle when attempting to implement wide-scale deployment of quantum key distribution: physical communication channels introduce transmission losses that increase exponentially with distance, greatly limiting the secure key rates that can be achieved over long ranges [2–4].

To be more specific, we are interested in the protocol, based on the entangled qubit pairs (EPR-Protocol). Qubits in our research are coded by Gaussian beam modes, which are sent to the receiver. We took some simplifications for the mathematical description of the turbulent atmosphere. We focus on the effect of beam wandering, which is dominant for the weak turbulence. Beam wandering is usually truncated by the aperture at the receivers, thus beam losses appear [5]. Passed light is evaluated by the transmission coefficient. The expression of the density operator of the quantum state after passing the receiver aperture can be obtained with the use of the input-output relations in terms of the Glauber–Sudarshan P-function. Our aim is to calculate probabilities of the detectors going off occurring the concrete detector in another quantum channel goes off.

### 2. Qubit representation

Let us introduce representation of a qubit through Gaussian beam modes. Assume that a photon can be in one of two fixed states (modes) with indices  $m_1, n_1$  and  $m_2, n_2$ ,  $m_1, n_1, m_2, n_2 \in \{\mathbb{N} \cup 0\}$ ,  $(m_1, n_1) \neq (m_2, n_2)$ . So the qubit can be represented as a linear combination of two states. We write a photon state in the form of Fock state  $|10\rangle$ , where “1” is at the first position means that the photon is in the mode  $\Psi_{m_1 n_1}$ . Let this state be the first basic state of the computational qubit. Correspondingly, the photon state  $|01\rangle$ , which means that the photon is in the mode  $\Psi_{m_2 n_2}$ , be the another basic state of the computational qubit. The mode set is orthonormal. The qubit can be represented as a linear combination of two states  $\alpha |10\rangle + \beta |01\rangle$ . We need an entangled two-qubit state, so we take four modes for two photons  $\Psi_{m_i n_i}$ ,  $i = 1, 2, 3, 4$ . For example, two “1” in the notation of two-photons state  $|0110\rangle$  mean that the first photon is in the mode  $\Psi_{m_2 n_2}$ , the second photon is in the mode  $\Psi_{m_3 n_3}$ .

### 3. The scheme of the algorithm

Figure 1 presents the idea of the cryptographic installation implementation. The source of EPR-pairs (E) generates an entangled pair of photons. If we use modes  $\Psi_{m_1, n_1}$ ,  $\Psi_{m_2, n_2}$  for qubit A coding and modes  $\Psi_{m_3, n_3}$ ,  $\Psi_{m_4, n_4}$  for qubit B, the EPR-pair of entangled qubits, generated by source is given by:

$$|\Phi\rangle_{in} = \frac{1}{\sqrt{2}} \left( |1\rangle_{m_1, n_1} |0\rangle_{m_2, n_2} |0\rangle_{m_3, n_3} |1\rangle_{m_4, n_4} - |0\rangle_{m_1, n_1} |1\rangle_{m_2, n_2} |1\rangle_{m_3, n_3} |0\rangle_{m_4, n_4} \right) = \frac{1}{\sqrt{2}} (|1001\rangle - |0110\rangle). \quad (1)$$

One photon from the pair is sent into the channel A and another into the channel B through the atmosphere. After passing the paths A and B, the corresponding photon comes into the measuring equipment, which consists in

symmetric beam splitter (S), four filters ( $F_i, i = 1, 2, 3, 4$ ) for each channel and detectors ( $D^i, i = 1, 2, 3, 4$ ), which are assumed to be perfect. There are four nonorthogonal states, which are used in quantum key distribution protocol. We noted them in a different way for the qubit A and qubit B:

$$|\Psi\rangle_1^A = |1\rangle_{m1,n1} |0\rangle_{m2,n2} = |10\rangle_A, \tag{2}$$

$$|\Psi\rangle_2^A = |0\rangle_{m1,n1} |1\rangle_{m2,n2} = |01\rangle_A, \tag{3}$$

$$|\Psi\rangle_3^A = \frac{1}{\sqrt{2}} (|10\rangle_A + |01\rangle_A), \tag{4}$$

$$|\Psi\rangle_4^A = \frac{1}{\sqrt{2}} (|01\rangle_A - |10\rangle_A), \tag{5}$$

$$|\Psi\rangle_1^B = |1\rangle_{m3,n3} |0\rangle_{m4,n4} = |10\rangle_B, \tag{6}$$

$$|\Psi\rangle_2^B = |0\rangle_{m3,n3} |1\rangle_{m4,n4} = |01\rangle_B, \tag{7}$$

$$|\Psi\rangle_3^B = \frac{1}{\sqrt{2}} (|10\rangle_B + |01\rangle_B), \tag{8}$$

$$|\Psi\rangle_4^B = \frac{1}{\sqrt{2}} (|01\rangle_B - |10\rangle_B). \tag{9}$$

Filters distinguish pairs of orthogonal states, so the  $F_1^{A/B}$  let the state  $|\Psi\rangle_1^{A/B}$  pass, and reflects the state  $|\Psi\rangle_2^{A/B}$ ,  $F_2^{A/B}$  let the state  $|\Psi\rangle_3^{A/B}$  pass, and reflects the state  $|\Psi\rangle_4^{A/B}$ .

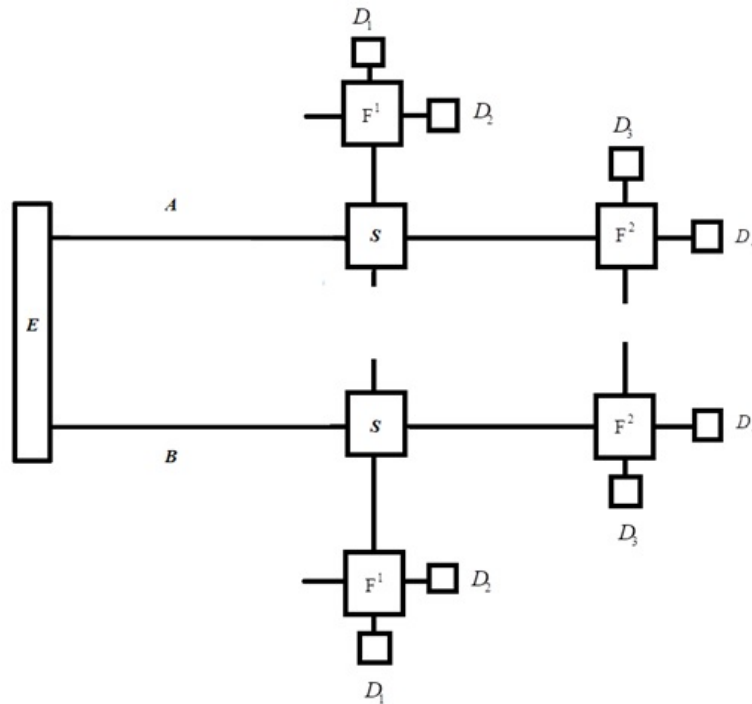


FIG. 1. The idea of the cryptographic installation scheme

#### 4. Stochastic Helmholtz equation

Generally speaking, the atmospheric turbulence can be expressed in random nature of the refraction index in a classical Helmholtz equation. It has been shown [6] that the Maxwell's equations for the amplitude of a propagating electromagnetic wave lead to the scalar stochastic Helmholtz equation for a component of field, where dependence on time, in the form of the monochromatic wave, is taken into account:

$$\Delta U(x, y, z) + k^2 n^2(x, y, z) U(x, y, z) = 0, \quad (10)$$

where  $k$  is the wave number of the electromagnetic wave,  $n(x, y, z)$  is the index of refraction, which is varies due to random properties of media and it can be expressed as  $n(x, y, z) = n_0 + n_1(x, y, z)$ ,  $n_0 = 1$  is the mean index of refraction,  $n_1(x, y, z)$  is the random deviation of index from its mean value, and it is delta correlated in the direction of the propagation.

We fix the exponential variation of  $U$  in respect to the coordinate  $z$ , which corresponds to the direction of the beams propagation:

$$U(x, y, z; k) = \Psi(x, y, z; k) \exp(ikz). \quad (11)$$

Substitution of function (11) into the equation (10) with taking the paraxial approximation leads to the paraxial form of the Helmholtz equation for the function  $\Psi$ :

$$\left( i \frac{\partial}{\partial z} + \frac{1}{2k} \Delta_{\perp} + kn_1(x, y, z) \right) \Psi_{in/out}(x, y, z; k) = 0, \quad (12)$$

where  $\Delta_{\perp}$  is the transverse part of the Laplacian:  $\Delta_{\perp} = \frac{\partial^2}{\partial x^2} + \frac{\partial^2}{\partial y^2}$ .

We find the eigenfunction of (12) in the same way as in [7], but we are interested in modes of high order:

$$\begin{aligned} \Psi_{mn}(x, y, z_{ap}, k) &= \\ &= \sqrt{\frac{2}{\pi W^2}} \exp\left(-((x-r)^2 + y^2) \left(\frac{1}{W^2} + \frac{ik}{2R}\right) + i(1+m+n)\phi\right) H_m\left(\frac{\sqrt{2}(x-r)}{W}\right) H_n\left(\frac{\sqrt{2}y}{W}\right), \end{aligned} \quad (13)$$

where  $W(z_{ap})$  is the beam-spot radius,  $R(z_{ap})$  is the curvature radius of the wavefront,  $\phi(z_{ap})$  is the Gouy phase,  $H_m(\xi)$  is the Hermite function, where  $z_{ap}$  is the position of the aperture plane at the  $Z$ -axis.

Correspondingly, for  $z_{ap} = 0$  we obtain the condition:

$$\Psi_{mn}(x, y, 0, k) = \sqrt{\frac{2}{\pi W_0^2}} \exp\left(- (x^2 + y^2) \left(\frac{1}{W_0^2} + \frac{ik}{2R_0}\right) + i(1+m+n)\phi_0\right) H_m\left(\frac{\sqrt{2}(x)}{W_0}\right) H_n\left(\frac{\sqrt{2}y}{W_0}\right),$$

where  $W_0, R_0, \phi_0$  are initial values for the  $W(z), R(z), \phi(z)$ .

Parameter  $r$  is the randomly generated distance of beam-deflection from the aperture center. One of the main problems for description of free space light propagation is finding the probability distribution of this parameter. Gaussian distribution approximates the index of refraction  $n_1(x, y, z)$  quite well for the case of week turbulence [6–8]. Then, the Rice distribution is the probability distribution function for  $r$  is:

$$f(r; d, \sigma) = \frac{r}{\sigma^2} I_0\left(\frac{rd}{\sigma^2}\right) \exp\left(-\frac{r^2 + d^2}{2\sigma^2}\right), \quad (14)$$

where  $I_0(x)$  is a modified Bessel function of the first kind and order zero,  $d$  is the distance between the aperture and the fluctuation centers,  $\sigma$  is the standard deviation of the beam deflection,  $\sigma^2 = 1, 23C_n^2 k^{7/6} L^{11/6}$ , where  $L$  is the path length of propagated light,  $C_n^2$  is the refractive-index structure parameter. For weak fluctuations  $\sigma^2 < 1$  [6].

#### 5. Gauss beam modes propagation

We will analyze the propagation of light through a turbulent atmosphere for the quantum entangled two-photon state (EPR-pair) (1). The density operator of the photons state is:

$$\hat{\rho}_{in} = |\Phi\rangle_{in} \langle\Phi|_{in}. \quad (15)$$

To obtain the density operator for the state of the transmitted light, we will use the approach of the input-output relations in terms of the Glauber–Sudarshan P-function. This approach was applied for deriving the output density matrices of the transmitted light in turbulent atmosphere by the authors of work [9].

The well-known Glauber–Sudarshan P-function is defined by determining the form of the density operator  $\hat{\rho}$  in the basis of coherent states  $\{|\alpha\rangle\}$ :

$$\hat{\rho} = \int P(\alpha) |\alpha\rangle \langle\alpha| d^2\alpha. \quad (16)$$

The next formula for the P-function is more important for the practical calculations:

$$P(\alpha) = \frac{1}{\pi^2} \int_{-\infty}^{+\infty} \chi(\beta) \exp(\alpha\beta^* - \alpha^*\beta) d^2\beta. \tag{17}$$

Here,  $\chi(\beta) = \text{Tr}[\hat{\rho} \exp(\hat{a}^+\beta) \exp(-\hat{a}\beta^*)]$  is the characteristic function;  $\hat{a}$ ,  $\hat{a}^+$  are the annihilation and creation operators.

Relations for the above functions between the input state and the transmitted through turbulent media state are given by the following expressions:

$$\hat{\rho}_{out} = \langle \hat{\rho}_T \rangle, \tag{18}$$

$$\hat{\rho}_T = \int P_T(\alpha) |\alpha\rangle \langle \alpha| d^2\alpha, \tag{19}$$

$$P_T(\alpha) = \frac{1}{T^2} P_{in}\left(\frac{\alpha}{T}\right), \tag{20}$$

$$\chi_T(\beta) = \chi_{in}(T\beta), \tag{21}$$

where  $\langle \dots \rangle$  means averaging with a probability distribution function of the transmission coefficient  $f(r; d, \sigma)$ , which comes to averaging with a probability distribution function of the beam-deflection distance  $r$ :

$$\langle g(r) \rangle = \int_0^\infty f(r; d, \sigma) g[T(r)] dr. \tag{22}$$

Formulas (16)–(21) allow one to derive the expression for the output density operator of the state (15):

$$\begin{aligned} \hat{\rho}_{out} = & \frac{1}{2} \left( \left\langle \left\langle \left(1 - |T_{m1,n1}|^2\right) \left(1 - |T_{m4,n4}|^2\right) \right\rangle \right\rangle + \left\langle \left\langle \left(1 - |T_{m2,n2}|^2\right) \left(1 - |T_{m3,n3}|^2\right) \right\rangle \right\rangle \hat{\rho}_0 \right. \\ & + \left\langle \left\langle \left(1 - |T_{m1,n1}|^2\right) |T_{m4,n4}|^2 \right\rangle \right\rangle \hat{\rho}_{m4,n4} + \left\langle \left\langle \left(1 - |T_{m2,n2}|^2\right) |T_{m3,n3}|^2 \right\rangle \right\rangle \hat{\rho}_{m3,n3} \\ & + \left\langle \left\langle \left(1 - |T_{m3,n3}|^2\right) |T_{m2,n2}|^2 \right\rangle \right\rangle \hat{\rho}_{m2,n2} + \left\langle \left\langle \left(1 - |T_{m4,n4}|^2\right) |T_{m1,n1}|^2 \right\rangle \right\rangle \hat{\rho}_{m1,n1} \\ & \left. + \left( \left\langle |T_{m1,n1}|^2 |T_{m4,n4}|^2 \right\rangle + \left\langle |T_{m2,n2}|^2 |T_{m3,n3}|^2 \right\rangle \right) \hat{\rho}_2 \right). \tag{23} \end{aligned}$$

Here,  $T_{mi,ni}$  is the transmission coefficient of the mode with indexes  $mi$ ,  $ni$ ,  $\hat{\rho}_0$  is the density operator of vacuum state,  $\hat{\rho}_{mi,ni}$ ,  $i = 1, 2, 3, 4$  are the density operator of one photon states,  $\hat{\rho}_2$  is the density operator of two photon states.

The expression (23) can't be written in any basis. But in the case of absence of the background radiation and dark counts we can take into account only contribution of the last term in (23). This term can be represented in a matrix form in the basis of states  $|0101\rangle, |1001\rangle, |0110\rangle, |1010\rangle$ :

$$\hat{\rho}_2 = \frac{1}{A + C} \begin{bmatrix} 0 & 0 & 0 & 0 \\ 0 & A & B & 0 \\ 0 & B' & C & 0 \\ 0 & 0 & 0 & 0 \end{bmatrix}, \tag{24}$$

where  $A = \langle |T_{m1,n1}|^2 |T_{m4,n4}|^2 \rangle$ ,  $B = -\langle T_{m1,n1}^* T_{m2,n2} T_{m1,n1} T_{m4,n4}^* \rangle$ ,  $B' = -\langle T_{m1,n1} T_{m2,n2}^* T_{m3,n3}^* T_{m4,n4} \rangle$ ,  $C = \langle |T_{m2,n2}|^2 |T_{m3,n3}|^2 \rangle$ .

The transmission coefficients are calculated in such a way:

$$T_{m,n}^2 \approx T_{m,n}^2(k_0) = \int_A |U_{m,n}(x, y, z_{ap}; k_0)|^2 dx dy, \tag{25}$$

where  $A$  is the area of aperture opening.

We need to find all components of the matrix (24). It is convenient to evaluate integral (25) in polar coordinates:

$$\begin{aligned} T_{m,n}^2(r) & \approx \int_A |U_{m,n}(\rho, \phi, z_{ap}; k_0)|^2 d\rho d\phi \\ & = \frac{2}{\pi W^2} \exp\left(-\frac{2r^2}{W^2}\right) \int_0^a \rho \exp\left(-\frac{2\rho^2}{W^2}\right) \int_0^{2\pi} \exp\left(\frac{4\pi\rho \cos\phi}{W^2}\right) H_m^2\left(\frac{\sqrt{2}(\rho \cos\phi - r)}{W}\right) H_n^2\left(\frac{\sqrt{2}\rho \sin\phi}{W}\right) d\phi d\rho. \end{aligned}$$

**6. The qubits measurement**

Let us describe all the ways of the density operator  $\hat{\rho}_2$  transformation when the qubits pass the filter and get on the detectors.

In our consideration, modes  $\Psi_{m1,n1}$  and  $\Psi_{m2,n2}$  define basic qubit state of the qubit A (noted above by  $|10\rangle_A$  and  $|01\rangle_A$ ). The states (2)–(9) can be associated with the matrix representation in a standard way:

$$|\Psi\rangle_1^A = |10\rangle_A \rightarrow \begin{bmatrix} 1 \\ 0 \end{bmatrix}_A, \quad |\Psi\rangle_2^A = |01\rangle_A \rightarrow \begin{bmatrix} 0 \\ 1 \end{bmatrix}_A,$$

$$|\Psi\rangle_3^A = \frac{1}{\sqrt{2}} (|10\rangle_A + |01\rangle_A) \rightarrow \frac{1}{\sqrt{2}} \begin{bmatrix} 1 \\ 1 \end{bmatrix}_A, \quad |\Psi\rangle_4^A = \frac{1}{\sqrt{2}} (|01\rangle_A - |10\rangle_A) \rightarrow \frac{1}{\sqrt{2}} \begin{bmatrix} -1 \\ 1 \end{bmatrix}_A.$$

Analogously, for modes  $\Psi_{m3,n3}$  and  $\Psi_{m4,n4}$ , one defines the basic qubit state of the qubit B:

$$|\Psi\rangle_1^B = |10\rangle_B \rightarrow \begin{bmatrix} 1 \\ 0 \end{bmatrix}_B, \quad |\Psi\rangle_2^B = |01\rangle_B \rightarrow \begin{bmatrix} 0 \\ 1 \end{bmatrix}_B,$$

$$|\Psi\rangle_3^B = \frac{1}{\sqrt{2}} (|10\rangle_B + |01\rangle_B) \rightarrow \frac{1}{\sqrt{2}} \begin{bmatrix} 1 \\ 1 \end{bmatrix}_B, \quad |\Psi\rangle_4^B = \frac{1}{\sqrt{2}} (|01\rangle_B - |10\rangle_B) \rightarrow \frac{1}{\sqrt{2}} \begin{bmatrix} -1 \\ 1 \end{bmatrix}_B.$$

The density operator of two-qubit state after the qubit A passing through the filter  $F_i^A$ , can be obtained by the projection operator  $\hat{D}_i^A$  on the state  $|\Psi\rangle_i^A$  applying [9]:

$$\hat{D}_i = |\Psi\rangle_i^A \langle \Psi|_i^A \otimes I,$$

$$\hat{D}_1^A = \begin{bmatrix} 1 \\ 0 \end{bmatrix}_A \cdot \begin{bmatrix} 1 & 0 \end{bmatrix}_A \otimes \begin{bmatrix} 1 & 0 \\ 0 & 1 \end{bmatrix} = \begin{bmatrix} 1 & 0 \\ 0 & 0 \end{bmatrix} \otimes \begin{bmatrix} 1 & 0 \\ 0 & 1 \end{bmatrix} = \begin{bmatrix} 1 & 0 & 0 & 0 \\ 0 & 1 & 0 & 0 \\ 0 & 0 & 0 & 0 \\ 0 & 0 & 0 & 0 \end{bmatrix}, \quad (26)$$

$$\hat{D}_2^A = \begin{bmatrix} 0 \\ 1 \end{bmatrix}_A \cdot \begin{bmatrix} 0 & 1 \end{bmatrix}_A \otimes \begin{bmatrix} 1 & 0 \\ 0 & 1 \end{bmatrix} = \begin{bmatrix} 0 & 0 & 0 & 0 \\ 0 & 0 & 0 & 0 \\ 0 & 0 & 1 & 0 \\ 0 & 0 & 0 & 1 \end{bmatrix}, \quad (27)$$

$$\hat{D}_3^A = \frac{1}{2} \cdot \begin{bmatrix} 1 \\ 1 \end{bmatrix}_A \cdot \begin{bmatrix} 1 & 1 \end{bmatrix}_A \otimes \begin{bmatrix} 1 & 0 \\ 0 & 1 \end{bmatrix} = \frac{1}{2} \cdot \begin{bmatrix} 1 & 0 & 1 & 0 \\ 0 & 1 & 0 & 1 \\ 1 & 0 & 1 & 0 \\ 0 & 1 & 0 & 1 \end{bmatrix}, \quad (28)$$

$$\hat{D}_4^A = \frac{1}{2} \cdot \begin{bmatrix} -1 \\ 1 \end{bmatrix}_A \cdot \begin{bmatrix} -1 & 1 \end{bmatrix}_A \otimes \begin{bmatrix} 1 & 0 \\ 0 & 1 \end{bmatrix} = \frac{1}{2} \cdot \begin{bmatrix} 1 & 0 & -1 & 0 \\ 0 & 1 & 0 & -1 \\ -1 & 0 & 1 & 0 \\ 0 & -1 & 0 & 1 \end{bmatrix}. \quad (29)$$

Let us apply the operators (26)–(29) to the density operator  $\hat{\rho}_2$ :

$$\hat{D}_1^A \hat{\rho}_2 (\hat{D}_1^A)^* = \frac{1}{A+C} \begin{bmatrix} 1 & 0 & 0 & 0 \\ 0 & 1 & 0 & 0 \\ 0 & 0 & 0 & 0 \\ 0 & 0 & 0 & 0 \end{bmatrix} \cdot \begin{bmatrix} 0 & 0 & 0 & 0 \\ 0 & A & B & 0 \\ 0 & B' & C & 0 \\ 0 & 0 & 0 & 0 \end{bmatrix} \cdot \begin{bmatrix} 1 & 0 & 0 & 0 \\ 0 & 1 & 0 & 0 \\ 0 & 0 & 0 & 0 \\ 0 & 0 & 0 & 0 \end{bmatrix} = \frac{1}{A+C} \begin{bmatrix} 0 & 0 & 0 & 0 \\ 0 & A & 0 & 0 \\ 0 & 0 & 0 & 0 \\ 0 & 0 & 0 & 0 \end{bmatrix},$$

$$\hat{D}_2^A \hat{\rho}_2 (\hat{D}_2^A)^* = \frac{1}{A+C} \begin{bmatrix} 0 & 0 & 0 & 0 \\ 0 & 0 & 0 & 0 \\ 0 & 0 & 1 & 0 \\ 0 & 0 & 0 & 1 \end{bmatrix} \cdot \begin{bmatrix} 0 & 0 & 0 & 0 \\ 0 & A & B & 0 \\ 0 & B' & C & 0 \\ 0 & 0 & 0 & 0 \end{bmatrix} \cdot \begin{bmatrix} 0 & 0 & 0 & 0 \\ 0 & 0 & 0 & 0 \\ 0 & 0 & 1 & 0 \\ 0 & 0 & 0 & 1 \end{bmatrix} = \frac{1}{A+C} \begin{bmatrix} 0 & 0 & 0 & 0 \\ 0 & 0 & 0 & 0 \\ 0 & 0 & B' & 0 \\ 0 & 0 & 0 & 0 \end{bmatrix},$$

$$\begin{aligned}\widehat{D}_3^A \widehat{\rho}_2 \left(\widehat{D}_3^A\right)^* &= \frac{1}{4(A+C)} \begin{bmatrix} 1 & 0 & 1 & 0 \\ 0 & 1 & 0 & 1 \\ 1 & 0 & 1 & 0 \\ 0 & 1 & 0 & 1 \end{bmatrix} \cdot \begin{bmatrix} 0 & 0 & 0 & 0 \\ 0 & A & B & 0 \\ 0 & B' & C & 0 \\ 0 & 0 & 0 & 0 \end{bmatrix} \cdot \begin{bmatrix} 1 & 0 & 1 & 0 \\ 0 & 1 & 0 & 1 \\ 1 & 0 & 1 & 0 \\ 0 & 1 & 0 & 1 \end{bmatrix} \\ &= \frac{1}{4(A+C)} \begin{bmatrix} C & B' & C & B' \\ B & A & B & A \\ C & B' & C & B' \\ B & A & B & A \end{bmatrix},\end{aligned}$$

$$\begin{aligned}\widehat{D}_4^A \widehat{\rho}_2 \left(\widehat{D}_4^A\right) &= \frac{1}{4(A+C)} \begin{bmatrix} 1 & 0 & -1 & 0 \\ 0 & 1 & 0 & -1 \\ -1 & 0 & 1 & 0 \\ 0 & -1 & 0 & 1 \end{bmatrix} \cdot \begin{bmatrix} 0 & 0 & 0 & 0 \\ 0 & A & B & 0 \\ 0 & B' & C & 0 \\ 0 & 0 & 0 & 0 \end{bmatrix} \cdot \begin{bmatrix} 1 & 0 & -1 & 0 \\ 0 & 1 & 0 & -1 \\ -1 & 0 & 1 & 0 \\ 0 & -1 & 0 & 1 \end{bmatrix} \\ &= \frac{1}{4(A+C)} \begin{bmatrix} C & -B' & -C & B' \\ -B & A & B & -A \\ -C & B' & C & -B' \\ B & -A & -B & A \end{bmatrix}.\end{aligned}$$

Then we normed the obtained matrixes in such a way:

$$\widehat{\rho}_2^{(i)} = \frac{1}{\text{Tr} \left( \widehat{D}_i^A \widehat{\rho}_2 \left( \widehat{D}_i^A \right) \right)} \left( \widehat{D}_i^A \widehat{\rho}_2 \left( \widehat{D}_i^A \right) \right).$$

Now, we come to the following density operators:

$$\begin{aligned}\widehat{\rho}_2^{(1)} &= \frac{1}{A} \begin{bmatrix} 0 & 0 & 0 & 0 \\ 0 & A & 0 & 0 \\ 0 & 0 & 0 & 0 \\ 0 & 0 & 0 & 0 \end{bmatrix}, \quad \widehat{\rho}_2^{(2)} = \frac{1}{B'} \begin{bmatrix} 0 & 0 & 0 & 0 \\ 0 & 0 & 0 & 0 \\ 0 & 0 & B' & 0 \\ 0 & 0 & 0 & 0 \end{bmatrix}, \\ \widehat{\rho}_2^{(3)} &= \frac{1}{2(A+C)} \begin{bmatrix} C & B' & C & B' \\ B & A & B & A \\ C & B' & C & B' \\ B & A & B & A \end{bmatrix}, \quad \widehat{\rho}_2^{(4)} = \frac{1}{2(A+C)} \begin{bmatrix} C & -B' & -C & B' \\ -B & A & B & -A \\ -C & B' & C & -B' \\ B & -A & -B & A \end{bmatrix}.\end{aligned}$$

The reduced density matrix of the qubit B after the qubit A is measurement can be calculated by taking the partial trace over system A:

$$\begin{aligned}\widehat{\rho}_B^{(i)} &= \text{Tr}_A \left( \widehat{\rho}_2^{(i)} \right) \\ &= \left( \left[ \begin{array}{cc} 1 & 0 \end{array} \right]_A \otimes \left[ \begin{array}{cc} 1 & 0 \\ 0 & 1 \end{array} \right] \right) \widehat{\rho}_2^{(i)} \left( \left[ \begin{array}{c} 1 \\ 0 \end{array} \right]_A \otimes \left[ \begin{array}{cc} 1 & 0 \\ 0 & 1 \end{array} \right] \right) + \left( \left[ \begin{array}{cc} 0 & 1 \end{array} \right]_A \otimes \left[ \begin{array}{cc} 1 & 0 \\ 0 & 1 \end{array} \right] \right) \widehat{\rho}_2^{(i)} \left( \left[ \begin{array}{c} 0 \\ 1 \end{array} \right]_A \otimes \left[ \begin{array}{cc} 1 & 0 \\ 0 & 1 \end{array} \right] \right) \\ &= \left[ \begin{array}{cccc} 1 & 0 & 0 & 0 \\ 0 & 1 & 0 & 0 \end{array} \right] \widehat{\rho}_2^{(i)} \begin{bmatrix} 1 & 0 \\ 0 & 1 \\ 0 & 0 \\ 0 & 0 \end{bmatrix} + \left[ \begin{array}{cccc} 0 & 0 & 1 & 0 \\ 0 & 0 & 0 & 1 \end{array} \right] \widehat{\rho}_2^{(i)} \begin{bmatrix} 0 & 0 \\ 0 & 0 \\ 1 & 0 \\ 0 & 1 \end{bmatrix}.\end{aligned}$$

We get the following matrixes:

$$\widehat{\rho}_B^{(1)} = \frac{1}{A} \begin{bmatrix} 0 & 0 \\ 0 & A \end{bmatrix}, \quad \widehat{\rho}_B^{(2)} = \frac{1}{B'} \begin{bmatrix} B' & 0 \\ 0 & 0 \end{bmatrix},$$

$$\hat{\rho}_B^{(3)} = \frac{1}{(A+C)} \begin{bmatrix} C & B' \\ B & A \end{bmatrix}, \quad \hat{\rho}_B^{(4)} = \frac{1}{(A+C)} \begin{bmatrix} C & -B' \\ -B & A \end{bmatrix}.$$

Now, we can calculate the probabilities of the detectors  $D_B^j$  triggering occurring given that detectors  $D_A^i$  is triggering:

$$P^{ij} = \frac{1}{2} |\Psi\rangle_j^B \hat{\rho}_B^{(i)} \langle \Psi|_j^B,$$

$$P^{11} = \frac{1}{2A} \begin{bmatrix} 1 & 0 \\ 0 & 1 \end{bmatrix} \cdot \begin{bmatrix} 0 & 0 \\ 0 & A \end{bmatrix} \begin{bmatrix} 1 \\ 0 \end{bmatrix} = 0,$$

$$P^{12} = \frac{1}{2A} \begin{bmatrix} 0 & 1 \\ 0 & 1 \end{bmatrix} \cdot \begin{bmatrix} 0 & 0 \\ 0 & A \end{bmatrix} \begin{bmatrix} 0 \\ 1 \end{bmatrix} = \frac{1}{2},$$

$$P^{13} = \frac{1}{4A} \begin{bmatrix} 1 & 1 \\ 0 & 1 \end{bmatrix} \cdot \begin{bmatrix} 0 & 0 \\ 0 & A \end{bmatrix} \begin{bmatrix} 1 \\ 1 \end{bmatrix} = \frac{1}{4},$$

$$P^{14} = \frac{1}{4A} \begin{bmatrix} -1 & 1 \\ 0 & 1 \end{bmatrix} \cdot \begin{bmatrix} 0 & 0 \\ 0 & A \end{bmatrix} \begin{bmatrix} -1 \\ 1 \end{bmatrix} = \frac{1}{4},$$

$$P^{21} = \frac{1}{2B'} \begin{bmatrix} 1 & 0 \\ 0 & 1 \end{bmatrix} \cdot \begin{bmatrix} B' & 0 \\ 0 & 0 \end{bmatrix} \begin{bmatrix} 1 \\ 0 \end{bmatrix} = \frac{1}{2},$$

$$P^{22} = \frac{1}{2B'} \begin{bmatrix} 0 & 1 \\ 0 & 1 \end{bmatrix} \cdot \begin{bmatrix} B' & 0 \\ 0 & 0 \end{bmatrix} \begin{bmatrix} 0 \\ 1 \end{bmatrix} = 0,$$

$$P^{23} = \frac{1}{4B'} \begin{bmatrix} 1 & 1 \\ 0 & 1 \end{bmatrix} \cdot \begin{bmatrix} B' & 0 \\ 0 & 0 \end{bmatrix} \begin{bmatrix} 1 \\ 1 \end{bmatrix} = \frac{1}{4},$$

$$P^{24} = \frac{1}{4B'} \begin{bmatrix} -1 & 1 \\ 0 & 1 \end{bmatrix} \cdot \begin{bmatrix} B' & 0 \\ 0 & 0 \end{bmatrix} \begin{bmatrix} -1 \\ 1 \end{bmatrix} = \frac{1}{4},$$

$$P^{31} = \frac{1}{2(A+C)} \begin{bmatrix} 1 & 0 \\ 0 & 1 \end{bmatrix} \cdot \begin{bmatrix} C & B' \\ B & A \end{bmatrix} \begin{bmatrix} 1 \\ 0 \end{bmatrix} = \frac{C}{2(A+C)},$$

$$P^{32} = \frac{1}{2(A+C)} \begin{bmatrix} 0 & 1 \\ 0 & 1 \end{bmatrix} \cdot \begin{bmatrix} C & B' \\ B & A \end{bmatrix} \begin{bmatrix} 0 \\ 1 \end{bmatrix} = \frac{A}{2(A+C)},$$

$$P^{33} = \frac{1}{4(A+C)} \begin{bmatrix} 1 & 1 \\ 0 & 1 \end{bmatrix} \cdot \begin{bmatrix} C & B' \\ B & A \end{bmatrix} \begin{bmatrix} 1 \\ 1 \end{bmatrix} = \frac{A+B+B'+C}{4(A+C)},$$

$$P^{34} = \frac{1}{4(A+C)} \begin{bmatrix} -1 & 1 \\ 0 & 1 \end{bmatrix} \cdot \begin{bmatrix} C & B' \\ B & A \end{bmatrix} \begin{bmatrix} -1 \\ 1 \end{bmatrix} = \frac{A-B-B'+C}{4(A+C)},$$

$$P^{41} = \frac{1}{2(A+C)} \begin{bmatrix} 1 & 0 \\ 0 & 1 \end{bmatrix} \cdot \begin{bmatrix} C & -B' \\ -B & A \end{bmatrix} \begin{bmatrix} 1 \\ 0 \end{bmatrix} = \frac{C}{2(A+C)},$$

$$P^{42} = \frac{1}{2(A+C)} \begin{bmatrix} 0 & 1 \\ 0 & 1 \end{bmatrix} \cdot \begin{bmatrix} C & -B' \\ -B & A \end{bmatrix} \begin{bmatrix} 0 \\ 1 \end{bmatrix} = \frac{A}{2(A+C)},$$

$$P^{44} = \frac{1}{4(A+C)} \begin{bmatrix} -1 & 1 \\ 0 & 1 \end{bmatrix} \cdot \begin{bmatrix} C & -B' \\ -B & A \end{bmatrix} \begin{bmatrix} -1 \\ 1 \end{bmatrix} = \frac{A+B+B'+C}{4(A+C)},$$

$$P^{43} = \frac{1}{4(A+C)} \begin{bmatrix} 1 & 1 \\ 0 & 1 \end{bmatrix} \cdot \begin{bmatrix} C & -B' \\ -B & A \end{bmatrix} \begin{bmatrix} 1 \\ 1 \end{bmatrix} = \frac{A-B-B'+C}{4(A+C)}.$$

### Acknowledgments

The reported study was funded by RFBR, project number 19-31-90154.

**References**

- [1] Derkach I., Usenko V.C., Filip R. Squeezing-enhanced quantum key distribution over atmospheric channels. *New J. Phys.*, 2020, **22**, P. 053006.
- [2] Dixon A., et al. High speed prototype quantum key distribution system and long term field trial. *Opt. Express*, 2015, **23**, P. 7583–7592.
- [3] Choi I., et al. Field trial of a quantum secured 10 gb/s dwdm transmission system over a single installed fiber. *Opt. Express*, 2014, **22**, P. 23121–23128.
- [4] Fröhlich B., et al. Quantum secured gigabit optical access networks. *Sci. Rep.*, 2015, **5**, P. 18121.
- [5] Bohmann M., Semenov A.A., Sperling J., Vogel W. Gaussian entanglement in the turbulent atmosphere. *Phys. Rev. A*, 2016, **94**, P. 010302(R).
- [6] Andrews L.C., Phillips R.L. *Laser beam propagation through random media*, SPIE Press, Bellingham, Washington, 2005.
- [7] Vasylyev D.Yu., Semenov A.A., Vogel W. Toward Global Quantum Communication: Beam Wandering Preserves Nonclassicality. *Phys. Rev. Lett.*, 2012, **108**, P. 220501.
- [8] Vasylyev D.Yu., Semenov A.A., Vogel W. Atmospheric Quantum Channels with Weak and Strong Turbulence. *Phys. Rev. Lett.*, 2016, **117**, P. 090501.
- [9] Semenov A.A., Vogel W. Entanglement transfer through the turbulent atmosphere, *Phys. Rev. A*, 2010, **81**, P. 023835.
- [10] Miroshnichenko G.P., Sotnikova A.A. Optimization of optical fiber parameters to reduce errors of quantum key distribution using entangled polarization states of biphotons. *Optics and Spectroscopy*, 2012, **112**, P. 327–334.
- [11] Gaidash A.A., Medmedeva S.S., Miroshnichenko G.P. Analysis of the unambiguous state discrimination with unequal a priori probabilities. *Nanosystems: Physics, Chemistry, Mathematics*, 2019, **10**(4), P. 398–401.
- [12] Kiselev F.D., Samsonov E.Y., Gleim A.V. Modeling of linear optical controlled-Z quantum gate with dimensional errors of passive components. *Nanosystems: Physics, Chemistry, Mathematics*, 2019, **10**(6), P. 627–631.

## Effective easy-axis anisotropy of the two-sublattice single-chain magnet with twisted easy planes

M. S. Shustin<sup>1</sup>, M. N. Potkina<sup>2,3,4</sup>

<sup>1</sup>L. V. Kirensky Institute of Physics, 660036, Krasnoyarsk, Russia

<sup>2</sup>ITMO University, Kronverkskiy, 49, St. Petersburg, 197101, Russia

<sup>3</sup>St. Petersburg State University, St. Petersburg, 198504, Russia

<sup>4</sup>Science Institute and Faculty of Physical Sciences, Univ. of Iceland 107 Reykjavík, Iceland

mshustin@yandex.ru, potkina.maria@yandex.ru

PACS 75.30.Gw, 75.47.-m, 75.10.Dg

DOI 10.17586/2220-8054-2020-11-6-659-665

An analytical solution for the spin-wave spectrum of the two-sublattice 1D magnet with  $S_A = S_B = 1$  and twisting easy planes has been obtained. Such planes are mutually twisted by an angle  $\varphi$  relative to each other. For the case of mutually orthogonal easy planes  $\varphi = \pi/2$ , the spectrum vs. quasi-momentum dependence has been compared with that of an easy-axis magnet with the easy axis aligned along the line of intersection of the planes. An analogy of the spectra of the models has been shown, indicating the possibility of the effective easy axis anisotropy in easy-plane two-sublattice single-chain magnets.

**Keywords:** single-chain magnets, magnonic spectrum, strong single-ion anisotropy.

Received: 18 October 2020

Revised: 10 November 2020

### 1. Introduction

In recent years, strongly anisotropic single-chain magnets (SCM) have attracted considerable attention in view of their promising use in magnetic memory and spintronics devices [1]. From a fundamental point of view, SCMs are of interest as low-dimensional magnetic materials with developed spin fluctuations [2–4]. To date, several tens of single-chain magnets have been synthesized with different properties. From the prospects for spintronics, compounds supporting radiation-induced long-lived magnetic excitations are of considerable interest [1, 5, 6]. Such compounds include the four-sublattice SCM *catena* –  $[\text{Fe}^{II}(\text{ClO}_4)_2\text{Fe}^{III}(\text{bpca})_2](\text{ClO}_4)$  [7–9] with twisting and mutually orthogonal easy planes. Due to the different orientations of the above easy planes, the effective easy-axis anisotropy is induced and microscopic magnetic domains with sharp domain walls are created [7, 9]. On the other hand, the presence of the easy-plane single-ion anisotropy induces strong spin fluctuations [10, 11] which have to be taken into account for consecutive analysis of experimental data [8, 12]. One should expect formation of similar easy-axis anisotropy in two-sublattice single-chain magnets with twisted directions of the easy planes. In this work, this effect is considered on the basis of analytical calculations of the spin-wave spectra of spin-one two-sublattice 1D magnets: an easy-plane magnet with twisted easy planes, and an easy-axis one. This problem has been solved with the use of atomic representation detailed in the works [7, 10, 13].

### 2. Spin-wave spectrum of the two-sublattice anisotropic SCMs

The main goal of this work is to formulate a quantum spin model of easy-plane single-chain magnet, for which the emergence of a macroscopic easy-axis can be demonstrated analytically. Since single-chain magnets are low-dimensional and highly anisotropic, it is important that such a consideration correctly takes into account strong anisotropy and spin fluctuations. These requirements lead to a certain compromise. On the one hand, the requirement of simple and analytical consideration leads to a model with a small number of sublattices and the small spin values of the sublattices. On the other hand, since the contribution of quantum fluctuations is significant for magnets with small spin moments, the theory under consideration should take into account these effects beyond the mean-field approximation. As a result, we propose a model of a two-sublattice spin-one single-chain magnet with alternating and mutually twisted on the angle  $\varphi$  easy-planes. This model is considered in the generalized spin-wave approximation, beyond anisotropic mean field approximation. In this work, we consider a low-energy excitation spectrum of the model, which determines its low-temperature thermodynamics.

Let us consider an anisotropic two-sublattice 1D magnet with sublattice spins  $S_A = S_B = 1$  and alternated easy planes mutually twisted on the angle  $\varphi$ . The Hamiltonian of the system is:

$$\widehat{\mathcal{H}} = \sum_{f \in A} \left[ \mathcal{H}_A^a(\vec{S}_f) - \bar{H}_A S_f^z \right] + \sum_{g \in B} \left[ \mathcal{H}_B^a(\vec{S}_g) - \bar{H}_B S_g^z \right] - J \sum_{\langle f, g \rangle} \Delta \vec{S}_f \Delta \vec{S}_g, \quad (1)$$

where the symbol  $\langle f, g \rangle$  means the summation over the neighboring sites,  $\vec{S}_f$  and  $\vec{S}_g$  are the vector operators of the spin moments of the sites  $f$  and  $g$  associated with  $A$  and  $B$  sublattices, respectively.  $\Delta \vec{S}_f = \vec{S}_f - \langle \vec{S}_A \rangle$ ,  $\Delta \vec{S}_g = \vec{S}_g - \langle \vec{S}_B \rangle$ . The single-ion anisotropy of the ions on the  $A$  and  $B$  sublattices are described by operators  $\mathcal{H}_A^a(\vec{S}_f)$  and  $\mathcal{H}_B^a(\vec{S}_g)$ , respectively:

$$\mathcal{H}_A^a(\vec{S}_f) = 2D(S_f^x)^2; \quad \mathcal{H}_B^a(\vec{S}_g) = 0.5 \cdot D(S_g^+ e^{-i\varphi} + S_g^- e^{i\varphi})^2. \quad (2)$$

where  $\bar{H}_{A(B)} = H - J \langle S_{g(f)}^z \rangle$  are the effective magnetic fields, which contribute to the sublattices  $A(B)$ , respectively. In this research, we assume the external magnetic field to be zero ( $H = 0$ ).  $D > 0$  is the parameter of easy-plane single-ion anisotropy;  $J > 0$  is the exchange parameter, wherein  $D$  is assumed to be comparable or superior to  $J$ . Thus, in the following theory the single-ion contributions to the Hamiltonian (the first two terms in (1)) are considered exactly, while the fluctuation correction to the exchange interaction (the last term in (1)) is considered as a perturbation. In the expression for the Hamiltonian, we omitted the constant term, since it does not contribute to the excitation spectrum and is not interesting for the present study. We note that excitation spectrum has been assumed to be gapped, which corresponds to the existence of the short-range magnetic ordering with averages  $\langle S_{f,g}^z \rangle$ .

For what follows, it is important to note two important cases (see Fig. 1): a)  $\varphi = 0$  and b)  $\varphi = \pi/2$ . At  $\varphi = 0$  the system is equivalent to the easy-plane 1D magnet (Fig. 1a) considered in [10]. Its spin-wave excitation spectrum is determined as:

$$\omega_{\perp}(q) = \sqrt{(\varepsilon_{21} - J_q)^2 - J_q^2 \sin^2 2\theta}; \quad \omega_{\parallel}(q) = \sqrt{(\varepsilon_{31} - 2\varepsilon_{31} J_q \sin^2 2\theta)}; \quad (3)$$

where

$$\begin{aligned} \varepsilon_{21} &= D + \sqrt{D^2 + \bar{H}^2}; & \varepsilon_{31} &= 2\sqrt{D^2 + \bar{H}^2} \\ \sin 2\theta &= -D/(\bar{H}^2 + D^2)^{1/2}; & \cos 2\theta &= \bar{H}/(\bar{H}^2 + D^2)^{1/2}; \end{aligned} \quad (4)$$

$\bar{H} = \bar{H}_A = \bar{H}_B$ ;  $J_q = 2J \cos q$  is the Fourier-transform with quasimomentum  $q$  of the exchange interaction amplitude. Note that due to introduction of two sublattices  $-\pi/2 < q < \pi/2$ , and for this case, there are also branches  $\omega_{\perp}(q + \pi/2)$  and  $\omega_{\parallel}(q + \pi/2)$ . For such a spectrum, the width of the spin-wave band is many times greater than the gap in the excitation spectrum, and there is no effective easy-axis anisotropy.

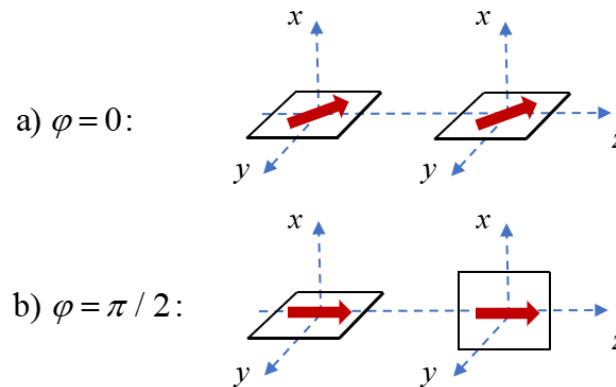


FIG. 1. Structure of the magnetic cells of the two-sublattice easy-plane 1D magnet with twisted on the angle  $\varphi$  easy planes. (a) the case of  $\varphi = 0$  then the system is equivalent to the easy-plane 1D magnet, (b) the case of twisted easy planes,  $\varphi = \pi/2$ .

At the  $\varphi = \pi/2$  case (mutually orthogonal easy-planes, Fig. 1b), we expect from the semiclassical analysis the formation of the effective easy axis. This is because the magnetic moments of two different sublattices, on the one hand, tend to lie in mutually orthogonal planes due to strong anisotropy, and, on the other hand, to be oriented parallel to each other due to exchange interaction. The only possible compromise in this case is the alignment of the moments

along the easy-planes intersection line (the z-axis in Fig. 1). This means that the thermodynamics of the system will be analogous to that of an easy-axis magnet. Since the thermodynamics of the system is determined by the excitation spectrum, let us consider the evolution of the one with a change of  $\varphi$ .

In order to take into account the anisotropy exactly we use the ideology of atomic representation [13]. This representation assumes a diagonalisation of the single sites operators of the Hamiltonian (2):

$$\left[ H_{A(B)}^a(\vec{S}) - \bar{H}_{A(B)} S^z \right] |\psi_p\rangle_{A(B)} = E_p |\psi_p\rangle_{A(B)} \quad (5)$$

where energy levels  $E_p$  ( $p = 1, 2, 3$ ) are independent of sublattice indices. They are related with the parameters  $\varepsilon_{21} = E_2 - E_1$  and  $\varepsilon_{31} = E_3 - E_1$  introduced earlier (4). Bearing in mind that the sublattice A is equivalent to sublattice B at  $\varphi = 0$ , we present expressions for single-ion states and their energies in general form as functions of  $\varphi$ :

$$\begin{aligned} |\psi_1\rangle &= e^{-i\varphi} \cos\theta |1\rangle + e^{i\varphi} \sin\theta |-1\rangle; & E_1 &= D - \sqrt{D^2 + \bar{H}^2}; \\ |\psi_2\rangle &= |0\rangle; & E_2 &= 2D; \\ |\psi_3\rangle &= -e^{-i\varphi} \sin\theta |1\rangle + e^{i\varphi} \cos\theta |-1\rangle; & E_3 &= D + \sqrt{D^2 + \bar{H}^2}; \\ \cos\theta &= \sqrt{\frac{1}{2} \left( 1 + \frac{\bar{H}}{\sqrt{D^2 + \bar{H}^2}} \right)}; & \sin\theta &= -\sqrt{\frac{1}{2} \left( 1 - \frac{\bar{H}}{\sqrt{D^2 + \bar{H}^2}} \right)}. \end{aligned} \quad (6)$$

Here, we used the eigenbasis  $|M\rangle$  of the  $S^z$  operator ( $M = \pm 1, 0$ ). Following to the [7, 10, 13] let us introduce the Hubbard operators  $X_{fj}^{pq} = |\psi_p; fj\rangle \langle \psi_q; fj|$  based on the eigenstates  $\{|\psi_p; fj\rangle\}$  on the sites  $f$  of the  $j = A, B$  sublattices. In this representation the spin operators have the form:

$$S_j^z = \sum_{\alpha} \gamma_{\parallel, j}(\alpha) X_j^{\alpha} + \sum_p \Gamma_{\parallel, j}(p) h_j^p; \quad S_j^+ = \sum_{\alpha} \gamma_{\perp, j}(\alpha) X_j^{\alpha} + \sum_p \Gamma_{\perp, j}(p) h_j^p, \quad (7)$$

Summation over  $\alpha$  means summation over the root vectors  $\alpha = \alpha(p, q)$  [13], which describes the transitions from the initial  $|\psi_p\rangle$  to the final  $|\psi_q\rangle$  single-ion eigenstate. The definition of root vectors follows from the system of equalities:  $X^{pq} = X^{\alpha(p, q)} = X^{\alpha}$ ;  $X^{qp} = X^{-\alpha(p, q)} = X^{-\alpha}$ . Moreover,  $\gamma_{\parallel}(\alpha)$ ,  $\Gamma_{\parallel}(\alpha)$  and  $\gamma_{\perp}(\alpha)$ ,  $\Gamma_{\perp}(\alpha)$  are, respectively, the longitudinal and transverse parameters of the representation of the operators  $S^z$  and  $S^+$  in terms of the Hubbard operators:

$$\gamma_{\parallel(\perp)j}(\alpha(p, q)) = \langle \psi_p^j | S_j^{z(+)} | \psi_q^j \rangle; \quad \Gamma_{\parallel(\perp)j}(p) = \langle \psi_p^j | S_j^{z(+)} | \psi_p^j \rangle. \quad (8)$$

Let us introduce the retarded Green functions:

$$G_{jj'}^{\alpha\beta}(f - f'; t - t') \equiv \langle \langle X_{fj}^{\alpha}(t) | X_{f'j'}^{-\beta}(t') \rangle \rangle = -i\theta(t - t') \langle [X_{fj}^{\alpha}(t), X_{f'j'}^{-\beta}(t')] \rangle. \quad (9)$$

where  $X_{fj}^{\alpha}(t)$  are the Hubbard operators in the Heisenberg representation. The exact system of equations of motion for such functions is infinite [14]. However, using the Hubbard I approximation [15]:  $\langle [X_{fj}^{\alpha}(t), X_{f'j'}^{-\beta}(t')] \rangle = \delta_{ff'} \delta_{jj'} \delta_{\alpha\beta} b_{j\alpha}$  a closed system of equations for the Green's functions can be found in the frequency-quasimomentum representation. The algorithm for finding the Green's functions is described in [12]. For the considered model (1) we obtain using this approach

$$\begin{aligned} G_{j\alpha; j\beta}(\vec{q}, \omega_n) &= \delta_{\alpha, \beta} G_{j\alpha}(\omega_n) b_j(\alpha) + \\ &J_q G_{j\alpha}(\omega_n) G_{j\beta}(\omega_n) b_j(\alpha) b_j(\beta) \left\{ \Delta_{\parallel}^{-1}(\vec{q}, \omega_n) \cdot 2J_q u_j(\omega_n) \gamma_{\parallel, j}(\alpha) \gamma_{\parallel, j}(-\alpha) + \right. \\ &+ \Delta_{\perp}^{-1}(\vec{q}, \omega_n) \cdot \left[ \gamma_{\perp, j}(\alpha) \left( \gamma_{\perp, j}(\beta) M_j(\vec{q}, \omega_n) - \gamma_{\perp, j}(-\beta) L_j(\vec{q}, \omega_n) \right) + \right. \\ &\left. \left. + (\alpha \rightarrow -\alpha; \beta \rightarrow -\beta; i\omega_n \rightarrow -i\omega_n) \right] \right\}; \end{aligned} \quad (10)$$

where  $G_{j\alpha(p, q)}(\omega) = [\omega + E_{jp} - E_{jq}]^{-1}$ ;  $b_{j\alpha(p, q)} = N_{jp} - N_{jq}$ . In the low temperature limit the occupation numbers  $N_{jp}$  of the quantum states  $|\psi_p; j\rangle$  are assumed to be  $N_{jp} = 1$  if  $|\psi_p; j\rangle$  is the ground state of eqn.(5), and  $N_{jp} = 0$  in other cases. The functions  $M_j(\vec{q}, \omega_n)$  can be found analytically, but we do not present them here because they are cumbersome and unnecessary.

The spectrum of elementary excitations of the system can be determined from finding the poles of the Green's functions, namely, from solving the equations

$$\begin{aligned}\Delta_{\parallel}(\vec{q}, \omega) &= 1 - 4J_q^2 u_A(\omega) u_B(\omega) = 0; \\ \Delta_{\perp}(\vec{q}, \omega) &= \left[1 - \frac{1}{4}J_q^2 z_A(\omega) z_B(\omega)\right] \left[1 - \frac{1}{4}J_q^2 z_A(-\omega) z_B(-\omega)\right] - \frac{J_q^4}{16} \times \\ &\left(z_A(\omega) z_A(-\omega) w_B^2(\omega) + z_B(\omega) z_B(-\omega) w_A^2(\omega) - w_A^2(\omega) w_B^2(\omega)\right) - \\ &- \frac{1}{2}J_q^2 w_A(\omega) w_B(\omega) = 0.\end{aligned}\quad (11)$$

The solutions of the equations  $\Delta_{\parallel}(\vec{q}, \omega) = 0$  and  $\Delta_{\perp}(\vec{q}, \omega) = 0$  determine the so-called longitudinal  $\omega_{\parallel}(q, \omega)$  and transverse  $\omega_{\perp}(q, \omega)$  branches of the magnonic spectrum, respectively. Recall, that in the case  $\varphi = 0$ , these branches are determined by eqn.(3). Note also that for the isotropic magnet, the above-used decoupling of the Green's functions (the Hubbard-I approximation) gives results equivalent to the well-known results that the spin-wave theory obtained, for example, using the Tyablikov approximation [14]. For this reason, the functions describe the transverse and longitudinal spectra of spin waves. In this case the damping of magnonic quasiparticles is not taken into account. And finally note that the above procedure for obtaining the spin-wave excitation spectrum is of a universal character and can be used to study magnets with an arbitrary single-ion anisotropy.

The functions  $u_j(\omega)$ ,  $z_j(\omega)$  and  $w_j(\omega)$  included in the expression (11) are determined through the characteristics of the single-ion spectrum  $E_p$ , matrix elements  $\gamma_{\perp j}(\alpha)$ , and single-ion occupation numbers  $N_{j,p}$  as follows ( $j = A, B$ ):

$$\begin{aligned}u_j(\omega) &= \sum_{\alpha} |\gamma_{\parallel j}(\alpha)|^2 G_{j\alpha}(\omega) b_A(\alpha); \quad z_j(\omega) = \sum_{\alpha} |\gamma_{\perp j}(\alpha)|^2 G_{j\alpha}(\omega) b_j(\alpha); \\ w_j(\omega) &= \sum_{\alpha} \gamma_{\perp j}(\alpha) \gamma_{\perp j}(-\alpha) G_{j\alpha}(\omega) b_j(\alpha).\end{aligned}\quad (12)$$

From the direct calculations it can be shown that:

$$u_B(\omega) = u_A(\omega); \quad z_B(\omega) = z_A(\omega); \quad w_B(\omega) = w_A(\omega) \cdot e^{2i\varphi}.\quad (13)$$

Thus, the longitudinal branches of spin-wave excitations do not change when the easy planes are rotated (when the angle  $\varphi$  changes) and the transverse branches of the spectrum  $\omega_{\perp}(q, \varphi)$  are of interest. In the case of  $\varphi = 0$  the functions  $z_A(\omega)$ ,  $w_A(\omega)$  can be obtained analytically in the low temperature limit: [10]:

$$z_A(\omega) = \frac{2\varepsilon_{21} + 2\omega \cos 2\theta}{(\omega)^2 - \varepsilon_{21}^2}; \quad w_A(\omega) = \frac{2\varepsilon_{21} \sin 2\theta}{(\omega)^2 - \varepsilon_{21}^2};\quad (14)$$

Hence, the  $\Delta_{\perp}(q, \omega)$  vs.  $\varphi$  dependence can be expressed through the characteristics of the spectrum of a single-sublattice easy-plane magnet (the case of  $\varphi = 0$ ):

$$\begin{aligned}\Delta_{\perp}(q, \omega, \varphi) &= \Delta_{\perp}(q, \omega, \varphi = 0) + J_q^2 w_A^2 \sin^2 \varphi; \\ \Delta_{\perp}(q, \omega, \varphi = 0) &= \frac{(\omega^2 - \omega_{\perp}^2(q))(\omega^2 - \omega_{\perp}^2(q + \pi))}{(\omega^2 - \varepsilon_{21}^2)^2}.\end{aligned}\quad (15)$$

With the use of these expressions, we obtain the dispersion equation for the system under consideration with arbitrary value  $\varphi$  (Fig. 1b):

$$\Delta_{\perp}(q, \omega, \varphi) = \frac{(\omega^2 - \omega_{\perp}^2(q))(\omega^2 - \omega_{\perp}^2(q + \pi)) + 4J_q^2 \varepsilon_{21}^2 \sin^2 2\theta \cdot \sin^2 \varphi}{(\omega^2 - \varepsilon_{21}^2)^2} = 0.$$

From the solution of this equation, the spin-wave spectrum vs. quasimomentum dependence has been obtained:

$$\omega_{\perp;1,2}^2(q, \varphi) = \frac{1}{2} \left[ \omega_{\perp}^2(q) + \omega_{\perp}^2(q + \pi) \pm \sqrt{(\omega_{\perp}^2(q) - \omega_{\perp}^2(q + \pi)) - 16J_q^2 \varepsilon_{21}^2 \sin^2 2\theta \cdot \sin^2 \varphi} \right].\quad (16)$$

In the case of mutually orthogonal easy planes ( $\varphi = \pi/2$ , Fig. 1b), the expressions are simplified and take the form:

$$\begin{aligned}\omega_{\perp,1}^2(q, \varphi = \pi/2) &= (\varepsilon_{21} - J_q \cos^2 2\theta)^2 = \omega_{\perp}^2(q) + \Delta_q^2; \\ \omega_{\perp,2}^2(q, \varphi = \pi/2) &= (\varepsilon_{21} + J_q \cos^2 2\theta)^2 = \omega_{\perp}^2(q + \pi) - \Delta_q^2; \\ \Delta_q^2 &= 4\varepsilon_{21} J_q \sin^2 \theta.\end{aligned}\quad (17)$$

The dependencies  $\omega_{\perp,1,2}(\varphi = \pi/2)$  vs.  $q$  are shown in Fig. 2 by the blue and green solid curves. Note that the branch  $\omega_{\perp,1}^2(q, \varphi = \pi/2)$  should make the main contribution to the low temperature magnetic properties of the system. As

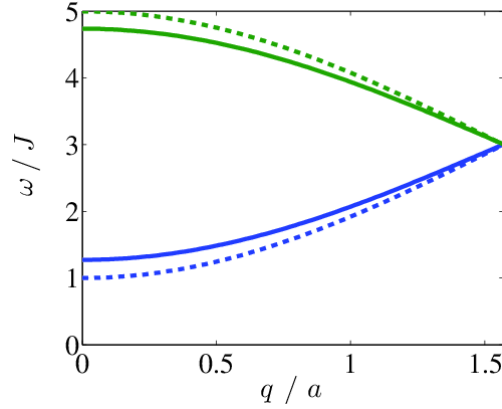


FIG. 2. Spin-wave spectra for 1D magnets with single-ion anisotropy of the easy plane and easy axis types. Solid and dashed lines corresponds to the  $\omega_{\perp,1,2}(\varphi = \pi/2)$  and  $\tilde{\omega}_{\perp,1,2}$  vs  $q$  dependencies defined by the eqn.(16) ( $D = J$ ) and eqn.(20) ( $D_{eff} = 0.5 \cdot J$ ), respectively.

can be seen from the Fig. 2, this branch is characterized by the excitation gap spectrum and by comparable to the value of this gap dispersion. Such features are characteristic of the excitations of easy-axis magnets.

In order to show the formation of an effective easy axis in the case of  $\varphi = \pi/2$  more formally, let us use that the dependence of the basic formulas (10)-(12) on the representation parameters (8) and single-ion energy spectrum  $E_p$  are universal and does not depend on specific structure of the single-ion operators in (1). This allows, within the framework of the same approach, to consider two-sublattice 1D magnet with  $S_{A,B} = 1$  and easy axis single-ion anisotropy. Its Hamiltonian is the (1) with the single-ion terms in the form:

$$\mathcal{H}_{A(B)}^a(\vec{S}_{f(g)}) \rightarrow \tilde{\mathcal{H}}_{A(B)}^a(\vec{S}_{f(g)}) = 2D_{eff}(S_{f(g)}^z)^2 - \tilde{H}S_{f(g)}^z; \quad (18)$$

where  $\tilde{H} = 2J - H$ . In this case we obtain the expressions for eigenfunctions and eigenvalues for the both sublattices:

$$|\tilde{\psi}_{1,3}\rangle = |\pm 1\rangle; \quad \tilde{E}_{1,3} = 2D_{eff} \mp \tilde{H}; \quad |\tilde{\psi}_2\rangle = |0\rangle; \quad \tilde{E}_2 = 0. \quad (19)$$

Computations similar to the case of easy-plane anisotropy, but using the eigenstates (19) of single-ion Hamiltonians  $\tilde{\mathcal{H}}_{A(B)}^a(\vec{S}_{f(g)})$ , make it possible to calculate the spin-wave spectrum of excitations of an easy-plane 1D magnet:

$$\tilde{\omega}_{\perp,1}^2(q, \pi/2) = (2D_{eff} + J - J_q)^2; \quad \tilde{\omega}_{\perp,2}^2(q, \pi/2) = (2D_{eff} + J + J_q)^2. \quad (20)$$

The dependencies  $\tilde{\omega}_{\perp,1,2}$  vs.  $q$  are shown in Fig. (2) by the blue and green dashed lines, respectively. It can be seen that the spectra  $\omega_{\perp,1,2}(q, \varphi = \pi/2)$  and  $\tilde{\omega}_{\perp,1,2}(q)$  are very closed to each other. Thus the thermodynamic properties of the strongly anisotropic 1D magnet with twisted and mutually orthogonal easy-planes and easy-axis 1D magnet should be similar. This achieves the goal of this work.

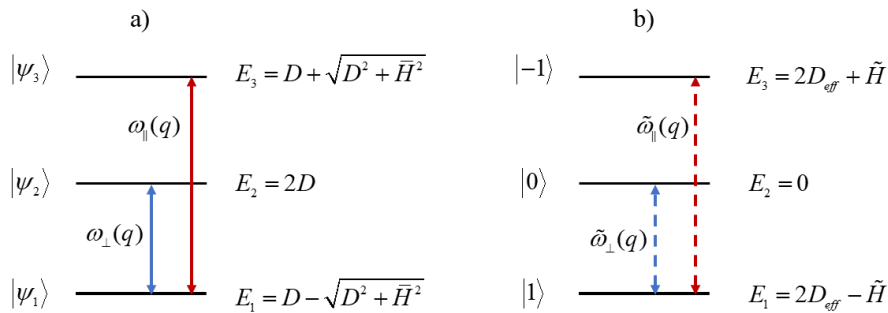


FIG. 3. The single-ion energy structure and quantum transitions responsible for the formation of quasiparticle bands of spin-wave excitations. a) the case of easy-plane magnet (eqns. (2), (5)). b) the case of easy-axis magnet (eqns. (18), (19)).

Let us briefly consider some of the peculiarities and the physical meaning of the obtained branches of the spin-wave spectrum. The expressions (11) and (12) show that the transverse  $\omega_{\perp}(q)$  and longitudinal  $\omega_{\parallel}(q)$  branches result from single-ion transitions with non-zero matrix elements of the operators  $S^+$  and  $S^z$ , respectively. The structures of the single-ion spectra of the easy-plane (eqns. (2) and (5)) and the easy-axis (eqns. (18) and (19)) magnets are shown in the Fig. 3a and Fig. 3b, respectively. For example, the transverse excitation branch  $\omega_{\perp}(q)$  in easy-plane magnet results from the hybridization of single-ion quantum transitions between the states  $|\psi_1\rangle = e^{-i\varphi} \cos\theta |1\rangle + e^{i\varphi} \sin\theta |-1\rangle$  and  $|\psi_2\rangle = |0\rangle$  with the energies  $E_1 = D - \sqrt{D^2 + H^2}$  and  $E_2 = 2D$ , respectively. In the case  $\varphi = 0$  we have the following spin-averages for the initial state  $|\psi_1\rangle$  of such transition:

$$\langle \psi_1 | S^{x,y} | \psi_1 \rangle = 0; \quad \langle \psi_1 | (S^{x,y})^2 | \psi_1 \rangle = \frac{1}{2} (1 \pm \sin 2\theta); \quad \langle \psi_1 | S^z | \psi_1 \rangle = \cos 2\theta. \quad (21)$$

In the limit  $D/J \gg 1$  such averages correspond to the spins lying in the easy plane. For the final state of the transition  $|\psi_2\rangle$  we have  $\langle \psi_2 | \vec{S} | \psi_2 \rangle = \langle \psi_2 | (S^z)^2 | \psi_2 \rangle = 0; \quad \langle \psi_2 | (S^{x,y})^2 | \psi_2 \rangle = 1$ . Thus in strongly anisotropic limit the quantum transition  $|\psi_1\rangle \rightarrow |\psi_2\rangle$  can be qualitatively considered as a spin flop from the easy plane into a plane perpendicular to the  $z$ -axis. In the limit of noninteracting ions, the single-ion transitions form highly degenerate levels, but when the exchange interaction between the sublattices is taken into account (the last term of the eqn.1), such transitions hybridize and form bands with the dependence of the excitation energy on the quasimomentum. The actual for this work single-ion transitions are shown by vertical lines with arrows. The corresponding quasi-momentum dependences of the spin-wave bands are depicted near the vertical lines. Note, that dependences  $\omega_{\perp}(q)$  and  $\tilde{\omega}_{\perp}(q)$  in Fig. 3 correspond to the low-lying quasiparticle branches shown in Fig. 2.

Note that in this work, the calculations were carried out under the assumption that at zero temperatures only the ground single-ion states are filled:  $N_{j;1} = 1; N_{j;2,3} = 0$  ( $j = A, B$ ). In other words, we have neglected the quantum fluctuations due to spin-wave renormalizations. To take such effects into account, the single-ion occupation numbers should be calculated using the spectral theorem [14] by the formula:

$$N_{jp} = \frac{1}{2} \sum_r \int_{-\pi/2}^{\pi/2} dq \left[ \frac{(F_j(\alpha, q, \omega_r) + F_j(\alpha, q, -\omega_r)) f_B(\frac{\omega_r}{T})}{\omega_r \prod_{l \neq r} (\omega_l^2 - \omega_r^2)} + \frac{F_j(\alpha, q, -\omega_r)}{\omega_r \prod_{l \neq r} (\omega_l^2 - \omega_r^2)} \right]. \quad (22)$$

Moreover, the calculation of the  $N_{jp}$  should be self-consistent with the calculation of the Green's functions (10). In the (22) the last ones has been represented in the form:

$$G_{j\alpha;j\alpha}(q, \omega) = \frac{F_j(\alpha, q, \omega_k(q))}{\prod_k (\omega^2 - \omega_k^2(q))}. \quad (23)$$

In this approximation, the energy spectrum and physical observables will be renormalized. However, such consideration is beyond the scope of this work.

### 3. Conclusion

In this work, on the basis of analytical solutions for the excitation spectra of simple 1D spin-models, we have demonstrated the effect of formation of effective easy axis in strongly anisotropic easy-plane magnets with several sublattices.

This effect is due to the different orientations of the easy planes for different sublattices. This result clarifies the low-temperature behavior of the anisotropic metal-organic single chain magnet *catena*-[Fe<sup>II</sup>(ClO<sub>4</sub>)<sub>2</sub>Fe<sup>III</sup>(*bpc*)<sub>2</sub>](ClO<sub>4</sub>).

### Acknowledgements

S. M. S. expresses deep gratitude to V. V. Val'kov. The main results of this work were with substantial use of the theory developed by him (see for example articles [10], [12] and references given in them), as well as on his previous advice. S. M. S. and M. N. P. acknowledges the support from the Foundation for the Advancement of Theoretical Physics and Mathematics "BASIS" (Grants No. 20-1-4-25-1 and 19-1-1-12-2, respectively).

### References

- [1] Zhang W.-X., Ishikawa R., Breedlove B., Yamashita M. Single-chain magnets: beyond the Glauber model. *RSC Advances*, 2013, **3**, P. 3772–3798.
- [2] Smirnov A.I., Glazkov V.N. Mesoscopic spin clusters, phase separation, and induced order in spin-gap magnets: A review. *Journal of Experimental and Theoretical Physics*, 2007, **105**, P. 861–879.
- [3] Kosmachev O.A., Fridman Yu.A., Galkina E.G., Ivanov B.A. Dynamic properties of magnets with spin  $S = 3/2$  and non-Heisenberg isotropic interaction. *Journal of Experimental and Theoretical Physics*, 2015, **147**, P. 320.
- [4] Kudasov Yu.B., Korshunov A.S., Pavlov V.N., Maslov D.A. Frustrated lattices of Ising chains. *Physics-Uspokhi*, 2012, **55**, P. 1169–1191.

- [5] Billoni O.V., Pianet V., Pescia A. V. Static and dynamic properties of single-chain magnets with sharp and broad domain walls. *Physical Review B*, 2011, **84**, P. 064415(1–16).
- [6] Liu T., Zhang Y.-J., Kanegawa S., Sato O. Photoinduced Metal-to-Metal Charge Transfer toward Single-Chain Magnet. *Journal of the American Chemical Society*, 2010, **132**, P. 8250–8251.
- [7] Val'kov, V. V., Shustin, M. S. Quantum Theory of Strongly Anisotropic Two-and Four-Sublattice Single-Chain Magnets. *Journal of Low Temperature Physics*, 2016, **185**, P. 564–568.
- [8] Kajiwara T., Tanaka H., Yamashita M. Single-chain magnets constructed with a twisting arrangement of the easy-plane of iron (II) ions. *Pure and Applied Chemistry*, 2008, **80**, P. 2297.
- [9] Kajiwara T., Tanaka H., Nakano M., Takaishi Sh., Nakazawa Ya., Yamashita M. Single-Chain Magnets Constructed by Using the Strict Orthogonality of Easy-Planes: Use of Structural Flexibility to Control the Magnetic Properties. *Inorganic Chemistry*, 2010, **49**, P. 8358
- [10] Val'kov V.V., Val'kova T.A. Low-temperature magnetization of an easy-plane ferromagnet. *Low Temperature Physics*, 1985, **11** (9), P. 951–959.
- [11] Fridman Yu.A., Kosmachev O.A. Quantum effects in an anisotropic ferrimagnet. *Physics of Solid State*, 2009, **51**, P. 1167.
- [12] Val'kov, V. V., Shustin, M. S. Quantum renormalizations in anisotropic multisublattice magnets and the modification of magnetic susceptibility under irradiation. *Journal of Experimental and Theoretical Physics*, 2015, **121**, P. 860.
- [13] Zaitcev R.O. Generalized diagram technique and spin waves in anisotropic antiferromagnet. *Soviet Journal of Experimental and Theoretical Physics*, 1975, **68**, P. 207 (Ru).
- [14] S.V. Tyablikov, *Methods in the Quantum Theory of Magnetism*. Nauka, Moskow, 1975.
- [15] J.Hubbard, *J. Proc. Roy. Soc. A*, 1963, **276**, P. 238.

## The novel polyindole based ZnO/MgO nanocomposite adsorbent for the removal of heavy metal ions from industrial effluents

Dedhila Devadathan<sup>1,3</sup>, V. Baiju<sup>1,3</sup>, J. P. Deepa<sup>2,3</sup>, R. Raveendran<sup>1,3</sup>

<sup>1</sup>Nanoscience Research Laboratory, PG & Research Department of Physics, Sree Narayana College, Kollam, India

<sup>2</sup>PG & Research Department of Chemistry, Sree Narayana College, Kollam, India

<sup>3</sup>University of Kerala, India

dedhila@yahoo.com

DOI 10.17586/2220-8054-2020-11-6-666-671

In the present work, ZnO/MgO nanocomposite was synthesized using a co-precipitation method, polyindole and the polyindole based ZnO/MgO nanocomposite were synthesized using chemical oxidation method. The synthesized materials were characterized using XRD and UV/Vis absorbance spectroscopy. The study investigates the applicability of polyindole based ZnO/MgO nanocomposite for the removal of Pb(II) heavy metal ion. Proper tuning can increase the removal efficiency of polyindole based ZnO/MgO nanocomposite and can be made a good candidate for the removal of lead ions.

**Keywords:** Adsorption, chemical oxidation, co-precipitation, nanocomposite.

*Received: 4 August 2020*

*Revised: 19 October 2020*

### 1. Introduction

Industrialization and urbanization have seriously led to high threat of pollutants like heavy metal ions to public health and environment [1]. So, it was necessary to find a new way to remove heavy metal ions before discharging them into the environment. Due to the economic constraints, development of a cost effective and clean process is essential. The various conventional technologies currently employed in the removal of effluents in industrial water are classical and do not lead to complete removal of pollutants. Therefore, there is a need to develop a novel treatment method that is more effective. Of all the known methods, adsorption has proved to be one of the most effective methods for the removal of heavy metal ions [2]. This method depends on factors such as the surface area, pore size distribution, polarity and functional groups of the adsorbent. Presently, nanotechnology is widely applied for purification and treatment of waste water. The novel properties of nanomaterials such as large surface area, potential for self assembly, high specificity, high reactivity and catalytic potential make them an excellent candidate for this application [3]. A developing trend for the nanomaterials is to synthesize composite structures and devices with materials capable of enhanced properties when compared to counter parts. This can be achieved either by utilizing the size advantage through templating on the nanomaterials and enhancing the properties to drive new synergetic properties of two combined materials [4]. In the present study, a polyindole based ZnO/MgO nanocomposite was prepared, analyzed and used as an adsorbent for the removal of Pb(II) ion. For comparative purposes the counter parts, polyindole and ZnO/MgO were also prepared.

### 2. Materials and methods

AR grade chemicals obtained from Merck were used for the preparation of ZnO/MgO, polyindole and the polyindole based nanocomposite. ZnO/MgO (ZMF) was prepared by the co-precipitation method in presence of capping agent. Polyindole (PI) and the polyindole based ZnO/MgO nanocomposite (PIZM) were prepared using chemical oxidation method. ZnO/MgO was annealed at 500 °C for three hours; polyindole and polyindole based nanocomposite in the as prepared form were used for analysis. For the preparation of the nanocomposite, ZMF was used. XRD study was carried out using XPERT-PRO model powder diffractometer (PAN analytical, Netherlands) employing Cu-K $\alpha$  radiation ( $\lambda = 1.54060 \text{ \AA}$ ) operating at 40 kV, 30 mA. The absorbance spectra of these samples were studied using JASCO V 650, UV/Vis spectrophotometer. Adsorption studies in the present work were carried out using GBC-AAS spectrometer having lamp current 5 mA and wavelength 270 nm.

### 3. Result and discussion

#### 3.1. XRD analysis

Figure 1 shows XRD of ZMF. ZMF showed well defined X-ray diffraction peaks which indicated that ZMF had crystalline nature. Again, the broader diffraction peaks indicated the smaller crystallite size. The interplanar spacing ( $d_{hkl}$  values),  $2\theta$  values and relative intensity values of ZMF corresponding to the observed diffraction peaks were compared with the standard values of ZnO and MgO as reported by JCPDS-International Centre for Diffraction Data. The data obtained for ZnO/MgO matched with JCPDS-ICDD pattern number #79-0205 of ZnO and #89-7746 of MgO separately. From JCPDS, MgO shows a cubic system with FCC lattice and ZnO shows hexagonal system with a primitive lattice. The presence of peaks of both ZnO and MgO indicates that the prepared sample is not a single phase but a composite. The variation observed in the  $d$  values of the crystal planes in case of ZMF when compared to ZnO and MgO from JCPDS, also confirms the formation of composite. The average crystallite size of ZMF calculated from the line broadening of the XRD pattern, using FWHM values of seven major peaks in the XRD spectrum making use of Scherrer formula:

$$D = \frac{k\lambda}{\beta_{hkl} \cos \theta_{hkl}}, \quad (1)$$

where  $D$  is the average crystallite size normal to the reflecting planes,  $k$  is the shape factor which lies between 0.95 and 1.15 depending on the shape of the grains ( $k = 1$  for spherical crystallites),  $\lambda$  is the wavelength of X-ray used and ( $\beta_{hkl}$ ) measured is the FWHM of the diffraction line in radians and  $\theta_{hkl}$  is the Bragg angle corresponding to the diffraction line arising from the planes designated by Miller indices ( $hkl$ ). The crystallite size for the sample as calculated from Scherrer equation is 22.85 nm. The XRD pattern of PI was found to match well with the XRD patterns in literature [5]. The XRD of polyindole shows the presence of numerous sharp crystalline peaks in the diffraction pattern having  $2\theta$  values between  $15^\circ$  and  $30^\circ$ . This can be related to the scattering from bare polymeric chains at the inter-planar spacing. Fig. 2 shows XRD obtained for PI.

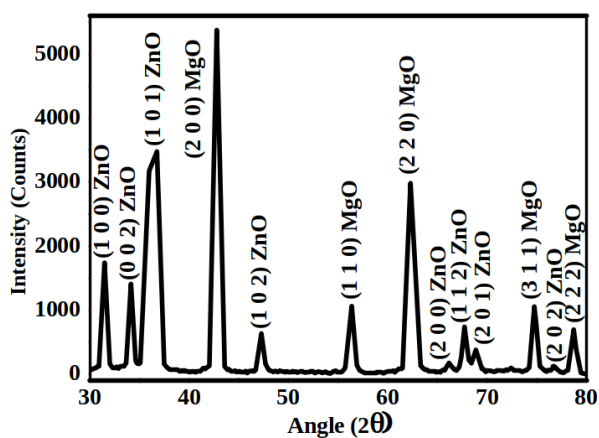


FIG. 1. XRD of ZnO/MgO

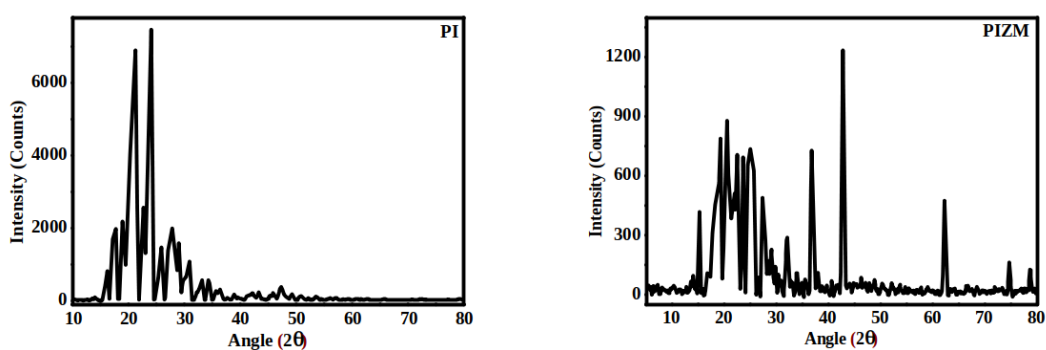


FIG. 2. XRD of polyindole and polyindole based ZnO/MgO nanocomposite

The appearance of peaks in the XRD of the polymer confirms the crystalline nature rather than amorphous nature. The higher the degree of regularity in arrangement or ordering of the polymer chain, the higher is the crystallinity [6]. The presence of sharp crystalline peaks in the XRD graph indicates good electrostatic (dipole–dipole) interactions among the adjoining molecular chains in the PI matrix and also their highly ordered state [7]. The XRD results justify the PI nanostructures as crystalline in nature. Fig. 2 shows XRD obtained for PIZM. XRD of PIZM confirms the formation of nanocomposite. The well defined peaks of planes (1 0 0), (0 0 2) and (1 0 1) of ZnO and (2 0 0), (2 2 0), (3 1 1) and (2 2 2) of MgO were found to be incorporated into the XRD spectrum of polyindole. It is clear from XRD of PIZM that the metal oxide particles are well distributed in the polymer matrix. Here the crystalline peaks between  $15^\circ$  and  $30^\circ$  were also observed. The variation of peaks observed in the XRD of PIZM in the region between  $15^\circ$  and  $30^\circ$  showed variations when compared to the XRD of PI which also supports the formation of nanocomposite.

### 3.2. UV Analysis

The UV/Vis absorption spectrum of the PI taken in the wavelength range 210 to 800 nm with 1 nm resolution is shown in Fig. 3. PI nanobelts depict a sharp absorption in the range 225 – 325 nm with  $\lambda_{\text{max}}$  situated at 292 nm, attributed to the conjugation of the benzene ring in the indole unit [8, 9]. The presence of small absorption band is observed in the range 435 – 543 nm with  $\lambda_{\text{max}}$  situated at 478 nm due to the  $\pi - \pi^*$  transitions of the benzene ring in the PI molecular chains [8]. The results indicate the presence of enhanced conjugated segments and easy flow of charge in PI molecular matrix. This band also relates to the extent of conjugation between adjacent rings in the polymer chain. The optical band gap of the material determined from the absorption spectrum using Tauc's relation was 3.82 eV. Due to large value of the optical band gap, the material is most suited in many applications in modern electronic industries. Fig. 4(a) shows the absorbance spectrum of ZMF. ZMF which displayed sub gaps. The optical band gap of ZMF determined from the absorption spectra using Tauc's relation are 1.75 and 3.3 eV respectively. Fig. 4(c) shows the Tauc plot obtained for ZMF. The UV/Vis absorbance spectrum of PIZM showed multiple absorption peaks in addition to the main peak observed in PI due to  $\pi - \pi^*$  transitions in the range 220 – 450 nm with  $\lambda_{\text{max}}$  value of 290 nm. The multiple peaks observed in the range 360 to 850 nm could be attributed to the  $n-\pi^*$  and  $n-\pi$  transitions as a result of the interactions between PI chains and ZMF nanoparticles. This causes easy charge transfer from PI to ZMF. The main optical band gap of PIZM determined from the absorption spectra using Tauc's relation was 3.68 eV.

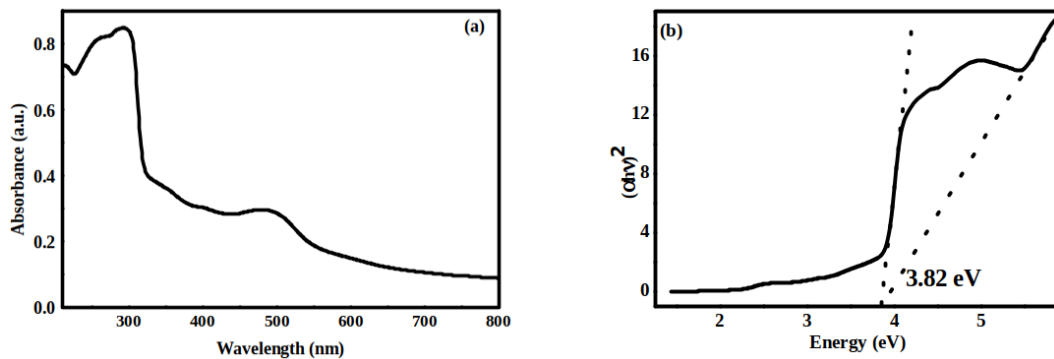


FIG. 3. UV/Vis Absorbance spectrum and (b) Tauc Plot of polyindole

### 3.3. Adsorption studies

Adsorption studies were performed by batch process by taking 0.1 gm of synthesized ZMF, PI and PIZM in a 100 ml clean and dried stoppered bottle. Known concentration of 50 ml  $\text{Pb}^{2+}$  solution was added in the same stoppered flask. This flask was placed on a mechanical shaker at 160 rpm and the rate of adsorption of lead on ZMF, PI and PIZM nanocomposite was studied. After desired time intervals (20, 40, 60, 80, 100 min etc.), the solution was filtered using Whatman filter paper no. 41 and reserved for atomic absorption spectroscopy study. The experiments were repeated for different solution pH values. The adsorption capacity ( $q$ ) and removal percentage are expressed as follows:

$$q = \frac{(C_0 - C_t)V}{W}, \quad (2)$$

$$\text{Removal Efficiency (\%)} = \frac{(C_0 - C_e)}{C_0} \times 100, \quad (3)$$

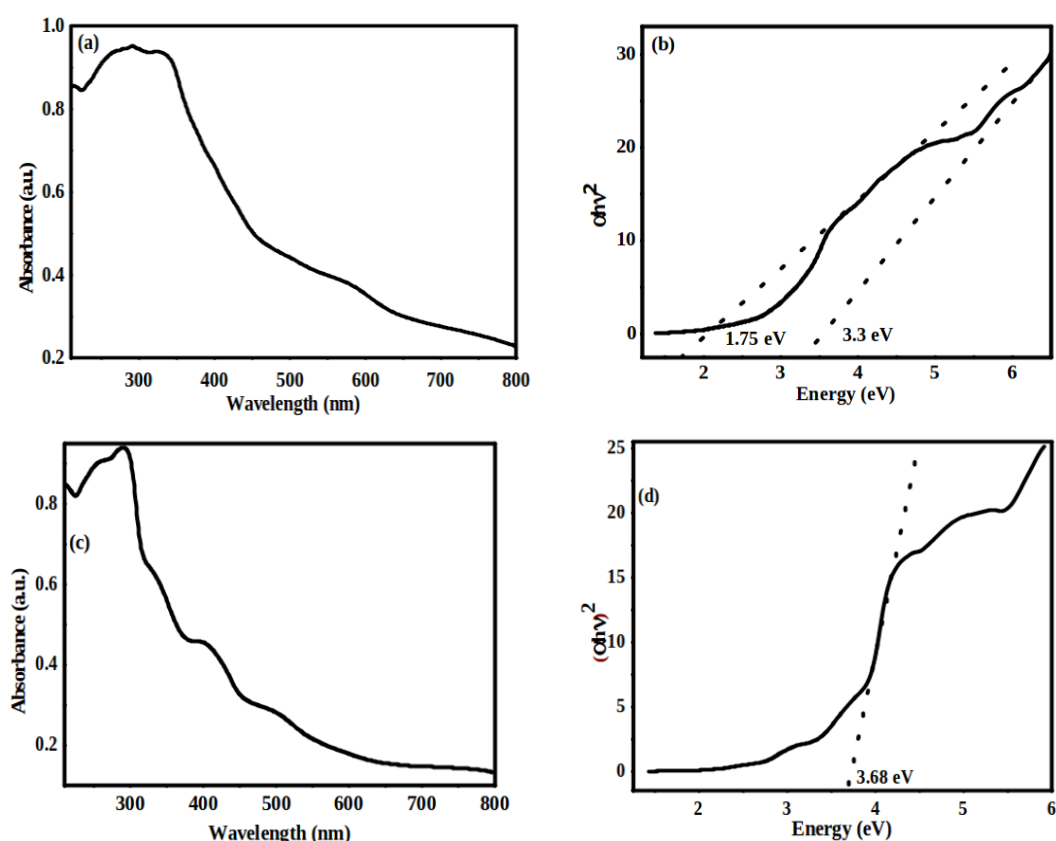


FIG. 4. UV/Vis Absorption spectrum of (a) ZnO/MgO (c) polyindole based ZnO/MgO nanocomposite and Tauc Plot of (b) ZnO/MgO (d) polyindole based ZnO/MgO nanocomposite

where  $q$  is the adsorption capacity of the adsorbate ( $\text{mg}\cdot\text{g}^{-1}$ ),  $W$  is the weight of adsorbent (g),  $V$  is the volume of solution (L), and  $C_0$  ( $\text{mgL}^{-1}$ ) and  $C_e$  ( $\text{mgL}^{-1}$ ) are initial and equilibrium concentration of adsorbate in solution.

For the adsorption of  $\text{Pb}^{2+}$  on the composite PIZM, it was found that the amount of adsorption increased with agitation time and attained equilibrium at 120 minutes i.e., the maximum removal efficiency was attained after 120 minutes (Fig. 5). The removal efficiency of ZMF for  $\text{Pb}^{2+}$  ions after 120 minutes was found to be 78.56%. The removal efficiency for polyindole was found to be 62.78% but, for the nanocomposite, it was 88.98%.

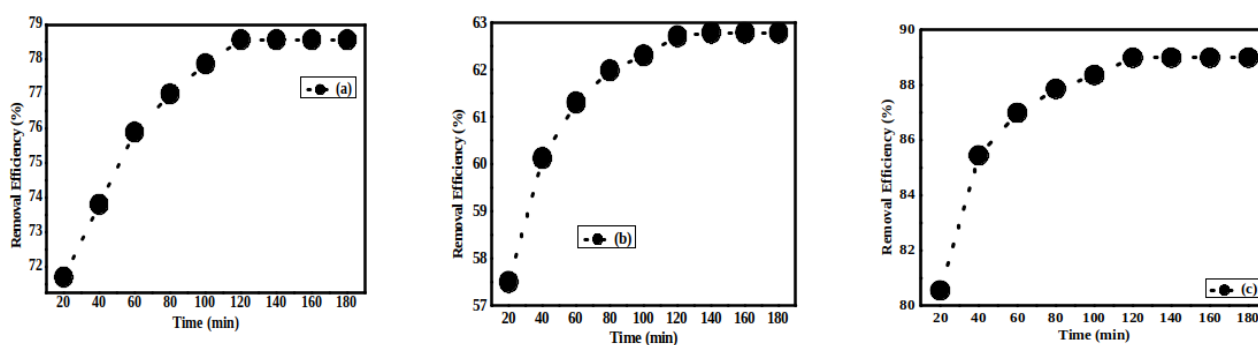


FIG. 5. Removal Efficiency vs Time using ZnO/MgO, polyindole and polyindole based ZnO/MgO nanocomposite for  $\text{Pb}^{2+}$  adsorption

Polyindole is an organic polymer that holds a large amount of polyfunctional groups (amino and imino groups) that can effectively adsorb heavy metal ions. The development of composite sorbents has opened up new opportunities of their application in deep removal of heavy metals from water. PIZM showed higher adsorption capacity when compared to its counter parts and this can be explained as follows. PIZM has both high specific area due to presence

of metal oxide and functional groups due to the presence of polyindole. In the case of all the three samples, the adsorption was higher in the beginning due to greater number of reaction sites available for  $Pb^{2+}$  adsorption.

The pH of the aqueous solution is an important operational parameter in the adsorption process because it affects the solubility of the metal ions, concentration of the counter ions on the functional groups of the adsorbent and the degree of ionization of the adsorbate during reaction [10]. Depending on the pH the active sites on an adsorbent can either be protonated or deprotonated and at the same time the adsorbate speciation in solution also depends on the pH too. Lead for example, exists as  $Pb^{2+}$ ,  $PbOH^+$  and  $Pb(OH)^{3-}$  depending on the solution's pH.

At lower pH values, low metal ion uptake was observed. The use of a very low pH may result in the competitive adsorption of the  $H^+$  and  $Pb^{2+}$  ions on the PIZM surface. At low pH values, the adsorbent is positively charged due to the presence of  $H^+$  ions on the surface of adsorbent and hence offers repulsive force to approaching  $Pb^{2+}$  ions. However, more  $Pb^{2+}$  uptake is observed as the pH increases which are due to the fact that at high pH values, lead still has a net positive charge but exists as  $PbOH^+$  while most active sites on the adsorbent are deprotonated. This leads to net attractive force that is responsible for high Pb removal from solution in the alkaline pH range.

At elevated pH values; in strong basic solutions, the chances of Pb(II) precipitation increase. It is therefore recommended to operate around the neutral pH to avoid precipitation effect. In the present study, the removal efficiency in the case of all the samples was found to increase with pH and attained maximum at pH 6 and then it was found to decrease (Fig. 6). The nanocomposite, PIZM showed maximum removal efficiency. From the present work it is concluded that proper tuning of PIZM nanocomposite can make it a good adsorbent for the removal of heavy metal ions. Proper tuning can increase the removal efficiency of PIZM and can be made a good candidate for the removal of lead ions.

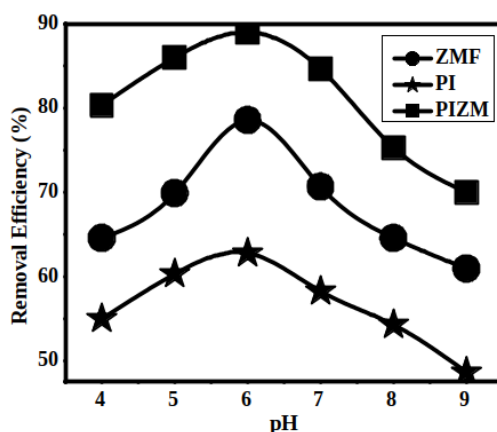


FIG. 6. Removal Efficiency vs pH using ZnO/MgO, polyindole and polyindole based ZnO/MgO nanocomposite for  $Pb^{2+}$  adsorption

#### 4. Conclusion

In the present work, ZnO/MgO nanocomposite (ZMF) was synthesized using co-precipitation method; polyindole (PI) and polyindole based ZnO/MgO nanocomposite (PIZM) were synthesized using a chemical oxidation method. The synthesized materials were characterized using XRD and UV/Vis absorbance spectroscopy. The presence of peaks of both ZnO and MgO in ZMF indicates that the prepared sample is not a single phase but a composite. The crystallite size for ZMF, as calculated from Scherrer equation, is 22.85 nm. The appearance of peaks in the XRD of the polymer confirms the crystalline nature rather than amorphous nature of PI. It is clear from XRD of PIZM that the metal oxide particles are well distributed in the polymer matrix. Energy band gaps of all the three samples were calculated from UV/Vis absorbance spectroscopic analysis. The study investigates the applicability of ZMF, PI and PIZM for the removal of Pb(II) heavy metal ion. The removal efficiency of ZMF for  $Pb^{2+}$  ions after 120 minutes was found to be 78.56%. The removal efficiency for polyindole was found to be 62.78%, but for the nanocomposite, it was 88.98%, which showed highest removal efficiency. The effect of pH on the removal efficiency of ZMF, PI and PIZM were studied. In the present study, the removal efficiency in the case of all the three samples was found to increase with pH and attained maximum at pH 6 and then it was found to decrease. Proper tuning can increase the removal efficiency of PIZM and can thus be made a good candidate for the removal of lead ions. PIZM was also found to be effective for the removal of  $Cd^{2+}$  ions and may possibly be used for the removal of other harmful metal ions, although that remains the scope of a future study.

## References

- [1] Ngah W.S.W., Hanafiah M.A.K.M. Removal of heavy metal ions from wastewater by chemically modified plant wastes as adsorbents: A review. *Bioresource Technology*, 2008, **99**, P. 3935–3948.
- [2] Manohar D.M., Noeline B.F., Anirudhan T.S. Adsorption performance of Al-pillared bentonite clay for the removal of cobalt (II) from aqueous phase. *Applied Clay Science*, 2006, **31**, P. 194–206.
- [3] Zhang S., Cheng F., et al. Removal of nickel ions from wastewater by Mg(OH)<sub>2</sub>/MgO nanostructures embedded in Al<sub>2</sub>O<sub>3</sub> membranes. *Journal of Alloys and Compounds*, 2006, **426**, P. 281–285.
- [4] Neamtu J., Verga N. Magnetic Nanoparticles for Magneto-Resonance Imaging and Targeted Drug Delivery. *Journal of Nanomaterials and Biostructures*, 2011, **6**, P. 969–978.
- [5] Goel S. Synthesis of polyindole nanoflakes through direct chemical oxidative route. *Advanced Science, Engineering and Medicine*, 2012, **4**, P. 438–441.
- [6] Hutten P.F.V., Hadziioannou G. Handbook of Organic Conductive Molecules and Polymers, edited by H.S. Nalwa, John Wiley, New York, 1997, **3**, P. 1–85.
- [7] Taylan N.B., Sari B., Unal H.I. Preparation of conducting poly(vinyl chloride)/polyindole composites and freestanding films via chemical polymerization. *Journal of Polymer Science Part B: Polymer Physics*, 2010, **48**, P. 1290–1298.
- [8] Eraldemir O., Sari B., Gok A., Unal H.B. Synthesis and characterization of polyindole/poly(vinylacetate) conducting composites. *Journal of Macromolecular Science, Part A: Pure and Applied Chemistry*, 2008, **45**, P. 205–211.
- [9] Xu J., Hou J., et al. <sup>1</sup>H NMR spectral studies on the polymerization mechanism of indole and its derivatives. *Spectrochimica Acta Part A*, 2006, **63**, P. 723–728.
- [10] Amuda O.S., Ojo O.I., Edewor T.I. Biosorption of Lead from Industrial Waste water using *Chrysophyllum albidum* seed shell. *Bioremediation Journal*, 2007, **11**, P. 183–194.

## ZnO nanoparticles as solar photocatalysts: Synthesis, effect of annealing temperature and applications

S. Sathya<sup>1</sup>, J. Vijayapriya<sup>1</sup>, K. Parasuraman<sup>1</sup>, D. Benny Anburaj<sup>2</sup>, S. Joshua Gnanamuthu<sup>3\*</sup>

<sup>1</sup>PG and Research Department of Physics, Poompuhar College (Affiliated to Bharathidasan University), Melaiyur, India

<sup>2</sup>PG and Research Department of Physics, D. G. Govt. Arts College (Affiliated to Bharathidasan University), Mayiladuthurai, India

<sup>3</sup>PG and Research Department of Physics, TBML College (Affiliated to Bharathidasan University), Porayar, India  
\*joshuagnanamuthu@gmail.com

DOI 10.17586/2220-8054-2020-11-6-672-679

ZnO nanoparticles were prepared by a hydrothermal method from the source materials of Zinc acetylacetonate hydrate and ammonium hydroxide. Further prepared samples were annealed at various temperatures for 3 hours. X-ray diffraction analysis was employed to study the structure and crystalline nature of synthesized nanoparticles. Scanning electron microscope images showed that the prepared ZnO nanoparticles acquired nano needle, hexagonal disk and porous nanorods structures due to the effect of annealing temperature. The photocatalytic activity of the prepared ZnO nanoparticles was evaluated for Methyl Blue (MB) dye which showed 94% of degradation and good stability for five cycles.

**Keywords:** ZnO, hydrothermal, nanorods, photocatalysis, degradation.

*Received: 13 August 2020*

*Revised: 30 August 2020*

*Final revision: 2 November 2020*

### 1. Introduction

In recent years, the implementation of water reclamation and reuse is gaining attention rapidly world-wide due to the water scarcity occurred as a result of climate change and poor water resource management (i.e. limited access to clean water resources and water demands exceed the available resources). Access to clean water is becoming an ever increasing problem in an expanding global economy and population countries [1]. One of the attractive solutions in response to water issues is implementation of wastewater reclamation and reuse projects to ensure a sustainable water development and management.

POPs (Persistent Organic Pollutants) are carbon-based chemical substances that are resistant to environment degradation and have been continuously released into the environment. POPs can cause severe harm to human beings and wildlife because of their poor biodegradability and carcinogenic characteristics in nature. Advanced treatment technologies are crucial to ensure that the reclaimed water is free of POPs. Various water treatment techniques have been employed to remove POPs from water streams including adsorption, membrane separation and coagulation [2]; however, these processes only concentrate or change the recalcitrant organic pollutants from the water to solid phase. For this reason, advanced oxidation processes (AOPs) have been proposed for the elimination of recalcitrant organic pollutants, especially for those with low biodegradability.

AOPs offer several advantages such as: (i) rapid degradation rate, (ii) mineralization of organic compounds to green products, (iii) ability to operate under ambient temperature and pressure, and (iv) reduction of the toxicity of organic compounds.

Photocatalytic oxidation (PCO) technology has been active in the field of pollution control since the 1980s due to the sustained developments in the photocatalyzed degradation of aqueous pollutants. Photocatalytic oxidation method finds wide applications in photocatalytic degradation of aqueous pollutants due to its high efficiency, low cost, energy saving and production of no other secondary pollutants in this process. Over the past few decades broadband semiconducting photocatalysis attracted great interest of many workers because of the potential of the process to solve environmental problems [3,4]. These photocatalysis exhibit appropriate energy potential to conduct oxidation and reduction process on their semiconducting surface [5]. ZnO is one of the important II–VI groups of n-type semiconductors which has direct band gap of 3.37 eV with large exciton binding energy of 60 meV. ZnO is proved to be a promising material for various applications, such as gas sensors [6], transistors [7], solar cells [8], hydrogen production [9] and photocatalysis [10] due to their electrical and optical properties.

Among the other semiconducting materials zinc oxide (ZnO) is extensively studied due to their unique physico-chemical, piezoelectric, optical and catalytic properties [11, 12]. These properties are correlated with shape, size and

morphology of ZnO nanoparticles [13, 14]. Santhosh et al. [15] reported that there are various proposed mechanisms for the degradation of dyes using the photocatalyst materials. One mechanism suggests that the oxidation of organic pollutants is first initiated by the free radicals, which are mainly induced by the electron-hole (e-/h+) pairs at the photocatalyst surface. Another mechanism states that the organic compound is firstly adsorbed on the photocatalyst surface and then reacts with excited superficial e-/h+ pair or OH radicals to form the final products. Hence, the photocatalytic performance of nanoparticles is determined by their shape and dimension. In recent years, investigation on the shape control synthesis of semiconducting nanostructures were carried out by many workers on ZnO nanostructures which lead to the formation of nanowires [16], nanotubes [17], nanobelts [18] and nanodisks [19] structures. ZnO nanostructures with different shapes and dimensions were developed by solution phase method such as sonochemical route [20, 21], sol-gel method [22, 23], reflux method [24] and hydrothermal method [25, 26]. Controlling the shape of the ZnO nanostructures and fast synthetic route under the ambient condition have become an important topic of investigation in the field of materials chemistry. In the present work, the effect of temperature on the structural, optical and morphological properties of ZnO nanoparticles prepared by hydrothermal method is presented and the photocatalytic activity of the synthesized ZnO nanoparticles is analyzed against Methyl Blue dye.

## 2. Materials and methods

### 2.1. Synthesis method

ZnO nanopowders were synthesized by simple hydrothermal method using the aqueous solution of Zinc acetylacetonate hydrate ( $\text{Zn}(\text{acac})_2 \cdot \text{H}_2\text{O}$ ) and  $\text{NH}_4\text{OH}$ . In a typical synthesis process, 1.3631 g of  $\text{Zn}(\text{acac})_2$  was dissolved in 100 ml of distilled water and  $\text{NH}_4\text{OH}$  was added dropwise to maintain the pH of solution 7 under constant stirring. Then this solution was continuously stirred for 1 hour and the resultant solution was transferred to Teflon-lined stainless steel autoclave of 100 ml volume and maintained at 150 °C for 3 hours in muffle furnace. After the hydrothermal reaction the autoclave was naturally allowed to cool to room temperature. The product of white precipitate was obtained and washed with distilled water and ethanol several times and dried at hot air oven at 60 °C. The dried particles were annealed at 300 °C for 3 hours. Similarly ZnO nanoparticles were prepared by hydrothermal method keeping the above experimental condition the same but the annealing temperature of the prepared dried particles was varying 400, 500 and 600 °C. The prepared ZnO nanoparticles were characterized for their structural, optical, and morphological properties and photocatalytic activities.

### 2.2. Characterization

Synthesized ZnO nanoparticles crystalline nature was analyzed by X-ray diffraction technique (PANalytical's X'Pert Pro with  $\text{CuK}\alpha$  radiation). Field Emission Scanning Electron Microscopy and Energy Dispersive X-ray Spectroscopy (FEI Quanta FEG200) were employed to analyze the surface morphology and elemental composition of synthesized samples. Shimadzu, UV-2600 spectrophotometer is used to measure the optical transmittance of the samples at wavelengths ranging from 300 – 1100 nm.

## 3. Results and discussion

### 3.1. XRD analysis

X-ray diffraction (XRD) pattern of synthesized ZnO nanoparticles are shown in Fig. 1 which confirm the formation of ZnO wurtzite (hexagonal) structure when compared with the corresponding peaks of JCPDS card no. 70-2205. One can observe that the intensity of the XRD peaks of ZnO particles prepared samples is relatively high. Further, the intensity of XRD peak of (101) plane is relatively stronger in all the samples. The average crystallite size ( $D$ ) of the synthesized ZnO nanoparticles was calculated from Debye–Scherrer formula from (101) plane:

$$D = \frac{K\lambda}{\beta \cos \theta}$$

The interplanar distance ( $d$ ) was calculated from Bragg's equation:

$$2d \sin \theta = n,$$

where  $\theta$  is the angle of diffraction in degree,  $n = 1$  and  $\lambda$  is wavelength of X-rays used (1.5406 Å). Lattice cell parameters  $a(= b)$ ,  $A = \pi r^2$  and  $c$  were calculated from the relation:

$$\frac{1}{d^2} = \left\{ \frac{4}{3} \left( \frac{h^2 + hk + a^2}{a^2} \right) + \frac{l^2}{c^2} \right\},$$

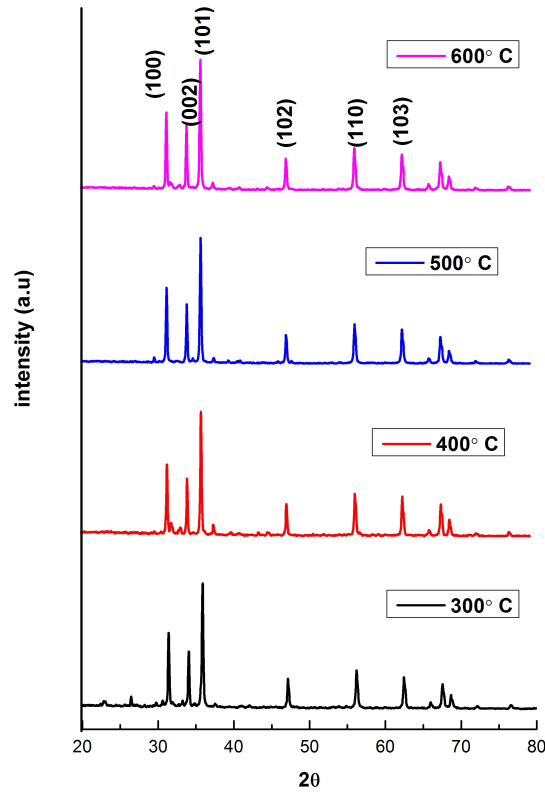


FIG. 1. XRD pattern of different annealed temperature ZnO

where  $d$  is the interplanar distance and  $h$ ,  $k$  and  $l$  are Miller indices of the plane. The average crystallite size of (101) plane was decreased from 46.01 to 33.85, 31.98 and 31.10 nm with increase in annealed temperature from 300, 400, 500 and 600 °C respectively. The calculated values are shown in Table 1.

TABLE 1. Variation of crystallite size and cell parameter of ZnO with different annealing temperatures

Temp °C	(101) Plane			Cell parameters (Å)	
	$2\theta$ degree	Average crystallite size $D$ (nm)	Inter planner distance $d$ (nm)	$a = b$	$c$
300	36.26	46.0	2.476	3.2521	5.2080
400	36.26	33.8	2.476	3.2513	5.2065
500	36.35	31.1	2.470	3.2403	5.1963
600	36.36	31.9	2.471	3.2423	5.1963

### 3.2. SEM analysis

Details on the growth factors controlling the shape and size of ZnO nanostructures are presented in Fig. 2, which shows the various morphology and shape selective synthesis of ZnO such as spindle like structure, hexagonal disks, spheroidal structures, and elongated porous hexagonal nanorods structure. Fig. 2 presents the hexagonal structure which shows the growth of ZnO nanorods obtained at 300 °C. Further increasing the temperature is suppressed the growth and the formed hexagonal shaped nanodisks. Nanorods with porous structure are formed in 500 °C.

Energy dispersive X-ray analyses (EDAX) spectrum of the prepared nanoparticle at 300, 400, 500 and 600 °C are shown in Fig. 3(a–d) respectively, which reveal the presence of Zn and O.

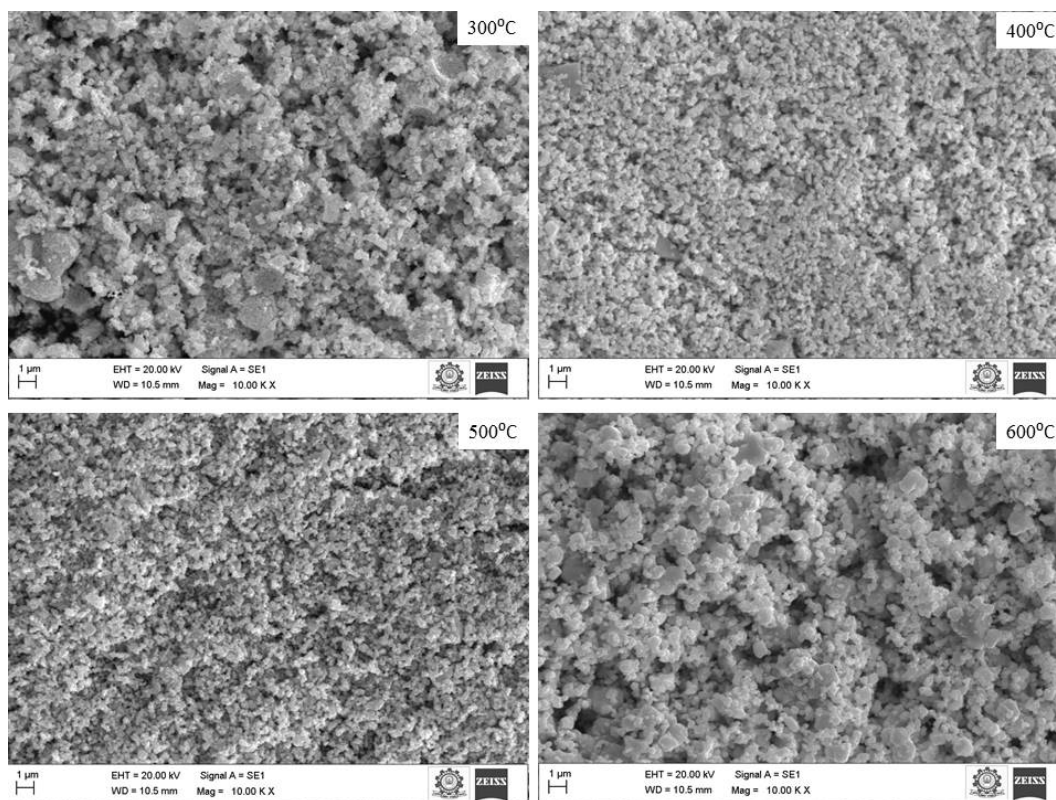


FIG. 2. SEM Images of ZnO particles

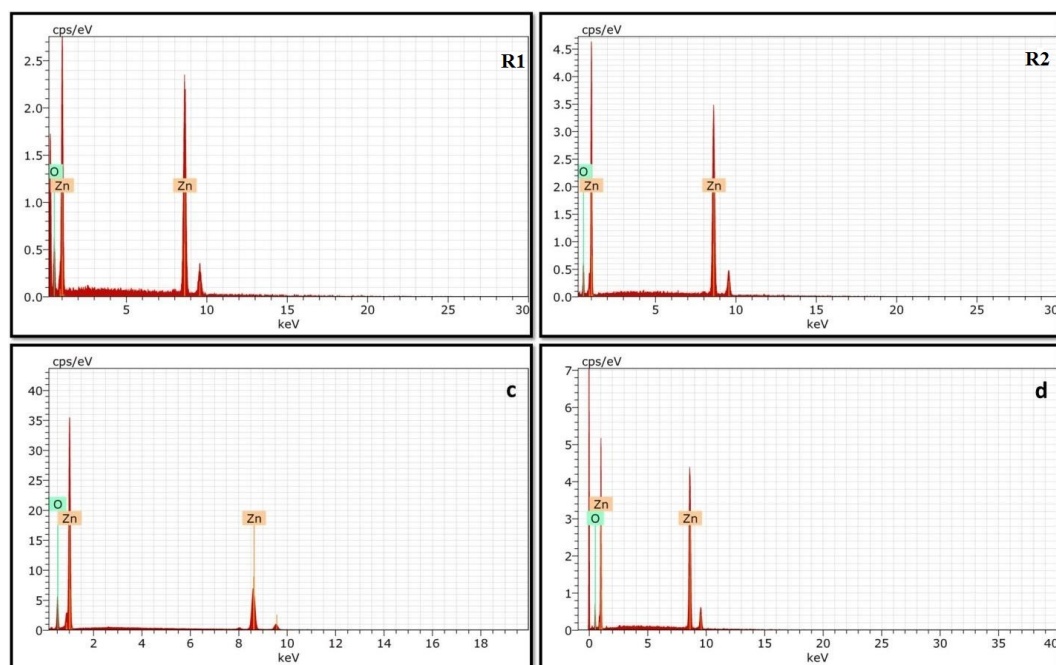


FIG. 3. EDAX analysis

### 3.3. Application of catalytic activity

The photocatalytic degradation of methylene blue by the prepared photocatalyst of ZnO/UV was studied under sun light. In this experiment, ZnO weight (10 mg) were dispersed well in (100 ml) aqueous methylene blue solution under stirring for (15 min) under dark conditions in order to make certain adsorption equilibrium on the surface of the catalysts.

After every 20 min of irradiation, part of the solution was collected and sealed in separate containers. They were centrifuged to separate the catalysts from the MB solution and then their UV-Vis spectra were recorded. Then absorption spectra were recorded and the rate of decolorization was observed in terms of change in intensity at  $\lambda_{\max}$  of the dyes. The efficiency of photocatalytic reaction was calculated from the following expression:

$$D \% = \frac{A_0 - A}{A_0} \times 100,$$

where  $A_0$  the initial dye absorbance ( $\text{gm}\cdot\text{L}^{-1}$ ) and  $A$  is the dye absorbance after the treatment. It can be noted that  $A_0 - A$  is referred to the loosing in the absorbance of solution by degradation process.

### 3.4. The photocatalytic degradation of the Methyl Blue (MB)

**3.4.1. Effect of catalyst loading under sunlight.** A series of experiments was carried out to assess the optimum catalyst loading by the amount of catalyst 0.5 g of which the dye solution was prepared. The percent ages of photodegradation under sunlight at 48 °C with ZnO were illustrated in Fig. 4. It was found that all samples give almost the same percentage removal at a certain concentration, so we will discuss here only prepared nanoparticle at 500 °C. It was observed that with an increased catalyst amount, the photodegradation increases. This could be attributed to the fact that the number of active sites increased as the amount of the catalyst increased, up to a certain point, after which, the higher concentrations of the catalyst increase the turbidity of the MB suspension and the penetration of sunlight.

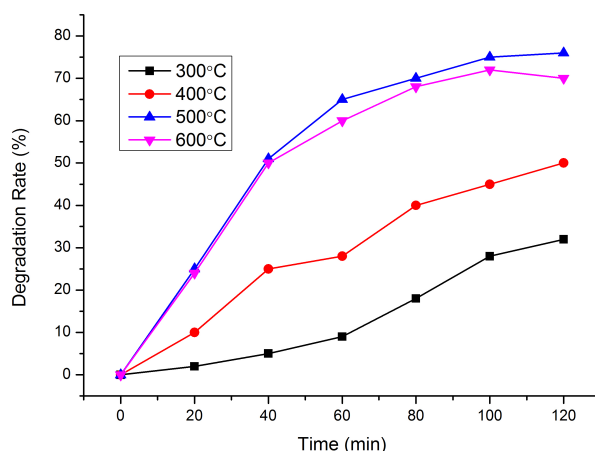


FIG. 4. Degradation efficiency graph

**3.4.2. Photodegradation properties.** To study the photodegradation abilities of the undoped ZnO particles prepared at various temperatures i.e. 300, 400, 500 and 600 °C; methyl blue (MB) dye was used as the model pollutant. The photocatalytic activity was performed by dispersing the films in 10 mL aqueous solution containing 0.1 M MB dye. After achieving adsorption-desorption equilibrium by stirring the dye solution with the catalysts in dark, they were exposed to visible light. With an increase in irradiation time, the color of the dye solutions degraded drastically. The order of the degradation ability after 120 min was as follows:

$$300\text{ }^{\circ}\text{C} \rightarrow 400\text{ }^{\circ}\text{C} \rightarrow 600\text{ }^{\circ}\text{C} \rightarrow 500\text{ }^{\circ}\text{C}.$$

A complete clear solution was observed for the co-doped sample confirming its enhanced degradation ability. The absorbance spectra taken at  $\lambda = 650\text{ nm}$  are displayed in Fig. 5(a) for the 300 °C ZnO, Fig. 5(b) for the 400 °C, Fig. 5(c) for the 500 °C and Fig. 5(d) for the 600 °C ZnO photocatalysts.

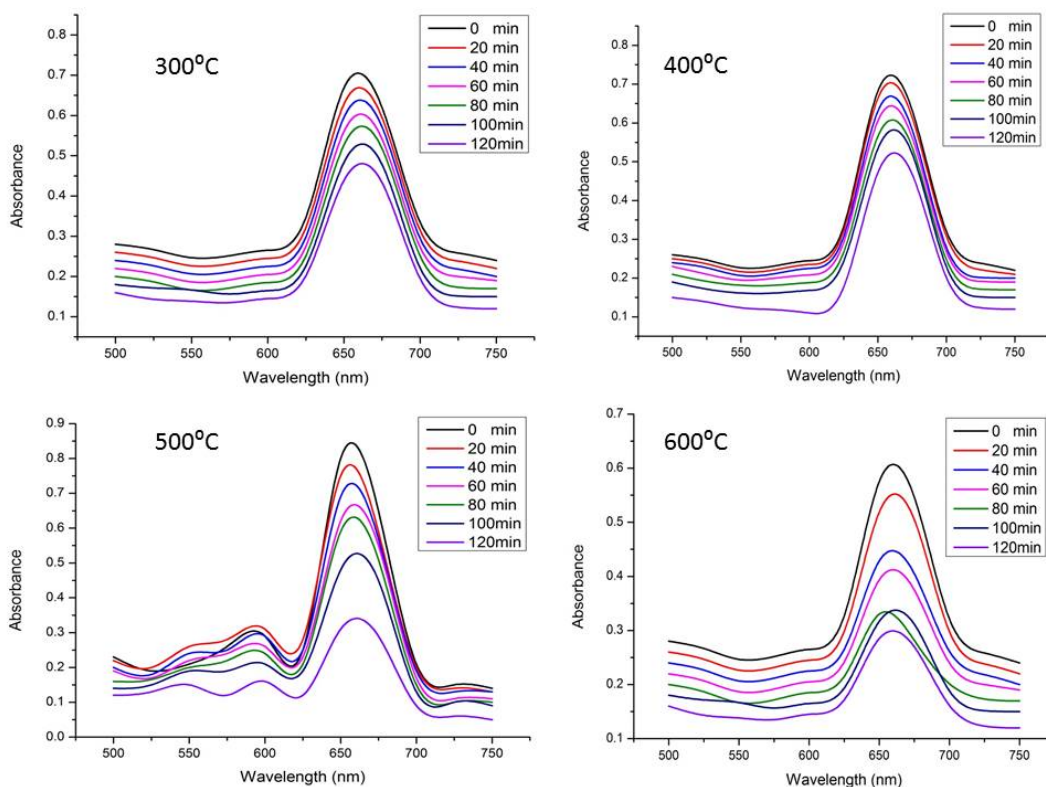


FIG. 5. Photocatalytic activity

Using the formula,  $\eta = (1 - C/C_0) \times 100$ , (where  $C$  and  $C_0$  represents the dye concentration under light and dark conditions), the degradation efficiency values of the tested catalysts were calculated and depicted in Fig. 6. Unanimously, for all the irradiation time intervals, the 500 °C ZnO photocatalyst showed better degradation efficiency.

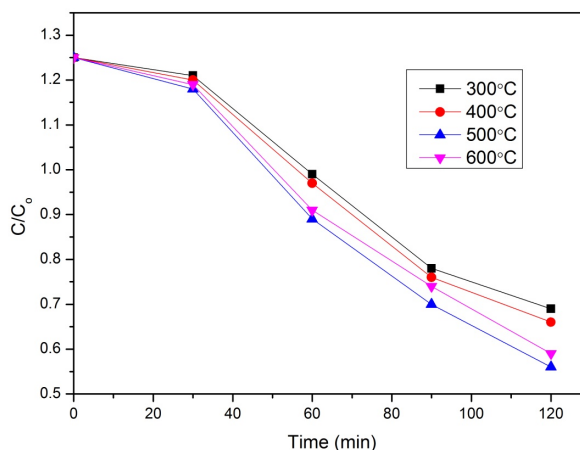


FIG. 6.  $C/C_0$  vs time

In general, the photocatalytic efficiency of the catalyst could be decreased because of the following possible reason. (a) The continuous adsorption of dyes on the catalyst surface can reduce the active sites of the catalyst and thereby decreases the photocatalytic activity. In addition, the surface adsorbed dye can decrease the incident light penetration to the catalyst surface and it affects the electron-hole pair generation.

To verify the reusable nature of the ZnO photocatalyst and durability of its catalytic activity in photodegradation process, 5 successive recycle tests were conducted by removing the catalyst from the dye solution. No significant loss was observed up to the first 4 cycles and a modest loss is observed in the 5th cycle (Fig. 7).

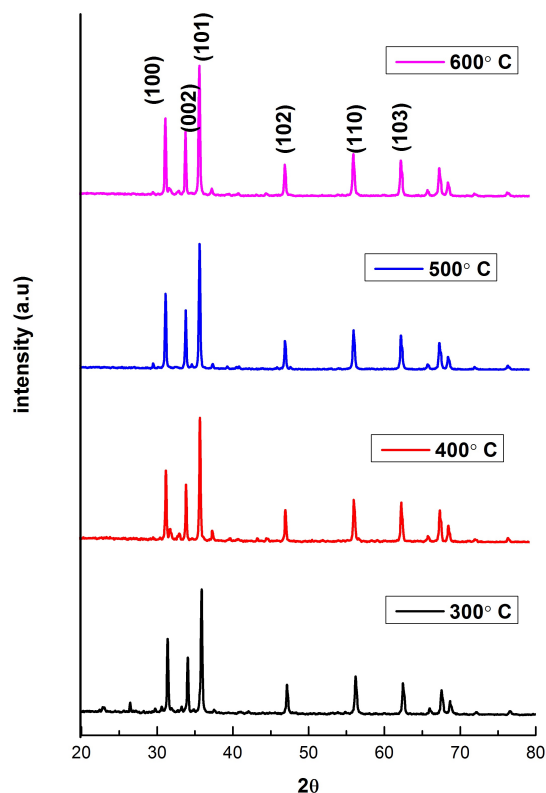


FIG. 7. Recycle test of the reused ZnO photocatalyst

#### 4. Conclusion

In this work spindle like, hexagonal disk, porous nanorods structures are successfully obtained through a simple hydrothermal method by varying the annealing temperature of the ZnO particles. The SEM images show that the porous like nano structures in all the samples the increased porosity was observed in sample prepared at 500 °C. ZnO nanoparticles possessing needle shaped structure showed 94 % photocatalytic activity at about 120 min against MB dye. The 500 °C hydrothermal synthesized ZnO nanoparticles showed relatively high degradation of MB.

#### References

- [1] Hartley T.W. Public perception and participation in water reuse. *Desalination*, 2006, **187**, P. 115–26.
- [2] Plumlee M.H, Larabee J., Reinhard M. Peruorochemicals in water reuse. *Chemosphere*, 2008, **72**, P. 1541–1547.
- [3] Peiyan Ma, Yan Wu, Zhengyi Fu, Weimin Wang. Shape-controlled synthesis and photocatalytic properties of three-dimensional and porous zinc oxide. *J. Alloys Compd.*, 2011, **509**, P. 3576–3581.
- [4] Qazi Inamur Rahman, Musheer Ahmad, Sunil Kumar Misra, Minaxi Lohani. Effective photocatalytic degradation of rhodamine B dye by ZnO nanoparticles. *Mater. Lett.*, 2013, **91**, P. 170–174.
- [5] Perera S.D., Mariano R.G., et al. Hydrothermal Synthesis of Graphene-TiO<sub>2</sub> Nanotube Composites with Enhanced Photocatalytic Activity. *ACS Catal.*, 2012, **2**, P. 949–956.
- [6] Rajesh Kumar, O. Al-Dossary, Girish Kumar, Ahmad Umar. Zinc Oxide Nanostructures for NO<sub>2</sub> GasSensor Applications: A Review. *Nano-Micro Lett.*, 2015, **7**, P. 97–120.
- [7] Hoffman R.L. ZnO-based transparent thin-film transistors. *Appl. Phys. Lett.*, 2003, **82**, P. 733–735.
- [8] Jia Huang, Zhigang Yin, Qingdong Zheng. Applications of ZnO in organic and hybrid solar cells. *Energy Environ. Sci.*, 2011, **4**, P. 3861–3877.
- [9] Steinfeld A. Solar hydrogen production via a two-step water-splitting thermochemical cycle based on Zn/ZnO redox reactions. *Int. J. Hydrogen Energy*, 2002, **27**, P. 611–619.

- [10] Eue Soon Jang, Jung-Hee Won, Seong-Ju Hwang, Jin-Ho Choy. Fine Tuning of the Face Orientation of ZnO Crystals to Optimize their Photocatalytic Activity. *Adv. Mater.*, 2006, **18**, P. 3309–3312.
- [11] Zhong Lin Wang. ZnO nanowire and nanobelt platform for nano technology. *Mater. Sci. Eng. R*, 2009, **64**, P. 33–71.
- [12] Hongqiang Wang, Guanghai Li, et al. Controllable Preferential-Etching Synthesis and Photocatalytic Activity of Porous ZnO Nanotubes. *J. Phys. Chem. C*, 2008, **112**, P. 11738–11743.
- [13] Qingzhi Wu, Xia Chen, et al. Amino Acid-Assisted Synthesis of ZnO Hierarchical Architectures and Their Novel Photocatalytic Activities. *Cryst. Growth Des.*, 2008, **8**, P. 3010–3018.
- [14] Xingfu Zhou, Dangyu Zhang, et al. Mechanistic Investigations of PEG-Directed Assembly of One-Dimensional ZnO Nanostructures. *J. Phys. Chem. B*, 2006, **110**, P. 25734–25739.
- [15] Santhosh C., Velmurugan V., et al. Role of nanomaterials in water treatment applications. *Chem. Eng. J.*, 2016, **306**, P. 1116–1137.
- [16] Kong Y.C., Yu D.P., et al. Ultraviolet-emitting ZnO nanowires synthesized by a physical vapor deposition approach. *Appl. Phys. Lett.*, 2001, **78**, P. 406–409.
- [17] Zhang B.P., Binh N.T., et al. Formation of highly aligned ZnO tubes on sapphire (0001) substrates. *Appl. Phys. Lett.*, 2004, **84**, P. 4098–4100.
- [18] Zheng Wei Pan, Zu Rong Dai, Zhong Lin Wan. Nanobelts of Semiconducting Oxides. *Science*, 2001, **291**, P. 1947–1949.
- [19] Xu C.X., Sun X.W., Dong Z.L., Yu M.B. Zinc oxide nanodisk. *Appl. Phys. Lett.*, 2004, **85**, P. 3878–3880.
- [20] Seung-Ho Jung, Eugene Oh, et al. Sonochemical Preparation of Shape-Selective ZnO Nanostructures. *Cryst. Growth Des.*, 2008, **8**, P. 265–269.
- [21] Yadav R.S., Priya Mishra, Pandey A.C. Growth mechanism and optical property of ZnO nanoparticles synthesized by sonochemical method. *Ultrasonics Sonochemistry*, 2008, **15**, P. 863–868.
- [22] Khizar Hayat, Gondal M.A., et al. Nano ZnO synthesis by modified sol gel method and its application in heterogeneous photocatalytic removal of phenol from water. *Appl. Catal. A: General*, 2011, **393**, P. 122–129.
- [23] Seema Rani, Poonam Suri, Shishodia P.K., Mehra R.M. Synthesis of nanocrystalline ZnO powder via solgel route for dye-sensitized solar cells. *Sol. Energy Mater. Sol. Cells*, 2008, **92**, P. 1639–1645.
- [24] Jaykrushna Das, Deepa Khushalani. Nonhydrolytic Route for Synthesis of ZnO and Its Use as a Recyclable Photocatalyst. *J. Phys. Chem. C*, 2010, **114**, P. 2544–2550.
- [25] Matt Law, Greene L.E., et al. Nanowire dye-sensitized solar cells. *Nat. Mater.*, 2005, **4**, P. 445–459.
- [26] Wang B.G., Shi E.W., Zhong W.Z. Twinning Morphologies and Mechanisms of ZnO Crystallites under Hydrothermal Conditions. *Cryst. Res. Technol.*, 1998, **33**, P. 937–941.

## Nanostructured SiGe:Sb solid solutions with improved thermoelectric figure of merit

M. V. Dorokhin, P. B. Demina, Yu. M. Kuznetsov, I. V. Erofeeva, A. V. Zdrovevshchev,  
M. S. Boldin, E. A. Lantsev, A. A. Popov, E. A. Uskova, V. N. Trushin

Lobachevsky State University of Nizhny Novgorod, Gagarin ave. 23, Nizhniy Novgorod, 603950, Russia  
dorokhin@nifti.unn.ru

PACS 72.15.Jf

DOI 10.17586/2220-8054-2020-11-6-680-684

Thermoelectric  $\text{Si}_{0.65}\text{Ge}_{0.35}\text{Sb}_\delta$  materials have been fabricated by spark plasma sintering of Ge–Si–Sb powder mixtures. The electronic properties of  $\text{Si}_{0.65}\text{Ge}_{0.35}\text{Sb}_\delta$  were found to be dependent on the uniformity of mixing of the components, which in turn is determined by the maximum heating temperature during solid-state sintering. Provided the concentration of donor Sb impurity is optimized the thermoelectric figure of merit for the investigated structures can be as high as 0.63 at 490 °C, the latter value is comparable with world-known analogues obtained for  $\text{Si}_{1-x}\text{Ge}_x\text{P}_\delta$ .

**Keywords:** thermoelectric energy converters, spark plasma sintering, doping, germanium-silicon, thermoelectric figure of merit.

Received: 9 September 2020

### 1. Introduction

The  $\text{Si}_{1-x}\text{Ge}_x$  substitutional solid solution is one of the most attractive silicon-based materials for the fabrication of thermoelectric energy converters [1–3]. The latter is due to a high chemical and mechanical stability at elevated temperatures which is some important advantage when concerning the applications in an air atmosphere. Some other advantages of  $\text{Si}_{1-x}\text{Ge}_x$  are low toxicity and a high degree of silicon-based technological processes development [4].

The main characterizing parameter of thermoelectric materials is the dimensionless thermoelectric figure of merit ( $ZT$ ):

$$ZT = \frac{\alpha^2 \sigma}{\chi} T, \quad (1)$$

where  $\chi$  is the thermal conductivity,  $\sigma$  is electrical conductivity (sometimes resistivity  $\rho = 1/\sigma$  can be used instead) and  $\alpha$  is the Seebeck coefficient, which can be determined by measuring the thermo-voltage ( $U_{TE}$ ) and a temperature difference ( $\Delta T$ ) between the “hot” and “cold” edges of the material:  $\alpha = -U_{TE}/\Delta T$ . As a rule, the parameters in (1) are not independent of each other within one material: with increasing  $\sigma$ , the absolute value of Seebeck coefficient decreases and  $\chi$  increases [5]. Modern technologies such as nanostructuring provide quasi-independent control of thermoelectric coefficients, which allows one to obtain simultaneously low values of  $\chi$  with high values of  $\alpha$  and  $\sigma$ , and, thus, to increase  $ZT$  [2, 3, 5].

In the present paper, we report on the results of the study of  $\text{Si}_{0.65}\text{Ge}_{0.35}$  thermoelectric structures fabricated by the spark plasma sintering (SPS) of mixture of Si, Ge and Sb powders. The SPS technique provides unique possibilities for the formation of nanostructured materials and controlling the thermoelectric coefficient as well as the parameters of nanostructuring [6, 7]. The main feature of this work is the use of Sb impurities for fabricating the  $\text{Si}_{1-x}\text{Ge}_x$ , with n-type conductivity, whereas in the majority of prior papers, As or P impurities are used. The advantages of antimony in comparison with P or As [1–6] are lower toxicity [7, 8], in addition using Sb provides a new technological option for fabricating the n-type material. Although antimony has limited solubility in Ge and Si [9], the use of non-equilibrium fabrication techniques such as SPS allows introduction of the impurity over the solubility limit and achieving the doping concentrations sufficient for obtaining high values of  $ZT$ . In this paper, the variation of Sb concentration as well as of the sintering modes has been carried out in order to obtain the increased  $ZT$  values.

The top value obtained was as high as  $ZT = 0.63$  at 490 °C which is comparable with values characteristic for a “classical” phosphorous or boron doped Ge–Si material [2, 6, 10].

### 2. Experimental

A series of 5 samples of nanostructured  $\text{Si}_{0.65}\text{Ge}_{0.35}\text{Sb}_\delta$  ( $\delta = 0.005 - 0.009$ ) was made for this study. The initial powder to be sintered was fabricated by milling the high-purity Ge, Si and Sb bulk pieces with Fritsch Pulverisette 6 ball mill filled with argon to prevent oxidation. The milling modes (6 hours, 250 RPM) provided the average particle size of  $\approx 500$  nm. The composition of the material was set by weighing the Ge, Si and Sb pieces and then converting the weight percent to atomic percent.

The sintering was carried out using the DR. Sinter Model SPS-625 spark plasma sintering system. The variable parameters were the Sb concentration (0.5 – 0.9 at.%) and a maximal sintering temperature ( $T_s = 1080 - 1180$  °C). The following reasons were taken into account when selecting the sintering modes:

- 1) The lower temperature limit was selected to provide efficient mixing of Ge and Si, whereas upper limit was close to the melting point of the Ge–Si mixture. Since the sintering system used was not designed for liquid-phase sintering, melting of the material would lead to a collapse of the process (because of leaking of the melted material through gaps between the mold, graphite paper, and punches).
- 2) The lower antimony concentration limit of 0.5 at.% was selected to provide sufficiently low conductivity to obtain high enough power factor ( $\alpha^2\sigma$ ). The upper limit of 0.9 at.% of antimony allowed us to prevent the formation of large Sb clusters during sintering [7]. As it has been shown in our earlier work [7] the introduction of 1 at.% of Sb or higher into  $\text{Ge}_x\text{Si}_{1-x}$  leads to formation of Sb clusters which is accompanied by the decrease of both conductivity and Seebeck coefficient. This significantly reduces the value of  $ZT$ .

The other sintering parameters (pressure of 70 MPa, heating rate of 50 °C/min) were kept constant. The sintering temperature was determined by a pyrometer on the outer wall of the mold with sintered powder, with further conversion to the temperature inside the mold [11]. The technological parameters are presented at Table 1.

TABLE 1. Technological parameters of fabricated Si–Ge samples

Sample	Technological Sb content ( $\delta$ ), at.%	Sintering temperature ( $T_s$ ), °C
1	0.5	1080±10
2	0.5	1180±10
3	0.7	1150±10
4	0.7	1180±10
5	0.9	1180±10

The sintered ingots of  $\text{Si}_{0.65}\text{Ge}_{0.35}\text{Sb}_\delta$  were cut into plates on which phase composition studies using X-ray diffraction (XRD) analysis, as well as measurements of thermoelectric coefficients were performed. The Seebeck coefficient was calculated from simultaneous temperature and thermoelectric voltage measurements using chromel-alumel thermocouples [12]. The resistivity was measured by the standard four-probe method. The thermal conductivity was measured by the stationary heat flux method [13]. The measurements were carried out at temperatures ranging from  $T_m = 50 - 490$  °C. The technology for structures fabrication, as well as all measurement techniques, are described in detail in [7, 12].

### 3. Results and discussion

Figure 1 shows X-ray diffraction spectra of the initial powder (1) and samples (1, 3, 5) fabricated at various temperatures. The lines corresponding to unmixed Ge and Si are present in the diffraction pattern of the initial powder (1). Lines associated with Sb were not resolved due to low concentration.

Sintering of a powder at  $T_s = 1080 - 1180$  °C leads to the interaction between the components and to the appearance  $\text{Si}_{1-x}\text{Ge}_x$  solid solution associated lines at the spectra (Fig. 1, curves 1, 3, 5). This is accompanied by vanishing the Ge-related lines from the spectra, whereas Si-related lines are preserved and their intensity monotonically decreases with the increase of  $T_s$ . The latter is attributed to increase of Si and Ge intermixing with the increase of sintering temperature.

Figure 2 shows the temperature dependence of resistivity. All samples displayed n-type conductivity. For the sample 1, fabricated at the lowest temperature of  $T_s = 1080$  °C, the dependence is a semiconductor type, and the resistivity value is the highest among the investigated structures. The  $\rho(T_m)$  dependences for the Samples 2–5 (which were fabricated at the elevated temperatures) are similar: all the curves are peak functions with the maximum at 200 – 300 °C and the resistivity values varying slightly in the range of  $T_m = 30 - 490$  °C. In the case of the same impurity concentration, a lower value of  $\rho$  is characteristic for samples sintered at higher temperatures. An increase in impurity concentration in the range of 0.5 – 0.9 at.% leads to decrease of  $\rho$ , which is typical for impurity doping of semiconductors.

The thermal conductivity values measured by stationary heat flux method [14] are presented in Table 2. The values are approximately the same for all nanostructures and lie within the range of 2.5 – 3.75 W/m·K. The latter fact

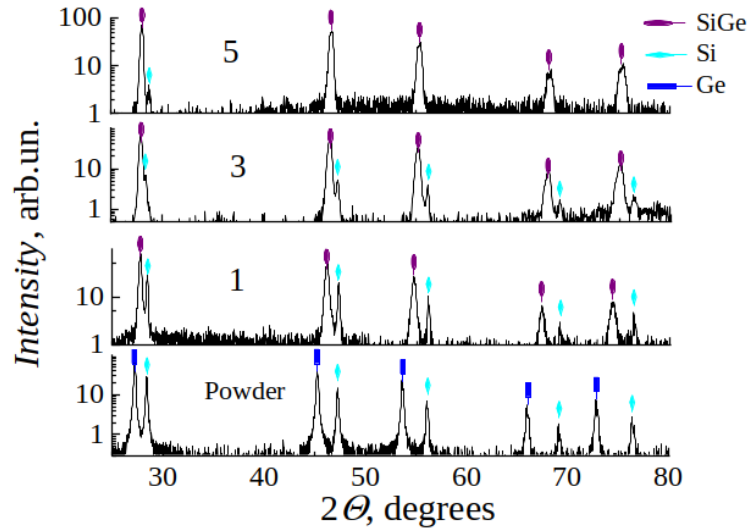


FIG. 1. X-ray diffraction pattern for samples 1, 3, and 5, as well as for the initial powder (Powder). The icons indicate the positions of the peaks for Si, Ge, and a GeSi solid solution

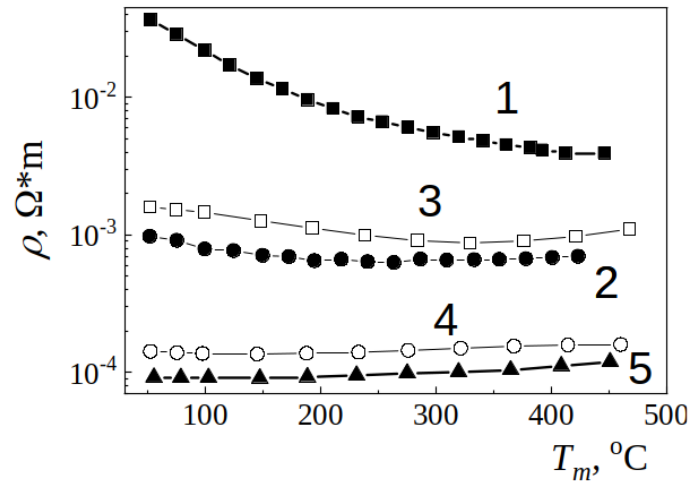


FIG. 2. Temperature dependence of resistivity measured for the samples shown in Table 1. The curve number corresponds to the sample number

can evidence on the similarity of the presented samples both in composition and in grain size. The values of  $\chi$  in Table 2 are close to the ones obtained for n-Si<sub>0.60</sub>Ge<sub>0.40</sub>, highly doped with As or P [14].

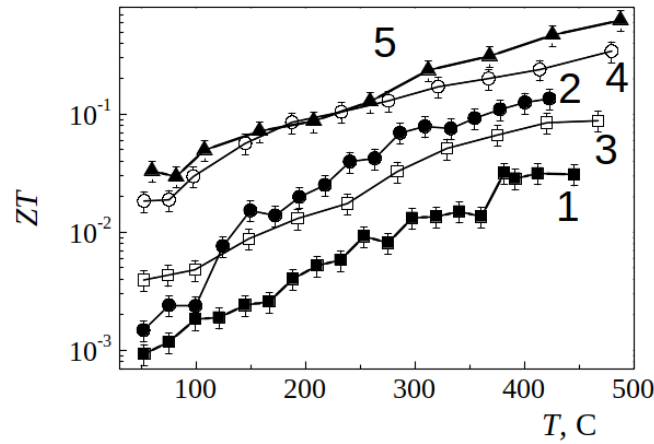
The Seebeck coefficient varies nonmonotonically with varying structural parameters (Table 2), which is believed to be due the  $\alpha$  being related with the resistivity. The latter depends not only on the concentration, but also on the homogeneity of the phase composition of the sample.

Figure 3 shows the temperature dependences of  $ZT$ , calculated by (1). With the increase of measurement temperature  $ZT$  value monotonically increases and the highest values are characteristic of nanostructures with a Sb content of 0.7 to 0.9 at.%. A decrease in impurity concentration, as well as a decrease in sintering temperature, leads to a significant decrease in  $ZT$ .

The obtained results can be explained in terms of the phase composition of the samples and the degree of the impurity incorporation into the substitution position of Ge or Si. An insufficient fabrication temperature leads to ineffective mixing of Ge and Si, which is accompanied by the conservation of the silicon phase (this can be seen from the XRD patterns in Fig. 1). The resulting heterogeneity of the Si<sub>1-x</sub>Ge<sub>x</sub> composition leads to modulation of the band gap, thereby causing a slight increase in resistance (compare samples 2 and 3 in Table 2 with the same Sb concentration, but different sintering temperatures). In turn the resistance increase causes a decrease in  $ZT$ .

TABLE 2. Thermoelectric parameters of  $\text{Si}_{0.65}\text{Ge}_{0.35}\text{Sb}_\delta$  samples. The parameter were measured at  $T_m = 450^\circ\text{C}$ 

Sample	$\rho \times 10^4$ , $\Omega\cdot\text{m}$	$\alpha$ , $\mu\text{V}/\text{K}$	$\chi$ , $\text{W}/\text{m}\cdot\text{K}$	$ZT$
1	$40 \pm 2$	$410 \pm 40$	$2.5 \pm 0.3$	$0.03 \pm 0.006$
2	$7 \pm 0.5$	$690 \pm 40$	$3.5 \pm 0.3$	$0.14 \pm 0.03$
3	$11 \pm 1$	$644 \pm 40$	$3.2 \pm 0.3$	$0.09 \pm 0.02$
4	$2.0 \pm 0.2$	$490 \pm 40$	$3.75 \pm 0.3$	$0.30 \pm 0.06$
5	$1.2 \pm 0.1$	$490 \pm 40$	$2.73 \pm 0.3$	$0.54 \pm 0.1$

FIG. 3. Temperature dependences of the thermoelectric figure of merit ( $ZT$ ) measured for the samples shown in Table 1. The curve number corresponds to the number of the sample

In addition, the incorporation of substitutional impurities into the solid solution substantially depends on the sintering temperature. We believe that the high resistance values of the low-temperature sample 1 are due to the both of the above factors. When sintering the sample with the highest Sb concentration of 0.9 at.% and at a higher temperature, the material with the highest value of  $ZT$  is obtained (sample 5, Table 2).

Finally, we should note that the conditions for efficient phase mixing and conditions for efficient Sb incorporation may differ. Indeed, one would need fundamentally nonequilibrium sintering conditions to incorporate the Sb impurity over the solubility level, whereas Ge and Si mixing may occur in the thermal equilibrium. In particular introduction of Sb with the concentration of over 1 at.% in [7] had led to a formation of antimony clusters in the  $\text{Si}_{0.65}\text{Ge}_{0.35}$  matrix accompanied with the sharp increase of the resistivity. The poor Ge and Si intermixing also leads to a resistivity increase, as has been shown in the present paper.

The experimental conditions described in section 1 allowed us to achieve both sufficient Ge and Si mixing and Sb impurity incorporation sufficient to obtain the high values of  $ZT$ . However, we believe that this combination can still be optimized by further manipulation of the sintering parameters.

#### 4. Conclusion

Thus, the study of the thermoelectric properties of  $\text{Si}_{0.65}\text{Ge}_{0.35}$  with Sb impurity has shown that the values of resistivity and thermal conductivity for given impurity concentration are determined mainly by the phase composition of  $\text{Si}_{0.65}\text{Ge}_{0.35}$  and the degree of impurity incorporation. The best thermoelectric characteristics were obtained for the structures fabricated at temperatures above  $1100^\circ\text{C}$ . The latter value is close to the melting temperature of  $\text{Si}_{0.65}\text{Ge}_{0.35}$  solid solution. The top value of  $ZT = 0.628$  was obtained at the maximal measurement temperature of  $490^\circ\text{C}$  for  $\text{Si}_{0.65}\text{Ge}_{0.35}$  with 0.9 at.% of Sb impurity. This value is comparable with the best known phosphorous doped  $\text{Si}_{0.8}\text{Ge}_{0.2}$  analogs [2, 6, 10]. As is known, Si-Ge alloys have a unique advantage in using waste heat at a high temperature of

~ 800 – 900 °C. On the other hand, the largest share of waste heat sources is in the range of 300 – 500 °C. Therefore, the operating temperature of approximately 500 °C is also of great interest for practical application.

In conclusion, it was demonstrated for the first time that antimony doping, similarly to phosphorus doping, can be used to obtain the n-type  $\text{Si}_{1-x}\text{Ge}_x$  thermoelectric solid solutions.

### Acknowledgements

The work was supported by Russian Science Foundation, project no. 17-79-20173, RFBR 20-38-70063, 20-32-90032.

### References

- [1] Yu B., Zebarjadi M., Wang H., et.al. Enhancement of thermoelectric properties by modulation-doping in silicon germanium alloy nanocomposites. *Nano Lett.*, 2012, **12**, P. 2077–2082.
- [2] Bathula S., Gahtori B., Jayasimhadri M., et.al. Microstructure and mechanical properties of thermoelectric nanostructured n-type silicon-germanium alloys synthesized employing spark plasma sintering. *Appl. Phys. Lett.*, 2014, **10**, 061902.
- [3] Chen Z.-G., Han G., Yang L., et.al. Nanostructured thermoelectric materials: Current research and future challenge. *Prog. Nat. Sci.: Materials International*, 2012, **22**, P. 535–549.
- [4] Shikari Y., Usami N. Silicon-Germanium (SiGe) nanostructures. Production, properties and application in electronics. *Woodhead publishing limited*, 2011.
- [5] Gayner C., Kar K.K. Recent advances in thermoelectric materials. *Progress Mater. Sci.*, 2016, **83**, P. 330–382.
- [6] Ovsyannikov D.A., Popov M.Y., Buga S.G., et.al. Transport properties of nanocomposite thermoelectric materials based on Si and Ge. *Physics of the Solid State*, 2015, **57**, P. 605–612.
- [7] Dorokhin M.V., Demina P.B., Erofeeva I.V., et.al. In-situ doping of thermoelectric materials based on SiGe solid solutions during their synthesis by the spark plasma sintering technique. *Semiconductors*, 2019, **53**, P. 1158–1163.
- [8] Health N.J. Hazardous substance Fact Sheet. Antimony. URL: <https://web.doh.state.nj.us/rtkhsfs/factsheets.aspx>.
- [9] Olesinski R.W., Abbaschian G.J. The Sb–Si (Antimony-Silicon) system. *Bulletin of Alloy Phase Diagrams*, 1985, **6**, P. 445–448.
- [10] Murugasami R., Vivekanandhan P., Kumaran S., et.al. Simultaneous enhancement in thermoelectric performance and mechanical stability of p-type SiGe alloy doped with Boron prepared by mechanical alloying and spark plasma sintering. *J. Alloys and Comp.*, 2019, **773**, P. 752–761.
- [11] Chuvildeev V.N., Boldin M.S., Dyatlova Y.G., et.al. Comparative study of hot pressing and high-speed electropulse plasma sintering of  $\text{Al}_2\text{O}_3/\text{ZrO}_2/\text{Ti}(\text{C},\text{N})$  powders. *Russian Journal of Inorganic Chemistry*, 2018, **60**, P. 987–993.
- [12] Erofeeva I.V., Dorokhin M.V., Zdoroveyshchev A.V., et.al. Production of Si- and Ge-based thermoelectric materials by spark plasma sintering. *Semiconductors*, 2018, **52**, P. 1559–1563.
- [13] Devyatkova E.D., Petrov A.V., Smirnov I.A., Moizhes B.Y. Fused silica as a reference material in measurements of thermal conductivity. *Soviet Phys. Solid State*, 1960, **2**, P. 738–746.
- [14] Schaffler F., Levinshtein M.E., Rumyantsev S.L., Shur M.S. Properties of Advanced Semiconductor Materials GaN, AlN, InN, BN, SiC, SiGe. John Wiley & Sons, Inc., New York, 2001, 188 p.

## Dependence of the electronic and crystal structure of a functionalized graphene on the concentration of chemically adsorbed fluorine

M. E. Belenkov, V. M. Chernov

Chelyabinsk State University, Br. Kashirinykh, 129, Chelyabinsk, 454001, Russia  
me.belenkov@gmail.com

PACS 61.50.Ah, 81.05.ue

DOI 10.17586/2220-8054-2020-11-6-685-689

In this paper, we study the change in the fluorine-functionalized graphene layers depending on the fluorine concentration. Ab initio calculations were performed using the density functional theory method in the generalized gradient approximation. It was established that the metallic properties of the graphene layer become semiconducting after functionalization even at low concentrations of chemically adsorbed fluorine  $\sim 10$  at.%. The band gap increases from 0.11 to 3.09 eV with an increase of the amount of adsorbed fluorine.

**Keywords:** graphene, fluorographene, ab initio calculations, chemical adsorption, crystal structure, electronic properties.

*Received:* 10 October 2020

*Revised:* 27 October 2020

### 1. Introduction

Graphene can be functionalized by chemical adsorption of non-carbon atoms on its surface, as a result of which its properties change from metallic to semiconducting [1, 2]. Various non-carbon atoms and molecular groups are chemically well adsorbed on the graphene surface [3, 4]. Fluorographene is the most promising for practical applications in electronics [5, 6]. The thermal stability of graphene functionalized by fluorine is higher than that of graphene functionalized with hydrogen, oxygen or chlorine [7–9]. The electronic properties of graphene functionalized by fluorine can be influenced by the order of addition of adsorbed fluorine atoms [10–13], as well as a number of other factors. So, in works [14, 15] it was found that the electronic structure of graphene changes during the chemical adsorption of individual fluorine atoms. A detailed study of the dependence of the graphene electronic properties on the concentration of chemically adsorbed fluorine was not in the scope of those prior works. Therefore, in this paper, such studies were carried out.

#### 1.1. Methods

Ab initio modeling of fluorine-functionalized graphene compounds was performed using the generalized gradient approximation for density functional theory (DFT-GGA) [16]. The calculations were performed using the QUANTUM Espresso software package [17]. An extended hexagonal unit cell containing 18 carbon atoms was chosen as the main unit cell of the initial graphene layer. During chemical adsorption, fluorine atoms were randomly attached to carbon atoms in a unit cell, and then the optimized crystal structure, band structure, and density of electronic states were calculated. We have considered the compounds obtained by the addition of 0, 2, 4, 6, 8, 10, 12, 14, 16 and 18 fluorine atoms to the extended unit cell of the graphene layer, which corresponds to the fluorine concentration in the compounds 0, 10, 18.2, 25, 30.8, 35.7, 40, 43.8, 47.1, 50 at.%. We have considered only those structures in which half of the fluorine atoms were attached on one side of the layer, and the other half of the atoms on the other. The calculations were performed for fluorine functionalized graphene layers, which were packed in stacks. The distance between the layers in the stacks was large (12 Å); therefore, adjacent layers did not affect the structure of each other. The calculations used a set of  $k$ -points  $12 \times 12 \times 12$ . The wave functions were decomposed using a truncated basis set of plane waves. The cutoff energy for the plane wave basis was 70 Rydberg.

#### 1.2. Results

As a result of DFT-GGA calculations, the structure of fluorine-functionalized graphene layers was found, which corresponds to the minimum total energy. Images for four calculated layers corresponding to fluorine concentrations in the structure of 10, 25, 35.7, and 43.8 at.% are shown in Fig. 1. At a low fluorine concentration, the structure of the graphene layer remains flat, and deformation of the structure is observed only around the attached fluorine atom. With increasing concentration, the layer gradually becomes corrugated, as a result the carbon atoms are displaced relative to the initial plane of the layer in the direction of the attached fluorine atoms.

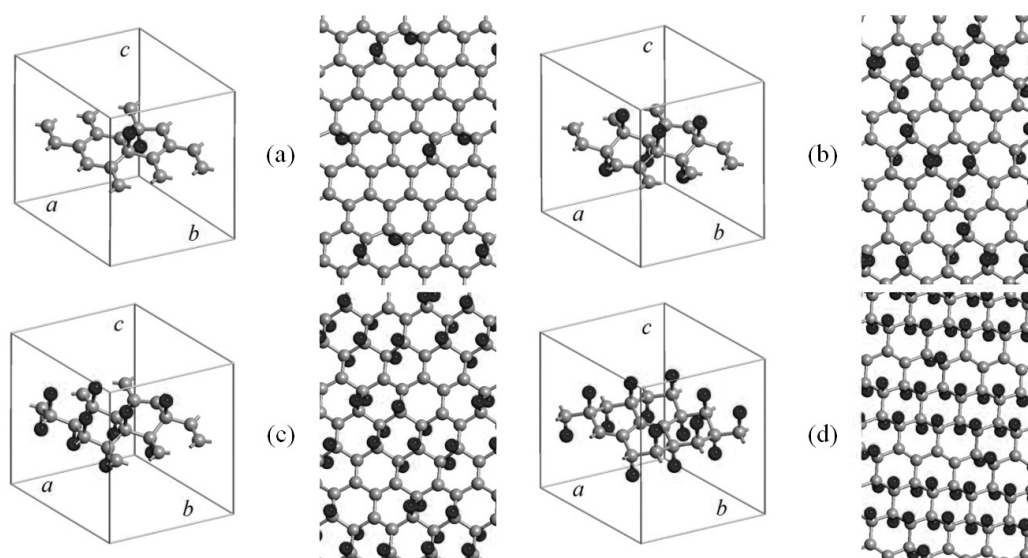


FIG. 1. The unit cells and the structure of graphene layers with different amount of chemically adsorbed fluorine atoms per unit cell: (a) 2 fluorine atoms; (b) 6 fluorine atoms; (c) 10 fluorine atoms; (d) 14 fluorine atoms. The unit cells contain 18 carbon atoms

The calculated values of the lattice translation vector lengths of graphene layers are given in Table 1. The minimum value of the translation vector length (7.4608 Å) is observed for the initial graphene layer. The maximum vector length (7.8050 Å) corresponds to a completely fluorinated graphene layer in which a fluorine atom is attached to each carbon atom. An increase in the crystal lattice parameter with an increase in fluorine concentration occurs despite the fact that initially flat layers are corrugated and if the interatomic carbon-carbon bonds remained constant, then an inverse relationship should have been observed. The observed increase in the parameter is associated with the fact that the order of carbon-carbon bonds changes and their average length increases. The change in the unit cell parameter of the initial graphene in comparison with fully fluorinated graphene was observed earlier in the article [18]. According to the data of this article, the experimentally measured lattice parameter of the graphene layer is 0.246 nm, and for fluorographene it is 0.257 nm. In our calculations, we used an extended unit cell with a translation vector 3 times larger than that of a primitive unit cell. Therefore, if the parameters of the unit cells we found are divided by 3, that is, reduced to a primitive cell, then the translation vector for graphene will be 0.249 nm, and for fluorographene, 0.260 nm. The calculated data obtained by us are in good agreement with the experimentally measured values. The dependence of the change in the lattice parameter on the concentration of adsorbed fluorine found in our work can find practical application for determining the concentration of fluorine from the experimentally measured values of the lattice parameter.

With an increase in the fluorine concentration in the compounds, the C–F bond length also changes from 1.634 Å in the graphene layer with a fluorine concentration of 10 at.% to 1.439 Å in the fluorographene layer, where the fluorine concentration is 50 at.%. Apparently, the reason for this is weaker chemical bond between fluorine and carbon atoms in graphene layers with a low fluorine concentration as compared to C–F bonds in the fluorographene layer. Calculations performed for carbon tetrafluoride molecules with different interatomic bond lengths have shown that the weakening of the C–F bond energy corresponding to the observed change in the bond length for fluorinated graphene layers can reach 11 %.

The calculated values of the total energy  $E_{\text{total}}$  per unit cell are presented in Table 1. This energy decreases with an increase of the number of fluorine atoms attached to the graphene layer. In this case, the energy of interatomic chemical bonds  $E_{\text{bind}}$  also decreases. The bond energy was calculated as the difference between the total energy and the energy of the same number of isolated carbon and fluorine atoms as in the unit cell of the corresponding layer. The decrease in bond energy with an increase in the number of atoms first and foremost is due to an increase in the number of bonds. Calculation of the energy of carbon-carbon  $E_{\text{C-C}}$  bonds showed that the energy of this bond gradually increases with increasing fluorine concentration. Indeed, in the initial graphene layer, the binding energy between a pair of neighboring carbon atoms was  $-6.881$  eV, while in the fluorographene layer this energy is  $-4.926$  eV. The energies of carbon-carbon bonds ( $-6.88 \div -4.93$  eV) found as a result of calculations correlate well with the experimentally established values of the energies of single and double carbon-carbon bonds ( $-7.05$ ,

TABLE 1. Structural parameters, energy characteristics, and electronic properties of a graphene layer functionalized with fluorine with different numbers of chemically adsorbed fluorine atoms ( $N_F$  – the number of fluorine atoms adsorbed into an expanded unit cell of the graphene layer, which contains 18 carbon atoms;  $a$  – the lattice translation vector;  $R_{C-F}$  – the average bond length between a fluorine and carbon atom;  $E_{\text{total}}$  – the total bond energy per unit cell;  $E_{\text{bind}}$  – the energy of all bonds in a unit cell;  $E_{C-C}$  – the average energy of one carbon-carbon bond;  $E_F$  – the Fermi energy;  $\Delta$  – the band gap)

$N_F$ , at.	$a$ , Å	$R_{C-F}$ , Å	$E_{\text{total}}$ , eV	$E_{\text{bind}}$ , eV	$E_{C-C}$ , eV	$E_F$ , eV	$\Delta$ , eV
0	7.4608	—	-2831.65	-185.78	-6.881	-4.054	0
2	7.4609	1.634	-4117.22	-192.70	-6.623	-4.721	0.114
4	7.4672	1.506	-5403.59	-200.42	-6.396	-5.312	1.573
6	7.4978	1.485	-6689.77	-207.95	-6.161	-5.647	1.092
8	7.5381	1.473	-7976.20	-215.73	-5.936	-5.965	1.785
10	7.5708	1.471	-9262.02	-222.91	-5.688	-6.413	1.338
12	7.6235	1.453	-10549.3	-231.54	-5.494	-6.487	1.779
14	7.6948	1.458	-11836.8	-240.39	-5.308	-6.402	2.445
16	7.7698	1.442	-13123.9	-248.84	-5.108	-6.201	2.909
18	7.8050	1.439	-14411.5	-257.80	-4.926	-6.053	3.094

-3.84 eV) [19], which indicates the correctness of the calculations. During fluorination, the energy of C–C bonds changes by about one third of the energy of the initial graphene. This is due to the fact that in the initial graphene layer the carbon bond order is 1.33, and in the fluorographene layer the bond order becomes 1. Therefore, the bond energy changes proportionally. Such a change in the binding energy should lead to a decrease in the mechanical properties of fluorinated graphene in comparison with the properties of the initial graphene layer.

DFT-GGA calculations of the band structure and the density of electronic states showed that they change significantly with an increase in the concentration of adsorbed graphene. Figs. 2 and 3 show examples of plots for some layers in which the fluorine concentration sequentially increases from 10, 25, 35.7, and 43.8 at.%. At the Fermi energy level, the band gap changes are the most clear when the concentration of fluorine changes. If there is no band gap in the initial graphene layer and there is a contact between the valence and conduction bands at the Fermi energy level, then a band gap appears during fluorine adsorption. At a fluorine concentration of 10 at.%, the band gap remains small at 0.114 eV (Fig. 2a, Fig. 2b, Table 1). With an increase of concentration, an increase of the band gap is observed (Fig. 4). This growth is not monotonous: in the concentration range 10 – 15 at.%, a jump in the band gap to  $\sim 1.5$  eV is observed, and then the band width gradually increases with increasing fluorine concentration, reaching 3.094 eV for a completely fluorinated graphene layer. The band gap (0.114 eV) found by us for the low fluorine concentration correlates well with the results given in [11] (0.118 – 0.400 eV) for a similar concentration. As a result of calculations of the electronic structure of the initial graphene layers, it was found that the band gap at the Fermi energy level for this layer is 0. This is in good agreement with the data of theoretical calculations performed earlier by other authors [20], as well as the results of experimental research [21]. The calculated value of the band gap in fully fluorinated graphene is 3.094 eV, which is in good agreement with the previously found theoretical values (2.7 – 3.5 eV [22], 3.07 eV [23]) and experimental values (3 eV [6]). Therefore, the bandgaps calculated by us for partially fluorinated graphene layers should also be correct.

### 1.3. Conclusion

Thus, in this work, we have performed calculations of changes in the structure and electronic characteristics of graphene layers with different concentrations of adsorbed fluorine atoms. It was found that an increase in the fluorine concentration leads to an increase in the unit cell parameter of the layer (from 7.4608 to 7.8050 Å), a decrease in the energy of the carbon-carbon bond (from -6.881 to -4.926 eV), and an increase in the band gap (0 to 3.094 eV). The results obtained in this work can be used to synthesize new graphene-based materials for micro- and nanoelectronics.

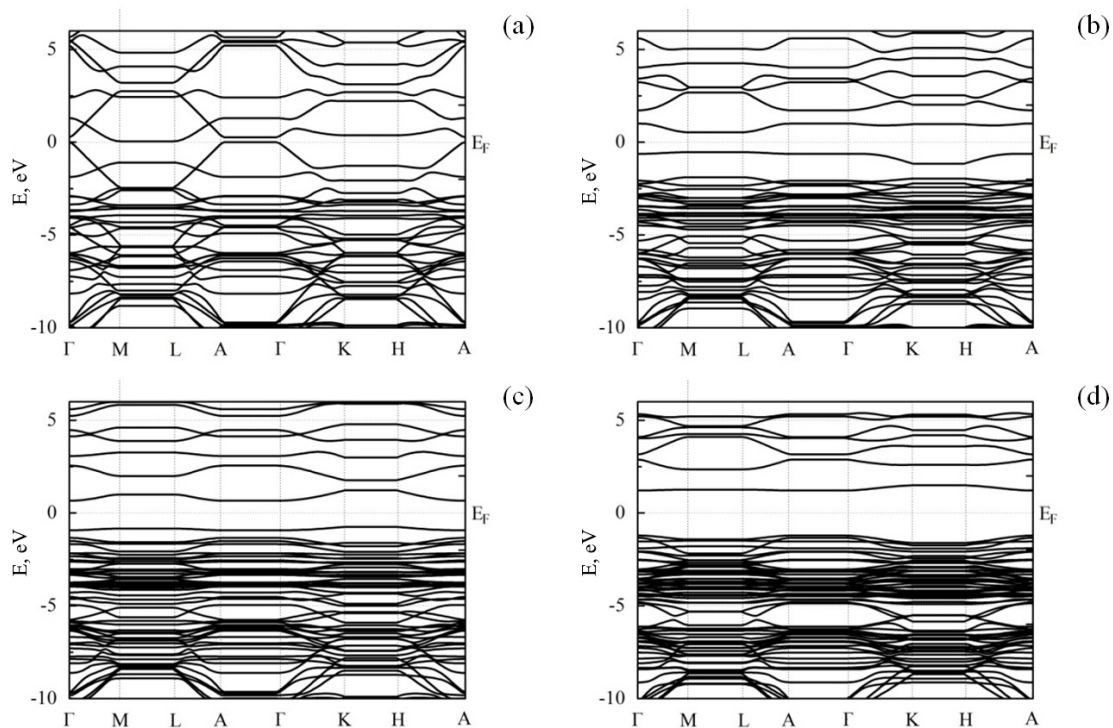


FIG. 2. The band structure of a graphene layer with chemically adsorbed fluorine atoms on the surface, the number of which per expanded unit cell is: (a) 2 atoms; (b) 6 atoms; (c) 10 atoms; (d) 14 atoms

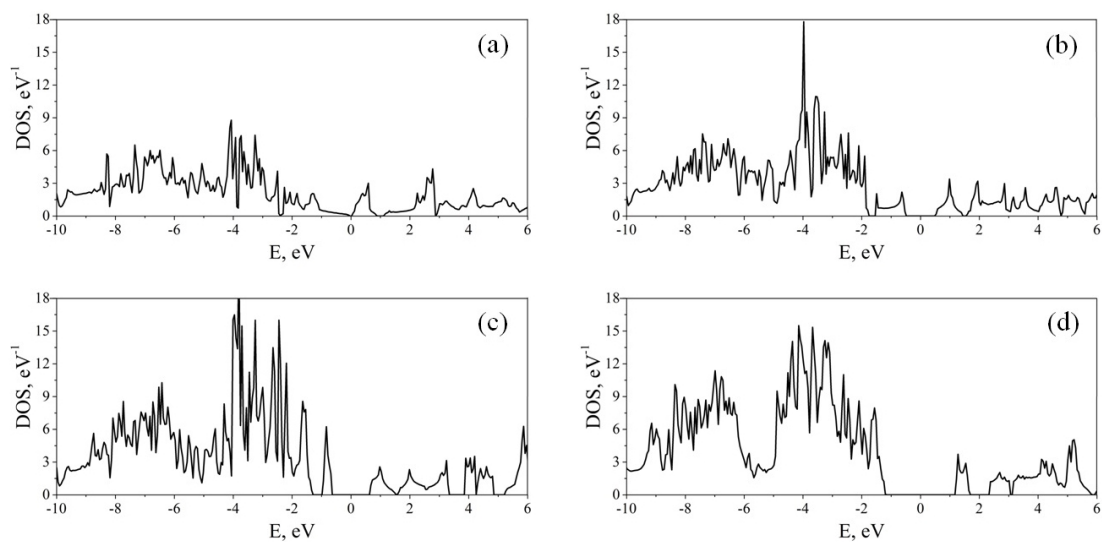


FIG. 3. The density of electronic states (DOS) of a graphene layer with chemically adsorbed fluorine atoms on the surface, the number of which per expanded unit cell is: (a) 2 atoms; (b) 6 atoms; (c) 10 atoms; (d) 14 atoms

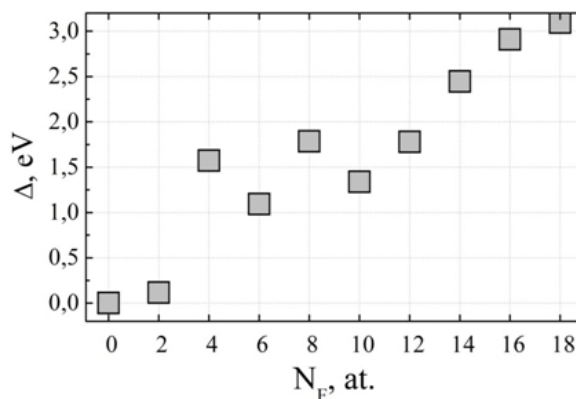


FIG. 4. The dependence of the band gap ( $\Delta$ ) on the number of fluorine atoms ( $N_F$ ) which are chemically adsorbed into the unit cell of the graphene layer, which contains 18 carbon atoms

### Acknowledgements

The reported study was funded by Russian Foundation for Basic Research (RFBR), project number 20-32-90002.

### References

- [1] Freitag M. Nanoelectronics goes flat out. *Nature nanotechnology*, 2008, **3**, P. 455–457.
- [2] Omar G., Salim M.A., et al. Electronic applications of functionalized graphene nanocomposites. In *Functionalized graphene nanocomposites and their derivatives*. Elsevier, Amsterdam, 2019, P. 245–263.
- [3] Sturala J., Luxa J., Pumera M., Sofer Z. Chemistry of graphene derivatives: synthesis, applications and perspectives. *Chem. Eur. J.*, 2018, **24**, P. 5992–6006.
- [4] Chernozatonskii L.A., Sorokin P.B., Artukh A.A. Novel graphene-based nanostructures: physicochemical properties and applications. *Russ. Chem. Rev.*, 2014, **83**(3), P. 251–279.
- [5] Robinson J.T., Burgess J.S., et al. Properties of Fluorinated Graphene Films. *Nano Lett.*, 2010, **10** (8), P. 3001–3005.
- [6] Nair R.R., Ren W., et al. Fluorographene: a twodimensional counterpart of Teflon. *Small*, 2010, **6**, P. 2877–2884.
- [7] Elias D.C., Nair R.R., et al. Control of graphene's properties by reversible hydrogenation: evidence for graphane. *Science*, 2009, **323**, P. 610–613.
- [8] Chen D., Feng H., Li J. Graphene oxide: preparation, functionalization, and electrochemical applications. *Chem. Rev.*, 2012, **112** (11), P. 6027–6053.
- [9] Li B., Zhou L., et al. Photochemical chlorination of graphene. *ACS Nano*, 2011, **5** (7), P. 5957–5961.
- [10] Belenkov M.E., Chernov V.M., Belenkov E.A. Structure of fluorographene and its polymorphous varieties. *J. Phys.: Conf. Ser.*, 2018, **1124**, 022010.
- [11] Grishakov K.S., Katin K.P., Maslov M.M., Prudkovskiy V.S. Relative stabilities of various fully functionalized graphene polymorphs under mechanical strain and electric field. *Applied Surface Science*, 2019, **463**, P. 1051–1057.
- [12] Belenkov M.E., Chernov V.M., Belenkov E.A. Simulation of the structure and electronic properties of fluorographene polymorphs formed on the basis of 4-8 graphene. *IOP Conf. Ser.: Mater. Sci. Eng.*, 2019, **537**, 022058.
- [13] Belenkov M.E., Chernov V.M. Structure and electronic properties of 4-6-12 graphene layers functionalized by fluorine. *Letters on Materials*, 2020, **10** (3), P. 254–259.
- [14] Withers F., Russo S., Dubois M., Craciun M.F. Tuning the electronic transport properties of graphene through functionalisation with fluorine. *Nanoscale Res. Lett.*, 2011, **6**, 526.
- [15] Yuhua D., Stinespring C.D., Chorpening B. Electronic structures, bonding configurations, and bandgapopening properties of graphene binding with lowconcentration fluorine. *Chemistry Open*, 2015, **4** (5), P. 642–650.
- [16] Koch W.A., Holthausen M.C. *Chemists guide to density functional theory*. 2nd edition. Wiley-VCH, Weinheim, 2001. 293 p.
- [17] Giannozzi P., Baroni S., et al. QUANTUM Espresso: a modular and open-source software project for quantum simulations of materials. *Journal of Physics: Condensed Matter*, 2009, **21** (39), 395502.
- [18] Cheng S.H., Zou K., et al. Reversible fluorination of graphene: Evidence of a two-dimensional wide bandgap semiconductor. *Physical Review B*, 2010, **81** (20), 205435.
- [19] Pierson H.O. *Handbook of carbon, graphite, diamond, and fullerenes: properties, processing, and application*. Noyes, Park Ridge, New Jersey, 1993, 402 p.
- [20] Wallace P.R. The band theory of graphite. *Physical Review*, 1947, **71** (9), P. 622–634.
- [21] Novoselov K.S., Geim A.K., et al. Electric field effect in atomically thin carbon films. *Science*, 2004, **306** (5696), P. 666–669.
- [22] Charlier J.C., Gonze X., Michenaud J.P. First-principles study of graphite monofluoride (CF)<sub>n</sub>. *Physical Review B*, 1993, **47** (24), P. 16162–16168.
- [23] Robinson J.T., Burgess J.S., et al. Properties of fluorinated graphene films. *Nano Letters*, 2010, **10** (8), P. 3001–3005.

## SANS studies of nanostructured low-melting metals at room temperature

A. A. Naberezhnov<sup>1</sup>, S. A. Borisov<sup>1</sup>, A. V. Fokin<sup>1</sup>, A. Kh. Islamov<sup>2</sup>, A. I. Kuklin<sup>2</sup>, Yu. A. Kumzerov<sup>1</sup>

<sup>1</sup>Ioffe Institute, Polytekhnicheskaya 26, St. Petersburg, 194021, Russia

<sup>2</sup>Frank Laboratory of Neutron Physics, Joint Institute for Nuclear Research, 141980 Dubna, Russia

alex.naberezhnov@mail.ioffe.ru, sergey.borisov@mail.ioffe.ru, Midbarzin@yandex.ru,  
akhmed.islamov@gmail.com, alexander.iv.kuklin@gmail.com

PACS 61.12.Ex, 61.46.+w, 62.23.St

DOI 10.17586/2220-8054-2020-11-6-690-697

Nanocomposite materials (NCM) based on micro- and macroporous glasses containing nanoparticles of In, Sn and Pb into porous space have been studied by small-angle neutron scattering (SANS) at room temperature. The dependencies of fractal characteristics of metals embedded into the pores from the value of transferred impulse  $Q$  have been obtained. The existence of a critical spatial scale (15 – 16 nm) has been established, at which a change in the fractal characteristics of embedded metals takes place. Distributions of pair correlation functions have been calculated for all types of the studied NCM. It is shown that in these NCM metals form the complicated space systems combining the crystalline and amorphous states of embedded metals.

**Keywords:** nanocomposites, small angle neutron scattering, porous matrices, fractal structures, low-melting metals.

*Received: 31 October 2020*

*Revised: 3 November 2020*

### 1. Introduction

It is well known that the macroscopic physical properties of metals under so-called “restricted geometry” conditions are essentially different from those of the bulk. For example, indium and gallium nanoparticles crystalline phases have been discovered that do not exist for bulk material metals [1–4]. Confinement changes the phonon spectra of metal nanoparticles [5–10] and the properties of their electron subsystems [11–14]. The most surprising changes have been observed for the superconducting properties of gallium, indium, lead and tin [15–20] nanoparticles obtained by introducing these metals into nanoporous alkali borosilicate glasses. Furthermore, for this type of porous glass, we will use the abbreviation PG. The special features of PG are the very flexible geometric form (i.e., as beads, rods, fibers, ultrathin membranes, flat plates) and the controllable average pore diameters in the broad range between 0.3 and 1000 nm [21]. Special heat treatment of initial alkali borosilicate glasses of a suitable composition between 500 and 700 °C initiates a phase separation and two different interconnected phases are obtained. The first one is an alkali-rich borate phase soluble in hot mineral acids, water or alcohols. The second one is almost pure silica. This procedure is used practically for the preparation of the commercial controlled-pore glasses (CPG) [22].

Pores in these glasses form through a multiply-connected system of interconnected channels. Porous glasses with a skeleton consisting almost entirely of amorphous silica (~ 96 %) are obtained after the leaching procedure. Currently, these glasses are widely used to create nanocomposite materials (NCM). In particular, for porous glasses with an average pore diameter of 7 nm (PG7), it has been shown that nanocomposites “Sn (or Pb) + porous glass” become the superconductors of the second type, and the critical magnetic fields leading to the destruction of the superconducting state in these composites increase by 60-100-fold [19,20]. The crystal structure of low-melting metals (Hg, Ga, In, Sn and Pb) embedded into PG7 has been studied by X-ray and neutron diffraction [1, 4, 10, 17, 23–25] and it has been found that these metals form into the pores of PG7 the nanoclusters with characteristic size slightly larger than the average pore diameter. It means that nanoparticles occupy space in several neighboring pores. In spite of the large amount of research devoted to studies of crystal and macroscopic properties of NCM with embedded low-melting metals the peculiarities of internal space organization of nanoparticles and fractal characteristics in these NCM remain unclear. To obtain such data, one of the most informative techniques is the method of small-angle neutron scattering (SANS), and in this paper, we have used this approach for studies of internal structure and fractal characteristics of low-melting metals (In, Sn and Pb) embedded into micro- (PG7) and macroporous (PG-MAP) alkali borosilicate glasses.

## 2. Samples and method

For sample preparation we used two types of PG: PG7 with average pore diameter  $7 \pm 1$  nm and macroporous glasses (PG-MAP) with a broad distribution of pore diameters from 20 nm up to  $\sim 100$  nm (distribution median was about 40 – 50 nm). Metals in the porous glasses were introduced from a melt at a pressure of  $\sim 6$  kbar (lead) and  $\sim 10 - 11$  kbar (indium, tin). After cooling a melt, the samples were removed, and their surfaces were thoroughly cleaned from the remnants of the bulk material. We prepared four NCM: S1 – In + PG7, S2 – In + PG-MAP, S3 – Sn + PG-MAP, S4 – Pb + PG-MAP. S0 was the reference sample of an initial alkali borosilicate glass after a thermal treatment with the composition 96 %  $\text{SiO}_2 - 3.8$  %  $\text{B}_2\text{O}_3 - 0.2$  %  $\text{Na}_2\text{O}$ , which has been determined by chemical analysis. This composition was used for the preparation of porous glasses PG7 and PG-MAP.

Small-angle neutron scattering (SANS) experiments were performed on YuMO time-of-flight spectrometer at high flux pulse IBR-2 reactor (JINR, Dubna, Russia) [26, 27]. YuMO is an instrument with two movable detectors system placed at sample-to-detectors distances of 5.28 and 13.4 m, resulting in a  $Q$  range of  $0.006 - 0.5 \text{ \AA}^{-1}$ , where  $Q = (4\pi/\lambda) \sin(\theta/2)$  is a transferred momentum and  $\theta$  is the scattering angle. The diameter of the sample in the beam was 14 mm. The measured neutron scattering spectra were corrected for the transmission and thickness of the sample, background scattering on the film substrate and on the vanadium reference sample using SAS software [28, 29], yielding a neutron scattering intensity in absolute units of  $\text{cm}^{-1}$ . All measurements were carried out at room temperature. The errors in determination of the alpha parameter for all samples (excepting the initial glass S0) on Fig. 2 in the dependences  $I(Q) \sim Q^{-\alpha}$  did not exceed 2 – 3 %. For S0 the error was about 7 %.

## 3. Results

Low resolution the SANS technique cannot give the detailed structure at the atomic level but is useful to describe structural features typical at distances of 1 to 100 nm.

In the case of disordered systems, such as glasses with embedded metals, in the absence of strong correlations between inhomogeneities (fluctuations in the scattering density), the scattered intensity can follow the power law of  $Q$ :

$$I(Q) = A \cdot Q^{-\alpha} + B, \quad (1)$$

where  $A$  and  $B$  are constants,  $B$  is the background. It has been shown [30] that for objects with a complex branched surfaces (surface fractal of dimension from  $2 \leq D_s \leq 3$ )  $3 < \alpha \leq 4$  scattering can be given by:

$$I(Q) = A \cdot Q^{-(6-D_s)} + B, \quad (2)$$

$$A = \pi N_0 (\Delta\rho)^2 \Gamma(5 - D_s) \sin(\pi(D_s - 1)/2), \quad (3)$$

where  $N_0$  is the measure of the fractal surface (in other words, a constant characteristic of the fractal boundaries),  $\Gamma$  – gamma function and  $\Delta\rho$  (contrast) is the difference between coherent scattering densities of the inner part of cluster and its boundary (surface) layer, which have different composition of elements or lower density packing. In the ideal case, where the interfacial region is sharp, one obtains the equation of Porod's law [31]:

$$I(Q) = 2\pi(\Delta\rho)^2 \left(\frac{S}{V}\right) Q^{-4}, \quad (4)$$

where  $S/V$  is the total area of the interface per unit of volume of the particle.

From the equation (4), it is easy to see that the parameter  $\Delta\rho$  plays the principle role in a dependence  $I$  vs.  $Q$ . The scattering densities of initial glasses with composition 96 %  $\text{SiO}_2 - 3.8$  %  $\text{B}_2\text{O}_3 - 0.2$  %  $\text{Na}_2\text{O}$  (mass. %) and metals embedded into porous glasses have been calculated using the program SLD [32] and are presented in Table 1.

TABLE 1. Densities of coherent scattering for glass and metals

Element	96 % $\text{SiO}_2 - 3.8$ % $\text{B}_2\text{O}_3 - 0.2$ % $\text{Na}_2\text{O}$	In	Sn	Pb	Air into the pores
$\rho_{\text{scatt}}, 10^{10} \text{ cm}^{-2}$	3.32	1.56	2.31	3.1	$\sim 0$

As has been mentioned above, the filling of porous glasses by metals has been performed from the melts. It is natural to expect that due to metal contraction in the pores at cooling, the voids are formed into porous space of glasses. Thus, in these nanocomposites, we have three types of objects (glass skeleton, metal nanoparticles and empty space) and three types of interfaces (“matrix-voids”, “matrix – metal nanoparticles” and “voids – metal nanoparticles”). Since the intensity of small-angle scattering into a zero angle is proportional to the square of the contrast ( $(\Delta\rho)^2$ ), the intensity of scattering with a complete filling of the pores with metal would be much less than for empty porous glass (see Table 1 and the equation (5)):

$$I(0) = \varphi_{\text{Met}} (\rho_{\text{Glass}} - \rho_{\text{Met}})^2 V, \quad (5)$$

where  $\rho_{\text{Glass}}$  and  $\rho_{\text{Met}}$  are the scattering densities of glass and embedded metal.  $V$  and  $\varphi$  are the volume and the volume fraction of metal nanoclusters. However, the experimental results show (Fig. 1) that scattering intensities from glasses filled by metals significantly exceeds the scattering from the glass PG7. This means the following: 1 – S0 is not really porous glass, 2 – in our samples S1 – S4 three types of scattering objects and interfaces exist and one of them is the interface “glass – empty porous space”, which increases the total scattering according to the contrast  $(\Delta\rho)^2$  (Table 1). The volume fractions of nanoclusters and voids in glass can be obtained using the Porod invariant of two and three phase systems, calculated from the equations (6) and (7) [34]:

$$2\pi\rho_{\text{Glass}}^2\varphi_{\text{pores}}(1 - \varphi_{\text{pores}}) = \int_0^{\infty} I(Q)Q^2 dQ, \quad (6)$$

$$2\pi \left[ \rho_{\text{Glass}}^2\varphi_{\text{pores}}\varphi_{\text{Glass}} + \rho_{\text{Met}}^2\varphi_{\text{pores}}\varphi_{\text{Met}} + (\rho_{\text{Glass}} - \rho_{\text{Met}})^2 \varphi_{\text{Met}}\varphi_{\text{Glass}} \right] = \int_0^{\infty} I(Q)Q^2 dQ, \quad (7)$$

where  $\varphi_{\text{pores}}$ ,  $\varphi_{\text{Glass}}$  and  $\varphi_{\text{Met}}$  – relative volume fractions of pores, glass skeleton and metals in these NCM. And from the additional equations (8,9) connecting the volume fractions of metals and voids with the mass densities of glasses  $\rho^{GL}$  (g/cm<sup>3</sup>) obtained from gravimetric measurements:

$$\rho_{\text{SiO}_2}\varphi_{\text{Glass}} + \rho_{\text{Met}}\varphi_{\text{Met}} = \rho^{GL} = \frac{M^{GL}}{V^{GL}}, \quad (8)$$

$$\varphi_{\text{Glass}} + \varphi_{\text{Met}} + \varphi_{\text{Pores}} = 1. \quad (9)$$

### 3.1. Initial alkali borosilicate glass S0

For our initial glass S0 we have observed the principle difference between this glass and the conventional porous glasses [35–38], i.e. in S0 there is no a correlation peak at  $Q_0 = 0.015 - 0.022 \text{ \AA}^{-1}$  (Fig. 2A). It is shown that this peak is characteristic of the presence of structural units with average size  $L \sim 2\pi/Q_0$  and has been earlier observed in papers [35–38] devoted to studies of porous glasses. Since  $L$  is essentially larger than the average pore diameter, one can conclude that these units (scatterers) are massive and refer to the internal structure of porous glasses. The origin of this phenomena it connected with a procedure of porous glass preparation – so-called spinodal decomposition [39] else phase separation at liquation process. In S0, we have observed a change of slope in the curve  $I(Q)$  near  $Q = 0.02 \text{ \AA}^{-1}$  only (Fig. 2A). According to calculation, the maximum size of inhomogeneities in glass is about 15 nm (Fig. 3 – black squares), the volume fraction of pores is 1 % of the total volume. The pair correlation function for S0 (Fig. 3) can be consider as a distribution of channel diameters which would be formed in this glass after leaching.  $I(Q)$  in the diapason  $0.02 - 0.11 \text{ \AA}^{-1}$  obeys the power law  $Q^{-\alpha}$  with  $\alpha = 3.25$  (Fig. 2A – red straight line): it corresponds to scattering from highly rough surfaces (surface fractals) due to the presence of secondary silicates into the channels in this glass forming at heat treatment (liquation process). Thus we can conclude that the S0 glass is practically non porous.

### 3.2. NCM In + PG7 and In+PG-MAP (S1 and S2 samples)

Porod’s law for In+PG7 (Fig. 2B) and In+PG-MAP (Fig.2D) at  $Q > 0.04 \text{ \AA}^{-1}$  is performed clearly and this results in scattering on smooth channel surfaces. In the S1 sample at  $Q < 0.04 \text{ \AA}^{-1}$ , the scattering extends to the Guinier’s region. In general, the picture looks like this: indium fills only a part of the total porous space in this sample, but a part of the pores remains empty (Table 2), that gives the Porod’s law at large  $Q$ . It is necessary to note that the maximum cluster size (inhomogeneities, i.e. empty pores + metal, in the S1 sample) increases up to 20 nm (Fig. 3 – red squares). The position of maximum corresponds to  $\sim 8$  nm, which is clearly smaller than the diffraction size ( $\sim 11 - 15$  nm) of indium nanoparticles obtained from analysis of diffraction patterns [4] for this NCM.

For NCM In+PG-MAP we have observed the crossover point at  $Q = 0.04 \text{ \AA}^{-1}$  at which the slope (parameter  $\alpha$ ) of the dependence  $I(Q) \sim Q^{-\alpha}$  changes from 4.02 to 3.19 (red straights on Fig. 2D). This  $Q$  value corresponds to a space scale  $d = 2\pi/Q = 15 - 16$  nm. The value  $\alpha = 3.19$  shows that in this NCM in porous space, the surface fractal structures exist on a spatial scale greater than 16 nm. In this case, the maximum size of inhomogeneities in this NCM increases up to 60 – 70 nm (Fig. 3 – blue squares).

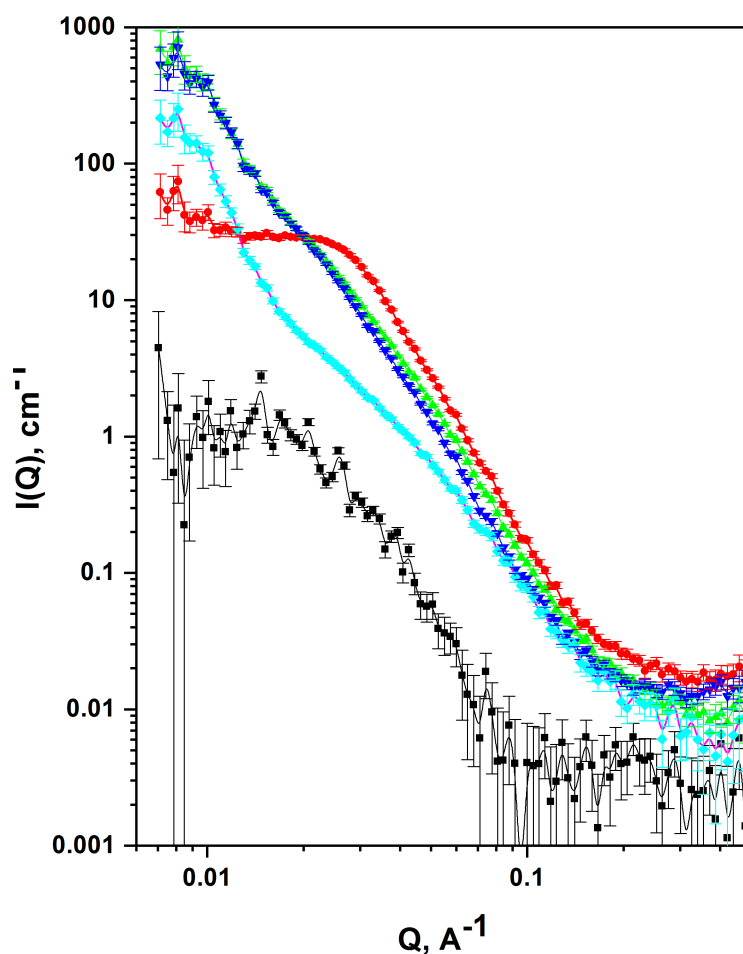


FIG. 1. Small-angle neutron scattering from samples: S0 – black squares, S1 (In + PG7) – red rounds, S2 (In+PG-MAP) – blue triangles, S3 (Sn+PG-MAP) – green triangles, S4 (Pb+PG-MAP) – cyan rhombs

TABLE 2. Volume fractions of metals ( $\varphi_{\text{Met}}$ ) and voids ( $\varphi_{\text{Pores}}$ ) in samples S0 – S4 obtained from the equations (6–9)

Sample	S0	S1 (In+PG7)	S2 (In+PG-MAP)	S3 (Sn+PG-MAP)	S4 (Pb+PG-MAP)
$\varphi_{\text{Met}}, \%$	0	12.8	12.5	8.9	19.1
$\varphi_{\text{Pores}}, \%$	1.0	8.6	7.2	10.8	4.4
$\varphi_{\text{Gl}}, \%$	99.0	78.6	80.3	80.3	76.4

### 3.3. NCM Sn+PG-MAP (S3 sample)

For NCM Sn+PG-MAP we have also observed the crossover point at  $Q = 0.04 \text{ \AA}^{-1}$  (as in for NCM In+PG-MAP), but at this case, the parameter  $\alpha$  in the dependence  $I(Q) \sim Q^{-\alpha}$  changes from 4.06 to 2.92 (red straights on Fig. 2C). The value  $\alpha = 2.92$  shows that in this NCM in porous space the mass fractal structures exist on a spatial scale greater than 16 nm. The maximum size of inhomogeneities in this NCM also increases to 60 – 70 nm (Fig. 3 – green squares).

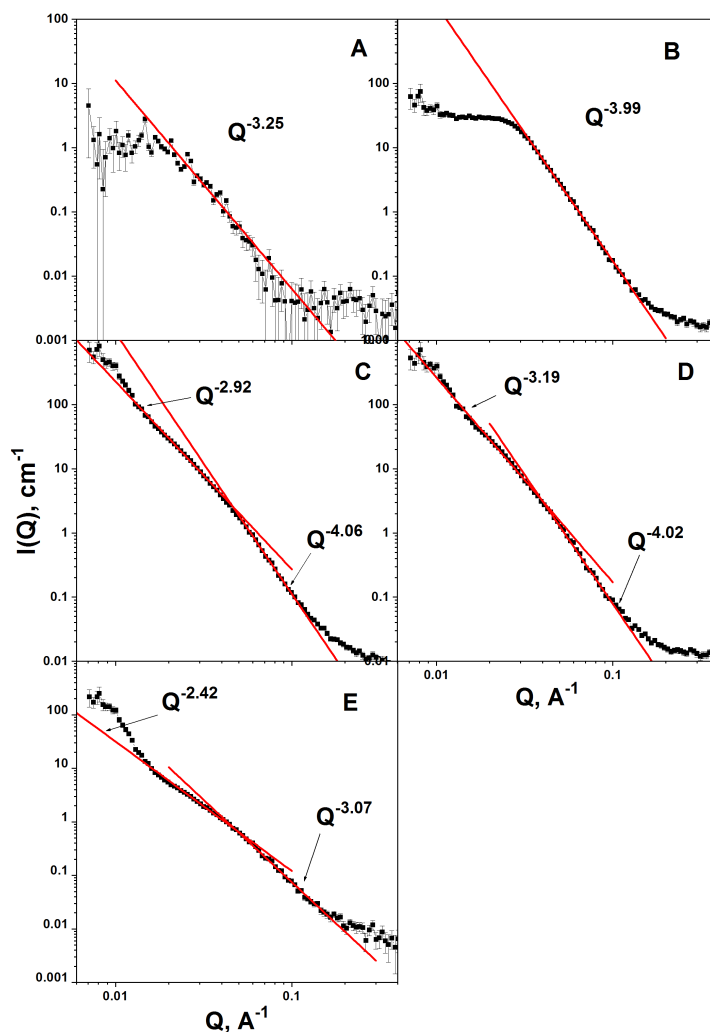


FIG. 2. SANS data and fractal characteristics of the samples S0 – S4: A – S0, B – S1, C – S3, D – S2, E – S4

### 3.4. NCM Pb+PG-MAP (S4 sample)

The scattering laws differ essentially from scattering on In+PG-MAP and Sn+PG-MAP (Fig. 2E). For the region  $Q > 0.04 \text{ \AA}^{-1}$   $I(Q)$  follows as  $\sim Q^{-3.07}$ , that is typical for a strongly rough surface. The intersection of the background constant with the scattering curve at  $Q = 0.2 \text{ \AA}^{-1}$  gives an approximate minimum roughness size of the order  $d \sim 3 \text{ nm}$ . Since the scattering density of lead is approximately the same as for glass itself (Table 1), the picture of scattering is similar to the glass before leaching, when there are a lot of secondary silica into the pore space. Starting from  $Q < 0.04 \text{ \AA}^{-1}$ , the scattering is described as  $I(Q) \sim Q^{-2.42}$  – which corresponds to scattering from mass fractals – polydisperse distribution of lead nanoparticles and empty pores with air. The volume fraction of free pores is significantly less than for other MAP samples (Table 2). NCM Pb+PG-MAP shows a typical correlation peak for alkali borosilicate glasses, but it is not at  $Q = 0.015 \text{ \AA}^{-1}$ , but at a position less than  $Q < 0.01 \text{ \AA}^{-1}$ . These peaks are also faintly visible on the samples starting from the second one. This is in agreement with the fact that if the cluster size for samples on base of MAP glasses is on the order of  $d \sim 60 - 70 \text{ nm}$ , then the position of the correlation peak  $Q_{\text{corr}} \sim 2\pi/d$  should be in the range from  $0.0089$  to  $0.01 \text{ \AA}^{-1}$ .

### 3.5. Summary remarks

For NCM In+PG7, In+PG-MAP and Sn+PG-MAP at  $Q > 0.04 \text{ \AA}^{-1}$ , we have observed Porod's law for scattering intensity that corresponds to a smooth surface. It means that in this  $Q$  region in the samples S1, S2 and S3 the interface "matrix-air", having the greatest contrast  $(\Delta\rho)^2$  among others (Table 1), plays the principle role. In the case of the S4 (Pb+PG-MAP) sample, the situation changes drastically: parameter  $\alpha$  becomes equal to 3.07 at large  $Q$ , i.e. here,

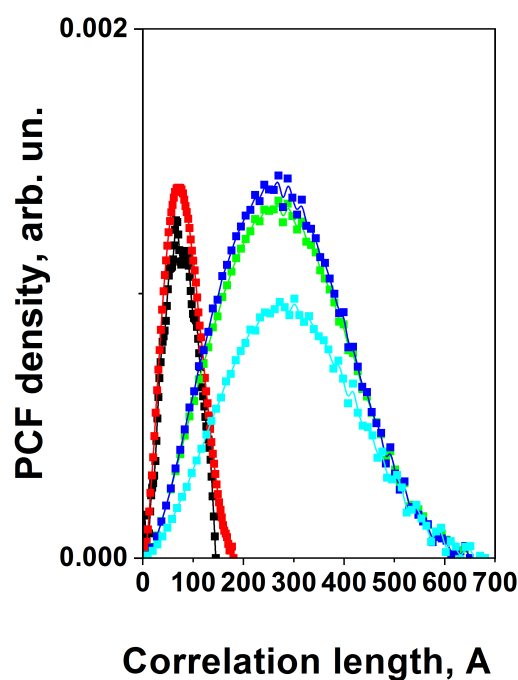


FIG. 3. Pair correlation functions (PCF) obtained after treatment by GNOM program (ATSAS package [33]) for samples: S0 – black squares, S1 – red squares, S2 – blue squares, S3 – green squares, S4 – cyan squares

we are dealing with a surface fractal structure mainly formed by lead atoms. Apparently, this is due to a significant difference in the surface tension coefficients ( $\sigma$ ) of these metals, since the filling takes place from the melt, followed by cooling and crystallization in the pores: indeed  $\sigma_{\text{Pb}} = 440 \cdot 10^{-3}$  n/m,  $\sigma_{\text{In}} = 556 \cdot 10^{-3}$  n/m,  $\sigma_{\text{Sn}} = 530 \cdot 10^{-3}$  n/m [40]. It looks like as, if a part of lead does not have time to shrink into large nanoparticles on cooling and at crystallization and becomes “smeared” in the matrix channels. Naturally, this process also takes place for indium and tin, but to a lesser extent due to the difference in surface tensions and the lower total pore filling (Table 2).

At  $Q < 0.04 \text{ \AA}^{-1}$  in NCM Pb+PG-MAP and Sn+PG-MAP the parameters  $\alpha$  are in the range from 2 to 3, which correspond to the mass fractal; however, for indium, this parameter ( $\alpha = 3.19$ ) indicates the formation of a surface fractal structure. Therefore, in wide-pore glass with the usual cooling mode of NCM. It is most likely, that this is due to the low melting point of indium: i.e. in the wide-pore glass at the usual cooling mode of NCM, some of the indium (similar to lead) does not have time to completely collect into nanoparticles and remains in a “smeared” state over the porous space. In the case of In+PG7, the pore diameter is essentially smaller, and indium has time to crystallize into nanoparticles to a greater extent.

Now let us discuss the results of pair correlation function (PCF) analysis presented in Fig. 3. As it has been shown in the paper [4] in NCM In+PG7 the nanoparticles have anisotropic form with two characteristic diffraction sizes: 11 and 15 nm. However, it can be seen from Fig. 3 that the value of the correlation length is in the range 0 – 17 nm, i.e. in the NCM there is a significant part of indium agglomerates much less than the diffraction size. On the other hand, we have not seen such small particles in the diffraction spectra. This disagreement is easy to explain. In diffraction studies, we have a response from a crystal structure only, since scattering from the amorphous metal phase “sinks” in the general strong diffuse background from the matrix. In SANS measurements, only a contrast  $\Delta\rho$  plays the principle role. The contrast for the crystalline and amorphous phases is the same. Thus, we can conclude that this NCM contains a considerable portion of indium in the amorphous state. A similar argumentation one can do for the samples S2 – S4, only in these samples, according to preliminary diffraction measurements, the diffraction size of nanoparticles is in the range of 25 – 40 nm.

There is one more argument in favor of the multicomponent structure of metals in these NCMs. For similar random dendrite 3D systems (as our glasses), it has been found that the percolation threshold  $\rho_c$  is equal to 0.2 [41]. As it is seen from Table 2, the total amount of embedded metals in all cases (excepting Pb+PG-MAP) is smaller than  $\rho_c$ , but a through conduction has been observed for all samples S1 – S4 [15, 18–20, 42]. This means that the spatial organization of the internal structure of embedded metals can be described as follows: there are sufficiently large

crystalline nanoparticles that either border directly on each other or are linked by weak bonds, which, apparently, are largely consisted of amorphous metals.

To clarify the situation and to obtain estimations of the content of the crystalline and amorphous phases, we are going to carry out additional combined diffraction and SANS studies of the temperature evolution of diffuse scattering in vicinities of principle Bragg peaks and  $\alpha$  parameters in the  $Q^{-\alpha}$  dependence at melting and crystallization of metals in these NCM.

#### 4. Conclusion

The fractal characteristics of NCM on base of porous alkali borosilicate glasses containing the low-melting metals (In, Sn and Pb) have been obtained from analysis of SANS data at room temperature. It is shown, that for all NCM there is the critical space scale near  $Q = 0.04 \text{ \AA}^{-1}$  (15 – 16 nm), at which one can see a crossover in the behavior of the scattering intensity  $I(Q) \sim Q^{-\alpha}$ .

It is shown that in these NCM we are dealing with a complex system that combines both the fractal properties of embedded metals and the matrix itself. Combined analysis of SANS spectra, pair correlation function and conventional diffraction patterns permits to conclude that the crystalline and amorphous phases of embedded metals coexist in these NCM.

#### Acknowledgements

A. A. Naberezhnov thanks the RFBR-BRICS grant 19-52-80019 for partial financial support. A. V. Fokin thanks the Russian Foundation for Basic Research, grant 19-02-00760. In FLNP JINR this work was partly supported by RF Ministry of Education and Science, grant number 19-52-44003\19.

#### Conflict interests

Authors declare that they have no conflict interests.

#### References

- [1] Lee M.K., Tien C., et al. Structural variations in nanosized confined gallium. *Physics Letters A*, 2010, **374**, P. 1570–1573.
- [2] Tanaka M., Takeguchi M., Furuya K. In situ observation of indium nanoparticles deposited on Si thin films by ultrahigh vacuum field emission transmission electron microscope. *Surface Science*, 1999, **433–435**, P. 491–495.
- [3] Balamurugan B., Kruis F.E., et al. Size-induced stability and structural transition in monodispersed indium nanoparticles. *Appl. Phys. Lett.*, 2005, **86**, 083102.
- [4] Naberezhnov A.A., Sovestnov A.E., Fokin A.V. Crystal Structure of Indium and Lead under Confined Geometry Conditions. *Technical Physics*, 2011, **56** (5), P. 637–641.
- [5] Bonetti E., Pasquini L., et al. Vibrational density of states of nanocrystalline iron and nickel. *Jour. Appl. Phys.*, 2000, **88** (8), P. 4571–4575.
- [6] Trampenau J., Bauszuz K., Petry W., Herr U. Vibrational behaviour of nanocrystalline Ni. *Nanostruct. Mater.*, 1995, **6**, P. 551–554.
- [7] Fultz B., Robertson J.L., et al. Phonon density of states of nanocrystalline Fe prepared by high-energy ball milling. *J. Appl. Phys.*, 1996, **79**, P. 8318–8322.
- [8] Suck J.B. Metallic Nanocrystals and Their Dynamical Properties. In: Gemming S., Schreiber M., Suck J.B. (eds) *Materials for Tomorrow*. Springer Series in Materials Science, 2007, **93**. Springer, Berlin, Heidelberg, 196 p.
- [9] Parshin P.P., Zemlyanov M.G., et al. Atomic Dynamics of Lead Introduced into Nanopores in Glass. *JETP*, 2011, **111** (6), P. 996–1002.
- [10] Parshin P.P., Zemlyanov M.G., et al. Atomic Dynamics of Tin Nanoparticles Embedded into Porous Glass. *JETP*, 2012, **114** (3), P. 440–450.
- [11] Borman V.D., Pushkin M.A., Tronin V.N., Troyan V.I. Evolution of the electronic properties of transition metal nanoclusters on graphite surface. *JETP*, 2010, **110** (6), P. 1005–1025.
- [12] Sovestnov A.E., Naberezhnov A.A., et al. Study of Palladium Nanoparticles Synthesized in Alkali Borosilicate Glass Pores by the X-Ray Line Shift Method. *Physics of the Solid State*, 2013, **55** (4), P. 837–841.
- [13] Balamurugana B., Maruyama T. Size-modified d bands and associated interband absorption of Ag nanoparticles. *Jour. Appl. Phys.*, 2007, **102**, 034306.
- [14] Rao C.N.R., Kulkarni G.U., et al. Metal nanoparticles, nanowires, and carbon nanotubes. *Pure Appl. Chem.*, 2000, **72** (1–2), P. 21–33.
- [15] Kumzerov Yu.A., Naberezhnov A.A. Effect of restricted geometry on superconducting properties of low-melting metals (Review). *Low Temperature Physics*, 2016, **42** (11), P. 1028–1040.
- [16] Tien C., Wur C.S., et al. Double-step resistive superconducting transitions of indium and gallium in porous glass. *Phys. Rev. B*, 2000, **61** (21), P. 14833–14838.
- [17] Charnaya E.V., Tien C., Lee M.K., Kumzerov Yu.A. Superconductivity and structure of gallium under nanoconfinement. *J. Phys.: Condens. Matter*, 2009, **21**, 455304.
- [18] Tien C., Charnaya E.V., et al. Vortex avalanches in a Pb-porous glass nanocomposite. *Phys. Rev. B*, 2011, **83**, 014502.
- [19] Panova G.Kh., Nikonov A.A., Naberezhnov A.A., Fokin A.V. Resistance and Magnetic Susceptibility of Superconducting Lead Embedded in Nanopores of Glass. *Physics of the Solid State*, 2009, **51** (11), P. 2225–2229.
- [20] Shikov A.A., Zemlyanov M.G., et al. Superconducting Properties of Tin Embedded in Nanometer-Sized Pores of Glass. *Physics of the Solid State*, 2012, **54** (12), P. 2345–2350.
- [21] Enke D., Janowski F., Schwieger W. Porous glasses in the 21st century – a short review. *Microporous and Mesoporous Materials*, 2003, **60**, P. 19–30.

- [22] Haller W. In *Solid Phase Biochemistry*, Scouten W.H. (Ed.), Wiley, New York, 1983, 535 p.
- [23] Kumzerov Yu.A., Naberezhnov A.A., Savenko B.N., Vakhrushev S.B. Freezing and melting of mercury in porous glass. *Phys. Rev. B*, 1995, **52** (7), P. 4772–4774.
- [24] Golosovsky I.V., Delaplane R.G., Naberezhnov A.A., Kumzerov Yu.A. Thermal motions in lead confined within porous glass. *Phys. Rev. B*, 2004, **69**, 132301.
- [25] Kibalin Y.A., Golosovsky I.V., et al. Neutron diffraction study of gallium nanostructured within a porous glass. *Phys. Rev. B*, 2012, **86**, 024302.
- [26] Ostanevich Yu.M. Timeoflight smallangle scattering spectrometers on pulsed neutron sources. *Makromol. Chem. Macromol. Symp.*, 1988, **15**, P. 91–103.
- [27] Kuklin A.I., Islamov A.Kh., Gordeliy V.I. Two-detector System for Small-Angle Neutron Scattering Instrument. *Neutron News*, 2005, **16**, P. 16–18.
- [28] Soloviev A.G., Solovieva T.M., et al. SAS. The package for Small-Angle Neutron Scattering Data Treatment. Version 2.4. Long Write-Up and User's Guide. *JINR Communication*, 2003, P10-2003-86, 24 p.
- [29] Soloviev A.G., Solovjeva T.M., et al. SAS program for two-detector system: seamless curve from both detectors. *Journal of Physics: Conf. Series*, 2017, **848** (1), 012020.
- [30] Bale H.D., Schmidt P.W. Small-Angle X-Ray-Scattering Investigation of Submicroscopic Porosity with Fractal Properties. *Phys. Rev. Lett.*, 1984, **53**, P. 596–599.
- [31] Teixeira J. Small-angle scattering by fractal systems. *J. Appl. Crystallogr.*, 1988, **21**, P. 781–785.
- [32] Neutron/X-ray Scattering Length Density Calculator. URL: <https://sld-calculator.appspot.com>.
- [33] Franke D., Petoukhov M.V., et al. ATSAS 2.8: a comprehensive data analysis suite for small-angle scattering from macromolecular solutions. *J. Appl. Cryst.*, 2017, **50**, P. 1212–1225.
- [34] Feigin L.A., Svergun D.I. *Structure Analysis by Small Angle X Ray and Neutron Scattering*, Princeton, New Jersey, 1987, 335 p.
- [35] Levitz P., Ehret G., Sinha S.K., Drake J.M. Porous vycor glass: The microstructure as probed by electron microscopy, direct energy transfer, smallangle scattering, and molecular adsorption. *Jour. Chem. Phys.*, 1991, **95**, 6151.
- [36] Naberezhnov A.A., Vakhrushev S.B., Okuneva N.M., Sysoeva A.A. SANS studies of nanocomposites Sodium nitrite + Porous glasses. *Ferroelectrics*, 2019, **539** (1), P. 16–21.
- [37] Höhr A., Neumann H.-B., et al. Fractal surface and cluster structure of controlled-pore glasses and Vycor porous glass as revealed by small-angle x-ray and neutron scattering. *Phys. Rev. B*, 1988, **38** (2), P. 1462–1467.
- [38] Wiltzius P., Bates F.S., Dierker S.B., Wignall G.D. Structure of porous Vycor glass. *Phys. Rev A Gen. Phys.*, 1987, **36** (6), 2991.
- [39] Cahn J.W. On spinodal decomposition. *Acta Metall.*, 1961, **9** (9), 795.
- [40] Surface tension of metals in liquid state. URL: <https://tehtab.ru/Guide/GuidePhysics/SurfaceTension/SurfaceTensionOfLiquidMetall> [In Russian]
- [41] Grannan D.M., Carland J.C., Tanner D.B. Critical Behavior of the Dielectric Constant of a Random Composite near the Percolation Threshold. *Phys. Rev. Lett.*, 1981, **46** (5), P. 375–378.
- [42] Tien C., Wur C.S., et al. Double-step resistive superconducting transitions of indium and gallium in porous glass. *Phys. Rev. B*, 2000, **61** (21), P. 14833–14838.

## Sol-gel synthesis and the investigation of the properties of nanocrystalline holmium orthoferrite

A. T. Nguyen<sup>1</sup>, H. L. T. Tran<sup>1</sup>, Ph. U. T. Nguyen<sup>1</sup>, I. Ya. Mittova<sup>2</sup>, V. O. Mittova<sup>3</sup>,  
E. L. Viryutina<sup>2</sup>, V. H. Nguyen<sup>4</sup>, X. V. Bui<sup>5</sup>, T. L. Nguyen<sup>6,7</sup>

<sup>1</sup>Ho Chi Minh City University of Education, Ho Chi Minh City 700000, Vietnam

<sup>2</sup>Voronezh State University, Universitetskaya pl. 1, Voronezh, 394018, Russia

<sup>3</sup>Burdenko Voronezh State Medical University, Voronezh, 394036, Russia

<sup>4</sup>Dong Thap University, Cao Lanh City 81000, Vietnam

<sup>5</sup>Sai Gon University, Ho Chi Minh City, 700000, Vietnam

<sup>6</sup>Institute of Fundamental and Applied Sciences, Duy Tan University, Ho Chi Minh City, 700000, Vietnam

<sup>7</sup>Faculty of Environmental and Chemical Engineering, Duy Tan University, Da Nang, 550000, Vietnam

tienna@hcmue.edu.vn, tran.hongle86@gmail.com, nguyenphuonguyen0110@gmail.com, imittova@mail.ru,  
vmittova@mail.ru, viryutina.helena@yandex.ru, nguyenvanhung@dthu.edu.vn,  
buixuanvuongsgu@gmail.com, nguyentuanloi@duytan.edu.vn

DOI 10.17586/2220-8054-2020-11-6-698-704

Holmium orthoferrite nanocrystals (HoFeO<sub>3</sub>) were synthesized from an aqueous solution by the sol-gel method, using polyvinyl alcohol as a stabilizer and annealing at temperatures of 650, 750, and 850 °C for an hour. According to the results of the performed analyses, it was found that with an increase in the annealing temperature, the average size of HoFeO<sub>3</sub> crystallites increases from 24 to 30 nm. The magnetic characteristics of the samples were measured and it was shown that holmium orthoferrite is a paramagnet with a low coercive force. The band gap of nanocrystalline holmium ferrite is determined.

**Keywords:** nanoparticles, holmium orthoferrite, sol-gel technique, magnetic properties, optical properties.

*Received:* 28 August 2020

*Revised:* 25 September 2020

*Final revision:* 20 October 2020

### 1. Introduction

One of the promising areas of materials science is the creation of effective magnetoelectric ferrites using various synthesis methods. Therefore, recently, orthoferrites of rare-earth metals, especially such a promising and still very poorly studied material as holmium ferrite with a perovskite structure were of interest. Nanocrystalline HoFeO<sub>3</sub> is a multiferroic with a potentially unusual combination of electrical, magnetic, and optical properties [1–4]. AFeO<sub>3</sub> samples are interesting due to their magnetic characteristics and application prospects. For example, they can be compatible with biological materials [5], their nanoparticles can be used as small probes [6–9], which would allow registering the cellular processes without affecting their course. In addition, particles of the nanometer size range are used to increase the density of magnetic recording of information [10–12], production of the transformer coils and other electrical devices with high efficiency [10, 13, 14].

Some orthoferrites are widely used in microwave devices due to their low coercive force ( $H_c$ ), remnantmagnetization ( $M_r$ ) and high saturation magnetization ( $M_S$ ), excellent mechanical and chemical stability, rectangular hysteresis loop, etc. [12, 15, 16].

For the synthesis of orthoferrites, the sol-gel method, which allows production of nanopowders with a narrow particle size distribution at relatively low temperatures, is especially important [15, 18]. The presented method allows production of highly dispersed powders, fibers or thin films from solutions at temperatures lower than in the case of traditional solid-phase systems [19–24]. Such materials can be imparted with completely new functional characteristics, completely different from the characteristics of conventional materials by controlling the composition, size, and shape of nanocrystals [14, 25].

One of the promising methods for producing orthoferrites, which allows improving the above parameters, is the solution combustion method. This method can lead to the synthesis of ferrites with small particle and grain sizes, high density and conversion rates, excellent electromagnetic parameters and a homogeneous microstructure [3, 26–30].

Previously, the features of the formation of orthorhombic and hexagonal holmium orthoferrite during heat treatment (625 – 725 °C for 8 hours) of the products of glycine-nitrate combustion were studied [3]. The photocatalytic activity of orthorhombic HoFeO<sub>3</sub> nanocrystals was studied in the process of photoinduced decomposition of methyl

orange in an aqueous solution under irradiation with visible light. Compared to this method, the sol-gel synthesis is simpler and therefore it is often more preferable. In prior research for the synthesis of holmium ferrite from a solution, absolute ethanol was used as the solvent [31]. However, for the production of a sufficiently large number of nanocrystals in large laboratories or research institutes, synthesis from an aqueous solution is more preferable for the following reasons. 1. Profitability. 2. Safety. There is no danger of ignition of vapors. 3. Possibility of changing the characteristics of absolute ethanol under the influence of the external environment.

Analysis of the literature data showed the feasibility of the synthesis of holmium ferrite by the sol-gel method. Based on these data, the goal of this study was the synthesis of  $\text{HoFeO}_3$  nanocrystals from an aqueous solution using the sol-gel method with the participation of PVA, to characterize them, to determine their magnetic characteristics and the band gap of the obtained nanocrystals, to compare the achieved results with results of other synthesis methods and properties of analogue materials.

## 2. Experimental

The starting materials for the synthesis of the target object were the following reagents: iron (III) nitrate nonahydrate  $\text{Fe}(\text{NO}_3)_3 \cdot 9\text{H}_2\text{O}$ , holmium nitrate pentahydrate  $\text{Ho}(\text{NO}_3)_3 \cdot 5\text{H}_2\text{O}$ , aqueous ammonia solution  $\text{NH}_3 \cdot \text{H}_2\text{O}$  (all – “chemically pure”), PVA – polyvinyl alcohol  $[-\text{CH}_2-\text{CH}(\text{OH})-]_n$  (GOST 10779-78), acting as a stabilizer-PVA, and distilled water.

Nanocrystalline holmium ferrite was synthesized from an equimolar mixture of holmium (III) and iron (III) nitrates of chemically pure grade in the presence of polyvinyl alcohol (56672 g/mol,  $n = 1288$ ) in an aqueous solution according to the following procedure.

The mixture of 0.05 mol/L  $\text{Fe}(\text{NO}_3)_3$  and  $\text{Ho}(\text{NO}_3)_3$  (30 ml) was added to 70 ml of boiling distilled water with stirring on a magnetic stirrer. After the addition of salts, magnetic stirring was continued for another 10 min at a temperature above 90 °C. Then, to 200 ml of a boiling solution containing polyvinyl alcohol, 100 ml of the resulting mixture was slowly added with stirring; the ratio of polyvinyl alcohol – sum of metal ions was 1: 3 by weight [32,33]. Over time, the resulting system became concentrated due to water evaporation and stirring was continued with a glass stirring rod until a yellow-brown powder formed.

Thermogravimetric analysis of the powders was carried out using a TGA-DSC thermal analyzer, LabsysEvo 1600 °C (dry air, high purity, 99.99 %; 10 deg/min). The phase composition of the samples was determined by X-ray phase analysis (XRD, D8-Advance diffractometer) with  $\text{CuK}\alpha$  radiation. The obtained diffraction patterns were analyzed using the JCPDS database [34]. Parameters  $a$ ,  $b$ ,  $c$  and crystal cell volume  $V$  were determined from the raw file data using the X'pert High Score Plus 2.2b program.

The size of holmium ferrite crystallites according to X-ray diffraction data was determined based on the analysis of the broadening of three maximum lines using the Scherrer formula [35].

The main method for controlling the size and shape of particles was electron microscopy: high-voltage transmission (TEM; JEM-1400) and scanning microscopy (SEM, S-4800).

The elemental composition of the product was monitored by local X-ray spectral microscopy (EDX, Horiba H-7593).

For measurement of the magnetic properties (specific magnetisation and coercive force, excess magnetisation), a VSM Microsene EV11 magnetometer with a vibrating sample was used.

## 3. Results and discussions

A comprehensive thermal analysis of a holmium ferrite sample obtained by the sol-gel method in the presence of polyvinyl alcohol (Fig. 1a) showed that the weight loss of the sample was 60.47 wt%, which is explained by the evaporation of water and the decomposition of organometallic compounds between  $\text{Ho}^{3+}$ ,  $\text{Fe}^{3+}$  cations and polyvinyl alcohol, as well as the decomposition of nitrates. A similar situation was observed for lanthanum orthoferrite in the study [20]. A fast and regular weight loss was observed in the range from 50 to ~ 400 °C, and at a higher temperature the sample weight decreased more slowly (about 5.6 %). The processes of decomposition-heating of organometallic compounds under the action of atmospheric oxygen and oxygen formed during the decomposition of nitrates, with the formation of holmium (III) and iron (III) oxides, are accompanied by a number of exothermic effects at 162.21, 216.27, 339.52, 581.69 and 652.36 °C; this can be used for the production of  $\text{HoFeO}_3$  nanoparticles by the method of gel combustion as described, for example, in studies [20, 32, 33]. The endothermic effect at 90.82 °C was due to the evaporation of water contained in the sample due to its storage in air.

XRD results show that holmium ferrite samples (Fig. 2) after annealing at 650, 750, and 850 °C for 60 min are single-phase products, all peaks correspond to the reference diffractogram of  $\text{HoFeO}_3$  with an orthorhombic structure (map number 046-0115) [34]. With an increase in the annealing temperature from 650 to 750 °C, the intensity of

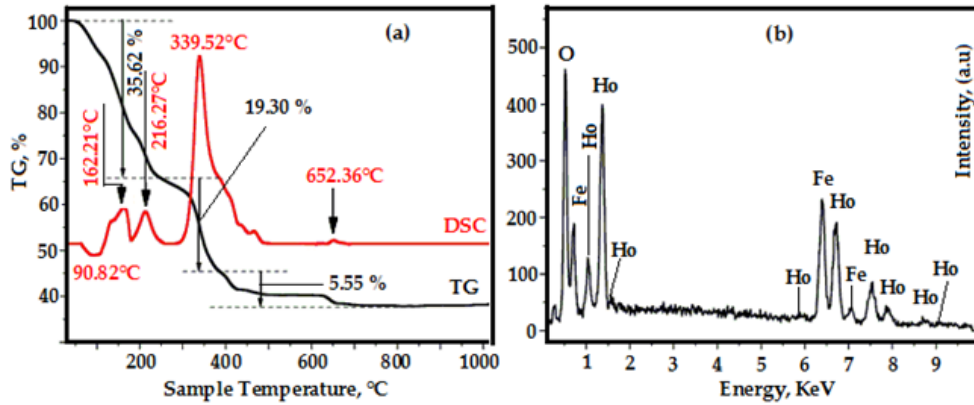


FIG. 1. TGA/DSC curves of the powders prepared by sol-gel technique using PVA (a) and Energy-Dispersive X-ray spectroscopy (EDX) of  $\text{HoFeO}_3$  nanoparticles annealed at  $750\text{ }^\circ\text{C}$  for 1 h (b)

crystallization of holmium ferrite samples increases, and after annealing the samples in the range  $750 - 850\text{ }^\circ\text{C}$ , it did not change. According to the results of local X-ray spectral microscopy, the composition of  $\text{HoFeO}_3$  after annealing at  $750\text{ }^\circ\text{C}$  for 1 h consisted of only three elements – Ho, Fe, and O, i.e. impurity components were not revealed (Fig. 1b). The atomic ratio  $\text{Ho}:\text{Fe} = 1:1.01$ , which, within the within the measurement accuracy corresponds to their specified nominal composition.

The broadening of X-ray diffraction lines was used to determine the average size of crystallites (regions of coherent scattering) by the Scherrer formula [35]; the results are presented in Table 1. Based on these calculations, we can conclude that the crystallite size does not exceed 30 nm for  $\text{HoFeO}_3$ . The calculation of the unit cell parameters from the diffractometry data showed that an increase in the annealing temperature led to a slight increase in the unit cell volume (Table 1), which was also observed in studies [36,37]. As shown in the study [36], a reliable estimate of the crystallite size from the broadening of diffraction peaks is possible only in combination with additional structural data, for example, with the results of electron microscopy.

TABLE 1. Unit cell parameters and average size of  $\text{HoFeO}_3$  crystals synthesized from an aqueous solution in the presence of PVA after annealing at different temperatures for 60 min

$t, \text{ }^\circ\text{C}$	$d, \text{ nm}$	$a, \text{ \AA}$	$b, \text{ \AA}$	$c, \text{ \AA}$	$V, \text{ \AA}^3$
650	24	5.2819	5.5801	7.6151	224.444
750	28	5.2824	5.5846	7.6085	224.451
850	30	5.2825	5.5785	7.6239	224.664

SEM, TEM images, and a histogram of the particle size distribution of  $\text{HoFeO}_3$  nanopowders synthesized by the sol-gel method from an aqueous solution in the presence of PVA after annealing at  $750\text{ }^\circ\text{C}$  for 60 min are shown in Fig. 3. SEM and TEM images showed that the holmium ferrite particles have different shapes: approximately round with a weakly expressed faceting and oval. The diameter of most crystallites (about 80 % of the number of particles) of the presented orthoferrite was in the range of 31 – 40 nm (TEM). In addition, some particles exhibited a shape characteristic of agglomerates, which complicated accurate determination of the size of crystallites and led to a wide distribution of nanoparticles by size.

The process of formation of agglomerates can be caused by the intergrowth of crystallites, including oriented intergrowth, in the process of nucleation and growth of nuclei, as was shown, for example, in studies [38–40] as well as the sintering of nanoparticles during annealing.

Differences in the values of the average diameter according to the Scherrer formula and according to the SEM and TEM data were due to the peculiarities of the methods: the first method allows the determination of the average crystal size in the entire sample, and electron microscopy provides information on a small sample of particles, the dispersed composition of which depends on the sample preparation procedure [42]. In addition, it is not always possible to distinguish between a crystallite and a particle consisting of intergrown crystallites from a micrograph.

Absorption spectrum of  $\text{HoFeO}_3$  nanoparticles after annealing at  $750\text{ }^\circ\text{C}$  for 1 h in UV light showed strong absorption in the region of ultraviolet and visible light ( $\sim 300 - 600\text{ nm}$ ) (Fig. 4a). This is interesting since  $\text{HoFeO}_3$

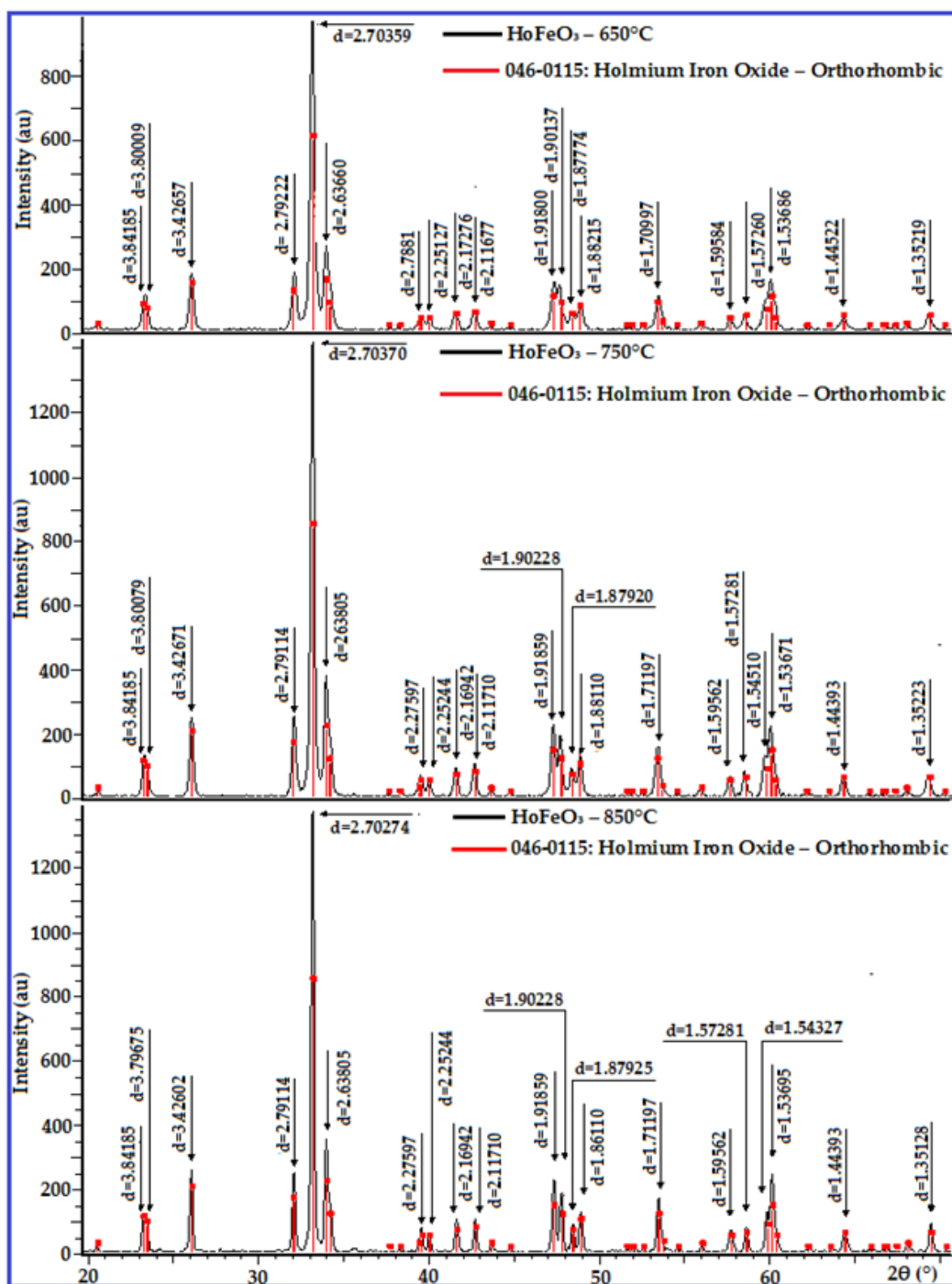


FIG. 2. XRD patterns of HoFeO<sub>3</sub> nanopowders annealed at 650, 750, and 850 °C for 1 h

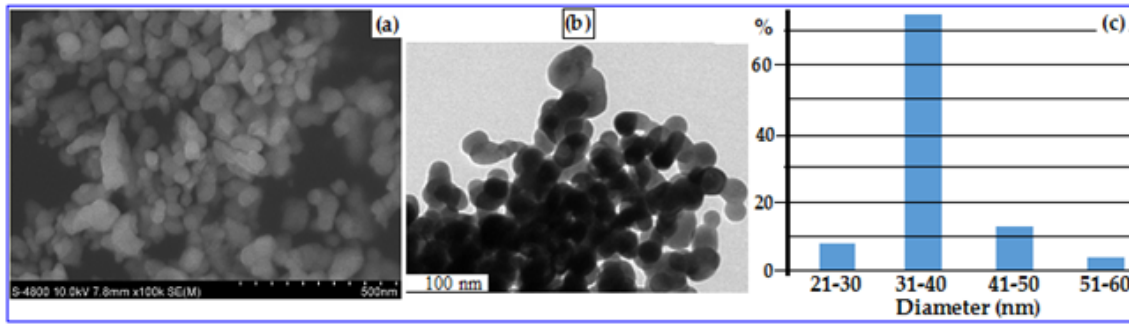


FIG. 3. SEM (a), TEM (b) images and particle size distribution histogram of  $\text{HoFeO}_3$  powders annealed at  $750^\circ\text{C}$  for 1 h

can be used as a new visible light photocatalyst. Results of determining the photocatalytic activity of the synthesized  $\text{HoFeO}_3$  nanocrystals are shown in Fig. 4a. The energy of direct transitions for the band gap was determined by fitting the absorption data to the direct transition, and is presented in the study [36]. As a consequence, the band gap of  $\text{HoFeO}_3$  nanoparticles is  $\sim 1.80$  eV (Fig. 4b). Such a small band gap is interesting for the potential application of  $\text{HoFeO}_3$  in photocatalysis, sensor and electrode materials in solid oxide fuel cells.

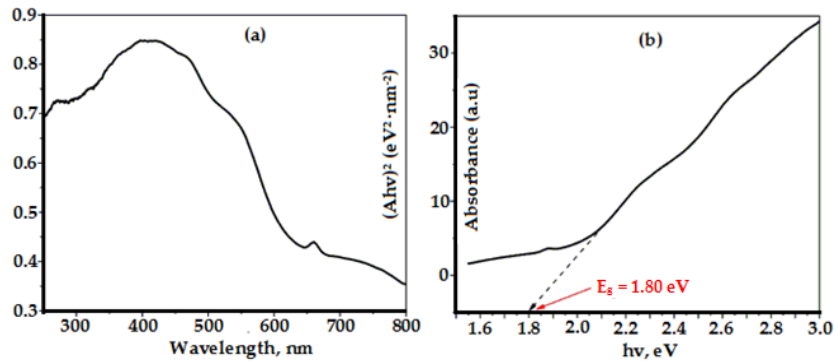


FIG. 4. (a) Room temperature optical absorbance spectrum of the  $\text{HoFeO}_3$  sample annealed at  $750^\circ\text{C}$ , (b) Plot of  $(Ah\nu)^2$  as a function of photon energy for  $\text{HoFeO}_3$  nanoparticles

Results of determining the field dependences of the magnetization of a holmium ferrite sample annealed at  $750^\circ\text{C}$ , measured at 300 K in a field of 5000 Oe, are presented in Fig. 5a. Nanoparticles  $\text{HoFeO}_3$ , obtained by the sol-gel method from an aqueous solution in the presence of PVA, are characterised at the selected annealing temperature by low values of remnant magnetization ( $M_r = 0.0044$  emu/g) and coercive force ( $H_c = 25.14$  Oe), with high value of the specific magnetization ( $M_s = 0.73$  emu/g) and a narrow hysteresis loop (Fig. 5b) and they did not reach magnetic saturation in a field of 5000 Oe. Thus, the synthesized object is paramagnetic.

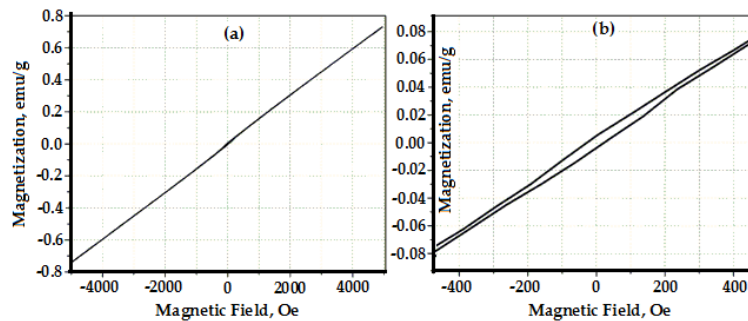


FIG. 5. MH curves at  $\pm 5$  kOe measured at RT of the  $\text{HoFeO}_3$  sample annealed at  $750^\circ\text{C}$  for 1 h

A comparison of the magnetic characteristics of holmium ferrite nanocrystals synthesized in this study from an aqueous solution using PVA is presented in Table 2. As can be seen from the Table 2, these characteristics are not

significantly different from characteristics of the samples synthesised in absolute ethanol [31] and strongly depend on the synthesis method [1, 42]. Interestingly, the synthesized nanocrystalline  $\text{HoFeO}_3$  characterized by lower values of  $H_c$ , but higher  $M_s$  compared with nanoparticles of orthoferrites of other rare earth elements such as  $\text{YFeO}_3$ ,  $\text{NdFeO}_3$  obtained by coprecipitation [20, 43], and  $\text{LaFeO}_3$  synthesized by the ceramic method [44].

TABLE 2. Magnetic characteristics of  $\text{HoFeO}_3$  nanoparticles in this study and from the literature as a comparison

Objects	Coercive force ( $H_c$ ), Oe	Remnant magnetization ( $M_r$ ), emu/g	Saturation magnetization ( $M_s$ ), emu/g
$\text{HoFeO}_3$ in this study	25.14	$4.4 \cdot 10^{-3}$	0.73
$\text{HoFeO}_3$ [31]	$8.19 \div 22.70$	$1.3 \cdot 10^{-3} \div 4.3 \cdot 10^{-3}$	$0.71 \div 0.79$
$\text{HoFeO}_3$ [1]	2959	$40.8 \cdot 10^{-1}$	2.55
$\text{HoFeO}_3$ [42]	461.13	$6.05 \cdot 10^{-2}$	—
$\text{YFeO}_3$ [20]	53.36	$0.19 \cdot 10^{-3}$	0.39
$\text{NdFeO}_3$ [43]	136.76	$68.0 \cdot 10^{-2}$	0.80
$\text{LaFeO}_3$ [44]	1217.6	$5.43 \cdot 10^{-4}$	$6.49 \cdot 10^{-3}$

#### 4. Conclusion

Based on the analysis of the data obtained, it can be concluded that the proposed synthesis procedure leads to the formation of a single-phase nanocrystalline orthoferrite  $\text{HoFeO}_3$  with an average crystallite size of about 30 nm. Changing the solvent from absolute ethanol to water with the addition of PVA did not adversely affect the properties of the final product, but it is preferable due to the higher cost effectiveness, safety, and stability of the solvent properties. Synthesized  $\text{HoFeO}_3$  nanopowders were characterized by a low band gap, demonstrating the properties of a paramagnetic material, therefore, it is potentially possible to use them not only in photocatalysis, but also as magnetic materials.

#### Conflict of interests

The authors maintain that they have no conflict of interest with respect to this communication.

#### Acknowledgements

Nguyen Anh Tien is grateful for the financial support of Ho Chi Minh City University of Education, Ho Chi Minh City, Vietnam, through Grant No. CS.2020.19.21.

#### References

- [1] Habib Z., Majid K., et al. Influence of Ni substitution at B-site for  $\text{Fe}^{3+}$  ions on morphological, optical, and magnetic properties of  $\text{HoFeO}_3$  ceramics. *Applied Physics A: Materials Science & Processing*, 2016, **122** (5), P. 550–557.
- [2] Shao M., Cao Sh., et al. Single crystal growth, magnetic properties and Schottky anomaly of  $\text{HoFeO}_3$  orthoferrite. *Journal of Crystal Growth*, 2011, **318** (1), P. 947–950.
- [3] Kondrashkova I.S., Martinson K.D., Zakharova N.V., Popkov V.I. Synthesis of nanocrystalline  $\text{HoFeO}_3$  photocatalyst via heat treatment of products of glycine-nitrate combustion. *Russian Journal of General Chemistry*, 2018, **88** (12), P. 2465–2471.
- [4] Martinson K.D., Kondrashkova I.S., et al. Magnetically recoverable catalyst based on porous nanocrystalline  $\text{HoFeO}_3$  for processes of n-hexane conversion. *Advanced Powder Technology*, 2020, **31** (1), P. 402–408.
- [5] Mushtaq M.W., Imran M., et al. Synthesis, structural and biological studies of cobalt ferrite nanoparticles. *Bulgarian Chemical Communications*, 2016, **48** (3), P. 565–570.
- [6] Nikiforov V.N., Filinova E.Yu. Biomedical applications of the magnetic nanoparticles. In book: *Magnetic Nanoparticles*, Wiley-VCH Verlag GmbH & CO. KGaA, Weinheim, 2009, **10**, P. 393–455.
- [7] Gu H., Xu K., Xu C., Xu B. Biofunctional magnetic nanoparticles for protein separation and pathogen detection. *Chemical Communications*, 2006, **37** (9), P. 941–949.
- [8] Albadi Y., Popkov V.I. Dual-modal contrast agent for magnetic resonance imaging based on gadolinium orthoferrite nanoparticles: synthesis, structure and application prospects. *Medicine: theory and practice*, 2019, **4** (S), P. 35–36.
- [9] Albadi Y., Martinson K.D., et al. Synthesis of  $\text{GdFeO}_3$  nanoparticles via low-temperature reverse co-precipitation: the effect of strong agglomeration on the magnetic behavior. *Nanosystems: Physics, Chemistry, Mathematics*, 2020, **11** (2), P. 252–259.
- [10] Zhou Zh., Guo L., et al. Hydrothermal synthesis and magnetic properties of multiferroic rare-earth orthoferrites, *Journal of Alloys and Compounds*, 2014, **583**, P. 21–31.

- [11] Park T., Papaefthymiou G.C., et al. Size-dependent magnetic properties of single-crystalline multiferroic BiFeO<sub>3</sub> nanoparticles. *Nano Letters*, 2007, **7** (3), P. 766–772.
- [12] Lomanova N.A., Tomkovich M.V., et al. Magnetic properties of Bi<sub>1-x</sub>Ca<sub>x</sub>FeO<sub>3-δ</sub> nanocrystals. *Physics of the Solid State*, 2019, **61**, P. 2535–2541.
- [13] Martinson K.D., Ivanov V.A., et al. Facile combustion synthesis of TbFeO<sub>3</sub> nanocrystals with hexagonal and orthorhombic structure. *Nanosystems: Physics, Chemistry, Mathematics*, 2019, **10** (6), P. 694–700.
- [14] Kovalenko A.N., Tugova E.A. Thermodynamics and kinetics of non-autonomous phases formation in nanostructured materials with variable functional properties. *Nanosystems: Physics, Chemistry, Mathematics*, 2018, **9** (5), P. 641–662.
- [15] Popkov V.I., Almjasheva O.V., et al. Magnetic properties of YFeO<sub>3</sub> nanocrystals obtained by different soft-chemical methods. *Journal of Materials Science: Materials in Electronics*, 2017, **28** (10), P. 7163–7170.
- [16] Lomanova N.A., Tomkovich M.V., et al. Thermal and magnetic behavior of BiFeO<sub>3</sub> nanoparticles prepared by glycine-nitrate combustion. *Journal of Nanoparticle Research*, 2018, **20** (2).
- [17] Dmitriev A.V., Vladimirova E.V., et al. Synthesis of hollow spheres of BiFeO<sub>3</sub> from nitrate solutions with tartaric acid: Morphology and magnetic properties. *Journal of Alloys and Compounds*, 2019, **77** (10), P. 586–592.
- [18] Tomina E.V., Kurkin N.A., Mal'tsev S.A. Microwave synthesis of yttrium orthoferrite doped with nickel. *Condensed Matter and Interphases*, 2019, **21** (2), P. 306–312.
- [19] Almjasheva O.V., Krasilin A.A., Gusarov V.V. Formation mechanism of core-shell nanocrystals obtained via dehydration of coprecipitated hydroxides at hydrothermal conditions. *Nanosystems: Physics, Chemistry, Mathematics*, 2018, **9** (4), P. 568–572.
- [20] Nguyen T.A., Almjasheva O.V., et al. Synthesis and magnetic properties of YFeO<sub>3</sub> nanocrystals. *Inorganic Materials*, 2009, **45** (11), P. 1304–1308.
- [21] Popkov V.I., Almyasheva O.V., Schmidt M.P., Gusarov V.V. Formation mechanism of nanocrystalline yttrium orthoferrite under heat treatment of the coprecipitated hydroxides. *Russian Journal of General Chemistry*, 2015, **85** (6), P. 1370–1375.
- [22] Nguyen T.A., Mittova I.Ya., et al. Sol-gel preparation and magnetic properties of nanocrystalline lanthanum ferrite. *Russian Journal of General Chemistry*, 2014, **84** (7), P. 1261–1264.
- [23] Proskurina O.V., Abiev R.S., et al. Formation of nanocrystalline BiFeO<sub>3</sub> during heat treatment of hydroxides co-precipitated in an impinging-jets microreactor. *Chemical Engineering and Processing – Process Intensification*, 2019, **143**, 107598.
- [24] Proskurina O.V., Nogovitsin I.V., et al. Formation of BiFeO<sub>3</sub> Nanoparticles Using Impinging Jets Microreactor. *Russian Journal of General Chemistry*, 2018, **88** (10), P. 2139–2143.
- [25] Gusarov V.V., Almjasheva O.V. *Nanomaterials: properties and promising applications*. Scientific world publishing house, Moscow, 2014, P. 378–403.
- [26] Martinson K.D., Kondrashkova I.S., Popkov V.I. Synthesis of EuFeO<sub>3</sub> nanocrystals by glycine-nitrate combustion method. *Russian Journal of Applied Chemistry*, 2017, **90** (8), P. 1214–1218.
- [27] Bachina A., Ivanov V.A., Popkov V.I. Peculiarities of LaFeO<sub>3</sub> nanocrystals formation via glycine-nitrate. *Nanosystems: Physics, Chemistry, Mathematics*, 2017, **8** (5), P. 647–653.
- [28] Popkov V.I., Almjasheva O.V., et al. Crystallization behaviour and morphological features of YFeO<sub>3</sub> nanocrystallites obtained by glycine-nitrate combustion. *Nanosystems: Physics, Chemistry, Mathematics*, 2015, **6** (6), P. 866–874.
- [29] Popkov V.I., Almjasheva O.V., et al. Effect of spatial constraints on the phase evolution of YFeO<sub>3</sub>-based nanopowders under heat treatment of glycine-nitrate combustion products. *Ceramics International*, 2018, **44** (17), P. 20906–20912.
- [30] Lomanova N.A., Tomkovich M.V., Sokolov V.V., Gusarov V.V. Special Features of Formation of Nanocrystalline BiFeO<sub>3</sub> via the Glycine-Nitrate Combustion Method. *Russian Journal of General Chemistry*, 2016, **86** (10), P. 2256–2262.
- [31] Nguyen T.A., Nguyen T.Tr.L., et al. Optical and magnetic properties of HoFeO<sub>3</sub> nanocrystals prepared by a simple co-precipitation method using ethanol. *Journal of Alloys and Compounds*, 2020, **834**, P. 155098–155103.
- [32] Jiang L., Liu W., et al. Low-temperature combustion synthesis of nanocrystalline powders via a sol-gel method using glycine. *Ceramics International*, 2012, **38** (5), P. 3667–3672.
- [33] Luu M.D., Dao N.N., et al. Sol-gel synthesis of LaFeO<sub>3</sub> nanomaterials with perovskite structure. *Vietnam Journal of Chemistry*, 2014, **52** (1), P. 130–134.
- [34] JCPDS PCPDFWIN: A Windows Retrieval/Display Program for Accessing the ICDD PDF-2 File, ICDD, 1997.
- [35] Patterson A.L. The Scherrer formula for X-ray particle size determination. *Physics Review*, 1939, **56** (10), P. 978–982.
- [36] Nguyen T.A., Chau H.D., et al. Structural and magnetic properties of YFe<sub>1-x</sub>Co<sub>x</sub>O<sub>3</sub> (0.1 ≤ x ≤ 0.5) perovskite nanomaterials synthesized by co-precipitation method. *Nanosystems: Physics, Chemistry, Mathematics*, 2018, **9** (3), P. 424–429.
- [37] Nguyen T.A., Nguyen V.Y., et al. Synthesis and magnetic properties of PrFeO<sub>3</sub> nanopowders by the co-precipitation method using ethanol. *Nanosystems: Physics, Chemistry, Mathematics*, 2020, **11** (4), P. 468–473.
- [38] Ivanov V.K., Fedorov P.P., Baranchikov A.Y., Osiko V.V. Oriented aggregation of particles: 100 years of investigations of non-classical crystal growth. *Chemical Reviews*, 2014, **83** (12), P. 1204–1222.
- [39] Popkov V.I., Tugova E.A., Bachina A.K., Almyasheva O.V. The formation of nanocrystalline orthoferrites of rare-earth elements XFeO<sub>3</sub> (X = Y, La, Gd) via heat treatment of coprecipitated hydroxides. *Journal of General Chemistry*, 2017, **87** (11), P. 2516–2524.
- [40] Almjasheva O.V., Gusarov V.V. Metastable Clusters and Aggregative Nucleation Mechanism. *Nanosystems: Physics, Chemistry, Mathematics*, 2014, **5** (3), P. 405–416.
- [41] Almjasheva O.V., Fedorov B.A., Smirnov A.V., Gusarov V.V. Size, morphology and structure of the particles of zirconia nanopowder obtained under hydrothermal conditions. *Nanosystems: Physics, Chemistry, Mathematics*, 2010, **1** (1), P. 26–37.
- [42] Bhat M., Kaur B., et al. Swift heavy ion irradiation effects on structural and magnetic characteristics of RFeO<sub>3</sub> (R = Er, Ho and Y) crystals. *Nuclear Instruments and Methods in Physics Research B*, 2006, **243**, P. 134–142.
- [43] Nguyen T.A., Pham V., et al. Simple synthesis of NdFeO<sub>3</sub> nanoparticles by the so-precipitation method based on a study of thermal behaviors of Fe (III) and Nd (III) hydroxides. *Crystals*, 2020, **10** (3), P. 219–227.
- [44] Sasikala C., Durairaj N., et al. Transition metal titanium (Ti) doped LaFeO<sub>3</sub> nanoparticles for enhanced optical structure and magnetic properties. *Journal of Alloys and Compounds*, 2017, **712**, P. 870–877.

## Formation of nanocrystals based on equimolar mixture of lanthanum and yttrium orthophosphates under microwave-assisted hydrothermal synthesis

M. O. Enikeeva<sup>1,2</sup>, O. V. Proskurina<sup>1,2</sup>, D. P. Danilovich<sup>2</sup>, V. V. Gusarov<sup>1</sup>

<sup>1</sup>Saint Petersburg State Institute of Technology, Moskovsky Pr., 26, Saint Petersburg, 190013, Russia

<sup>2</sup>Ioffe Institute, Politekhnickeskaya St. 26, Saint Petersburg, 194021, Russia

odin2tri45678@gmail.com, proskurinaov@mail.ru, dmitrydanilovich@gmail.com, victor.v.gusarov@gmail.com

DOI 10.17586/2220-8054-2020-11-6-705-715

The effect of hydrothermal-microwave treatment time at 180 °C on the phase composition, dimensional parameters of crystallites and nanoparticles of solid solutions of lanthanum and yttrium orthophosphates in the system  $0.53\text{LaPO}_4-0.47\text{YPO}_4-(n\text{H}_2\text{O})$  has been determined. It has been proposed the mechanism for structural transition of lanthanum-yttrium orthophosphate solid solution with rhabdophane structure into monazite structure, which consists in the degeneration of nanocrystals having rhabdophane structure along certain edges into monazite structure. It is shown that phase nanoparticles of monazite structure having average crystallite size of 15–17 nm begin to form after 30 minutes of hydrothermal-microwave treatment at 180 °C immediately after complete crystallization of amorphous phase in the system. The nanoparticle size increase (length of nanorods) with monazite structure after the stage of their formation occurs, mainly due to matter transfer from nanoparticles having rhabdophane structure to nanoparticles having monazite structure. In this case, the system considered conditions of hydrothermal treatment (temperature – 180 °C, pressure  $\sim 1-1.5$  MPa, duration – up to 120 min) remains two-phase.

**Keywords:** nanocrystals, lanthanum and yttrium orthophosphates, monazite, rhabdophane, hydrothermal treatment, microwave heating, phase transition.

*Received: 28 August 2020*

### 1. Introduction

Much attention to the study of formation processes, structure and properties of materials, including nanocrystalline materials, based on orthophosphates of rare earth elements is associated with set of practically important properties that they possess. Ceramic materials based on rare earth element (REE) orthophosphates due to their high strength, thermal stability and resistance to aggressive media are used as high-temperature insulation [1–3]. They have a high isomorphic capacity for large number of lanthanides and actinides [4–7], are resistant to radiation damage [8], which makes them promising as ceramic matrices for radioactive waste immobilization. Among the numerous REE orthophosphates, two- and multicomponent phases [9, 10] are of considerable interest. They have applicability as structural [11] and luminescent materials [12, 13], thermal barrier coatings [14], as proton-conducting electrolyte [15–18]. Lanthanum orthophosphate is used as component of two-phase mixtures with refractory oxides to produce reinforced high-temperature ceramics [19].

A number of papers [20–26] have shown that some properties of materials change significantly in cases when the crystal size is of the nanoscale region. This behavior pattern of nanocrystalline materials also applies to REE orthophosphates [27–31]. In this regard, it is interesting, particularly, to study the processes of phase formation, structural transformations and physicochemical properties of nanocrystalline solid solutions in the system  $\text{LaPO}_4-\text{YPO}_4-(\text{H}_2\text{O})$ . Phase formation and their properties in this system were considered in [5, 32–35], however, the discrepancies in obtained results make it relevant to continue such studies.

To obtain multicomponent nanocrystalline orthophosphates, methods of soft chemistry are successfully applied, such as precipitation [36], sol-gel [37, 38], microreactor synthesis [39], hydrothermal [40–43] and hydrothermal microwave-assisted synthesis [43–45]. Hydrothermal conditions make it possible to obtain nanocrystalline particles with different structures and morphologies by varying the pH, treatment time and temperature of synthesis [9, 10, 46, 47]. One of the advantages for microwave-assisted synthesis is the rapid heating of reaction medium. This feature, along with possibility of sensitive control of temperature and treatment time, is important for studying the kinetics of nanocrystalline particles formation [43].

This paper is aimed at studying processes of formation and structural transformations under microwave-assisted conditions of nanocrystalline solid solutions based on lanthanum-yttrium orthophosphates in the system  $0.5\text{LaPO}_4-0.5\text{YPO}_4-(n\text{H}_2\text{O})$ . The article discusses the effect of isothermal holding time on formation and change in dimensional parameters of nanocrystals of lanthanum-yttrium orthophosphates with rhabdophane and monazite structures.

## 2. Experimental

Nanocrystalline samples of solid solutions of lanthanum-yttrium orthophosphates in the system  $\text{LaPO}_4\text{-YPO}_4\text{-(H}_2\text{O)}$  were synthesized in an Anton Paar Monowave 400 hydrothermal microwave reactor. Equimolar solutions of lanthanum nitrate hexahydrate (C.P.), yttrium nitrate pentahydrate (C.P.) and ammonium dihydrogen phosphate (C.P.) were used as mother substances. The ammonium phosphate solution was added at constant stirring for 10 minutes to water solution of premixed lanthanum and yttrium nitrates with  $\text{pH} = 1$ . The ratio of reagent solutions was selected to ensure the pre-set stoichiometry of products. The resulting suspension was transferred into glass autoclave flask of microwave reactor (the fill factor 0.3). The daughter of reaction was stirred at 600 rpm during the whole treatment time. The reactive atmosphere treated at  $180^\circ\text{C}$  and was recorded inside the autoclave using the ruby thermometer. The pressure into autoclave flask was about 1–1.5 MPa. The reactive atmosphere was heated to pre-set temperature for 1 minute, the isothermal holding time from 5 up to 120 minutes, followed by cooling to  $70^\circ\text{C}$  for 8 minutes. Treatment products were precipitated by centrifugation, washed several times with distilled water, and dried at  $80^\circ\text{C}$ .

The elemental composition of the samples was determined by EDAX attachment for X-ray spectral microanalysis for FEI Quanta 200 scanning electron microscope (SEM) having composition determination error was about 2%.

Powder X-ray diffraction patterns were taken with a Rigaku SmartLab 3 X-ray diffractometer The X-ray ( $\text{Cu}_{K\alpha}$  radiation) within the angle range  $2\theta = 10\text{--}65^\circ\text{C}$  with an  $0.01^\circ\text{C}$  step at a scanning speed  $1^\circ\text{C}/\text{min}$ . Qualitative X-ray diffraction analysis was carried out using the PDF-2 database. The rhabdophane and monazite phase ratio in these samples was calculated according to the peaks that did not overlap in the pahse mixture: the characteristic peak for rhabdophane is (100), and for monazite – (200). The X-ray amorphous phase portion was determined using corundum as the internal standard. The average crystallite sizes, as well as lognormal size distributions, were defined using the SmartLab Studio II software by Rigaku according to the specified reflexes.

Sample micrographs and electron microdiffraction data were obtained using the JEOL JEM-2100F transmission electron microscope at accelerating voltage 200 kV. The images were processed using the ImageJ program. The particle size were determined were determined from the data on approximately 100 separate particles for each sample.

## 3. Results and discussion

Elemental analysis of samples shows that the ratio of elements La:Y is 53:47 ( $\pm 1\text{--}2\%$ ) atm %, the ratio of elements (La + Y): P is 51:49 ( $\pm 2\%$ ) at.%, corresponding within the analysis uncertainty to the ratio set by synthesis  $\text{LaPO}_4 : \text{YPO}_4 = 0.5 : 0.5$ .

The X-ray diffraction data (Fig. 1) show that in as-precipitated sample, before the hydrothermal microwave-assisted treatment, are presented rhabdophane reflexes.

Figure 2 shows data on quantitative phase ratio in the system depending on the isothermal holding time during hydrothermal-microwave treatment at  $180^\circ\text{C}$ . It should be pointed out that the sample contains  $\sim 30\%$  of amorphous phase before the heating treatment.

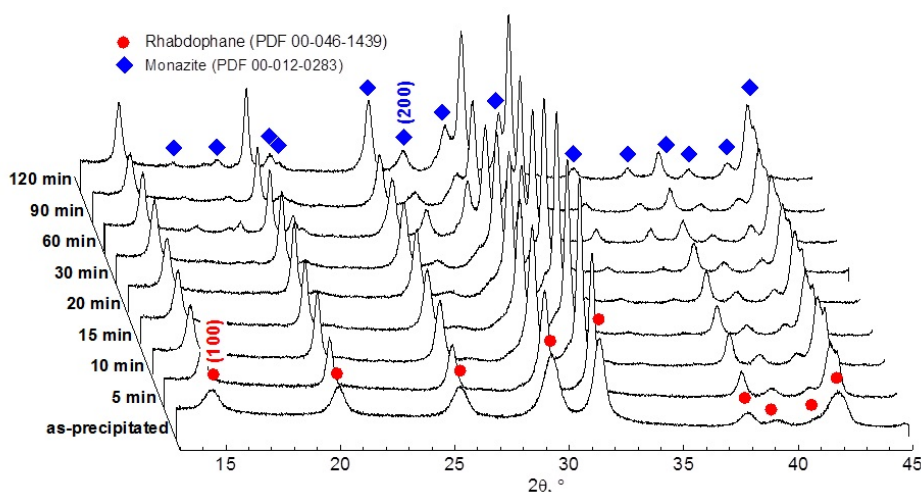


FIG. 1. The X-ray diffraction pattern of samples before and after hydrothermal-microwave treatment at  $180^\circ\text{C}$

After hydrothermal treatment for 20 minutes, the X-ray amorphous phase completely disappears, the sample is contented solely by the phase with rhabdophane structure. Taking into account the lack of other phases and the ratio of elements in the system due to the analysis data –  $0.53\text{LaPO}_4\text{--}0.47\text{YPO}_4\text{--}(n\text{H}_2\text{O})$ , it can be concluded after microwave hydrothermal treatment at  $180\text{ }^\circ\text{C}$  and under a pressure of 1–1.5 MPa for 20 min, the solid solution is formed with the averaged composition  $\text{La}_{0.53}\text{Y}_{0.47}\text{PO}_4(n\text{H}_2\text{O})$ . Isothermal holding under hydrothermal conditions at  $180\text{ }^\circ\text{C}$  for 30 min leads to the occurrence of phase with monazite structure (Fig. 1, 2). It is worth noting that for all samples in the studied system,  $0.5\text{LaPO}_4\text{--}0.5\text{YPO}_4\text{--}(n\text{H}_2\text{O})$  do not complete the transition of the rhabdophane phase into monazite. Phase ratio in samples with isothermal holding from 60 up to 120 min almost does not change (phase with monazite structure): (phase with rhabdophane structure)  $\approx 70: 30 (\pm 5\%) \text{ wt\%}$  (Fig. 2). Thus it is impossible *a priori* to state that the transformation of the solid solution with rhabdophane into monazite structure occurs without composition change. The complexity of determining the elemental composition of individual nanoparticles in two-phase composition does not allow one to answer the question of the phase composition coexisting in the system by their direct elemental analysis. In such cases, the necessary information phase can be given by the correlation between the composition and parameters of the lattice constants.

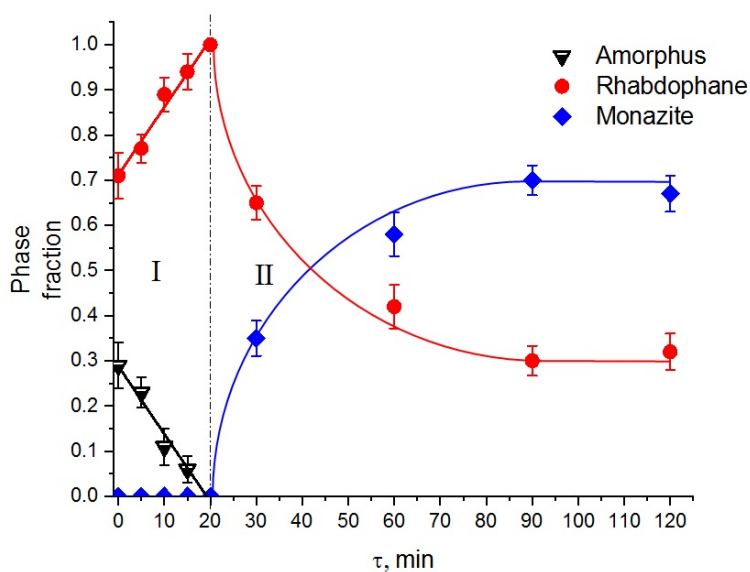


FIG. 2. The phase ratio depending on the isothermal holding time under hydrothermal microwave-assisted conditions at  $180\text{ }^\circ\text{C}$

The available literature data on the of elementary cells volume of solid solutions  $\text{La}_{1-x}\text{Y}_x\text{PO}_4$  with monazite structure and solid solutions  $\text{La}_{1-x}\text{Y}_x\text{PO}_4(n\text{H}_2\text{O})$  with rhabdophane structure are represented in Fig. 3. According to prior research on the dependence of the elementary cell volume of phase with monazite structure on the composition of the  $\text{La}_{1-x}\text{Y}_x\text{PO}_4$  solid solution significantly differ from the data of other papers, further analysis was carried out without taking into account the results of this paper [35]. The data of this work on the elementary cell volume of monazite structure led us to conclude that the composition of the solid solution corresponds to the values  $x \approx 0.25\text{--}0.28$ . The hydrothermal treatment time increase results in slight increase values  $x$  – from  $\sim 0.25$  to  $0.28$ . It is much more difficult to draw any quantitative conclusions about the lanthanum and yttrium ratio change in the solid solution with rhabdophane structure during the structural transformation process, since the unit cell volume of phase with rhabdophane structure depends upon, to a large extent, the water content in the structure. Particularly, this is reflected in large fluctuations in the volume of the unit cell, in depending on the synthesis conditions (Fig. 3). However, the data from this research shows that that with an increase in the duration of hydrothermal treatment, the unit cell volume of the solid solution with a rhabdophane structure systematically and significantly decrease (Fig. 3), as may be a consequence of an increase in the content of yttrium orthophosphate in it. Overall it compensates for the precipitation of the solid solution with a monazite structure enriched with lanthanum orthophosphate in comparison with the initial composition of the system. In such a way, the analysis carried out allows one to conclude the transition of the solid solution  $\text{La}_{1-x}\text{Y}_x\text{PO}_4(n\text{H}_2\text{O})$  the rhabdophane structure into monazite structure leads to a phase composition change. There can be an explanation for the simultaneous coexistence in two systems of phases observed in this experiment, that is to say, under hydrothermal conditions at the temperature of  $180\text{ }^\circ\text{C}$  and a pressure of  $\sim 1\text{--}1.5\text{ MPa}$  in the  $\text{LaPO}_4\text{--YPO}_4\text{--}(\text{H}_2\text{O})$  system in the range of  $\text{LaPO}_4:\text{YPO}_4 = 0.53:0.47$ . There exists a solid solution with a monazite structure

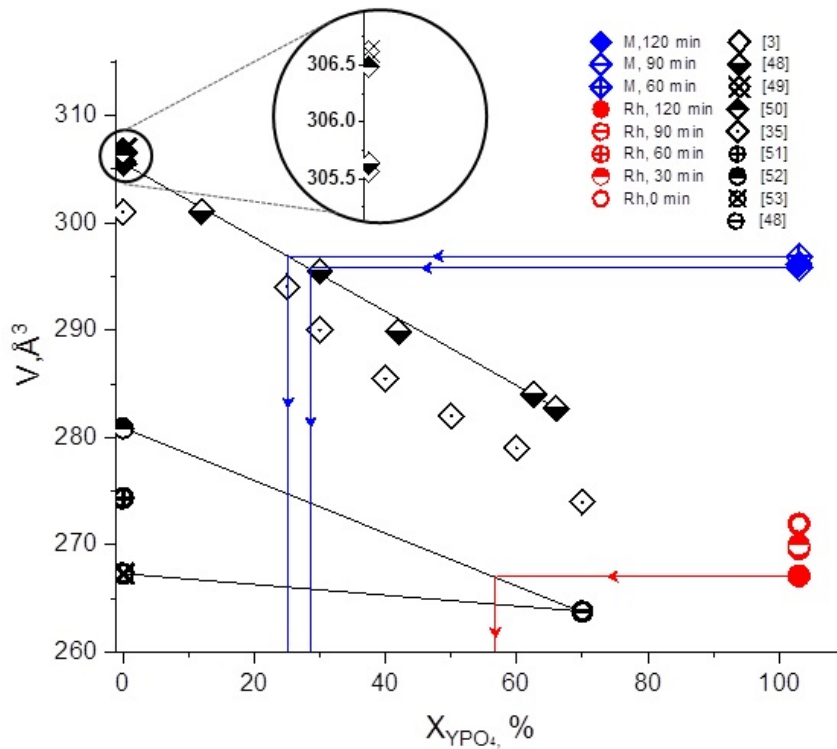


FIG. 3. Unit cell volume of phases of variable composition with the structure of rhabdophane and monazite

of the composition  $\text{La}_{1-x}\text{Y}_x\text{PO}_4$ , where  $x \approx 0.25\text{--}0.28$ , and another solid solution with the structure of rhabdophane  $\text{La}_{1-y}\text{Y}_y\text{PO}_4 (n\text{H}_2\text{O})$ , where  $y > 0.47$  ( $\sim 0.57$ ).

The dependence of crystallite sizes of solid solutions of lanthanum-yttrium orthophosphates with rhabdophane and monazite structure, determined from non-overlapping reflections (100) and (200), respectively, on the isothermal holding time is shown in Fig. 4. The size distribution of crystallites determined from the same reflexes is shown in Fig. 5. From the analysis of the data presented in Fig. 4, it follows that with an increase holding time from 0 to 20 minutes, the average crystallite size of solid solutions with rhabdophane structure increases from  $\sim 10$  to  $\sim 22$  nm.

The size distribution of crystallites of the solid solution with rhabdophane structure for sample with the isothermal holding for 20 minutes becomes wider (Fig. 5). The existence of the solid solution of lanthanum-yttrium orthophosphate with monazite structure in the sample after 30 minutes leads to the narrow size distribution (Fig. 5) with the subsequent growth of crystallites to 26 nm (and distribution width) for sample with isothermal holding for 120 minutes, which is consistent with the data [43].

Crystallites of solid solutions of lanthanum-yttrium orthophosphates with monazite structure, formed after 30 min of isothermal holding, have the average size of about 14 nm, and for longer period, the average crystallite size, determined by the (200) reflection, stabilizes at level of  $\sim 18$  nm (Fig. 4). Size distribution of crystallites of solid solution with monazite structure as the isothermal holding time increases from 60 to 120 minutes does not undergo any significant changes (Fig. 5). However, it should be noted that these results were formulated based on the X-ray data for only one non-overlapping reflex (200).

TEM data analysis shows that the particles of the solid solution of lanthanum-yttrium orthophosphate with rhabdophane structure within the occurrence of single crystalline phase (after hydrothermal treatment for 20 minutes) have characteristic shape of short rods with average thickness of 20–30 nm and length range of  $\sim 25\text{--}100$  nm (Fig. 6a). Rhabdophane nanoparticles of the same morphology also can be found in TEM images of samples after hydrothermal treatment with isothermal holding at 30 and 120 minute (Fig. 6c,e), even if, the monazite phase appears in significant quantities according to X-ray diffraction data. At the same time, in the samples after hydrothermal treatment at 30 and 120 minutes, when the monazite phase is present, there occurs in the samples (Fig. 1,2), long and thin nanorods which are clearly visible, which can be reliably correlated with the monazite phase structure according by electron

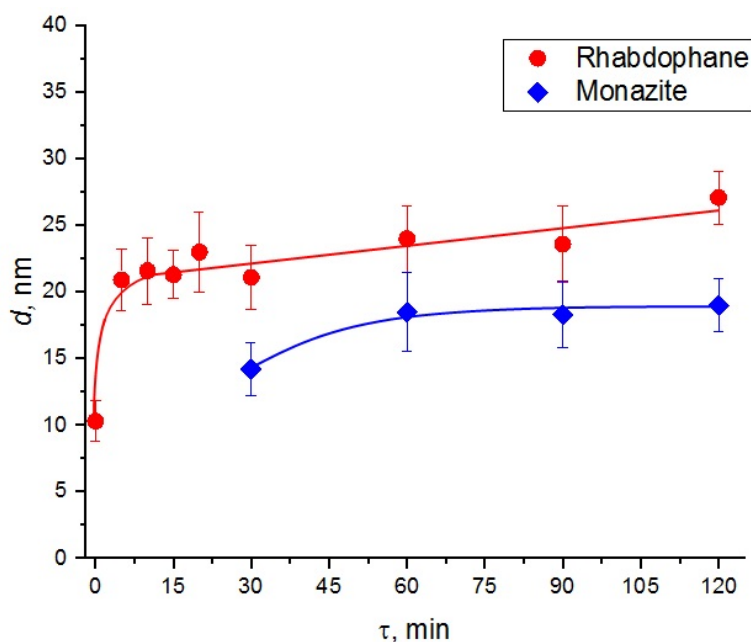


FIG. 4. Average crystallite size (according to reflex (100) – rhabdophane structure, and according to reflex (200) – monazite structure)

microdiffraction data. Fig. 6b,d,f show interplanar distances corresponding to phases with rhabdophane and monazite structures, as well as electron microdiffraction data, showing available crystalline phases with rhabdophane and monazite structures in the samples.

The size distribution of nanorod thickness and length is shown in Fig. 7. The determination of each particle belonging to the phases with rhabdophane and monazite was made according to their morphological features.

A bimodal type of thickness distribution of nanoparticles with rhabdophane structure phase for the sample after microwave-assisted treatment with isothermal holding at 180 °C for 20 minutes to a certain extent agrees with unusually wide crystallite size distribution data for this sample, which is not typical for other samples (Fig. 5). Apparently, the distribution of crystallites in this sample also has bimodal character, which cannot be determined within the framework of the existing possibilities of analyzing X-ray diffraction lines, based on the assumption about lognormal shape of the crystallite size distribution curve. It should be noted that the average thickness sizes of nanoparticles of this sample and the corresponding sizes of crystallites, determined from the reflection (100), are pretty close to each other. This allows us to conclude that nanorods of solid solutions of lanthanum-yttrium orthophosphate with rhabdophane structure at the stage of their formation are mainly represented by single-crystal particles. The bimodal size distribution of thickness of particles with rhabdophane structure for the sample after 20 minutes under hydrothermal conditions may be associated with the different nature of their formation when mixing reagents at room temperature and during the amorphous phase crystallization under hydrothermal conditions. Nanoparticles with rhabdophane structure having greater thickness remain in the sample after hydrothermal treatment for 30 minutes, while thinner particles are transformed into particles with monazite structure. After transformation of some particles with rhabdophane structure into monazite structure – after 30 min of isothermal holding, the rhabdophane particle thickness distribution becomes unimodal (Fig. 7c), which correlates with the crystallite size distribution narrowing data for this sample (Fig. 5). The average length of particles with rhabdophane structure more than doubles during the hydrothermal treatment process: from ~37 to ~83 nm. The occurrence in the sample after prolonged hydrothermal treatment (120 minutes) of wide, close to uniform thickness distribution of particles with rhabdophane structure at interval of particle size variation of ~20–55 nm can be associated with coalescence of particles of solid solutions of lanthanum-yttrium orthophosphates, for example, by the aggregation-accommodation mechanism [48]. It should be noted that coalescence of nanorods with rhabdophane structure in fluent media is characteristic for these nanoparticles [39]. This pattern of nanoparticle thickness increasing is confirmed by comparison of the TEM data with the data on the crystallite sizes of these particles, which shows that their average values after prolonged hydrothermal treatment remain at level of ~25 nm.

Figure 6d shows conjugated nanorods of monazite phase and rhabdophane phase. The rhabdophane phases are attached to the planes corresponding to the elementary cell parameter  $c = 6.37 \text{ \AA}$ , at angle of 40 °C to the (101) plane of monazite phases (at interplanar distance 4.1 Å).

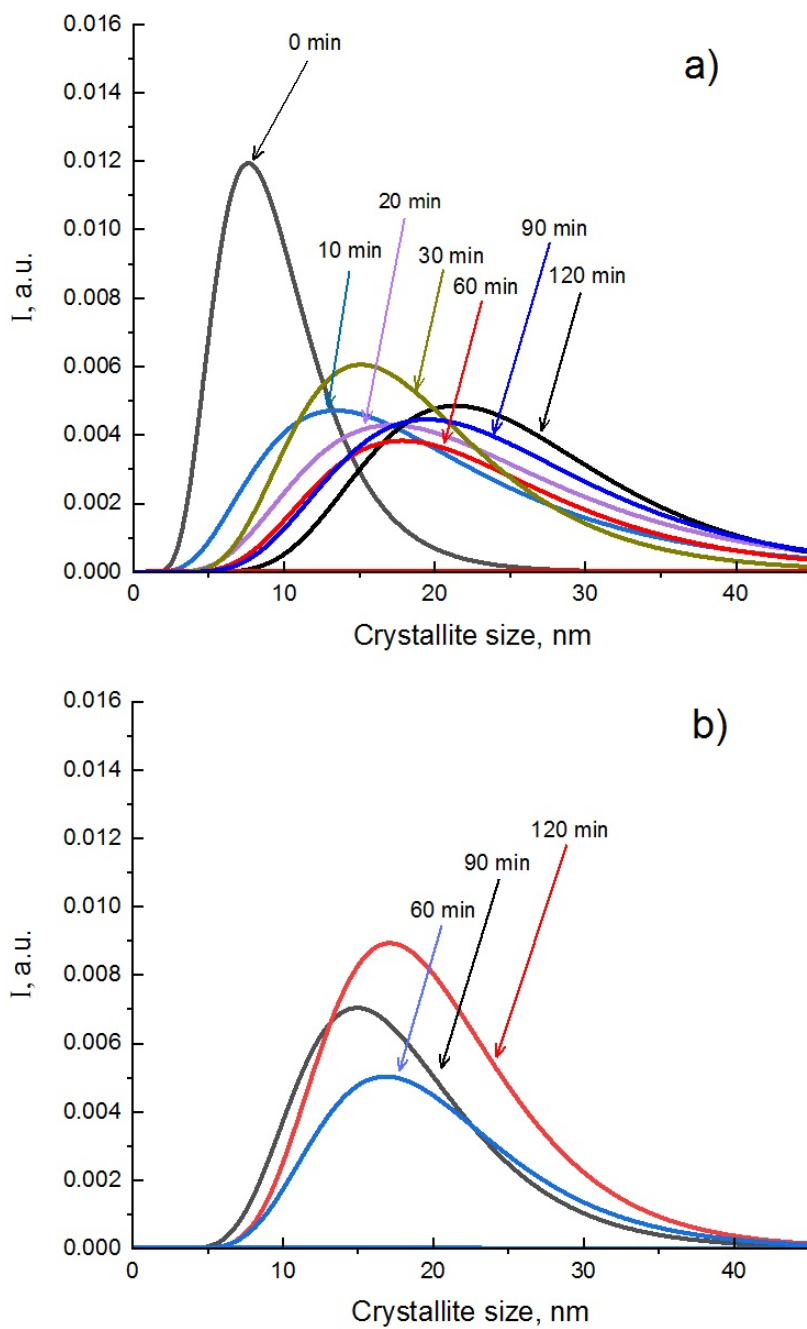


FIG. 5. Size distribution of crystallites of solid solutions of lanthanum-yttrium orthophosphates with rhabdophane (a) and monazite (b)

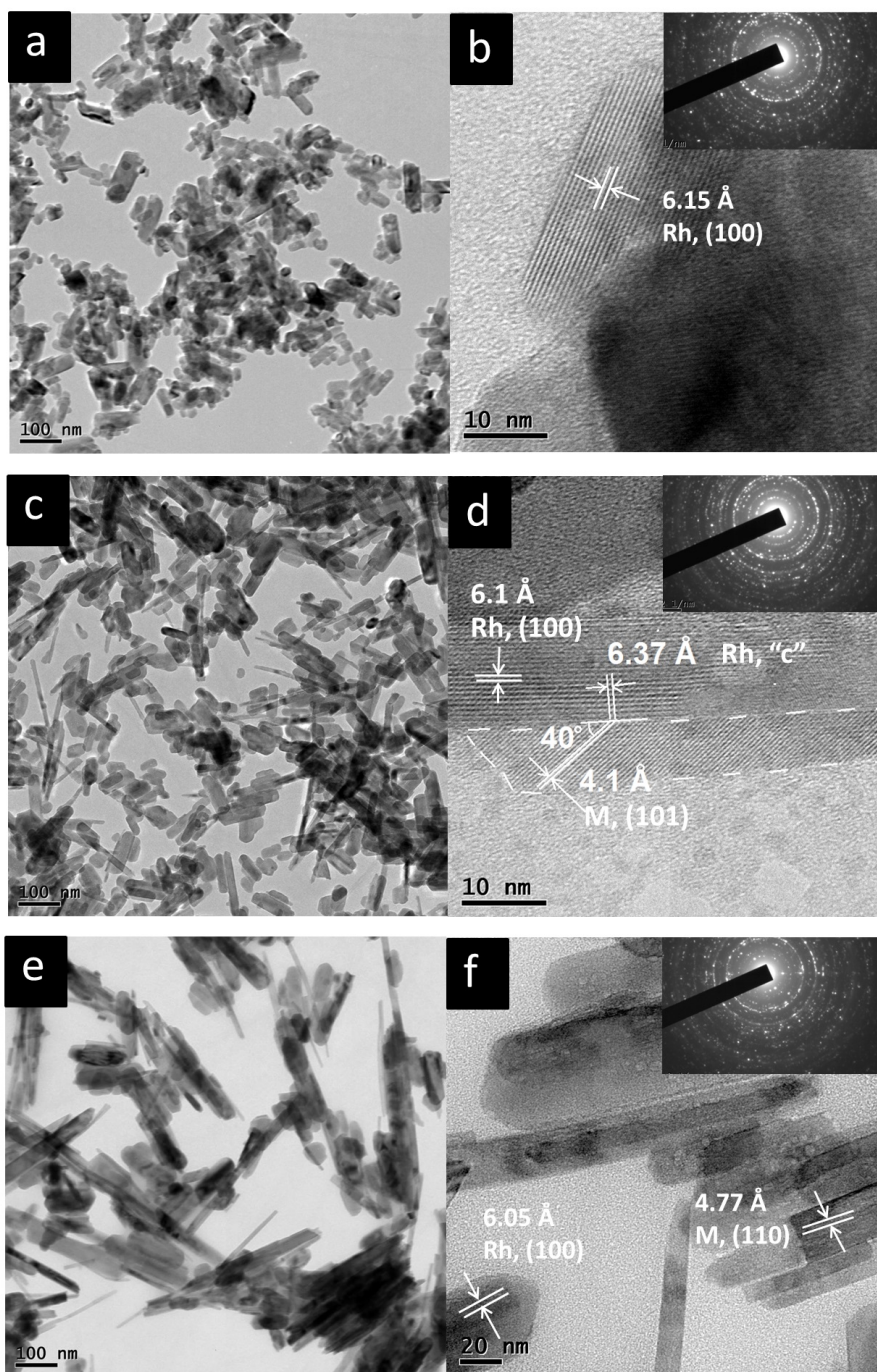


FIG. 6. Fig. 6. TEM micrographs of samples after hydrothermal treatment with isothermal holding at 180 °C for various durations: (a,b) – 20 minutes; (c,d) – 30 minutes; (e,f) – 120 minutes. The rhabdophane phase is designated as Rh, the monazite phase as M

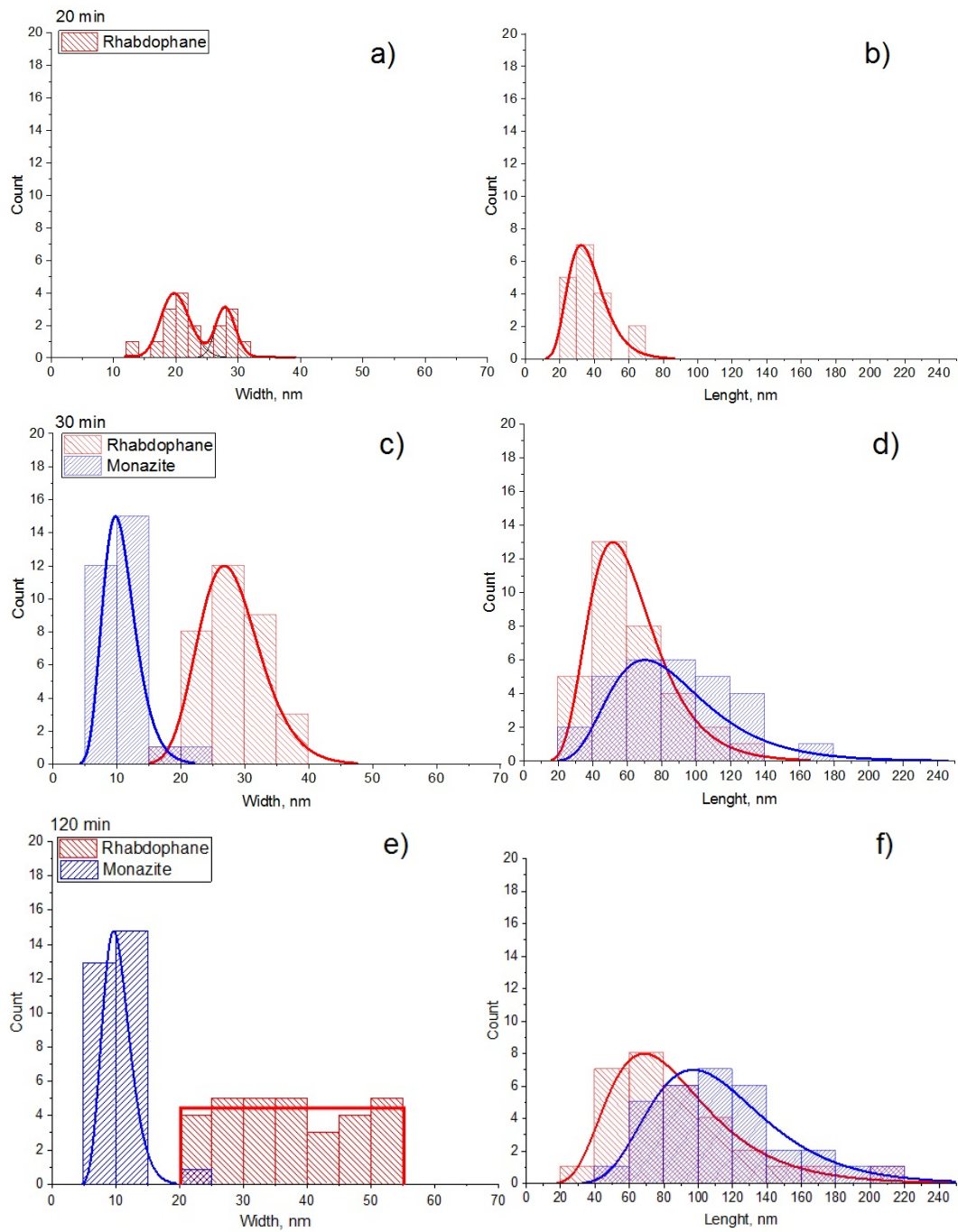


FIG. 7. Size distributions of thickness and length of rhabdophane and monazite nanoparticles according to TEM data. Samples after isothermal holding under hydrothermal conditions at 180 °C for various durations: (a,b) – 20 minutes; (c,d) – 30 minutes; (e,f) – 120 minutes

The average thickness of nanorods with monazite structure does not change for the samples obtained after hydrothermal treatment at 30 and 120 minutes of isothermal holding, and is  $\sim 12$  nm, which corresponds to the crystallite size at monazite phase, determined from X-ray diffraction data. That is, these nanoparticles can be considered mainly as monocrystalline. The average length of nanorods with monazite structure increases from  $\sim 90$  to  $\sim 120$  nm. Such length increase of nanorods of the phase with monazite structure correlates well with the fraction change of phases with monazite and rhabdophane structures in the system (Fig. 2); with a high degree of confidence can be associated with transfer of matter under hydrothermal conditions from the phase with rhabdophane structure to the phase with monazite structure while increase the isothermal holding time from 30 to 120 min.

A comparative data analysis on changes in the phase ratio, elementary cell volumes, dimensional parameters of crystallites and particles with rhabdophane and monocytte structures during the microwave hydrothermal treatment process of precipitated lanthanum-yttrium orthophosphates, as well as direct observation of structural transformations in TEM micrographs (see, for example, Fig. 6d) allows us to represent the formation pattern of solid solutions in the system  $0.53\text{LaPO}_4-0.47\text{YPO}_4-(n\text{H}_2\text{O})$ , as a series of the following processes:

1. a precipitation of lanthanum-yttrium orthophosphate with formation of nanocrystals with rhabdophane structure and amorphous phase;
2. crystallization of the amorphous phase under hydrothermal conditions with the formation of nanocrystals with rhabdophane structure and the formation of bimodal size distribution of monocrystalline (predominantly) nanoparticles;
3. the transformation of some nanocrystals with rhabdophane structure (the thinnest rod-like particles formed under hydrothermal conditions from amorphous phase) into monazite structure by degenerating one structure into another along the nanocrystal edges at the initial phase;
4. differentiation according to the composition of solid solutions of lanthanum-yttrium orthophosphates during structural transformation and stabilization as result of this two-phase state of the system;
5. the length increase (without changing the thickness) of nanoparticles of solid solutions of lanthanum-yttrium orthophosphates with monazite structure by transfer of matter under hydrothermal conditions from particles with rhabdophane structure;
6. the thickness increase of nanoparticles of solid solutions with rhabdophane structure by accretion of initially single-crystal nanoparticles;
7. the length increase of nanoparticles of lanthanum-yttrium orthophosphate with rhabdophane structure by mass transfer of matter under hydrothermal conditions.

#### 4. Conclusion

As a result of studies, it has been shown that nanoparticles of phase with monazite structure having average crystallite size of 15–17 nm begin to form after 30 minutes of hydrothermal microwave-assisted treatment at  $180^\circ\text{C}$  immediately after complete crystallization of amorphous phase in the system, the structural transition of the solid solution from phosphate lanthanum-yttrium with rhabdophane structure into monazite structure is based on degeneration of nanocrystals with rhabdophane structure along certain edges into monazite structure. The nanoparticle size increase (length of nanorods) with monazite structure after the stage of their formation occurs mainly due to matter transfer from nanoparticles having rhabdophane structure to nanoparticles having monazite structure, while thickness increase of rod-like particles with rhabdophane structure occurs due to their aggregation-accommodation coalescence. The system under considered conditions of hydrothermal treatment (temperature –  $180^\circ\text{C}$ , pressure  $\sim 1-1.5$  MPa, duration – up to 120 min) remains two-phase due to composition differentiation of coexisting phases.

#### Acknowledgments

X-ray diffraction studies and elemental analysis of the samples performed using devices of the Engineering Center of the St. Petersburg State Technological Institute (Technical University).

Studies on transmission electron microscope were performed using equipment from the Federal Common Use Center “Materials Science and Diagnostics in Advanced Technologies” at the Ioffe Physical-Technical Institute of the Russian Academy of Sciences.

These studies were financially supported by the Russian Fundamental Research Fund (Project No. 18-29-12119).

#### References

- [1] Du A., Wan C., Qu Z., Wu R., Pan W. Effects of texture on the thermal conductivity of the  $\text{LaPO}_4$  monazite. *Journal of the American Ceramic Society*, 2010, **93**, P. 2822–2827.
- [2] Hikichi Y., Ota T., Daimon K., Hattori T., Mizuno M. Thermal, Mechanical, and Chemical Properties of Sintered Xenotime-Type  $\text{RPO}_4$  (R = Y, Er, Yb, or Lu). *Journal of the American Ceramic Society*, 1998, **81**, P. 2216–2218.

- [3] Ushakov S.V., Helean K.B., Navrotsky A., Boatner L.A. Thermochemistry of rare-earth orthophosphates. *J. Mater. Res.*, 2001, **16**(9), P. 2623–2633.
- [4] Schlenz H., Heuser J., Neumann A., Schmitz S., Bosbach D. Monazite as a suitable actinide waste form. *Crystalline Materials*, 2013, **228**(3), P. 113–123.
- [5] Mezentseva L., Osipov A., Ugolkov V., Akatov A., Doil'nitsyn V., Maslennikova T., Yakovlev A. Synthesis and Thermal Behavior of Nanopowders in LaPO<sub>4</sub>-YPO<sub>4</sub>(-H<sub>2</sub>O), LaPO<sub>4</sub>-LuPO<sub>4</sub>(-H<sub>2</sub>O) and YPO<sub>4</sub>-ScPO<sub>4</sub>(-H<sub>2</sub>O) Systems for Ceramic Matrices. *J. Nanomed. Res.*, 2017, **6**(1), P. 00145.
- [6] Gausse C., Szenknect S., Mesbah A., Clavier N., Neumeier S., Dacheux N. Dissolution kinetics of monazite LnPO<sub>4</sub> (Ln = La to Gd): A multiparametric study. *Applied Geochemistry*, 2018, **93**, P. 81–93.
- [7] Toro-González M., Dame A.N., Foster C. M., Millet L.J., Woodward J.D., Rojas J.V., Mirzadeh S., Davern S.M. Quantitative encapsulation and retention of <sup>227</sup>Th and decay daughters in core-shell lanthanum phosphate nanoparticles. *Nanoscale*, 2020, **12**, P. 9744–9755.
- [8] Lenz C., Thorogood G., Aughterson R., Ionescu M., J. Gregg D., Davis J., Lumpkin, G. The quantification of radiation damage in orthophosphates using confocal  $\mu$ -luminescence spectroscopy of Nd<sup>3+</sup>. *Frontiers in Chemistry*, 2019, **7**, Art.13.
- [9] Osipov A.V., Mezentseva L.P., Drozdova I.A., Kuchaeva S.K., Ugolkov V.L., Gusarov V.V. Crystallization and thermal transformations in nanocrystals of the YPO<sub>4</sub>-LuPO<sub>4</sub>-H<sub>2</sub>O system. *Glass. Phys. Chem.*, 2007, **33**, P. 169–173.
- [10] Osipov A.V., Mezentseva L.P., Drozdova I.A., Kuchaeva S.K., Ugolkov V.L., Gusarov V.V. Preparation and thermal transformations of nanocrystals in the LaPO<sub>4</sub>-LuPO<sub>4</sub>-H<sub>2</sub>O system. *Glass. Phys. Chem.*, 2009, **35**, P. 431–435.
- [11] Ruigang W., Wei P., Jian C., Minghao F., Zhenzhu C., Yongming L. Synthesis and sintering of LaPO<sub>4</sub> powder and its application. *Mater. Chem. Phys.*, 2003, **79**(1), P. 30–36.
- [12] Ferhi M., Horchani-Naifer K., Férid M. Combustion synthesis and luminescence properties of LaPO<sub>4</sub>: Eu (5%). *J. Rare Earths*, 2009, **27**(2), P. 182–186.
- [13] Lai H., Bao A., Yang Y., et al. UV luminescence property of YPO<sub>4</sub>:RE (RE = Ce<sup>3+</sup>, Tb<sup>3+</sup>). *J. Phys. Chem. C*, 2007, **112**(1), P. 282–286.
- [14] Pan W., Phillpot S.R., Wan C., Chernatynskiy A., Qu Z. Low thermal conductivity oxides. *MRS Bull.*, 2012, **37**(10), P. 917–922.
- [15] Grechanovsky A.E., Eremin N.N., Urusov V.S. Radiation resistance of LaPO<sub>4</sub> (monazite structure) and YbPO<sub>4</sub> (zircon structure) from data of computer simulation. *Phys Solid State*, 2013, **55**, P. 1929–1935.
- [16] Terra O., Clavier N., Dacheux N., Podor R. Preparation and characterization of lanthanum–gadolinium monazites as ceramics for radioactive waste storage. *New Journal of Chemistry*, 2003, **27**(6), P. 957–967.
- [17] Ohtaki K.K., Heravi N.J., Leadbetter J.W., Peter E.D. Morgan, Mecartney M.L. Extended solubility of Sr in LaPO<sub>4</sub> monazite. *Solid State Ionics*, 2016, **293**, P. 44–50.
- [18] Gallini S., Hänsel M., Norby T. Impedance spectroscopy and proton transport number measurements on Sr-substituted LaPO<sub>4</sub> prepared by combustion synthesis. *Solid State Ionics*, 2003, **162-163**, P. 167–173.
- [19] Bryukhanova K.I., Nikiforova G.E., Gavrichev K.S. Synthesis and study of anhydrous lanthanide orthophosphate (Ln= La, Pr, Nd, Sm) nanowhiskers. *Nanosystems: Physics, Chemistry, Mathematics*, 2016, **7**(3), P. 451–458.
- [20] Larina L.L., Alexeeva O.V., Almjasheva O.V., Gusarov V.V., Kozlov S.S., Nikolskaia A.B., Vildanova M.F., Shevaleevskiy O.I. Very wide-bandgap nanostructured metal oxide materials for perovskite solar cells. *Nanosystems: Physics, Chemistry, Mathematics*, 2019, **10**(1), P. 70–75.
- [21] Vildanova M.F., Nikolskaia A.B., Kozlov S.S., Karyagina O.K., Larina L.L., Shevaleevskiy O.I., Almjasheva O.V., Gusarov V.V. Nanostructured ZrO<sub>2</sub>-Y<sub>2</sub>O<sub>3</sub>-based system for perovskite solar cells. *Doklady Physical Chemistry*, 2019, **484**(2), P. 36–38.
- [22] Yorov Kh.E., Khodan A.N., Baranchikov A.E., Utochnikova V.V., Simonenko N.P., Beltiukov A.N., Petukhov D.I., Kanaev A., Ivanov V.K. Superhydrophobic and luminescent highly porous nanostructured alumina monoliths modified with tris(8-hydroxyquinolino)aluminium. *Microporous and Mesoporous Materials*, 2020, **293**, P. 109804.
- [23] Sklyarova A., Popkov V.I., Pleshakov I.V., Matveev V.V., Stěpánková P.H., Chlan V. Peculiarities of <sup>57</sup>Fe NMR Spectrum in Micro- and Nanocrystalline Europium Orthoferrites. *Applied Magnetic Resonance*, 2020.
- [24] Popkov V.I., Bachina A.K., Valeeva A.A., Lobinsky A.A., Gerasimov E.Y., Rempel A.A. Synthesis, morphology and electrochemical properties of spherulite titania nanocrystals. *Ceramics International*, 2020, **46**(15), P. 24483–24487.
- [25] Kovalenko A.N., Tugova E.A. Thermodynamics and kinetics of non-autonomous phase formation in nanostructured materials with variable functional properties. *Nanosystems: Physics, Chemistry, Mathematics*, 2018, **9**(5), P. 641–662.
- [26] Roca A.G., Gutiérrez L., Gavilán H., Fortes Brollo M.E., Veintemillas-Verdaguer S., Puerto Morales M. Design strategies for shape-controlled magnetic iron oxide nanoparticles. *Advanced Drug Delivery Reviews*, 2019, **138**, P. 68–104.
- [27] Davis J.B., Marshall D.B., Morgan P.E.D. Monazite-Containing Oxide/Oxide Composites. *J. Eur. Ceram. Soc.*, 2000, **20**(5), P. 583–587.
- [28] Arinicheva Y., Clavier N., Neumeier S., Podor R., Bukaemskiy A., Klinkenberg M., Roth G., Dacheux N., Bosbach D. Effect of powder morphology on sintering kinetics, microstructure and mechanical properties of monazite ceramics. *J. Europ. Ceram. Soc.*, 2018, **38**(1), P. 227–234.
- [29] Kenges K.M., Proskurina O.V., Danilovich D.P., Aldabergenov M.K., Gusarov V.V. Influence of the Conditions for Preparing LaPO<sub>4</sub>-Based Materials with Inclusions of the LaP<sub>3</sub>O<sub>9</sub> Phase on Their Thermal and Mechanical Properties. *Russ. J. App. Chem.*, 2018, **91**(9), P. 1539–1548.
- [30] Shijina K., Sankar S., Midhun M., Firozkhan M., Nair B.N., Warriar K.G., Hareesh U.N.S. Very low thermal conductivity in lanthanum phosphate–zirconia ceramic nanocomposites processed using a precipitation–peptization synthetic approach. *New J. Chem.*, 2016, **40**(6), P. 5333–5337.
- [31] Zainurul A.Z., Rusop M., Abdullah S., Effect of annealing temperature on surface morphology of lanthanum phosphate (LaPO<sub>4</sub>) nanostructures thin films. *Advanced Materials Research*, 2012, **626**, P. 302–305.
- [32] Ugolkov V.L., Mezentseva L.P., Osipov A.V., Popova V.F., Maslennikova T.P., Akatov A.A., Doil'nitsyn V.A. Synthesis of nanopowders and physicochemical properties of ceramic matrices of the LaPO<sub>4</sub>-YPO<sub>4</sub>(-H<sub>2</sub>O) and LaPO<sub>4</sub>-HoPO<sub>4</sub>(-H<sub>2</sub>O) systems. *Rus. J. Appl. Chem.*, 2017, **90**(1), P. 28–33.
- [33] Maslennikova T.P., Osipov A.V., Mezentseva L.P., Drozdova I.A., Kuchaeva S.K., Ugolkov V.L., Gusarov V.V. Synthesis, Mutual Solubility, and Thermal Behavior of Nanocrystals in the LaPO<sub>4</sub>-YPO<sub>4</sub>-H<sub>2</sub>O System. *Glass Physics and Chemistry*, 2010, **36**(3), P. 351–357.
- [34] Mezentseva L., Osipov A., Ugolkov V., Kruchinina I., Popova V., Yakovlev A., Maslennikova T. Solid Solutions and Thermal Transformations in Nanosized LaPO<sub>4</sub>-YPO<sub>4</sub>-H<sub>2</sub>O and LaPO<sub>4</sub>-LuPO<sub>4</sub>-H<sub>2</sub>O Systems. *J. Ceram. Sci. Tech.*, 2014, **05**(03), P. 237–244.

- [35] Mezentseva L.P., Kruchinina I.Yu., Osipov A.V., Kuchaeva S.K., Ugolkov V.L., Popova V.F., Pugachev K.E. Nanopowders of Orthophosphate  $\text{LaPO}_4\text{-YPO}_4\text{-H}_2\text{O}$  System and Ceramics Based on Them. *Glass Physics and Chemistry*, 2014, **40**(3), P. 356–361.
- [36] Wang R., Pan W., Chen J., Fang M., Meng J. Effect of  $\text{LaPO}_4$  content on the microstructure and machinability of  $\text{Al}_2\text{O}_3/\text{LaPO}_4$  composites. *Mater Lett*, 2002, **57**(4), P. 822–827.
- [37] Sankar S., Raj A.N., Jyothi C.K., Warriar K.G.K., Padmanabhan P.V.A. Room temperature synthesis of high temperature stable lanthanum phosphate-yttria nano composite. *Mater Res Bull*, 2012, **47**(7), P. 1835–1837.
- [38] Mezentseva L., Osipov A., Ugolkov V., Kruchinina I., Maslennikova T., Koptelova L. Sol-gel synthesis of precursors and preparation of ceramic composites based on  $\text{LaPO}_4$  with  $\text{Y}_2\text{O}_3$  and  $\text{ZrO}_2$  additions. *J. Sol-Gel Sci Technol*, 2019, **92**(2), P. 427–441.
- [39] Proskurina O.V., Sivtsov E.V., Enikeeva M.O., Sirotkin A.A., Abiev R.S., Gusarov V.V. Formation of rhabdophane-structured lanthanum orthophosphate nanoparticles in an impinging-jets microreactor and rheological properties of sols based on them. *Nanosyst Physics, Chem Math*, 2019, **10**(2), P. 206–214.
- [40] Wang S., Xu D., Guo Y., et al. Supercritical Hydrothermal Synthesis of Inorganic Nanomaterials. *Supercritical Water Processing Technologies for Environment, Energy and Nanomaterial Applications*, 2020, P. 117–147.
- [41] Darr J.A., Zhang J., Makwana N.M., Weng X. Continuous Hydrothermal Synthesis of Inorganic Nanoparticles: Applications and Future Directions. *Chem. Rev.*, 2017, **117**(17), P. 11125–11238.
- [42] Kenges K., Aldabergenov M., Proskurina O., Gusarov V. Hydrothermal synthesis of monostructured  $\text{LaPO}_4$ : morphology and structure. *Chem Bull Kazakh Natl Univ.*, 2018, **3**(90), P. 12–19.
- [43] Enikeeva M.O., Kenges K.M., Proskurina O.V., Danilovich D.P., Gusarov V.V. Influence of Hydrothermal Treatment Conditions on the Formation of Lanthanum Orthophosphate Nanoparticles of Monazite Structure. *Russ. J. Appl. Chem.*, 2020, **93**(4), P. 540–548.
- [44] Patra C.R., Alexandra G., Patra S., et al. Microwave approach for the synthesis of rhabdophane-type lanthanide orthophosphate (Ln = La, Ce, Nd, Sm, Eu, Gd and Tb) nanorods under solvothermal conditions. *New J. Chem.*, 2005, **29**(5), P. 733–739.
- [45] Ekthammathat N., Thongtem T., Phuruangrat A., Thongtem S. Microwave-assisted synthesis and characterisation of uniform  $\text{LaPO}_4$  nanorods. *J. Exp Nanosci*, 2012, **7**(6), P. 616–623.
- [46] Zhang F.X., Wang J.W., Lang M., Zhang J.M., Ewing R.C., Boatner L.A. High-pressure phase transitions of  $\text{ScPO}_4$  and  $\text{YPO}_4$ . *Phys. Rev. B - Condens Matter Mater Phys.*, Published online 2009, **80**, P. 184114.
- [47] Ochiai A., Utsunomiya S. Crystal chemistry and stability of hydrated rare-earth phosphates formed at room temperature. *Minerals*, 2017, **7**(5), P. 84.
- [48] Mogilevsky P., Boakye E.E., HayAlder R.S. Solid Solubility and Thermal Expansion in a  $\text{LaPO}_4\text{-YPO}_4$  System. *Journal of the American Ceramic Society*, 2007, **90**(6), P. 1899–1907.
- [49] Aldred A.T. Cell volumes of  $\text{APO}_4$ ,  $\text{AVO}_4$ , and  $\text{AnBO}_4$  compounds, where A = Sc, Y, La-Lu. *Acta Cryst.*, 1984, **B40**, P. 569–574.
- [50] de Biasi R.S., Fernandes A.A.R., Oliveira J.C.S. Cell volumes of  $\text{LaPO}_4\text{-CePO}_4$  solid solutions. *J. Appl. Cryst.*, 1987, **20**, P. 319–320.
- [51] Dumler F.L., Skorniyakova K.P., Shul'ga G.G. Lanthanum rhabdophane in the weathered mantle on limestones—a new type of rare earth mineralization. *International Geology Review*, **12**(9), P. 1140–1145.
- [52] Mooney R.C.L. Crystal structures of a series of rare earth phosphates. *The Journal of Chemical Physics*, 1948, **16**, P. 1003–1004.
- [53] Bowles J., Morgan D.J. The composition of rhabdophane. *Mineralogical Magazine*, **48**(1), P. 146–148.
- [54] Almjasheva O.V., Gusarov V.V. Metastable Clusters and Aggregative Nucleation Mechanism. *Nanosystems: Physics, Chemistry, Mathematics*, 2014, **5**(3), P. 404–416.

## Perovskite solar cells: recent progress and future prospects

O. I. Shevaleevskiy

Solar Photovoltaic Laboratory, Emanuel Institute of Biochemical Physics, Russian Academy of Sciences,  
Kosygin St. 4, Moscow, 119334, Russia  
shevale2006@yahoo.com

PACS 73.63.Bd

DOI 10.17586/2220-8054-2020-11-6-716-728

Nanotechnologies and nanostructured materials are attracting significant attention as most promising candidates for achieving drastic improvement of solar energy conversion efficiency in next-generation nanostructured-based perovskite solar cells (PSCs). In this review, we focus on the latest achievements in construction of efficient PSCs and describe new trends in perovskite solar photovoltaics including the development of high-performance perovskite-silicon tandem solar cells, inorganic PSCs with stabilized efficiency and a new generation of PSCs for low lighting conditions that opens great possibilities for indoor applications. A special attention is paid also to the development of new types of efficient photoelectrodes for PSCs based on very large band gap metal oxides.

**Keywords:** nanostructures, nanotechnologies, perovskite solar cells,  $ZrO_2$ , thin films, semiconductors, tandem solar cells.

*Received:* 3 August 2020

*Revised:* 23 August 2020

### 1. Introduction

Nanotechnologies and nanostructured materials are attracting significant attention as most promising candidates for achieving drastic improvement of solar energy conversion efficiency in next-generation nanostructured solar cells (SCs) [1, 2]. In recent years, considerable interest has been focused on a new generation of inorganic-organic metal halide perovskite solar cells (PSCs).

The first report on a new type of PSC with 3.8 % efficiency emerged in 2009 [3]. In this study perovskites were used as sensitizers in Gratzel-type dye-sensitized solar cells (DSCs) [4, 5]. In short order, the efficiency of PSCs was increased up to 6.5 % [6]. However, the application of liquid electrolyte in the hole-transporting material (HTM) created a situation in which the stability of SCs was weak and the future of such type of perovskite DSCs looked questionable [6]. Serious progress was gained with the emergence of solid-state PSCs where perovskite material  $MAPbI_3$  was spin-coated on nanostructured  $TiO_2$  photoelectrode. The PSC n-i-p junction configuration was then accomplished by coating the molecular spiro-MeOTAD HTM film and Au back contact [7]. During short period of time the power conversion efficiency (PCE) of such cells has been dramatically increased and the best cell efficiency has now reached 25.5 % [8, 9]. Thus, the above-mentioned achievements in PSC solar photovoltaics have made these devices nearly as efficient as the best conventional SCs based on crystalline silica (c-Si).

In the meantime, the construction of solid state PSCs comprise organic-inorganic hybrid perovskite materials, like  $ABX_3$ , where A is an organic cation such as methylammonium ( $MA^+$ ), B is  $Pb^{2+}$  and X is Br, or I [10]. The main problem of perovskite materials appeared to be due to their organic nature possessing poor stability when exposed to heat, oxygen and moisture and also due to their rapid degradation under illumination [11–13]. To overcome the stability problems a number of solutions have been proposed [14, 15]. However, the long-term stability of PSCs still does not meet the necessary requirements for large scale production. While the stability remains a major problem to be overcome, many other aspects of PSCs are now investigated. In this short overview, attention is given to the latest achievements in constructing more efficient photoelectrodes for PSCs and also to the new trends in perovskite-based photovoltaics associated with the development of high performance tandem PSC-based SCs and a new generation of PSCs for low lighting conditions that opens great possibilities for indoor applications.

### 2. Current status of solar photovoltaics

The key challenge facing the global energy industry is the transfer towards resource-saving technologies and the large-scale introduction of renewable energy sources. Among all the available renewable energy resources, the greatest potential is for that of solar radiation energy, which can be directly converted into electricity using solar cells (SCs). The global production of dominant silicon solar panels (mainly monocrystalline (c-Si) and polycrystalline (multi-Si)) is exponentially growing, and their cost is declining and currently stands at \$0.21 – 0.35/W [16]. Silicon solar cells have a number of undoubted advantages, including long-term stability and high efficiency when working under high

intensity AM1.5G lighting conditions. Fig. 1 illustrates the exponential growth in global solar panel production during the recent decades and the parallel drop in the cost of silicon solar panels. Long-term forecast of changes in the average cost of electricity generated in the world by silicon solar panels assumes that after 2020, the cost of kWh of electricity, received from the solar cells, will approach the cost of electricity obtained from conventional sources (coal, gas, oil), which will mean the achievement of grid parity.

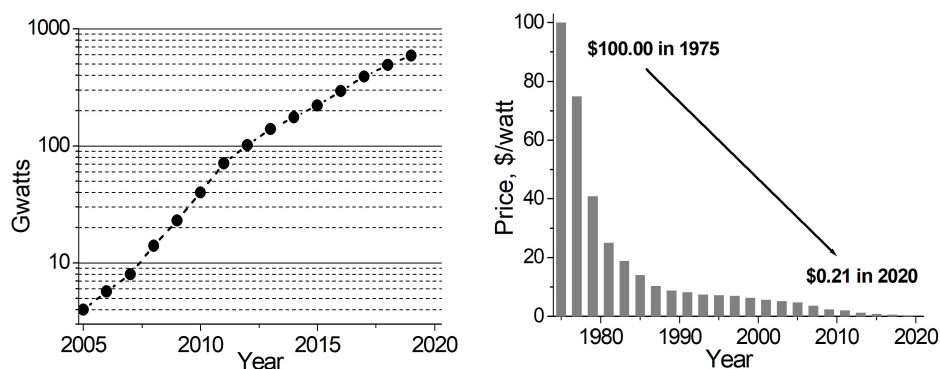


FIG. 1. Illustration of the exponential growth of world installed solar energy capacity (left) and the dramatic drop in the cost of solar PV modules (right)

Other less common types of solar cells, mainly thin-film, which in the last decade have been claimed as potential competitors to Si-based SCs, include solar cells based on amorphous and micromorphous silicon, SCs based on thin chalcogenide films (CIGS), and SCs based on cadmium telluride (CdTe). To date, these technologies totally occupy about 5 % of the global annual solar panels production, and no significant changes are expected in this distribution. Returning to the question of grid parity, it should be noted that for solar photovoltaics, achieving sustainable grid parity can lead to significant changes not only in this industry, but throughout the whole global energy sector. It is worth mentioning that the level of such parity can vary significantly depending not only on the geography of the region, but also on the features of its economic development and energy policy. However, despite the “exponential” achievements of recent decades, the current situation in the field of solar photovoltaics is not so inspiring. The main problem of photovoltaics lies in impossibility of further improvement, most importantly, costs reduction for silicon solar panels, since the potential for the further decline in costs for this technology is greatly limited. In this respect, the scientific community needs to establish new approaches which would allow, based on basic research or through the use of new designs and materials, to create alternative types of SCs, which could provide the grid parity in the majority of world regions and fundamentally change the global energy structure. If we analyze the work of the majority of scientific teams in the field of solar photovoltaics throughout the world, it becomes obvious that the research aimed at the development of the novel SC types is the most relevant currently.

### 3. Current status of perovskite solar cells

The perovskite material, used in conventional solid-state PSCs, such as  $\text{CH}_3\text{NH}_3\text{PbX}_3$  demonstrates a tunable band gap ranging from 1.5 to 2.3 eV [17] and possesses high light absorption coefficient suitable for solar photovoltaic applications [18]. At the same time, perovskite materials are low-cost while fabrication methods for PSCs have a number of advantages over fabrication process of conventional c-Si solar cells. PSC’s architecture comprises a mesoscopic layer of metal-oxide nanoparticles on a conductive substrate, which plays a role of the electron-conductive photoelectrode, a perovskite ( $\text{CH}_3\text{NH}_3\text{PbI}_3$ ) layer deposited on top of the photoelectrode, a hole-conductive layer and a metallic counter electrode [19]. The illustration of the PSC architecture and the laboratory samples of PSC devices prepared in the Solar Photovoltaic Laboratory (IBCP RAS, Russia) is given in Fig. 2.

The initial meaning of “perovskite” was about the crystal structure of calcium titanate, which was discovered in 1839 by Gustav Rose and was named by the Russian mineralogist Lev Perovski. Since then, the term “perovskite” has referred to all compounds with the same crystal structure as calcium titanate [20].

The first perovskite-based solar cell construction was reported by T. Miyasaka one decade ago [3]. This device used a liquid electrolyte as an s hole-transporting material (HTM) and have shown poor stability. Later, N. Park et al. [6] improved the PSC efficiency but the problem of the instability was not solved. The situation has changed dramatically with the appearance of solid-state HTM (2,20,7,70-tetrakis(N,N-di-p-methoxyphenylamine)-9,90-spirobifluorene, i.e., Spiro-OMeTAD). They succeeded in the improvement of the device stability and reached an efficiency of 10.9 %



FIG. 2. Device architecture of the PSC (left) and the laboratory PSCs prepared in the Solar photovoltaic laboratory of IBCP RAS (right)

with an open-circuit voltage higher than 1.1 V [6]. Even better results were obtained in 2013 with the introduction of graphene nanoparticles into PSCs which increased the efficiency up to 15.6 % [21]. In 2015, a new record of 20 % efficiency was achieved by using perovskite material based on, formamidinium iodide  $\text{HC}(\text{NH}_2)_2\text{PbI}_3$  together with poly-triarylamine (PTAA) HTM [22]. Finally, in 2017, the record efficiency of 22.1 %, was reported [23]. At the same time, perovskite-based tandem cells with c-Si bottom cell with the efficiency of 26.7 % appeared [24]. Very recently Oxford PV declared 28.0 % efficiency tandem perovskite-silicon solar cell while Helmholtz–Zentrum Berlin (HZB) announced a certified efficiency of 29.15 %. However, in both cases, no scientific publications have yet appeared.

The efficiency progress of PSCs in comparison with other photovoltaic devices is discussed in [25]. Perovskite solar photovoltaics, as compared to other photovoltaic technologies, including thin film CIGS, organic SCs, DSCs and a variety of Si-based devices, aims to become the best alternative to solar photovoltaics of the future.

#### 4. PSC research history

Currently, one of the most promising areas of basic research in the field of photovoltaics is the development of perovskite solar cells (PSCs). Perovskite materials have a unique structure in which organic and inorganic components are alternating. That is what causes the presence of perovskite unusual electrical, magnetic and optical properties. First solar cells sensitized with perovskites have been presented in the article of T. Miyasaka (Tokyo, Japan) in 2009 in which the chemical compound using  $\text{CH}_3\text{NH}_3\text{PbI}_3$  (band gap 1.55 eV) in combination with a liquid electrolyte reached the energy conversion efficiency of 3.8 % [3]. Later, through the optimization of the surface of the titanium dioxide and the further processing in the laboratory perovskite N. Park (Suwon, South Korea) in 2011 managed to get the efficiency value of 6.5 % [6]. However, the fabricated cells worked poorly as perovskites decomposed by contact with sodium iodide/triiodide ions. In this regard, in 2012 M. Gratzel and H. Park (Lausanne, Switzerland) proposed to use an organic semiconductor Spiro-MeO-TAD as a hole transporter [11]. The efficiency of sunlight conversion was increased to 8 – 10 %. Thus, there was a transition from the standard solar cells working in conjunction with liquid electrolyte for solid state solar cells. In 2013, M. Gratzel and coworkers have shown that nanocrystals sequential deposition precursors ( $\text{CH}_3\text{NH}_3\text{PbI}_3$  and  $\text{PbI}_2$ ) solution on the surface of mesoporous titanium dioxide can effectively control the morphology of the applied perovskite layer  $\text{CH}_3\text{NH}_3\text{PbI}_3$  [26]. Maximum efficiency of thus obtained solid solar cell based on mesoscopic layers of titanium dioxide was 15 %. The research team, headed by Snaith (Oxford, UK) has proposed a way to create PSCs [7]. Based on the results obtained, they published a paper in 2012, according to which, the replacement in the solar cell layer of mesoporous titanium dioxide similar in structure to the insulating layer of aluminum oxide voltage not only changed, but also increased. This indicates that the perovskite has  $\text{CH}_3\text{NH}_3\text{PbI}_3$  intrinsic conductivity, while it can move in both electrons and holes, i.e. ambipolar material has such properties. Referring to ambipolar properties perovskites in 2013 H. Snaith and colleagues (Oxford, UK) developed solid-state solar cell with a heterojunction type “pin”, which takes the role of an active layer of perovskite layer disposed between the dense titanium dioxide layer (n-type) layer and Spiro-MeO-TAD (p-type) [27]. The mesoporous titania layer was absent, as perovskites, which are synthesized by mixing  $\text{PbI}_2$  and  $\text{CH}_3\text{NH}_3\text{PbI}_3$  in  $\gamma$ -butyrolactone, were deposited by vapor deposition. In this case, the conversion efficiency of solar energy into electric energy reaches 15.6 % [21]. After the scientific papers mentioned above, from 2013 to the present day, a large number of publications have emerged devoted to finding ways to improve the efficiency of solar cells based on perovskites. For example, in early 2015, M. Gratzel and colleagues suggested before application to the mesoscopic layer of titanium dioxide added to the solution of the perovskite in a mixture of  $\gamma$ -butyrolactone and dimethylformamide (DMF) 4-butylphosphonic acid 4-ammonium chloride. This additive acts as a crosslinker formed on the surface of the electrode grains of perovskite structures by means of hydrogen bonds between  $-\text{PO}(\text{OH})_2$ , and  $-\text{NH}_3$  groups that facilitates penetration of the particles into the pores  $\text{CH}_3\text{NH}_3\text{PbI}_3$  titanium dioxide and provides a more uniform layer of the light absorber. The

efficiency of the solar cell, created in accordance with this methodology, reached 16.7 % [28]. In 2014, S. Seok and colleagues (Daejeon, South Korea) conducted research of perovskite mixed composition  $\text{CH}_3\text{NH}_3\text{Pb}(\text{I}_{1-x}\text{Br}_x)_3$ . It has been found that the partial replacement of iodide ions, bromine ions ( $x = 0.1 - 0.15$ ) increases the stability of the desired material. In such a PSC, where poly-triarylamine was used as a hole carrier, the efficiency reached 16.2 % [29]. In the same laboratory, mixed perovskites of  $\gamma$ -butyrolactone and dimethyl sulfoxide (DMSO) were synthesized and twice applied on a mesoscopic titania layer. Wherein the second time toluene was added to the solution recommended perovskite. By this the most uniform and dense layers of absorbent material were obtained [29]. At the end of 2014 S. Seok (Daejeon, South Korea) used a more complex structure of perovskite, containing methylammonium ions and formamidinium as a sensitizer, achieving an efficiency of 17.9 %. This result was certified in a photovoltaic calibration laboratory, and was the highest for that time [10]. Perovskite  $\text{HC}(\text{NH}_2)_2\text{PbI}_3$  used was characterized by band gap (1.47 eV) which was more narrow than in  $\text{CH}_3\text{NH}_3\text{PbBr}_3$  (2.0 eV). In 2015, in the laboratory of H. Park (Seoul, South Korea), they have established more than 40 samples of PSCs, which amounted to an average efficiency of 18.3 %, with the maximum efficiency equal to 19.7 % [30]. In later works, by optimizing the design of a device architecture with a precise controlling of the perovskite grains and grain boundaries, a power conversion efficiency of 22 % was achieved [31]. The research group of S. Seok (Daejeon, South Korea) has provided the compositional engineering of low band gap formamidinium lead iodide based layers,  $(\text{FAPbI}_3)_{1-x}(\text{MAPbBr}_3)_x$ , which allowed the synthesis of a more stable microstructured dense layers of efficient PSCs [32,33].

In recent years, the possibility of using PSCs in tandem was actively studied [34]. Different types of solar cells may be combined with each other either mechanically (i.e., when they are simply connected to contacts), or monolithically configured, when both cells are combined into one monolithic device and between them there is an additional layer of conductive material. The efficiency of first tandem solar cells was 18.7 % [35]. Tandem solar cells based on perovskite with a silicon element in a monolithic configuration was shown to achieve the efficiencies exceeding 25 % [36,37]. The advantages of using perovskites as sensitizers in solar cells are obvious. First, they absorb light across a wider range than those solar cells with dyes in a liquid electrolyte (in DSCs) used to date and secondly, they have ambipolar characteristics, and thirdly, they are cheap and lead to efficiencies exceeding 20 %. However, there are some unsolved problems to date [34,38]:

- 1) Perovskites are unstable and degrade by prolonged exposure to sunlight;
- 2) Lead ions that are part of perovskites, are highly toxic;
- 3) PSCs are characterized by a strong hysteresis in the measurement of current-voltage characteristics in forward and reverse modes;
- 4) Creating PSCs with a large area is complicated;
- 5) Stability problems and the development of inorganic PSCs.

As it was previously mentioned, for a short period, the efficiency of laboratory scale PSCs increased from 3 – 5 to 20 – 24 %, which made them competitive with conventional Si-based SCs and the most promising candidates for solving the problems of global photovoltaics. However, it soon became apparent that the key component of the PSC – the photoactive absorber layer of perovskite material  $\text{CH}_3\text{NH}_3\text{PbI}_3$  – was structurally unstable under conditions of ambient humidity, light exposure, and rapidly and noticeably degraded under increased temperatures. Studies have shown that under real outdoor conditions, the efficiency of  $\text{MAPbI}_3$ -based PSCs decreases to zero over a short period of time [39]. As a result, the main photovoltaic parameter of the PSCs, i.e. stabilized efficiency, remains uncompetitive with respect to Si-based SCs which possess high long-term stability.

Since the problem of achieving the long-term stability of conventional PSCs remains unresolved, in the past few years attempts have been made to replace classical organo-inorganic materials in PSCs with inorganic systems based on lead halides with perovskite structure of  $\text{APbX}_3$  type, where A is an inorganic cation, and the anion is  $\text{PbX}_3^-$  (where  $\text{X} = \text{Cl}, \text{Br}, \text{I}$ ). In this respect, the works carried out by the scientific team headed by P. Troshin (ICCP RAS, Russia) attract a considerable attention. In their studies, perovskite materials were used with the structure of  $\text{CsPbI}_3$ , which showed significant advantages in terms of stability of the photovoltaic parameters being introduced in PSCs [40,41]. Similar investigations have been carried out in the world most recognized photovoltaic research group NREL (NREL, USA), where high efficiency values were achieved in such PSCs [42]. At the same time, a number of studies indicate that the proposed compounds based on lead halides could be unstable over prolonged periods. The latter may happen due to the high diffusion ability of halogen atoms and their high ionic mobility, which could be initiated by temperature and photoeffects and as a result can lead to structural changes in the crystal lattice of halogen-containing compounds.

## 5. Inorganic PSCs based on complex oxides

Recently, compounds with the general structure  $\text{A}_2\text{B}'\text{B}''\text{O}_6$ , which are double oxide perovskites of rare-earth elements  $-\text{R}_2\text{NiMnO}_6$  (R is a rare-earth element), have attracted special interest [43–47]. Unique semiconductor and

optical properties were found for  $\text{Sm}_2\text{NiMnO}_6$  (SNMO). Its high dielectric constant helps to reduce the recombination rate of electron-hole pairs and the optical band gap ( $E_g = 1.4$  eV) corresponds to the maximum of the solar radiation spectrum. Both of these parameters are critical for the effective operation of photovoltaic converters [48, 49]. One of the main advantages of this class of compounds is that such inorganic systems, *a priori*, have high long-term stability under various temperature conditions, the absence of photodegradation and resistance to atmospheric humidity. Complex oxides with a double perovskite structure have the optical absorption range close to that of the solar spectrum and high photoconductivity. The optical band gap values  $E_g$  are in the range of 2 – 2.5 eV, and with doping, could be varied to 1 – 1.5 eV. Attempts to use such compounds for the fabrication of PSCs led to relatively low efficiencies of photo-conversion, however, comprehensive fundamental and engineering efforts in this area have not yet been undertaken. At the same time, preliminary studies carried out in several world laboratories have shown promising opportunities for optimizing the design of PSCs based on these compounds and improving their photovoltaic parameters, which opens up the possibility of developing a new class of PSCs with high long-term stability.

To conclude, perovskite photovoltaics currently plays a significant role in the field of solar cell research. Many hundreds of laboratories across the world are specialized in this field and their number is constantly growing. Analysis of research activities by competing groups within the perovskite photovoltaics area shows that the studies could be divided into three groups in accordance with the type of photoactive materials used for PSCs fabrication. The largest group studies the conventional organic-inorganic PSCs based on  $\text{CH}_3\text{NH}_3\text{PbI}_3$  or similar (mixed cation and/or mixed halide) perovskite structures. The smaller second one is focused on the development of more stable inorganic PSCs with  $\text{APbX}_3$  structure, where A is an inorganic cation. Finally, the main activities of the third group are related to the studies aimed at the development of highly stable inorganic perovskite-type rare-earth oxides (e.g.  $\text{Sm}_2\text{NiMnO}_6$ ) and their photovoltaic applications [45].

## 6. Perovskite cells for indoor photovoltaics

### 6.1. Emerging of photovoltaics for low-intensity sources

Decades ago, when only Si-based SCs dominated in solar photovoltaics, efforts were provided to fabricate perfect and efficient devices for application under indoor low-intensity illumination. Silicon SCs have a number of definite advantages, including long-term stability and high efficiency when working under standard conditions AM1.5G ( $1000 \text{ W/m}^2$ ). However, it was shown that the efficiency of c-Si SCs decreases at low levels of solar radiation and significantly decreases under diffuse lighting conditions [50]. Fig. 3 shows the effects of light intensity and incidence light angle on the efficiency for DSC and c-Si solar cells. A similar behavior, somewhat less pronounced, was observed for other types of conventional, but less common solid-state PCs based on amorphous silicon (a-Si:H) and chalcogenides (CIGS). In this regard, one of the relevant tasks of modern photovoltaics is the search for alternative types of PCs, effective both in high solar radiation conditions and under low-intensity and defused light fluxes.

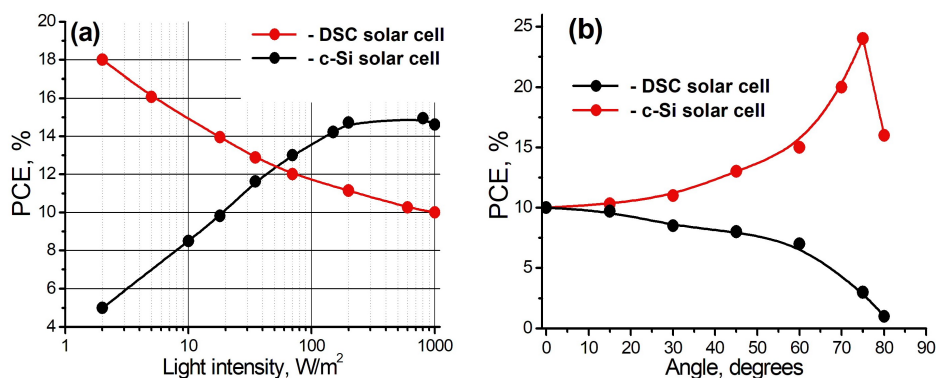


FIG. 3. Comparison of the effects of light-intensity (a) and incidence light angle (b) on the efficiencies of DSC and c-Si solar cells

Perovskite cells for indoor photovoltaics looks to promise a significant future for local power generation [51]. Fig. 4 illustrates the difference in the behavior of PCE dependence on light intensity for PSC and c-Si solar cells. It was also shown that PSCs can efficiently convert waste lighting from different artificial sources into electric power. Perovskite photovoltaic cells are highly efficient and cost-effective. Recently, it was shown that stoichiometry-controlled perovskite-based photovoltaic cells illuminated under the dim light-emitting diode (LED) are highly effective and provide unusually large PCE. It was found that 10 % bromide-doped perovskite photoactive layers exhibit the best

performance as a result of better crystallization and uniform surface that helped to form larger grains of perovskite with reduced defect concentrations, which suppressed carrier trapping and recombination and resulted in improved PSC performance [53]. As a result, under dim LED indoor illumination of 1000 lx, these types of PSCs have gained PCE of 34.5 % [54]. Actually, the result obtained demonstrates the appearance of the new indoor electronics.

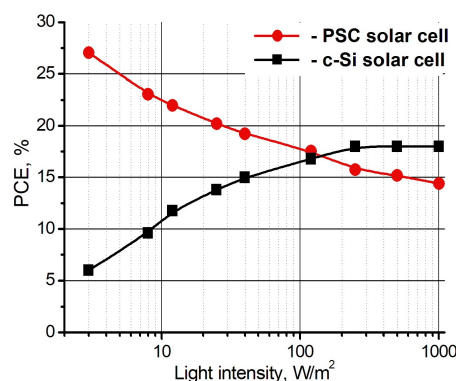


FIG. 4. Dependence of power conversion efficiency (PCE) on light intensity for PSC and c-Si solar cells

Two new rapidly developing areas have emerged recently as a part of global energy trends. One of them is related to the development of the Internet of Things (IoT) environment and the upcoming need for off-grid power for a large number of electronic devices with low power consumption. Another one, called “energy harvesting” (“collection by crumbs”), still not directly intersecting with the first, is the development of the low-power collecting systems from various energy sources. Photovoltaic devices that do not need to be replaced, which should be adapted to work in ambient lighting conditions, are considered as ideal candidates for indoor light harvesting and powering the IoT devices. As was shown above, there is no practical prospects in using the traditional solar cells based on crystalline silicon or chalcogenides for this purpose.

Application of PCs for efficient indoor light harvesting could be carried out by adapting solar cells based on organo-inorganic compounds, in which the absorption spectrum of photoactive materials more closely matches the spectral characteristic of radiation from the artificial light sources. Dye-sensitized solar cells (DSCs) and perovskite solar cells (PSCs) could be regarded as the most promising candidates for this purpose. It has been shown that in DSCs the efficiency increases as the illumination decreases from 10 – 12 % in AM1.5G mode to values exceeding 20 % under diffuse artificial lighting (200 – 1000 lx). Under similar conditions, PSCs demonstrate even more impressive results when the efficiency increases from ~ 18 – 20 % in AM1.5G mode to ~ 30 % under 200 – 1000 lx ambient lighting [51, 53, 54].

## 6.2. Nanocrystalline solar cells performance under variable outdoors illumination

In recent years efforts have been focused on the development of DSC and PSC solar cells for efficient operation under both high solar radiation during sunny days and under low-light conditions in cloudy weather. It was found that under the diffuse lighting conditions in cloudy weather, DSCs and PSCs remain the only really functioning types of solar photoconverters. The data obtained indicated that the efficiency for either PSCs or DSCs in outdoor conditions demonstrated an increase in conversion efficiency with a decrease in light intensity. The data available from the literature have shown great promise for the use of DSC- and PSC-based light energy SCs for highly efficient indoor operation under low-power artificial light sources with a relatively narrow spectral range [50, 54]. Thus, increase in the efficiency and development of novel stable photoconverters based on DSC and PSC, optimized for indoor operation under diffuse artificial lighting, is a new and relevant problem for modern photovoltaics.

In the field of basic research, regarding the processes of light energy conversion in DSC and PSC, optimized for operation in a specific spectral range of artificial lighting, it becomes necessary to address a number of poorly studied issues related to the specific energetic characteristics of interfaces under conditions of predominant absorption of photons with energies ranging from 2.5 – 3 eV (solar cells are illuminated outdoors by the solar spectrum in the range of ~ 0.6 – 3.5 eV). Another important aspect is that the light fluxes and therefore the number of photogenerated charge carriers when operating under ambient lighting conditions are about 3 orders of magnitude lower compared to the standard AM1.5G mode, which makes it critically important to optimize charge transfer carrier processes of across the interfaces in conditions of low-intensity artificial lighting. In the applied aspect, bearing in mind the lack of direct illumination of the photoconverter surface located indoors, new engineering solutions are required to create

more efficient SCs designs, for which, in particular, it is possible to use the double-sided PC architecture. Fig. 5 shows an example of such a design realized in a double-sided photovoltaic device for indoor operation under ambient lighting introduced by O. Shevaleevskiy and coworkers (IBCP RAS, Russia) [55]. Development of double-sided SCs architectures for efficient indoor light harvesting opens a possibility to reach outstanding efficiencies. Bearing in mind that with the appropriate location of a PSC with more than 30 % efficiency [54], where low intensity diffuse lighting falls on the PSC surface from all sides, the efficiency of a double-sided photovoltaic device can be doubled, compared to the one-sided conventional scheme, and could reach the value of around 60 % efficiency per unit area.

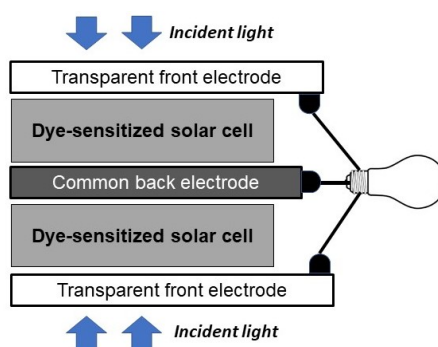


FIG. 5. Architecture of a double-sided DSC solar cell [55]

### 6.3. Current status of indoor photovoltaics

To date, the world production of solar cells, can be conventionally divided into the following categories: solar modules of a large area for powerful solar power plants that generate network electricity, modules for distributed systems of local consumers, and small-sized systems to power portable electronic devices [54]. In turn, the latter category also includes SCs for low-power autonomous SC devices and systems (energy harvesting) for the application in the enclosed areas under low-intensity artificial lighting. A decade ago DSCs only looked to be the most promising for this purpose, where they demonstrated obvious advantages [56,57]. Unlike conventional SCs, DSCs demonstrated a unique advantage of maintaining high indoor efficiency in low-intensity artificial lighting [58]. Despite the obvious interest in using DSCs for these purposes, there appeared only a few significant publications on DSCs in indoor environments under ambient lighting conditions [59–62]. The main milestone lies in a significant difference between the AM1.5G solar radiation spectrum and the illumination parameters, adapted for indoor work with predominantly artificial light. In the spectrum of the incident solar radiation AM1.5G, almost half of the energy is in the infrared range. However, the limits of spectral absorption in conventional SCs based on crystalline silicon or chalcogenide (CIGS) are located in the region of 1000 nm. The same concerns and PSCs while for both several requirements should be met for efficient indoor operation. Fig. 5 shows the results which demonstrate the remarkable difference between c-Si and perovskite solar cell behavior under varied illumination.

Alternatively, photovoltaic devices for the enclosed areas explores the behavior of the elements in artificial light from the following light sources: incandescent bulbs, fluorescent lamps CFL (compact fluorescent lights) and LED sources [63]. The intensity of the lighting sources when working indoors depends heavily on many factors, including the type of room, the location of the SC, its orientation, etc., which can vary widely from dozens of  $\mu\text{W}/\text{cm}^2$  to dozens of  $\text{mW}/\text{cm}^2$  [64]. The intensity of indoor lighting is measured in lx ( $\text{lm}/\text{m}^2$ ) and can be correlated with  $P(\text{W}/\text{m}^2)$  insolation capacity through the appropriate formulas. Typically, artificial light sources with a light flow level of 200 – 500 lx or solar simulators with a radiation capacity of 50 – 5  $\mu\text{W}/\text{cm}^2$  are used to study and operate SCs indoors. In accordance with the standards established, the minimum lighting values in the office space should be within 200 – 500 lx. It is also accepted that the lighting levels of the rooms correspond appropriately to: (1) low-light (0 – 200 lx, or 0 – 180  $\mu\text{W}/\text{cm}^2$ ); (2) medium light (200 – 500 lx, or 180 – 450  $\mu\text{W}/\text{cm}^2$ ), and (3) high light (> 500 lx, or > 450  $\mu\text{W}/\text{cm}^2$ ). The scope of the ongoing scientific efforts for the constructing PSCs with specific characteristics is directly related to the emerging of new direction in the world, called “Energy harvesting” (also “Energy scavenging”), i.e. collection and accumulation of low-density energy from non-carbon sources, such as sun, wind, thermal, gradient and kinetic energy. The introduction of “Energy harvesting” ideology in the industrial world is aimed at using small amounts of energy (the “small-cut” energy collection) to power electronic devices with low energy consumption, primarily for small low energy wireless standalone devices like sensors, switches, “smart dust” etc. PV energy harvesting is a low-density solar energy collection that combines a combination of technologies to

generate SC electricity in low-light environments indoors, and as a result of accumulation energy using batteries or supercapacitors. Initially such devices were powered by SCs on the basis of amorphous silicon (a-Si), the effectiveness of which, unlike other types of solid-state SCs, was less dependent on the light intensity. It is important to emphasize that efficiency of a-Si SCs under low lighting conditions does not exceed 4 – 5 % [65]. Alternatively, DSCs in similar conditions may show 4 times greater efficiency exceeding 20 % while PSCs promise to reach more than 30 % efficiency [54]. It denotes that the required lighting period for powering the indoor electronic device using PSC will be 5 times less than in case of using conventional a-Si SC for this purpose.

### 7. New materials for PSC fabrication: efficient nanocrystalline photoelectrodes

In PSCs, the photoelectrode plays a key role of the electron transport layer, which transfers charge carriers generated by a perovskite layer, absorbing photons, to the back contact of the device. To be effective, the electron transport layer should minimize the recombination processes at the perovskite/electrode interface. While a number of different metal oxides have been examined to find a proper electron transport material for this purpose the best performance was reached using a conventional TiO<sub>2</sub> layer [66, 67]. A sufficient increase of electron transport parameters in TiO<sub>2</sub> mesoscopic electrodes can be gained by niobium doping that was first used in Nb-doped TiO<sub>2</sub> photoelectrodes for DSCs [68–70]. It was shown that with the increase of Nb concentration from 0 to 3 mol.% the conductivity of a nanocrystalline layered TiO<sub>2</sub> photoelectrode was also increased [69, 71]. Later, a similar behavior was observed in PSCs where the use of a TiO<sub>2</sub> layer doped with Nb content of 2.7 mol.%, which resulted in 19 % improvement of a power conversion efficiency [72, 73]. The transmittance spectra in Nb-doped TiO<sub>2</sub> photoelectrodes presented in Fig. 6 have shown a blue shift, which was increased with doping concentration. Thus, the TiO<sub>2</sub> band gap increases with doping from 3.0 eV in the undoped sample to 3.2 eV in 2.7 mol.% Nb doped TiO<sub>2</sub>.

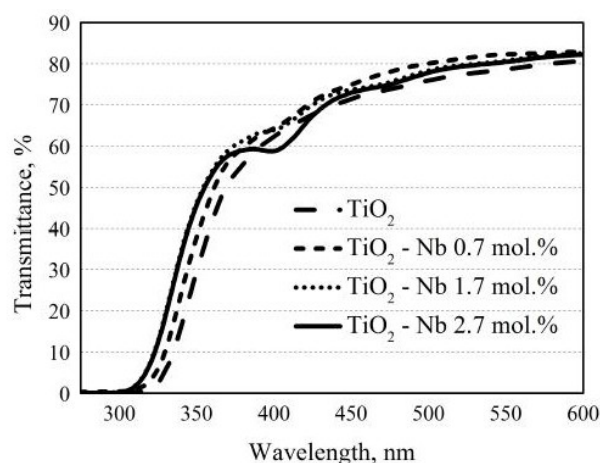


FIG. 6. Optical transmittance of Nb-doped TiO<sub>2</sub> layers with varied Nb content [72]

The new trend of the last few years is the application of very wide-band gap oxides, such as ZrO<sub>2</sub>, with  $E_g \sim 6$  eV [74]. Nanostructured layers based on a very large band gap metal oxides provide effective electron transfer, even when the electron density in the conduction band remains negligible [75]. The effective electron conduction through the nanostructured ZrO<sub>2</sub> observed was explained on the basis of the hopping conduction mechanism through localized states within forbidden zone of ZrO<sub>2</sub> [74, 75]. Fig. 7 shows schematic energy band diagrams demonstrating the energy band structure for PSCs based on a ZrO<sub>2</sub> photoelectrode (Fig. 7a) and on traditional TiO<sub>2</sub> photoelectrode (Fig. 7b). The band diagram in Fig. 7a demonstrates that the conduction band edge of perovskite has the energy above the conduction band edge of TiO<sub>2</sub> photoelectrode that enables a classic photoexcited electron transfer from the conduction band of perovskite layer to the conduction band of a TiO<sub>2</sub> photoelectrode [76].

In order to change the optoelectronic characteristics of a ZrO<sub>2</sub> it can be doped with yttrium oxide (Y<sub>2</sub>O<sub>3</sub>), which permits a more suitable design for the photoelectrode based on ZrO<sub>2</sub>-Y<sub>2</sub>O<sub>3</sub> nanostructured material [77]. Doping with rare-earth metals was shown to improve the transport characteristics of the photoelectrodes and increased the efficiency of the PSCs. It was recently reported the construction and investigation of PSCs with a device architecture of glass/FTO/ZrO<sub>2</sub>-Y<sub>2</sub>O<sub>3</sub>/CH<sub>3</sub>NH<sub>3</sub>PbI<sub>3</sub>/spiro-MeOTAD/Au, in which the doping content of Y<sub>2</sub>O<sub>3</sub> in ZrO<sub>2</sub>-Y<sub>2</sub>O<sub>3</sub> was varied from 0 to 10 mol.% [76].

Figure 8 demonstrates a comparative view of diffuse reflection spectra ( $R$ ) for undoped ZrO<sub>2</sub> and for ZrO<sub>2</sub>-Y<sub>2</sub>O<sub>3</sub> powders where the Y<sub>2</sub>O<sub>3</sub> content varies from 3 to 10 mol.%. The  $E_g$  values for ZrO<sub>2</sub> and ZrO<sub>2</sub>-Y<sub>2</sub>O<sub>3</sub> system

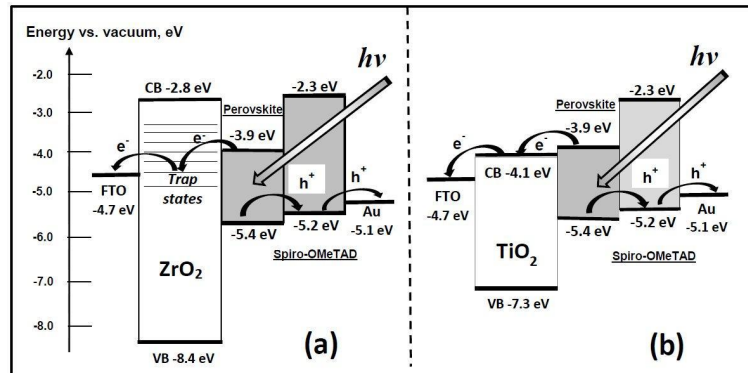


FIG. 7. Schematic energy band diagrams for PSCs based on  $\text{ZrO}_2$  (a) and  $\text{TiO}_2$  photoelectrodes (b) [76]

were obtained from the linear extrapolation of  $(\alpha h\nu)^2$  which revealed that the increase of doping concentration also increases the  $E_g$  value from 5.74 eV in  $\text{ZrO}_2$  to 5.63 eV in  $\text{ZrO}_2\text{-Y}_2\text{O}_3$  (3 %) [76].

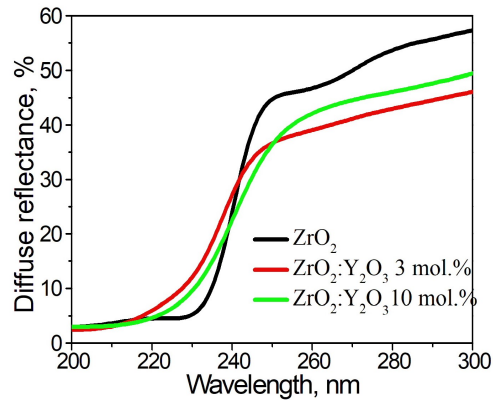


FIG. 8. Diffuse reflectance spectra for the powders of undoped  $\text{ZrO}_2$  and  $\text{ZrO}_2\text{-Y}_2\text{O}_3$  system [76]

Figure 9 presents I-V characteristics, recorded for PSCs under standard illumination conditions AM1.5 G. A comparison between the efficiencies of the PSCs fabricated with pristine and  $\text{Y}_2\text{O}_3$ -doped  $\text{ZrO}_2$  photoelectrodes clearly shows the advantages of the doped systems which sufficiently increases the short circuit currents and fill factors of PSCs, thus increasing the power conversion efficiencies.

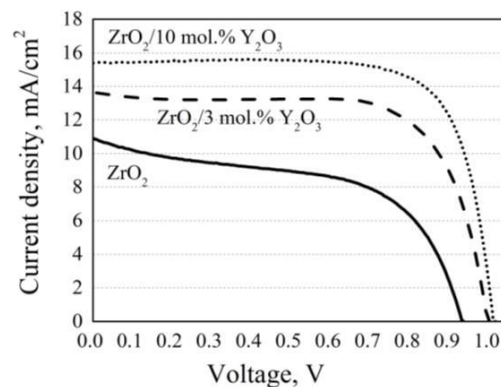


FIG. 9. J-V characteristics of the PSCs based on  $\text{ZrO}_2\text{-Y}_2\text{O}_3$  photoelectrodes [76]

## 8. High efficiency tandem PSC/c-Si solar cells

Initially, tandem configurations with transparent top cells were successfully applied for the design of tandem DSC/c-Si solar cells [79] and tandem DSC/PSC solar cells [78, 79]. However, in the meantime the most promising design comprise the combination of perovskite and silicon solar cells [81]. Tandem perovskite-silicon solar cell with the optimized design of the perovskite top cell and c-Si bottom cell reached certified efficiencies of 26.7 % [24]. Very recently Oxford PV declared 28.0 % efficiency tandem perovskite-silicon solar cell while Helmholtz-Zentrum Berlin (HZB) announced a certified efficiency of 29.15 %. However, in both cases no scientific publications appeared to-date.

Here, we focus on the structural adjustment of the top cell based on the structural evolution of perovskite/silicon tandem solar cells to improve their performance [81, 82]. To date, c-Si-based SCs under AM1.5G lighting conditions have demonstrated an efficiency greater than 25 %, but it is already approaching their practical limit. Further increase in the efficiency of c-Si cells is possible in case of integrating into the tandem structures. For the construction of a tandem system, in which a solid c-Si solar cell is used as bottom element, we need partially transparent SC as a top device, through which with minimal losses passes a certain part of the solar spectrum, corresponding to the of optical absorption characteristics of the bottom cell.

Extensive possibilities for the design of tandem cells are associated with the recent appearance of effective thin-film transparent cells based on organic materials, DSCs and PSCs. PSCs opened a new promising research area, focused on the development and study of different configurations for tandem structures on their basis. The best results to-date are obtained using so-called 4T-configuration in the four-terminal tandem perovskite-silicon solar cell PSC/c-Si [24]. Fig. 10 demonstrates the difference between the two-terminal and four-terminal configurations used for construction of tandem perovskite-silicon solar cells.

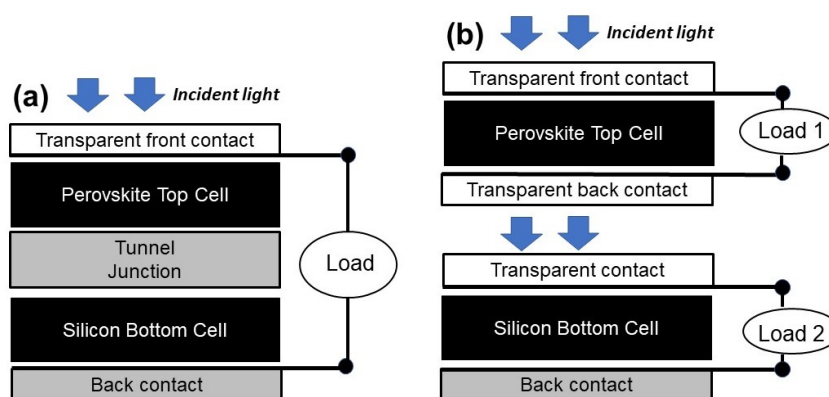


FIG. 10. Monolithic two-terminal (a) and four-terminal (b) tandem perovskite-silicon solar cells

While PSCs show the efficiencies exceeding 20 %, the combination of the overlapping optical absorption areas for PSC and c-Si elements, which possess, respectively, a width of 1.6 eV (PSC) and 1.1 eV (c-Si) opens a possibility of obtaining in this configuration the efficiency of tandem PSC/c-Si cells exceeding 30 % [82]. A number of papers describe the effective PSC/c-Si tandem solar cells. The design of such a tandem may use one of two possibilities. The first one can concern the design of monolithic SC based on the so-called two-terminal tandem solar cell, where the top PSC is formed directly on the surface of the bottom c-Si SC, and its top electrical contact serves as both a bottom contact for the whole device (Fig. 10b) [36, 37]. In this configuration, the electrodes of both tandem elements are sequentially connected [81].

The monolithic two-terminal tandem cell has certain advantages, as it has only two output electrodes. However, from our point of view, the monolithic system possesses one fundamental flaw inherent in its scheme. When constructing any type of monolithic two-electrode tandem SC, either with a parallel or with a series connection of the individual elements, the main technical problem is to adjust their output electrical parameters (either by voltage or by current), which should provide the optimal parameters of I–V characteristics of the device to achieve the maximum efficiency under AM1.5G. However, with decreasing the illumination levels the efficiency of a two-terminal device may drop due to the disproportionate deviation of the parameters for each cell.

These problems can be solved by using the so-called four-terminal solar cell, in which the two elements are combined not electrically, but “mechanically stacked”, i.e. have a common optical circuit, while their electrical contacts are not connected to each other [83]. It is implied that the electrical power is generated by the top and bottom elements independently. The generated power is then transferred to the electronically controlled device, the task of which is to

adjust their output parameters (Fig. 10a). The power consumed by such an electronic converter is negligible and will not result neither in the power losses nor in the efficiency of the entire solar cell system.

## 9. Conclusion

In this review, we focused on the latest achievements in the construction of the efficient PSCs and described new trends in perovskite solar photovoltaics, including the development of high-performance perovskite-silicon tandem solar cells, inorganic PSCs with stabilized efficiency and a new generation of PSCs for low lighting conditions that opens great possibilities for indoor applications. Special attention was paid to the development of new types of efficient photoelectrodes for PSCs based on very large band gap metal oxides.

## Acknowledgements

The author gratefully acknowledges the support from the Russian Foundation for Basic Research by grant No. 19-18-50429.

## References

- [1] Yin J., Molini A., Porporato A. Impacts of solar intermittency on future photovoltaic reliability. *Nature Communications*, 2020, **11**, 4781.
- [2] Shi Z., Jayatissa A.H. Perovskite solar cells: from the atomic level to film quality and device performance. *Materials*, 2018, **57**, P. 2554–2569.
- [3] Kojima A., Teshima K., Shirai Y., Miyasaka T. Organometal halide perovskites as visible-light sensitizers for photovoltaic cells. *J. Am. Chem. Soc.*, 2009, **131**, P. 6050–6051.
- [4] Kim H.S., Lee C.R., et al. Lead iodide perovskite sensitized all-solid-state submicron thin film mesoscopic solar cell with efficiency exceeding 9%. *Sci. Rep.*, 2012, **2**, 591, P. 1–7.
- [5] Burschka J., Pellet N., et al. Sequential deposition as a route to high-performance perovskite-sensitized solar cells. *Nature*, 2013, **499**, P. 316–319.
- [6] Im J.H., Lee C. R., et al. 6.5% efficient perovskite quantum-dot-sensitized solar cell. *Nanoscale*, 2011, **3**, P. 4088–4093.
- [7] Lee M.M., Teuscher J., et al. Efficient hybrid solar cells based on meso-structured organometal halide perovskites. *Science*, 2012, **338**, P. 643–647.
- [8] Ahn N., Son D.-Y., et al. Highly reproducible perovskite solar cells with average efficiency of 18.3% and best efficiency of 19.7% fabricated via Lewis base adduct of lead(II) iodide. *J. Am. Chem. Soc.*, 2015, **137**, P. 8696–8699.
- [9] Park N.-G. Research direction toward scalable, stable, and high efficiency perovskite solar cells. *Adv. Aenerg. Mater.*, 2019, **13**, 1903106.
- [10] Jeon N.J., Noh J.H., et al. Solvent engineering for high-performance inorganic–organic hybrid perovskite solar cells. *Nat. Mater.*, 2014, **13**, P. 897–903.
- [11] Kim H.S., Lee C.R., et al. Lead iodide perovskite sensitized all-solid-state submicron thin film mesoscopic solar cell with efficiency exceeding 9%. *Sci. Rep.*, 2012, **2**, 591.
- [12] Song Z., Wathage S.C., et al. Pathways toward high-performance perovskite solar cells: review of recent advances in organo-metal halide perovskites for photovoltaic applications. *J. Photon. Energ.*, 2016, **6**, 022001.
- [13] Nazeeruddin M.K., Snaith H. Methylammoniumlead triiodide perovskite solar cells: a new paradigm in photovoltaics. *MRS Bulletin*, 2015, **40**, P. 641–645.
- [14] Saliba M., Matsui T., et al. Cesium-containing triple cation perovskite solar cells: improved stability, reproducibility and high efficiency. *Energ. Environ. Sci.*, 2016, **9**, P. 1989–1997.
- [15] Saliba M., Matsui T., et al. Incorporation of rubidium cations into perovskite solar cells improves photovoltaic performance. *Science*, 2016, **354**, P. 206–209.
- [16] Crystalline Silicon Photovoltaic Module Manufacturing Costs and Sustainable Pricing, URL: <https://www.nrel.gov/docs/fy19osti/72134.pdf>.
- [17] Shin S.S., Yeom E.J., et al. Colloidally prepared La-doped BaSnO<sub>3</sub> electrodes for efficient, photostable PSCs. *Science*, 2017, **356**, P. 167–171.
- [18] Quiroz R.C.O., Shen Y., et al. Balancing electrical and optical losses for efficient 4-terminal Si–PSCs with solution processed percolation electrodes. *J. Mater. Chem. A*, 2018, **6**, P. 3583–3592.
- [19] Kumar M.H., Yantara N., et al. Flexible, low-temperature, solution processed ZnO-based perovskite solid state solar cells. *Chem. Commun.*, 2013, **49**, P. 11089–11091.
- [20] Shi Z., Jayatissa A.H. Perovskite-based solar cells: a review of recent progress, materials and processing methods. *Materials*, 2018, **11**, 729.
- [21] Cui, J., Yuan, H., et al. Recent progress in efficient hybrid lead halide PSCs. *Sci. Technol. Adv. Mater.*, 2015, **16**, 036004.
- [22] Yang W.S., Noh J.H., et al. High-performance photovoltaic perovskite layers fabricated through intramolecular exchange. *Science*, 2015, **348**, P. 1234–1237.
- [23] Shin S.S., Yeom E.J., et al. Colloidally prepared La-doped BaSnO<sub>3</sub> electrodes for efficient, photostable PSCs. *Science*, 2017, **356**, P. 167–171.
- [24] Rohatgi A., Zhu K., et al. 26.7% efficient 4-terminal perovskite–silicon tandem solar cell composed of a high-performance semitransparent perovskite cell and a doped poly-Si/SiO<sub>x</sub> passivating contact silicon cell. *IEEE Journal of Potovoltaics*, 2020, **10**, P. 417–422.
- [25] Leo K. Perovskite photovoltaics: signs of stability. *Nat. Nanotechnol.*, 2015, **10**, P. 574–575.
- [26] Burschka J., Pellet N., et al. Sequential deposition as a route to high-performance perovskite-sensitized solar cells. *Nature*, 2013, **499**, P. 316–319.
- [27] Liu M., Johnston M.B., Snaith H.J. Efficient planar heterojunction perovskite solar cells by vapour deposition. *Nature*, 2013, **501**, P. 305–308.
- [28] Li X., Dar M.I., et al. Improved performance and stability of perovskite solar cells by crystal crosslinking with alkylphosphonic acid  $\omega$ -ammonium chlorides. *Nat. Chem.*, 2015, **7**, P. 703–711.
- [29] Jeon N.J., Noh J.H., et al. Solvent engineering for high-performance inorganic–organic hybrid perovskite solar cells. *Nat. Mater.*, 2014, **13**, P. 897–903.

- [30] Ahn N., Son D.-Y., et al. Highly reproducible perovskite solar cells with average efficiency of 18.3% and best efficiency of 19.7% fabricated via Lewis base adduct of lead(II) iodide. *J. Am. Chem. Soc.*, 2015, **137**, P. 8696–8699.
- [31] Park N.-G., Grätzel M., et al. Towards stable and commercially available perovskite solar cells. *Nat. Energy*, 2016, **1**, 16152.
- [32] Jeon N.J., Noh J.H., et al. Compositional engineering of perovskite materials for high performance solar cells. *Nature*, 2015, **517**, P. 476–480.
- [33] Yang W.S., Noh J.H., et al. High-performance photovoltaic perovskite layers fabricated through intramolecular exchange. *Science*, 2015, **348**, P. 1234–1237.
- [34] Nazeeruddin M.K., Snaith H. Methylammoniumlead triiodide perovskite solar cells: a new paradigm in photovoltaics. *MRS Bulletin*, 2015, **40**, P. 641–645.
- [35] Song Z., Wathage S.C., et al. Pathways toward high-performance perovskite solar cells: review of recent advances in organo-metal halide perovskites for photovoltaic applications. *J. Photon. Energy*, 2016, **6**, 022001.
- [36] Sahli F., Werner J., et al. Fully textured monolithic perovskite/silicon tandem solar cells with 25.2% power conversion efficiency. *Nature Mater.*, 2018, **17**, P. 820–826.
- [37] Nogay G., Sahli F., et al. 25.1%-efficient monolithic perovskite/silicon tandem solar cell based on a p-type monocrystalline textured silicon wafer and high-temperature passivating contacts. *ACS Energy Lett.*, 2019, **4**, P. 844–849.
- [38] Zhou Y., Zhu K. Perovskite solar cells shine in the “Valley of the Sun”. *ACS Energy Lett.*, 2016, **1**, P. 64–67.
- [39] Schoonman J., Organic-inorganic lead halide perovskite solar cell materials: a possible stability problem. *Chem. Phys. Lett.*, 2015, **619**, P. 193–195.
- [40] Akbulatov A.F., Luchkin S.Yu., et al. Probing the intrinsic thermal and photochemical stability of hybrid and inorganic lead halide perovskites. *J. Phys. Chem. Lett.*, 2017, **8**, P. 1211–1218.
- [41] Adomin S.A., Froliva L.A., et al. Hybrid solar cells: antimony (V) complex halides: lead-free perovskite-like materials for hybrid solar cells. *Adv. Energy Mater.*, 2018, **8**, 1870026.
- [42] Swarnkar A., Marshall A.R., et al. Quantum dot-induced phase stabilization of  $\alpha$ -CsPbI<sub>3</sub> perovskite for high-efficiency photovoltaics. *Science*, 2016, **354**, P. 92–95.
- [43] Spurgeon S.R., Du Y., et al. Competing pathways for nucleation of the double perovskite structure in the epitaxial synthesis of La<sub>2</sub>MnNiO<sub>6</sub>. *Chem. Mater.*, 2016, **28**, P. 3814–3822.
- [44] Sheikh M.S., Ghosh D., et al. Lead free double perovskite oxides Ln<sub>2</sub>NiMnO<sub>6</sub> (Ln = La, Eu, Dy, Lu), a new promising material for photovoltaic application. *Mater. Sci. Eng. B*, 2017, **226**, P. 10–17.
- [45] Lan C., Zhao S., et al. Investigation on structures, band gaps, and electronic structures of lead free La<sub>2</sub>NiMnO<sub>6</sub> double perovskite materials for potential application of solar cell. *J. Alloy. Compd.*, 2016, **655**, P. 208–214.
- [46] Sheikh M.S., Sakhya A.P., et al. Light induced charge transport in La<sub>2</sub>NiMnO<sub>6</sub>-based Schottky diode. *J. Alloy. Compd.*, 2017, **727**, P. 238–245.
- [47] Barbosa D.A.B., Lufaso M.W., et al. Ba-doping effects on structural, magnetic and vibrational properties of disordered La<sub>2</sub>NiMnO<sub>6</sub>. *J. Alloy. Compd.*, 2016, **663**, P. 899–905.
- [48] Montcada N.F., Marín-Belouqui J.M., et al. Analysis of photoinduced carrier recombination kinetics in flat and mesoporous lead perovskite solar cells. *ACS Energy Lett.*, 2017, **2**, P. 182–187.
- [49] Zhang N., Chen D., et al. Enhanced visible light photocatalytic activity of Gd doped BiFeO<sub>3</sub> nanoparticles and mechanism insight. *Sci. Rep.*, 2016, **6**, 26467.
- [50] Freitag M., Teuscher, J., et al. Dye-sensitized solar cells for efficient power generation under ambient lighting. *Nat. Photonics*, 2017, **11**, P. 372–378.
- [51] Juang S.S.Y., Lin P.Y., et al. Energy harvesting under dim-light condition with dye-sensitized and perovskite solar cells. *Frontiers in Chemistry*, 2019, **7**, 00209.
- [52] Chen C.Y., Chang, J.H., et al. Perovskite photovoltaics for dim-light applications. *Adv. Funct. Mater.*, 2015, **25**, P. 7064–7070.
- [53] Biswas S., Kim H. Solar cells for indoor applications: progress and development. *Polymers*, 2020, **12**, 1338.
- [54] Lim J., Kwon H., et al. Unprecedentedly high indoor performance (efficiency >34 %) of perovskite photovoltaics with controlled bromine doping. *Nano Energy*, 2020, **75**, 104984.
- [55] Double-sided solar photoconverter (options). Varfolomeev S.D., Todinova A.V., Shevaleevskiy O.I. Patent. RU 2531768: MPK H01 L 31/04, 27.10.2014, Issue 30, P. 7.
- [56] Mathew S., Yella A., et al. Dye-sensitized solar cells with 13% efficiency achieved through the molecular engineering of porphyrin sensitizers. *Nat. Chem.*, 2014, **6**, P. 242–247.
- [57] Saygili Y., Soberger M., et al. Copper bipyridyl redox mediators for dye-sensitized solar cells with high photovoltage. *J. Am. Chem. Soc.*, 2016, **138**, P. 15087–15096.
- [58] Michaels H., Rinderle M., et al. Dye-sensitized solar cells under ambient light powering machine learning: towards autonomous smart sensors for the internet of things. *Chem Sci.*, 2020, **11**, P. 2895–2906.
- [59] Sakamoto R., Katagiri S., et al. Electron transport dynamics in redox-molecule-terminated branched oligomer wires on Au(111). *J. Am. Chem. Soc.*, 2015, **137**, P. 734–741.
- [60] Mathews I., King P.J., et al. Performance of III–IV solar cells as indoor light energy harvesters. *IEEE J. Photovolt.*, 2016, **6**, P. 230–235.
- [61] Barber G., Hoertz P.G., et al. Utilization of direct and diffuse sunlight in a dye-sensitized solar cell-silicon photovoltaic hybrid concentrator system. *J. Phys. Chem. Lett.*, 2011, **2**, P. 581–585.
- [62] Lechene B., Cowell P. et al. Organic solar cells and fully printed super-capacitors optimized for indoor light energy harvesting. *Nano Energy*, 2016, **26**, P. 631–640.
- [63] Minnaert B., Veelaert P., et al. A proposal for typical artificial light sources for the characterization of indoor photovoltaic applications. *Energies*, 2014, **7**, P. 1500–1516.
- [64] Freunek M., Freunek M., Reindtl L.M. Maximum efficiencies of indoor photovoltaic devices. *IEEE J. Photovoltaics*, 2013, **3**, P. 59–64.
- [65] Apostolou G., Reiders A., Verwaal M. Comparison of the indoor performance of 12 commercial PV products by a simple mode. *Energy Science & Engineering*, 2016, **4**, P. 69–85.
- [66] Su T.S., Hsieh T.Y., et al. Electrodeposited ultrathin TiO<sub>2</sub> blocking layers for efficient perovskite solar cells. *Scientific reports*, 2015, **5**, 16098.
- [67] Murugadoss G., Mizuta G., et al. Double functions of porous TiO<sub>2</sub> electrodes on CH<sub>3</sub>NH<sub>3</sub>PbI<sub>3</sub> perovskite solar cells: enhancement of perovskite crystal transformation and prohibition of short circuiting. *APL Materials*, 2014, **2**, 081511.

- [68] Kozlov S., Nikolskaia A., et al. Rare earth and Nb doping of TiO<sub>2</sub> nanocrystalline mesoscopic layers for high efficiency dye sensitized solar cells. *Physica status solidi A*, 2016, **213**, P. 1801–1806.
- [69] Tsvetkov N., Larina L., Shevaleevskiy O., Ahn B.T. Electronic structure study of lightly Nb doped TiO<sub>2</sub> electrode for dye sensitized solar cells. *Energ. Environ. Sci.*, 2011, **4**, P. 1480–1486.
- [70] Tsvetkov N.A., Larina L.L., et al. Design of conduction band structure of TiO<sub>2</sub> electrode using Nb doping for highly efficient dye sensitized solar cells. *Progress in Photovoltaics: Research and Applications*, 2012, **20**, P. 904–911.
- [71] Kozlov S., Nikolskaia A., et al. Rare earth and Nb doping of TiO<sub>2</sub> nanocrystalline mesoscopic layers for high efficiency dye-sensitized solar cells. *Phys. St. Sol. A*, 2016, **213**, P. 1801–1806.
- [72] Vildanova M.F., Kozlov S.S., Nikolskaia A.B., Shevaleevskiy O.I. Niobium-doped titanium dioxide nanoparticles for electron transport layers in perovskite solar cells. *Nanosystems: Phys. Chem. Math.*, 2017, **8**, P. 540–545.
- [73] Shevaleevskiy O.I., Nikolskaya A.B., et al. Nanostructured TiO<sub>2</sub> films with a Mixed Phase for Perovskite Solar Cells. *Rus. J. Phys. Chem. B*, 2018, **12**, P. 663–668.
- [74] Rath M.S., Ramakrishna G., Mukherjee T., Ghosh H.N. Electron injection into the surface states of ZrO<sub>2</sub> nanoparticles from photoexcited quinizarin and its derivatives: effect of surface modification. *J. Phys. Chem. B*, 2005, **109**, P. 20485–20492.
- [75] Bugrov A.N., Almjashaeva O.V. Effect of hydrothermal synthesis conditions on the morphology of ZrO<sub>2</sub> nanoparticles. *Nanosystems: Phys. Chem. Math.*, 2013, **4**, P. 810–815.
- [76] Larina L.L., Alexeeva O.V., et al. Very wide-band gap nanostructured metal oxide materials for perovskite solar cells. *Nanosystems: Phys. Chem. Math.*, 2019, **10**, P. 70–75.
- [77] Almjashaeva O.V., Krasilin A.A., Gusarov V.V. Formation mechanism of coreshell nanocrystals obtained via dehydration of coprecipitated hydroxides at hydrothermal conditions. *Nanosystems: Phys. Chem. Math.*, 2018, **9**, P. 568–572.
- [78] Choi Y., Kim C.U., et al. Two-terminal mechanical perovskite/silicon tandem solar cells with transparent conductive adhesives. *Nano Energy*, 2019, **65**, 104044.
- [79] Nikolskaia A.B., Vildanova M.F., Kozlov S.S., Shevaleevskiy O.I., Two-terminal tandem solar cells DSC/c-Si: optimization of TiO<sub>2</sub>-based photoelectrode parameters. *Semiconductors*, 2018, **52**, P. 88–92.
- [80] Vildanova M.F., Nikolskaia A.B., Kozlov S.S., Shevaleevskiy O.I. Novel types of dye-sensitized and perovskite-based tandem solar cells with a common counter electrode. *Technical Physics Letters*, 2018, **44**, P. 126–129.
- [81] Wali Q., Elumalai N.K., et al. Tandem perovskite solar cells. *Renewable and Sustainable Energy Reviews*, 2018, **84**, P. 89–110.
- [82] Quiroz C.O., Shen, Y., et al. Balancing electrical and optical losses for efficient 4-terminal Si–perovskite solar cells with solution processed percolation electrodes. *J. Mater. Chem. B*, 2018, **6**, P. 3583–3592.
- [83] Jaysankar M., Filipic M., et al. Perovskite–silicon tandem solar modules with optimised light harvesting. *Energ. Environ. Sci.*, 2018, **11**, P. 1489–1498.

## Structure of nanoparticles in the $ZrO_2$ – $Y_2O_3$ system, as obtained under hydrothermal conditions

A. I. Shuklina<sup>1</sup>, A. V. Smirnov<sup>2</sup>, B. A. Fedorov<sup>2</sup>, S. A. Kirillova<sup>1</sup>, O. V. Almjashaeva<sup>3</sup>

<sup>1</sup>Saint Petersburg State Electrotechnical University “LETI”,  
ul. Professora Popova, 5, Saint Petersburg, 197376, Russia

<sup>2</sup>ITMO University, Kronverksky Pr. 49, bldg. A, Saint Petersburg, 197101, Russia

<sup>3</sup>Ioffe Institute, Politekhnikeskaya St. 26, Saint Petersburg, 194021, Russia  
almjasheva@mail.ru

PACS 61.46.+w, 81.40.-z

DOI 10.17586/2220-8054-2020-11-6-729-738

It is shown that monocrystalline nanoparticles with fluorite structure are formed in the  $ZrO_2$ – $Y_2O_3$  system, under hydrothermal conditions. The limiting content of  $Y_2O_3$  in the nanocrystals based on zirconium dioxide is 21.7–22.6 mol.%. Yttrium oxide not included in the structure forms an amorphous phase, which is stable even upon thermal treatment at 1000–1300 °C. It has been found that under hydrothermal conditions the structure of the nanocrystals based on  $ZrO_2(Y_2O_3)$  solid solution includes water, its content depending on yttrium oxide concentration in the solid solution.

**Keywords:** nanocrystals, hydrothermal synthesis, solid solution, zirconia.

*Received: 10 August 2020*

*Revised: 15 October 2020*

### 1. Introduction

Due to the presence of several polymorphic modifications [1–4] zirconium dioxide is of interest as a model for studying the effect of the synthesis methods and parameters on the formation of nanocrystals with different structure [5–15]. Zirconium dioxide based nanomaterials with various structures, morphologies, and particle size parameters have a wide range of applications [16–27], which makes the above studies relevant from a practical point of view as well.

In particular, papers [20, 21] show the perspective of using the photoelectrodes based on nanocrystals formed in the  $ZrO_2$ – $Y_2O_3$  system in perovskite solar cells. At the same time, it is noted in these works that the change in the band gap in such materials may depend not only on their composition, but also on the features of the nanoparticle structure [20, 21]. As known, the band gap and other properties of functional materials can be sensitive to the methods and parameters of synthesis [5–12, 23, 28–32]. As mentioned in papers [28–30], one of the specific features of formation of the nanoparticles based on solid solutions in the  $ZrO_2$ – $M_2O_3$  ( $M = Gd_2O_3, Y_2O_3, In_2O_3$ ) systems is the possibility of forming the nanoparticles with a “core-shell” structure. Studying the possibility of forming the nanoparticles with a particular structure and particular dimensional parameters, depending on the method and conditions of synthesis, will make it possible to intentionally synthesize the nanoparticles with the required properties.

The perspectives of using the  $ZrO_2(Y_2O_3)$  nanocrystals to convert solar energy necessitate a systematic study of the formation processes of nanomaterials with a certain structure, morphology and dimension parameters of the particles. The present study is aimed at solving these issues.

### 2. Experimental part

Zirconium dioxide based nanoparticles in the  $ZrO_2$ – $Y_2O_3$  system were obtained, in a wide range of the components’ ratios, by dehydration of co-precipitated hydroxides under hydrothermal conditions, according to the method described in [6].

The precipitation was carried out from a mixture of aqueous solutions of zirconium oxychloride ( $ZrOCl_2 \cdot 8H_2O$ , chemically pure (TU 6-09-3677-74)) and yttrium chloride ( $YCl_3 \cdot 6H_2O$ , pure (TU 6-09-4773-79)), with 12 M ammonium hydroxide solution ( $NH_4OH$ , reagent grade (GOST 3760-79)). The obtained precipitates were rinsed with distilled water and dried at a temperature of 100 °C. Hydrothermal treatment was carried out at a temperature  $T = 250$  °C and pressure  $P = 70$  MPa. Time of the hydrothermal treatment was recorded according to the duration of isothermal holding of autoclaves in the furnace. The duration of isothermal holding was 4 h.

The elemental composition was determined by energy-dispersive X-ray spectroscopy (EDS) with the use of a scanning electron microscope (Hitachi S-570) with energy-dispersive analyzer (Bruker Quantax 220).

The structural state of the samples and the parameters of the unit cells were determined from the data of X-ray powder diffraction obtained using Shimadzu XRD-7000 X-ray diffractometer. Diffractograms were taken using  $\text{CuK}\alpha$  radiation in the range of angles  $2\theta$  from 10 to 60 °C. When determining the unit cell parameters of compounds in the samples, silicon was introduced as an internal standard.

To study the structural changes during heating, the Shimadzu XRD-7000 diffractometer is equipped with a high temperature furnace (Anton Paar HTN 1200 K). The sample was air-heated from room temperature to 1100 °C, with a stop after every 100 °C. At each temperature step, the isothermal holding time was 10 min.

Dimensional parameters of the crystallites were determined from the data on the X-ray diffraction lines' profile. The crystallites' distribution was determined using software (SmartLabStudio II). Average dimensions of the crystallites were calculated using the Scherrer formula and also data on the crystallites' size distribution.

The dimensional characteristics of nanoparticles were determined from the data of small-angle X-ray scattering [33, 34]. Two methods were applied for the calculation, i.e. the "Guinier method" [33] and the method of "standard curves" [34]. The small-angle measurements were made using Kratky block-camera.  $\text{CuK}\alpha$  radiation was used. The absorption factor of the sample was determined using an attachment with a moving slit.

The pycnometric density was measured by helium pycnometry, using the gas pycnometer Ultra Pycnometer 1000 (Quanta Chrome). For measurements, all the samples were pre-dried at 100 °C for 30 minutes. The measurements were carried out in a 10 cm<sup>3</sup> cell, with preliminary degassing of the sample for 5 min. in stream mode. The number of consecutive measurements was 10, the preset limit of measurement error was maximum 0.01 g/cm<sup>3</sup>.

Thermal transformations were studied by differential scanning calorimetry combined with thermogravimetric analysis, using the thermal analyzer NETZSCH (STA 429CD).

### 3. Results and discussion

The results of elemental analysis showed that, subject to the method sensitivity limits, there were no elements other than Zr, Y, O. According to EDS analysis, subject to error limits of the method, the ratio of elements, in terms of the oxides  $\text{ZrO}_2$  and  $\text{Y}_2\text{O}_3$ , corresponded to (nominal) composition of the samples specified for the synthesis, as shown in Table 1.

TABLE 1. Results of elemental analysis of the samples based on the system  $\text{ZrO}_2\text{-Y}_2\text{O}_3$

Content of $\text{YO}_{1.5}$ in the system, mol.%	
Nominal composition	EDS
5	5.0
8	8.6
12	12.0
15	16.4
20	19.7
25	23.3
30	31.0
45	46.4
55	57.2

According to X-ray diffraction analysis, all the samples obtained by co-precipitation of the components were X-ray amorphous. After their hydrothermal treatment at 250 °C, for 4 h, at  $\text{Y}_2\text{O}_3$  content in the samples of up to 46.4 mol.%, zirconium dioxide based phases with fluorite structure (Fig. 1a) were formed. For the sample containing 57.2 mol.%  $\text{Y}_2\text{O}_3$ , narrow peaks corresponding to  $\text{Y}(\text{OH})_3$  were recorded (Fig. 1b) against the background of X-ray maxima corresponding to the zirconium dioxide based phase with fluorite structure.

Based on the X-ray diffraction data, parameter values of the unit cell of the zirconium dioxide based phase with fluorite structure were calculated, and the unit cell parameter was plotted against the amount of yttrium oxide in the system (Fig. 2). The obtained values correlate well with literature data, up to the  $\text{Y}_2\text{O}_3$  content in the system corresponding to 19.7 mol.%, and can be described by a linear relationship:

$$a(x) = a_0 + \alpha \cdot x, \quad (1)$$

where  $a$  is a parameter of the cubic unit cell of the phase based on zirconium dioxide with fluorite structure;  $x$  is content of  $\text{YO}_{1.5}$  in the system  $\text{ZrO}_2\text{-YO}_{1.5}$ , expressed in mole fractions;  $a_0 = 5.116 \pm 0.004 \text{ \AA}$ ,  $\alpha = 0.29 \text{ \AA/mole}$

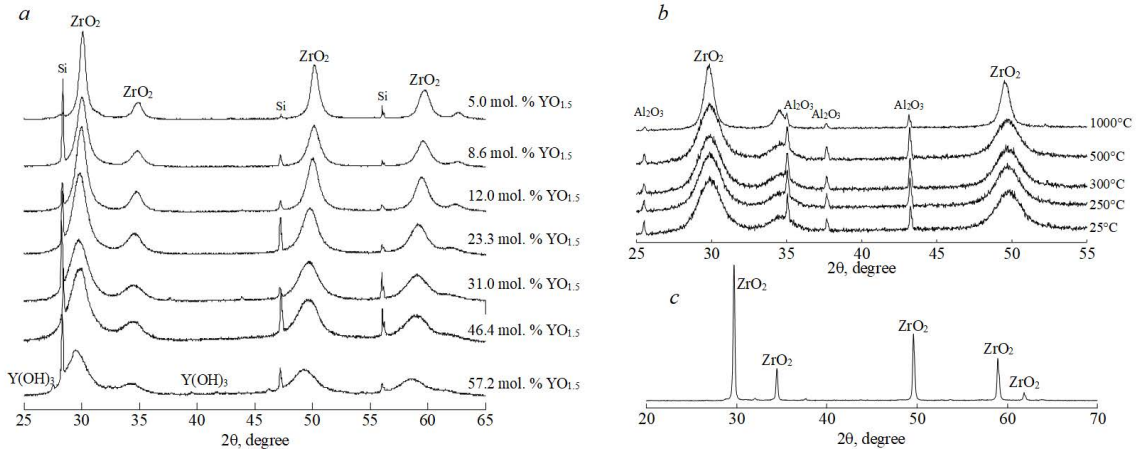


FIG. 1. X-ray diffractograms of the samples in the system  $ZrO_2$ - $YO_{1.5}$ : (a) samples obtained by hydrothermal treatment of co-precipitated hydroxides at  $T = 250\text{ }^\circ\text{C}$ ,  $P = 70\text{ MPa}$ ,  $\tau = 4\text{ h}$  (Si – peaks of the internal standard); (b) the sample containing 31.0 mol.%  $Y_2O_3$ , after heat treatment during high temperature X-ray diffraction ( $Al_2O_3$  – peaks of the high temperature cell); (c) the sample containing 46.4 mol.%  $Y_2O_3$ , after additional heat treatment by air at  $T = 1300\text{ }^\circ\text{C}$

fractions. However, starting from  $YO_{1.5}$  content in the system of 19.7 mol.%, the dependence of  $a(x)$  greatly deviates from the straight line (1), actually taking the following form in the range 31.0–46.4 mol.%  $Y_2O_3$ :

$$a(x) = a_\infty, \tag{2}$$

where  $a_\infty$  is a constant, which in this case equals to the value  $a_\infty = 5.178 \pm 0.002$ .

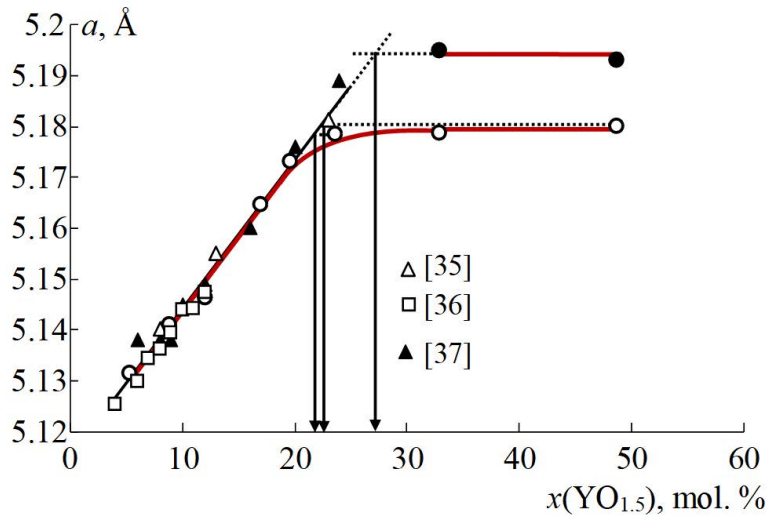
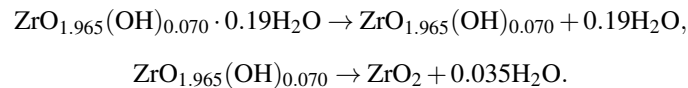


FIG. 2. Unit cell parameter vs. amount of yttrium oxide in the system

The independence of the unit cell parameter on the phase composition indicates that increasing of yttrium oxide content in the system does not lead to increase in its concentration in the phase of variable composition –  $Zr_{(1-x)}Y_xO_{(2-0.5x)}$ . The fact that in this range of compositions the X-ray diffractogram does not show any other crystalline phases leads one to conclude that yttrium oxide not included in the structure of the variable composition phase based on zirconium dioxide is in X-ray amorphous state. In papers [28, 29] this state was classified as a state of yttrium oxide in the X-ray amorphous shell surrounding nanocrystalline particles. Thus, in the range of  $Y_2O_3$  content of 23.3 to 46.4 mol.%, a noticeable amount of amorphous phase can be expected in the system, since the concentration  $Y_2O_3$  in these samples, as calculated from the data on the unit cell parameter values, varies in the range 21.7–22.6 mol.%, i.e. differs from the system composition.

After high temperature treatment, the X-ray diffraction data (Fig. 1) showed that the system comprising 31.0 and 46.4 mol.%  $Y_2O_3$  did not contain any other crystalline phases except for the phase of variable composition with fluorite structure. Meanwhile, based on the data on the unit cell parameter values of the variable composition phase  $Zr_{(1-x)}Y_xO_{(2-0.5x)}$  with fluorite structure for these samples (Fig. 2.), we can conclude that yttrium oxide concentration therein equals to  $x \approx 0.272$  mole fractions ( $\approx 27.2$  mol.%  $Y_2O_3$ ), i.e. significantly less than the content of yttrium oxide in the system. Thus, even after thermal treatment a significant portion of yttrium oxide remains in the X-ray amorphous state. However, based on the state diagram of the system  $ZrO_2$ – $Y_2O_3$  [1–4] we could expect yttrium oxide entering the solid solution at a treatment temperature of 1000–1300 °C. Apparently, insufficient thermal treatment time does not allow the formation of  $Zr_{(1-x)}Y_xO_{(2-0.5x)}$  phase with fluorite structure of equilibrium composition, and spatial constraints, presented as grains of the zirconium dioxide based phase with fluorite structure, do not allow the transformation of the amorphous phase based on yttrium oxide into crystalline one. The possibility of realizing such an effect was noted in [38] and was theoretically analyzed in [39].

As shown in [40], in the course of heat treatment nanocrystalline zirconium dioxide loses water in several stages, at different temperatures. However, the weight loss is associated not only with the removal of the surface adsorbed water, but also with composition change and with the corresponding structural transitions in the nanocrystals based on zirconium dioxide, in the temperature range 200–500 °C [40, 41]:



A similar situation, as Fig. 3 shows, is observed in the samples based on the system  $ZrO_2$ – $Y_2O_3$ . When studying the samples behavior by means of synchronous thermal analysis, prominent endothermic effect is observed in the range of temperatures of  $\sim 25$ – $150$  °C, which is accompanied by weight loss and corresponds to the removal of water adsorbed on the nanoparticles surface. At higher temperatures, two more steps of water loss in the samples are observed: in the range of temperatures of  $\sim 150$ – $570$  °C and  $\sim 570$ – $1120$  °C, respectively.

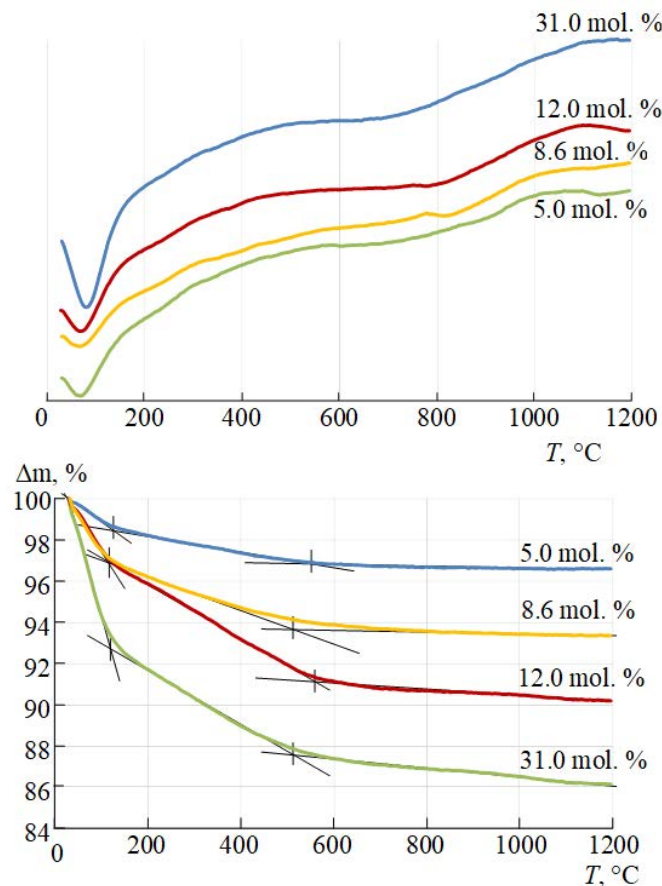


FIG. 3. Results of synchronous thermal analysis

Analysis of the thermogravimetric study results allowed us to conclude that the composition of the zirconium dioxide based nanoparticles obtained by hydrothermal treatment can be presented as a formula comprising a certain amount of chemically bound water:  $Zr_{(1-x)}Y_xO_{(2-0.5x)} \cdot nH_2O$ . The results of estimating the amount of chemically bound water, depending on the content of yttrium oxide in the system, are shown in Fig. 4. Considering the results of [41] relating to water state in the structure of nanoparticles based on zirconium dioxide, we can conclude that in the nanoparticles, where zirconium dioxide is partially substituted by yttrium oxide, water is presented both in the form of crystallization water with dehydration temperature range of  $\sim 150$ – $570$  °C, and in the form of constitution water – the temperature range of removal of  $\sim 570$ – $1120$  °C.

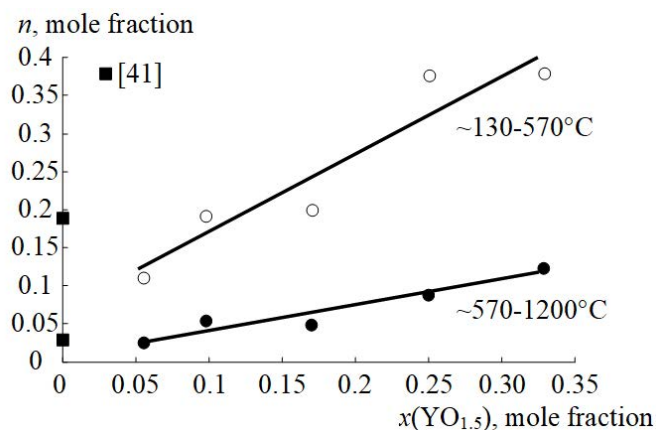


FIG. 4. Amount of water  $n_1(H_2O)$  and  $n_2(H_2O)$  ( $n_2(OH) = 2 \cdot n_2(H_2O)$ ) in the nanoparticles of variable composition ( $n_1(H_2O) + n_2(H_2O) = n(H_2O)$ ) vs. yttrium oxide content in the system

Considering the results of [41] relating to the hydrated state in the nanocrystals based on zirconium dioxide and the relationships shown in Fig. 4, or in the analytical form:

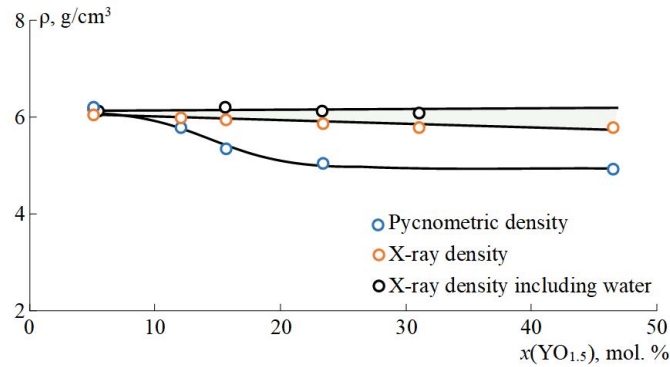
$$n_1(H_2O) = 0.07 + 1.022 \cdot x,$$

$$n_2(H_2O) = 0.012 + 0.325 \cdot x,$$

$$n_2(OH) = 2 \cdot n_2(H_2O) = 0.024 + 0.675 \cdot x,$$

where  $n_1$  is the amount of crystallization water, mole fractions;  $n_2$  is the amount of constitution water, mole fractions, ( $n(H_2O) = n_1(H_2O) + n_2(H_2O)$ ), the formula of the solid solution comprising yttrium oxide and water can be recorded as follows:  $Zr_{1-x}Y_xO_{2-0.5x-0.5(0.024+0.675 \cdot x)}OH_{(0.024+0.675 \cdot x)} \cdot (0.07 + 1.022 \cdot x)H_2O$ . The values obtained are in qualitative compliance with data presented in [41], wherein comprehensive studies by means of proton magnetic resonance, X-ray phase analysis and comprehensive thermal analysis were used to determine the composition of nanoparticles based on zirconium dioxide, expressed by the formula  $ZrO_{1.965}(OH)_{0.07} \cdot 0.19H_2O$ . Some quantitative differences between the chemical composition of a nanocrystalline zirconium dioxide based compound obtained for nanocrystals not containing yttrium oxide in the structure –  $ZrO_{1.965}(OH)_{0.07} \cdot 0.19H_2O$  [41], and the composition obtained by extrapolation  $x \rightarrow 0$  of the expression  $Zr_{1-x}Y_xO_{1.988-0.838x}OH_{(0.024+0.675 \cdot x)} \cdot (0.07 + 1.022 \cdot x)H_2O$ , i.e.  $ZrO_{1.988}OH_{0.024} \cdot 0.07H_2O$ , are apparently due to their structural differences. In the case described in [41], the nanocrystals have a structure close to tetragonal one, which is stabilized by water entry into the lattice. The paper discusses the case of nanocrystals of solid solutions based on zirconium dioxide, whose structure is described as a cubic one, stabilized by the substitution of zirconium ions by yttrium ions in the crystal lattice, with charge compensation in the anion sublattice.

The density of the samples was determined by the method of helium pycnometry, in comparison with the X-ray density shown in Fig. 5. The X-ray density of the crystalline samples was determined from data on the volume of the unit cells and their elemental composition, with and without regard for water included in their structure. Based on the analysis of the relationship in Fig. 5, it can be concluded that as the yttrium oxide amount in the system increases, the values of pycnometric density of the samples somewhat decrease as compared with the X-ray density, calculated both with and without regard for water in the structure. This is most likely due to the presence in the samples enriched with yttrium oxide, especially at a content of  $x > 19.7$  mol.%, where, under hydrothermal synthesis conditions, an amorphous phase is produced that is enriched with hydrated forms of yttrium oxide having significantly lower density than zirconium dioxide based crystalline phases of interest. Since the substance density decreases

FIG. 5. Samples density vs. amount of  $Y_2O_3$ 

during the transition to the amorphous state [42, 43], the density of hydrated forms of yttrium oxide can be estimated as:  $\rho(YOOH) < 4.48 - 4.63 \text{ g/cm}^3$  [44–46],  $\rho(Y(OH)_3) < 3.80 - 3.90 \text{ g/cm}^3$  [44, 47–49].

Based on the analysis of data obtained by small-angle X-ray scattering, size distribution of the particles was determined, and mean values of the particle sizes were calculated (Table 2). Data in Fig. 6 show that as yttrium oxide amount in the system increases, both mean dimensions of crystallites and mean dimensions of particles decrease remarkably. Almost complete matching, within error limits, of the mean dimensions of crystallites and particles (except for the point at 46.4 mol.% of  $Y_2O_3$ ) indicates that the obtained nanoparticles are predominantly monocrystalline. Comparison of the size distribution curves of crystallites and particles (Fig. 7) shows their similar nature. In both cases, there is a tendency towards narrowing of the sizes distribution region and shifting of the size distribution maxima towards smaller sizes both of particles and crystallites, as yttrium oxide content in the system increases, and this is another proof of the above conclusion about monocrystalline nature of the nanoparticles, which is irrespective of the size thereof.

TABLE 2. Results of the study by means of small-angle X-ray analysis

$Y_2O_3$ content in the sample	Particle diameter, nm		Particle surface per unit volume, $m^2/cm^3$  $(S/V)_{particle}$	Density*)	Specific surface
	standard curve method $D$	Guinier method $D_r$		$\rho$	$S_{specific}$
5.0	$12.0 \pm 0.2$	$11.98 \pm 0.05$	$917 \pm 39$	6.21	$151 \pm 9$
8.6	$8.90 \pm 0.04$	$8.77 \pm 0.06$	$1224 \pm 3$	6.19	$197 \pm 5$
16.4	$8.26 \pm 0.06$	$8.29 \pm 0.04$	$1400 \pm 2$	6.17	$225 \pm 3$
23.3	$7.92 \pm 0.8$	$7.84 \pm 0.06$	$1539 \pm 8$	6.14	$248 \pm 2$
31.0	$5.9 \pm 0.2$	$5.7 \pm 0.1$	$1777 \pm 47$	6.12	$293 \pm 7$
46.4	$9.7 \pm 0.6$	$9.4 \pm 0.1$	$1571 \pm 12$	6.11	$254 \pm 5$
57.2	$5.12 \pm 0.06$	$5.08 \pm 0.04$	$1887 \pm 32$	6.06	$309 \pm 3$

\*) X-ray density with regard for water included in the structure

Based on the data on the particle size and their X-ray density with regard for water included in the structure, specific surface areas of the samples were calculated (Fig. 8).

Note the inverse relationship between the samples' specific surface areas on the one hand and the size of nanoparticles and the content of yttrium oxide in the system on the other. This is due to the fact that the nanoparticle sizes themselves steadily decrease as the amount of yttrium oxide in the samples increases. The nature of the relationship between water adsorbed on the nanoparticles' surface on the one hand and their specific surface areas and  $Y_2O_3$  content in the system on the other (Fig. 9) is explained similarly.

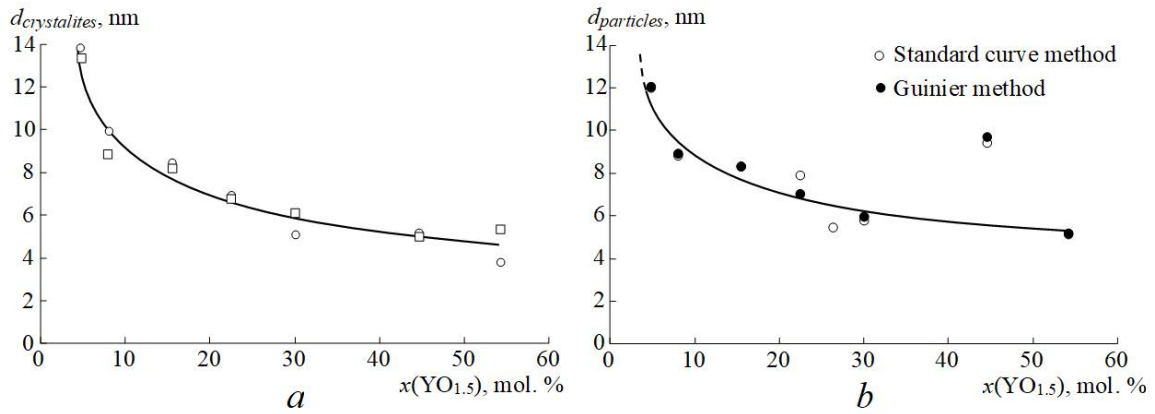


FIG. 6. Crystallite (a) and particles (b) size in the system  $ZrO_2$ - $Y_2O_3$  vs. amount of yttrium oxide

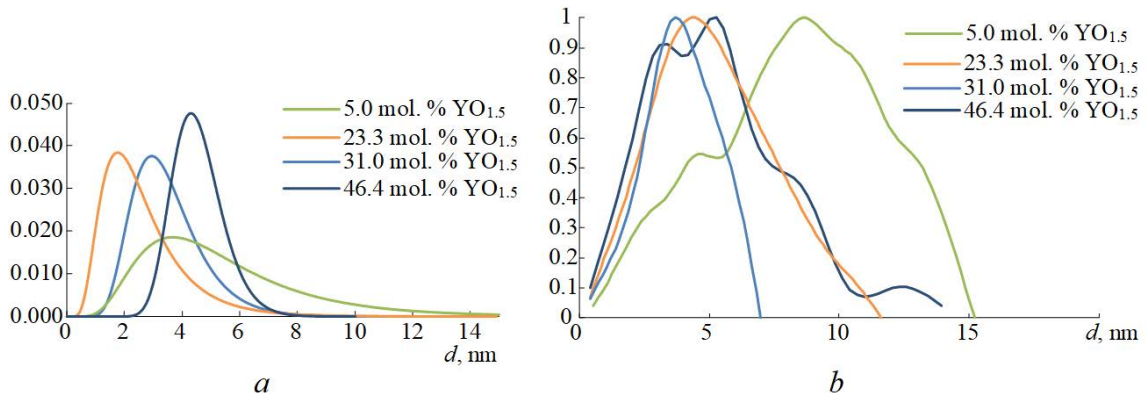


FIG. 7. Size distribution of crystallites (a) and particles (b)

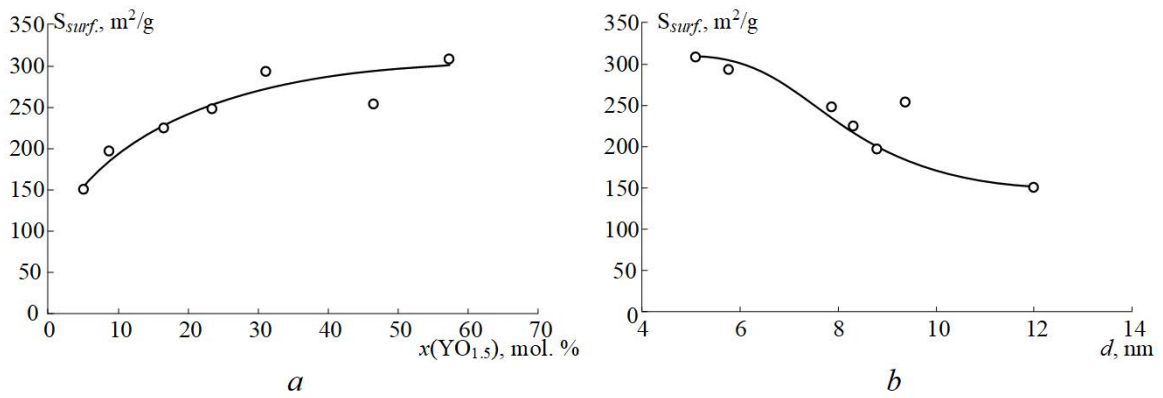


FIG. 8. Specific surface areas of the samples vs composition (a) and size (b) of the particles

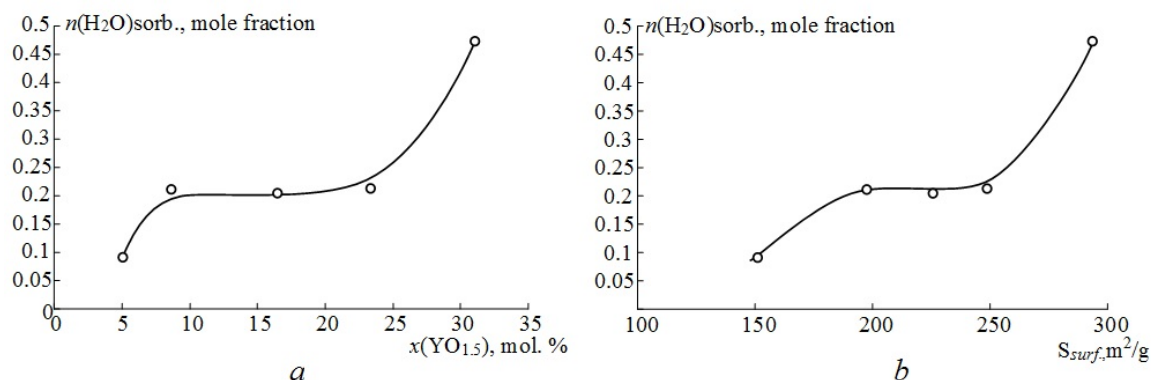


FIG. 9. Amount of water adsorbed on the surface of nanoparticles vs. their specific surface areas and amount of yttrium oxide in the system

#### 4. Conclusion

The study showed that nanocrystalline particles are formed in the  $\text{ZrO}_2\text{-Y}_2\text{O}_3$  system under hydrothermal conditions, with the particle size decreasing as yttrium oxide content in the system increases. The limiting content of  $\text{Y}_2\text{O}_3$  in the nanocrystals based on zirconium dioxide with fluorite-like structure is 21.7–22.6 mol.%, when they are formed by hydrothermal treatment of co-precipitated hydroxides at  $T = 250\text{ }^\circ\text{C}$ , pressure  $P = 70\text{ MPa}$ , for 4 h. Yttrium oxide not included in the structure forms an amorphous phase, stable even upon high-temperature treatment of the samples. It is shown that under hydrothermal conditions the structure of nanocrystals based on  $\text{ZrO}_2(\text{Y}_2\text{O}_3)$  solid solution includes water, its content depending on yttrium oxide concentration in the solid solution. Comparison of the data on the crystallites' and particles' size distribution showed that the nanoparticles formed under hydrothermal conditions are monocrystalline structures.

#### Acknowledgments

The authors express their gratitude to V. V. Gusarov for the attention he paid to the work.

X-ray diffraction and SEM/EDS was performed using the equipment of the Engineering Center Saint Petersburg State Institute of Technology.

This study was financially supported by the Russian Science Foundation (project no. 20-63-47016).

#### References

- [1] Degtyarev S.A., Voronin G.F. Solution of ill-posed problems in thermodynamics of phase equilibria. The  $\text{ZrO}_2\text{-Y}_2\text{O}_3$  system. *Calphad*, 1988, **12**(1), P. 73–82.
- [2] Stubican V.S., Hink R.C., Ray S.P. Phase equilibria and ordering in the system  $\text{ZrO}_2\text{-Y}_2\text{O}_3$ . *J. Am. Ceram. Soc.*, 1978, **61**(1-2), P. 17–21.
- [3] Srivastava K.K., Patil R.N., Choudhary C.B., Gokhale K.V.G.K., Subbarao E.C. Revised phase diagram of the system  $\text{ZrO}_2\text{-YO}_{1.5}$ . *Trans. J. Br. Ceram. Soc.*, 1974, **73**(5), P. 85–91.
- [4] Andrievskaya E.R. Phase equilibria in the refractory oxide systems of zirconia, hafnia and yttria with rare-earth oxides. *J. Eur. Ceram. Soc.*, 2008, **28**, P. 2363–2388.
- [5] Bugrov A.N., Almjasheva O.V. Effect of hydrothermal synthesis conditions on the morphology of  $\text{ZrO}_2$  nanoparticles. *Nanosystems: Physics, Chemistry, Mathematics*, 2013, **4**(6), P. 810.
- [6] Pozhidaeva O.V., Korytkova E.N., Drozdova I.A., Gusarov V.V. Phase state and particle size of ultradispersed zirconium dioxide as influenced by condition of hydrothermal synthesis. *Russian Journal of General Chemistry*, 1999, **69**(8), P. 1219–1222.
- [7] Yaprntsev A.D., Baranchikov A.E., Gubanova N.N., Ivanov V.K., Tret'yakov Yu.D. Synthesis of nanocrystalline  $\text{ZrO}_2$  with tailored phase composition and microstructure under high-power sonication. *Inorganic Materials*, 2012, **48**(5), P. 494–499.
- [8] Wang H., Li G., Xue Y., Li L. Hydrated surface structure and its impacts on the stabilization of t- $\text{ZrO}_2$ . *Journal of Solid State Chemistry*, 2007, **180**(10), P. 2790–2797.
- [9] Meskin P.E., Gavrilov A.I., Maksimov V.D., Ivanov V.K., Churagulov B.R. Hydrothermal/microwave and hydrothermal/ultrasonic synthesis of nanocrystalline titania, zirconia, and hafnia. *Russian Journal of Inorganic Chemistry*, 2007, **52**(11), P. 1648–1656.
- [10] Ivanov V.K., Baranov A.N., Oleinikov N.N., Tret'yakov Y.D. Fractal Surfaces of  $\text{ZrO}_2$ ,  $\text{WO}_3$  and  $\text{CeO}_2$ . Powders. *Inorganic materials*, 2002, **38**(12), P. 1224–1227.
- [11] Taguchi M., Nakaneb T., Matsushita A., Sakkab Y., Uchikoshib T., Funazukuria T., Nakab T. One-pot synthesis of monoclinic  $\text{ZrO}_2$  nanocrystals under subcritical hydrothermal conditions. *The Journal of Supercritical Fluids*, 2014, **85**, P. 57–61.
- [12] Stenina I.A., Voropaeva E.Y., Veresov A.G., Kapustin G.I., Yaroslavtsev A.B. Effect of precipitation pH and heat treatment on the properties of hydrous zirconium dioxide. *Russian Journal of Inorganic Chemistry*, 2008, **53**(3), P. 350–356.
- [13] Glushkova, V.B., Lapshin, A.V., Vershinin, A.A. et al. Phase formation of zirconia-based solid solutions synthesized from peroxides. *Glass Physics and Chemistry*, 2004, **30**(6), P. 558–563.

- [14] Zhang Y., Li A., Yan Z., Xu G., Liao C., Yan C.  $(ZrO_2)_{0.85}(ReO_{1.5})_{0.15}$  (Re = Sc, Y) solid solutions prepared via three Pechini-type gel routes: 1-gel formation and calcination behaviors. *Journal of Solid State Chemistry*, 2003, **171**, P. 434–438.
- [15] Popov V.V., Menushenkov A.P., Yastrebtev A.A., Arzhatkina L.A., Tsarenko N.A., Shchetinin I.V., Zheleznyi M.V., Ponkratov K.V. Regularities of formation of complex oxides with the fluorite structure in the  $ZrO_2$ - $Y_2O_3$  system. *Russian Journal of Inorganic Chemistry*, 2017, **62**(9), P. 1147–1154.
- [16] Almjasheva O.V., Gusarov V.V., Danilevich Ya.B., Kovalenko A.N., Ugolkov V.L. Nanocrystals of  $ZrO_2$  as sorption heat accumulators. *Glass Physics and Chemistry*, 2007, **33**(6), P. 587–589.
- [17] Fokin B.S., Belenkiy M.Ya., Almjashev V.I., Khabensky V.B., Almjasheva O.V., Gusarov V.V. Critical heat flux in a boiling aqueous dispersion of nanoparticles. *Technical Physics Letters*, 2009, **35**(5), P. 440–442.
- [18] Kablov E.N., Stolyarova V.L., Vorozhtcov V.A., Lopatin S.I., Karachetvsev F.N. Thermodynamics and vaporization of ceramics based on the  $Y_2O_3$ - $ZrO_2$  system studied by KEMS. *Journal of Alloys and Compounds*, 2019, **794**, P. 606–614.
- [19] Bugrov A.N., Smyslov R.Yu., Zavialova A.Yu., Kopitsa G.P. The influence of chemical prehistory on the structure, photoluminescent properties, surface and biological characteristics of  $Zr_{0.98}Eu_{0.02}O_{1.99}$  nanophosphors. *Nanosystems: Physics, Chemistry, Mathematics*, 2019, **10**(2), P. 164–175.
- [20] Vildanova M.F., Nikolskaia A.B., Kozlov S.S., Karyagina O.K., Larina L.L., Shevaleevskiy O.I., Almjasheva O.V., Gusarov V.V. Nanostructured  $ZrO_2$ - $Y_2O_3$ -based system for perovskite solar cells. *Doklady Physical Chemistry*, 2019, **484**(2), P. 36–38.
- [21] Larina L.L., Alexeeva O.V., Almjasheva O.V., V.V. Gusarov, Kozlov S.S., Nikolskaia A.B., Vildanova M.F., Shevaleevskiy O.I. Very wide-bandgap nanostructured metal oxide materials for perovskite solar cells. *Nanosystems: Physics, Chemistry, Mathematics*, 2019, **10**(1), P. 70–74.
- [22] Zadorozhnaya O.Y., Napochatov Y.K., Agarkova E.A., Tiunova O.V. Layered solid-electrolyte membranes based on zirconia: production technology. *Russian Journal of Electrochemistry*, 2020, **56**(2), P. 124–131.
- [23] Kalitina, E.G., Pikalova, E.Y. Preparation and properties of stable suspensions of  $ZrO_2$ - $Y_2O_3$  powders with different particle sizes for electrophoretic deposition. *Inorganic Materials*, 2020, **56**(9), P. 941–948.
- [24] Rylski A., Siczek K. The effect of addition of nanoparticles, especially  $ZrO_2$ -based, on tribological behavior of lubricants. *Lubricants*, 2020, **8**(3), P. 1–25.
- [25] Hu C., Sun J., Long C., Wu L., Zhou C., Zhang X. Synthesis of nano zirconium oxide and its application in dentistry. *Nanotechnol Rev.*, 2019, **8**(1), P. 396–404.
- [26] Bumajdad A., Nazeer A.A., Al Sagheer F, Nahar S. Zaki Mohamed I. Controlled synthesis of  $ZrO_2$  nanoparticles with tailored size, morphology and crystal phases via organic/inorganic hybrid films. *Scientific Reports*, 2018, **8**, P. 3695.
- [27] Precious-Ayanwale A, Donohué-Cornejo A., Cuevas-González J.C., Espinosa-Cristóbal L.F., Reyes-López S.Y. Review of the synthesis, characterization and application of zirconia mixed metal oxide nanoparticles. *International Journal of Research – GRANTHAALAYAH*, 2018, **6**(8), P. 136–145.
- [28] Almjasheva O.V., Smirnov A.V., Fedorov B. A., Tomkovich M.V., Gusarov V.V. Structural features of  $ZrO_2$ - $Y_2O_3$  and  $ZrO_2$ - $Gd_2O_3$  nanoparticles formed under hydrothermal conditions. *Russian Journal of General Chemistry*, 2014, **84**(5), P. 804–809.
- [29] Almjasheva O.V., Krasilin A.A., Gusarov V.V. Formation mechanism of core-shell nanocrystals obtained via dehydration of coprecipitated hydroxides at hydrothermal conditions. *Nanosystems: Physics, Chemistry, Mathematics*, 2018, **9**(4), P. 568–572.
- [30] Tomkovich M.V., Andrievskaya E.R., Gusarov V.V. Formation under hydrothermal condition and structural features of nanoparticles based on the system  $ZrO_2$  -  $Gd_2O_3$ . *Nanosystems: Physics, Chemistry, Mathematics*, 2011, **2**(2), P. 139.
- [31] Enikeeva M.O., Kenges K.M., Proskurina O.V., Danilovich D.P., Gusarov V.V. Influence of hydrothermal treatment conditions on the formation of lanthanum orthophosphate nanoparticles of monazite structure. *Russian Journal of Applied Chemistry*, 2020, **93**(4), P. 540–548.
- [32] Popkov V.I., Bachina A.K., Valeeva A.A., Lobinsky A.A., Gerasimov E.Y., Rempel A.A. Synthesis, morphology and electrochemical properties of spherulite titania nanocrystals. *Ceramics International*, 46(15), P. 24483–24487.
- [33] Guinier A., Fournet G. *Small-angle Scattering of X-rays*. New-York, Wiley, 1955. 268 .
- [34] Kuchko A.V., Smirnov A.V. The computation of the nanoparticles volume distribution function and the specific surface area based on the small-angle x-ray scattering indicatrix by the meyhod of the statistical regularization. *Nanosystems: Physics, Chemistry, Mathematics*, 2012, **3**(3), P. 76–91.
- [35] Fabregas I.O., Craievich A.F., Fantini M.C.A., Millen R.P., Temperini M.L.A, Lamas D.G. Tetragonal-cubic phase boundary in nanocrystalline  $ZrO_2$ - $Y_2O_3$  solid solutions synthesized by gel-combustion. *Journal of Alloys and Compounds*, 2011, **509**, P. 5177–5182.
- [36] Dell'Agli G., Mascolo G. Hydrothermal synthesis of  $ZrO_2$ - $Y_2O_3$  solid solutions at low temperature. *J. Eur. Ceram. Soc.*, 2000, **20**(2), P. 139–145.
- [37] Kim D.-J. Lattice parameters, ionic conductivities, and solubility limits in fluorite-structure  $MO_2$  oxide [M =  $Hf^{4+}$ ,  $Zr^{4+}$ ,  $Ce^{4+}$ ,  $Th^{4+}$ ,  $U^{4+}$ ] solid solutions. *J. Am. Ceram. Soc.*, 1989, **72**(8), P. 1415–1421.
- [38] Almjasheva O.V., Gusarov V.V. Hydrothermal synthesis of nanosized and amorphous alumina in the  $ZrO_2$ - $Al_2O_3$ - $H_2O$  system. *Russian Journal Inorganic Chemistry*, 2007, **52**(8), P. 1194–1200.
- [39] Al'myashev O.V., Gusarov V.V. Features of the phase formation in the nanocomposites. *Russian Journal of General Chemistry*, 2010, **80**(3), P. 385–390.
- [40] Al'myasheva O.V., Ugolkov V.L., Gusarov V.V. Thermochemical analysis of desorption and adsorption of water on the surface of zirconium dioxide nanoparticles. *Russian Journal of Applied Chemistry*, 2008, **81**(4), P. 609–613.
- [41] Almjasheva O.V., Denisova T.A. Water state in nanocrystals of zirconium dioxide prepared under hydrothermal conditions and its influence on structural transformations. *Russian Journal of General Chemistry*, 2017, **87**(1), P. 1–7.
- [42] Amorphous Metallic Alloys, Ed. by F.E. Lyuborsky (Butterworths, London, 1983; Metallurgiya, Moscow, 1987).
- [43] Gabelkov S.V., Tarasov R.V., Poltavtsev N.S., Logvinkov D.S., Mironova A.G. Phase transformation in the nanocrystallization of amorphous zirconium oxide. *Questions of atomic science and technology. Series: Physics of radiation damage and radiation materials science 2004*, **3**, P. 116–120. (in Russian)
- [44] Klevtsov P.V., Klevtsova R.F., Sheina L.P. Crystalline yttrium hydroxides. *Journal of Structural Chemistry*, 1965, **5**(4), P. 536–541.
- [45] Klevtsova R.F., Klevtsov P.V. The crystal structure of YOOH. *J. Struct. Chem.*, 1965, **5**, P. 795–797.
- [46] Christensen A.N. A Reinvestigation of the Crystal structure of YOOH. *Acta Chem. Scand*, 1965, **19**(6), P. 1504–1505.

- [47] Landolt-Börnstein – Group III Condensed Matter 7b1. Ed by K.-H. Hellwege, A.M. Hellwege – Key Element O. Part 1.1975, Springer-Verlag Berlin Heidelberg.
- [48] Christensen A.N., Hazell R.G., Nilsson A. Hydrothermal investigation of the systems  $Y_2O_3-H_2O-Na_2O$ ,  $Y_2O_3-D_2O-Na_2O$ ,  $Y_2O_3-H_2O$ , and  $Y_2O_3-H_2O-NH_3$ . *Acta Chem. Scand.*, 1967, **21**(2), P. 481–492.
- [49] Schubert K., Seitz A. Kristallstruktur von  $Y(OH)_3$ . *Zeitschrift für anorganische und allgemeine Chemie (ZAAC)*, 1947, **254**(12), P. 116–125.



# **NANOSYSTEMS:**

**PHYSICS, CHEMISTRY, MATHEMATICS**

## **INFORMATION FOR AUTHORS**

The journal publishes research articles and reviews, and also short scientific papers (letters) which are unpublished and have not been accepted for publication in other magazines. Articles should be submitted in English. All articles are reviewed, then if necessary come back to the author to completion.

The journal is indexed in Web of Science Core Collection (Emerging Sources Citation Index), Chemical Abstract Service of the American Chemical Society, Zentralblatt MATH and in Russian Scientific Citation Index.

### **Author should submit the following materials:**

1. Article file in English, containing article title, the initials and the surname of the authors, Institute (University), postal address, the electronic address, the summary, keywords, MSC or PACS index, article text, the list of references.
2. Files with illustrations, files with tables.
3. The covering letter in English containing the article information (article name, MSC or PACS index, keywords, the summary, the literature) and about all authors (the surname, names, the full name of places of work, the mailing address with the postal code, contact phone number with a city code, the electronic address).
4. The expert judgement on possibility of publication of the article in open press (for authors from Russia).

Authors can submit a paper and the corresponding files to the following addresses: nanojournal.ifmo@gmail.com, popov1955@gmail.com.

### **Text requirements**

Articles should be prepared with using of text editors MS Word or LaTeX (preferable). It is necessary to submit source file (LaTeX) and a pdf copy. In the name of files the English alphabet is used. The recommended size of short communications (letters) is 4-6 pages, research articles– 6-15 pages, reviews – 30 pages.

#### Recommendations for text in MS Word:

Formulas should be written using Math Type. Figures and tables with captions should be inserted in the text. Additionally, authors present separate files for all figures and Word files of tables.

**Recommendations for text in LaTeX:**

Please, use standard LaTeX without macros and additional style files. The list of references should be included in the main LaTeX file. Source LaTeX file of the paper with the corresponding pdf file and files of figures should be submitted.

References in the article text are given in square brackets. The list of references should be prepared in accordance with the following samples:

- [1] Surname N. *Book Title*. Nauka Publishing House, Saint Petersburg, 2000, 281 pp.
- [2] Surname N., Surname N. Paper title. *Journal Name*, 2010, **1** (5), P. 17-23.
- [3] Surname N., Surname N. Lecture title. In: Abstracts/Proceedings of the Conference, Place and Date, 2000, P. 17-23.
- [4] Surname N., Surname N. Paper title, 2000, URL: <http://books.ifmo.ru/ntv>.
- [5] Surname N., Surname N. Patent Name. Patent No. 11111, 2010, Bul. No. 33, 5 pp.
- [6] Surname N., Surname N. Thesis Title. Thesis for full doctor degree in math. and physics, Saint Petersburg, 2000, 105 pp.

**Requirements to illustrations**

Illustrations should be submitted as separate black-and-white files. Formats of files – jpeg, eps, tiff.



# **NANOSYSTEMS:**

**PHYSICS, CHEMISTRY, MATHEMATICS**

**Журнал зарегистрирован**

Федеральной службой по надзору в сфере связи, информационных технологий и массовых коммуникаций

(свидетельство ПИ № ФС 77 - 49048 от 22.03.2012 г.)

ISSN 2220-8054

**Учредитель:** федеральное государственное автономное образовательное учреждение высшего образования

«Санкт-Петербургский национальный исследовательский университет информационных технологий, механики и оптики»

**Издатель:** федеральное государственное автономное образовательное учреждение высшего образования

«Санкт-Петербургский национальный исследовательский университет информационных технологий, механики и оптики»

**Отпечатано** в Учреждении «Университетские телекоммуникации»

Адрес: 197101, Санкт-Петербург, Кронверкский пр., 49

**Подписка на журнал НФХМ**

На первое полугодие 2021 года подписка осуществляется через

ОАО Агентство «Роспечать»

Подписной индекс 57385 в каталоге «Издания органов научно-технической информации»